Doctoral dissertation

Thesis submitted at the Faculty of Engineering by

Julien BOSSU

in fulfillment of the requirements for the degree of

Doctor in Engineering Sciences and Technology

Eco-Design of Pellets-Based Additive Manufacturing Feedstock: Development of a Sustainable Binder and Environmental Impact Assessment

---

Composition of the Jury:

Prof.	Maurice Gonon	Université de Mons	Chairman
Prof.	Fabienne Delaunois	Université de Mons	Supervisor
Prof.	Edouard Rivière-Lorphèvre	Université de Mons	Co-supervisor
Prof.	Jean-Marie Raquez	Université de Mons	Secretary
Dr.	Grégory Martic	Belgian Ceramic Research Centre	Member
Prof.	Stéphane Godet	Université Libre de Bruxelles	Member
Prof.	Jérémie Soulestin	IMT Nord Europe	Member

June, 2025

Faculty of Engineering
Metallurgy Lab
Machine Design and Production Engineering Lab
Materials Institute

This doctoral thesis represents one of the most intellectually and personally enriching undertakings of my life. Its completion would not have been possible without the guidance, support, and encouragement of numerous individuals to whom I am profoundly grateful.

I wish to express my deepest gratitude to my supervisor, Professor Fabienne Delaunois, and my co-supervisor, Professor Edouard Rivière-Lorphèvre, for their expert guidance, critical insights, and unwavering support throughout the duration of this work. Their mentorship has been instrumental in shaping both the scientific direction of this research and my development as an independent researcher.

I also extend my sincere thanks to the members of my doctoral committee, Professor Jean-Marie Raquez, Professor Maurice Gonon, and Dr. Grégory Martic, for their constructive feedback, valuable suggestions, and ongoing support, which have significantly enriched the quality and scope of this research.

This research was carried out within the framework of the HyProPAM project, to which I am immensely grateful. The Walloon regional government funded this research under grant 2110084 (Win^{2}Wal HyProPAM research project). I would like to warmly thank all those who contributed directly or indirectly to the success of this project, with special mention to the Belgian Ceramic Research Center (BCRC) and to Dr. Cathy Delmotte for her exceptional involvement, expert advice, and support throughout several phases of this work. I am equally grateful to Dr. Samira Benali for the training she provided on various forming and analytical techniques available at the Faculty of Science.

To my colleagues and lab mates, thank you for fostering a collegial and stimulating work environment. The many discussions, collaborative moments, and shared challenges have not only enhanced this research but also made this journey memorable. I am especially thankful for the friendships built along the way and the light-hearted moments that brought balance to demanding periods.

I would like to express my deep gratitude to my family. To my parents, thank you for your unconditional love, support, and sacrifices that made this academic path possible. To my partner, Blandine Lebegue, your patience, understandment, and unwavering encouragement have been a true pillar of strength throughout this journey.

Lastly, I am thankful to my friends outside academia, who have provided perspective, kept me grounded, and reminded me of the world beyond research. Your presence and encouragement have been essential in helping me maintain motivation and balance.

This thesis is not only the result of my efforts but also the product of a collective journey shared with many remarkable individuals. To each of you, I extend my most sincere thanks.

Abstract

In response to the growing demand for sustainable and efficient manufacturing of complex metallic parts, this thesis presents a comprehensive study on the design, characterization, and environmental evaluation of a sustainable feedstock formulation for titanium-based additive manufacturing using the Pellet Additive Manufacturing (PAM) process. Driven by the need for more environmentally responsible and technically versatile fabrication methods for complex metallic components, this research investigates PAM as a promising alternative to conventional techniques such as Metal Injection Molding (MIM). An initial qualitative assessment of energy consumption was conducted to compare PAM with MIM. Due to limited data availability, software-based modeling was not feasible. The study highlights PAM's advantages in terms of material efficiency, reduced tooling requirements, lower scrap rates, and suitability for small-batch or customized production. These sustainability drivers served as a strategic foundation for feedstock development.

A thorough literature review was conducted to identify the limitations of existing binder systems and the critical rheological and thermal requirements for feedstocks in metal AM.

Based on this, a novel hybrid binder system was formulated, combining polyethylene glycol (PEG) and polyvinyl butyral (PVB) as the primary matrix, with methylcellulose (MC) and stearic acid (SA) as rheological and stabilizing additives. Several formulations were prepared with Ti6Al4V powder, varying MC and SA contents. Rheological tests revealed that the formulation with 3 vol.% MC and 3 vol.% SA achieved an optimal balance of shear-thinning behavior, structural consistency, and printability, without the instability observed at higher MC concentrations. Thermogravimetric analysis confirmed the compatibility of the binder components and the feasibility of staged thermal debinding. Morphological and flow assessments indicated a well-homogenized system with minimal phase separation. Experimental printing trials demonstrated that the formulation with 3 vol.% MC and 3 vol.% SA outperforms commercial feedstocks in visual quality, dimensional accuracy, and ease of parameter tuning.

Beyond its technical contributions, this thesis adopts an integrated approach that aligns materials engineering with environmental responsibility. By incorporating energy and material efficiency considerations into the early design stages and validating performance through rigorous experimentation, this work contributes to the advancement of greener, high-performance feedstocks for emerging metal AM technologies like PAM.

The originality of this research lies in its dual focus—technological innovation and environmental responsibility—offering a holistic perspective on PAM's viability as a sustainable solution for manufacturing complex titanium components. The outcomes are expected to support industrial adoption, inform future eco-design strategies, and inspire continued innovation in hybrid additive-subtractive manufacturing platforms.

Contents

List of Figures

List of Tables

Nomenclature

Abbreviation / Symbol	**Definition**
3D	Three-Dimensional
AM	Additive Manufacturing
DfAM	Design for Additive Manufacturing
CAD	Computer-Aided Design
STL	Standard Tessellation Language
MEX	Material Extrusion
FDM	Fused Deposition Modeling
FFF	Fused Filament Fabrication
PAM	Pellet Additive Manufacturing
MIM	Metal Injection Molding
PIM	Powder Injection Molding
Ti6Al4V	Titanium alloy with 6% Aluminium and 4% Vanadium
PEG	Polyethylene Glycol
PVB	Polyvinyl Butyral
MC	Methylcellulose
SA	Stearic Acid
VOC	Volatile Organic Compounds
LCI	Life Cycle Inventory
LCIA	Life Cycle Impact Assessment
LCA	Life Cycle Assessment
SLM	Selective Laser Melting
EBM	Electron Beam Melting
SLA	Stereolithography
SLS	Selective Laser Sintering
LOM	Laminated Object Manufacturing
BJ	Binder Jetting
WAAM	Wire Arc Additive Manufacturing
LENS	Laser Engineered Net Shaping
G’	Storage Modulus (elastic component)
G”	Loss Modulus (viscous component)
η	Viscosity

τ	Shear stress (Pa)
$\dot{\gamma}$	Shear rate (s^{-1})
T_g	Glass Transition Temperature
HV	Vickers Hardness
wt.%	Percentage in mass
vol.%	Percentage in volume

CHAPTER 1

General Introduction

Additive Manufacturing (AM) is transforming the manufacturing landscape by enabling the layer-by-layer fabrication of complex geometries directly from digital designs. Unlike traditional subtractive or formative methods, AM allows for greater design freedom, material efficiency, and on-demand production. Among the various AM techniques, Material Extrusion (MEX) processes—such as Fused Deposition Modeling (FDM) and Pellets Additive Manufacturing (PAM)—stand out due to their accessibility, cost-effectiveness, and adaptability to a wide range of materials.

In recent years, MEX-based processes have expanded from polymers to metals and ceramics, opening up new industrial applications. While FDM is widely used and well-documented, PAM, which uses pelletized feedstocks instead of filaments, offers additional advantages, including compatibility with highly filled materials and easier recycling of unused material. However, PAM remains underdeveloped, particularly in the domain of metal AM, where challenges in feedstock formulation, process control, and sustainability are yet to be fully addressed.

Context and Motivation of the PhD Thesis

This doctoral research is part of the HyProPAM project, funded by the Walloon Region, which aims at developing a hybrid manufacturing platform combining PAM with mechanical and laser machining. This hybrid approach offers a flexible and versatile solution for producing high-performance, complex parts. Among the target materials, the titanium alloy Ti6Al4V was selected for its strategic importance in aerospace, biomedical, and industrial applications, due to its high strength-to-weight ratio, corrosion resistance, and biocompatibility.

However, implementing PAM for Ti6Al4V presents significant obstacles, particularly in feedstock formulation. At the beginning of the project, a commercial Metal Injection Molding MIM feedstock (PolyMIM Ti6Al4V) was tested as a reference. Despite being one of the few water-soluble titanium feedstocks available in Europe, it was not optimized for extrusion: it required high processing temperatures, exhibited poor flow behavior, limited interlayer adhesion, and necessitated bed heating, making it poorly suited for PAM in terms of printability and energy efficiency.

Moreover, PAM belongs to the family of indirect AM processes, requiring debinding and sintering steps after shaping. These steps often involve the use of toxic solvents (e.g., acetone, chloroform, THF), raising concerns about operator safety and environmental impact. While PAM can use feedstocks developed for injection molding, the surface quality of printed parts remains inferior due to the staircase effect inherent in layer-by-layer deposition.

Scientific Objectives

This thesis addresses two major scientific and technological challenges:

1. Development of a Sustainable Feedstock for PAM
   The primary objective is to develop a tailored feedstock for PAM, specifically for Ti6Al4V, using a partially or fully water-soluble binder. The formulation strategy focuses on combining:

   - Polyethylene glycol (PEG) as the main water-soluble phase,
   - Polyvinyl butyral (PVB) as the structural backbone polymer,
   - Stearic acid (SA) as a dispersant and plasticizer,
   - Methylcellulose (MC) as a bio-based viscosity modifier.

   These components were selected to improve printability, reduce processing temperatures, and eliminate the need for toxic solvents during debinding. The goal is to create a feedstock that flows easily at low temperatures, adheres spontaneously to the print bed without heating, and maintains good interlayer cohesion—thereby reducing energy consumption and improving sustainability.

2. Environmental Evaluation through Qualitative Assessment of Energy and Materials Consumption
   A qualitative assessment of energy and materials consumption was carried out to compare the environmental performance of PAM and MIM for the same Ti6Al4V part. While FDM has been widely studied, data for PAM and metal MEX processes remain scarce. Due to limited data availability, a full Life Cycle Assessment (LCA) could not be performed as initially intended. Instead, the analysis focused on a cradle-to-gate perspective, considering energy and material inputs, emissions, and waste generation. This approach provides meaningful insights into the sustainability potential of PAM and identifies key areas for further optimization.

Conclusion

In light of the growing demand for sustainable and high-performance manufacturing technologies, this thesis addresses a timely and critical challenge: the development of an eco-responsible feedstock for PAM of titanium alloy Ti6Al4V, and the evaluation of its environmental impact through a comparative qualitative assessment of energy and materials consumption with MIM. Although a complete LCA could not be conducted due to data limitations, the study offers meaningful indicators of environmental performance. By combining material formulation, process optimization, and environmental analysis, this research aims at contribute both to the scientific understanding of metal extrusion-based AM and to the goal of reducing the ecological footprint of advanced manufacturing processes.

The originality of this work lies in its dual approach, technological and environmental, offering a comprehensive perspective on the viability of PAM as a sustainable alternative for producing complex, high-value titanium components. The outcomes of this thesis are expected to support the industrial deployment of PAM, inform future eco-design strategies, and pave the way for further innovations in hybrid additive-subtractive manufacturing platforms.

Figure 1.1 presents an overview of the objectives of the PhD thesis.

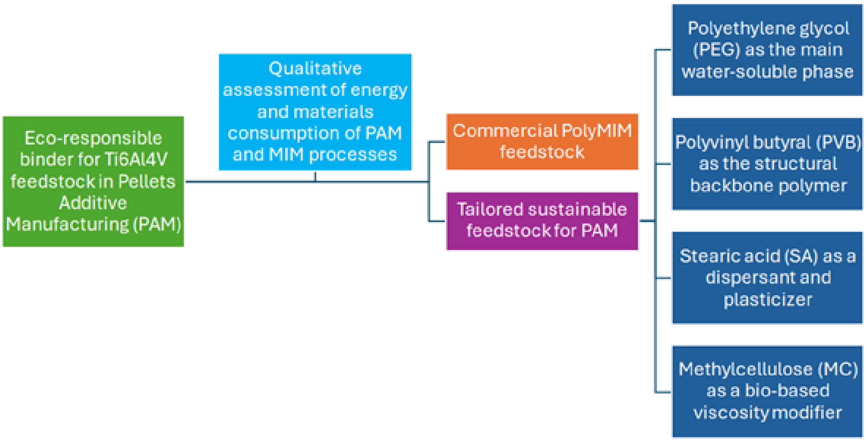

Figure 1.1: Overview of the objectives of the thesis

Each chapter in this PhD thesis is summarized as follows:

Chapter I: General Introduction; presentation of the context of the research and of the originality of the PhD thesis.

Chapter II: State-of-the-art; summary of the background of this work and the literature review.

Chapter III: Comparative Study on Energy and Materials Consumption in PAM and MIM Processes; comparison of the environmental impact of two manufacturing methods—PAM and MIM—for producing titanium dental implants; evaluation of which process is more efficient in terms of energy and material use, depending on production volume.

Chapter IV: Context of experimental research; presentation of the research context within its framework in the HyProPAM project.

Chapter V: Materials, Methods, and Characterizations; explanation of the detailed information of the materials used, with the detailed information about the applied methods and their condition, as well as the techniques that were used for the characterization and validation of the results.

Chapter VI: Commercial Ti6Al4V feedstock for PAM process; study of the properties of the HyProPAM feedstock, a feedstock initially dedicated to MIM process

Chapter VII: Feedstock for PAM; study of various eco-responsible Ti6Al4V feedstocks using sustainable compounds.

Chapter VIII: Conclusions and Prospects

Part I

Literature review

CHAPTER 2

State of the art

This chapter provides a comprehensive overview of the current knowledge and technological context relevant to the development of eco-responsible feedstock for pellet-based additive manufacturing.

2.1 Introduction

Additive manufacturing, commonly knows as 3D printing, is defined by the ISO/ASTM52900 as a process of joining materials to make parts from 3D model data, usually layer-by-layer, as opposed to subtractive manufacturing and formative manufacturing methodologies [1]. This process has gained popularity in recent years for the fabrication of various materials, including ceramics, polymers, and metals [2, 3].

Table 2.1: AM Technologies with Descriptions, Energy Sources, and Materials [4]

AM category	**Technologies**	**Description**	**Energy source**	**Materials**
Binder Jetting	BJ	A liquid bonding agent is selectively deposited to join powdered materials.	Thermal energy	Metal powders
Directed Energy Deposition	LENS, WAAM	Material is melted by focused thermal energy followed by their fusion and deposition.	Laser beam/electric arc	Metal powders, wires
Material Extrusion	FDM, LDM, MJP	Material is selectively deposited through a nozzle orifice. Droplets of materials are selectively deposited.	Thermal energy	Polymer filaments, polymers, wax, composites
Powder Bed Fusion	SLS, SLM, DMLS	Powder bed is selectively fused using thermal energy.	Laser/electron-beam, photo-curing	Polymers, metal, and ceramic powders
Sheet Lamination	LOM	Sheets of material are bonded to create a part.	Thermal energy	Plastic/Metal sheets
Vat Polymerization	SLA	Liquid photopolymer is vat and is selectively cured by light-activated polymerization.	Ultraviolet light	Photopolymers

AM encompasses a variety of technologies categorized according to their material deposition mechanism and energy source, as summarized in Table 2.1. Binder Jetting (BJ) uses thermal energy to selectively deposit a liquid binding agent onto a powder bed, typically composed of metal or ceramic particles. Directed Energy Deposition (DED) includes processes such as Laser Engineered Net Shaping (LENS) and Wire Arc Additive Manufacturing (WAAM), where focused energy sources like lasers or electric arcs melt feedstock material (powder or wire) during deposition. Material Extrusion, including processes such as Fused Deposition Modeling (FDM), Low-Temperature Deposition Manufacturing (LDM), and Material Jetting Printing (MJP), involves pushing thermoplastic polymers, waxes, or slurries through a nozzle. Powder Bed Fusion (PBF), which includes Selective Laser Sintering (SLS), Selective Laser Melting (SLM), and Direct Metal Laser Sintering (DMLS), relies on lasers or electron beams to selectively fuse powder particles layer-by-layer. Sheet Lamination, such as Laminated Object Manufacturing (LOM), involves bonding thin layers of plastic, paper, or metal sheets using adhesives or ultrasonic welding. Finally, Vat Photopolymerization, typified by Stereolithography (SLA), uses ultraviolet (UV) light to selectively cure liquid photopolymer resins within a vat, enabling the production of parts with high resolution and surface quality.

The most important techniques are SLA, MEX such as Fused Filament Fabrication (FFF), and SLM or electron beam melting (EBM) [5].

As illustrated in Figure 2.1, the AM market is experiencing continuous and rapid growth. Starting at approximately $15 billion in 2022, it is projected to exceed $95 billion by 2032.

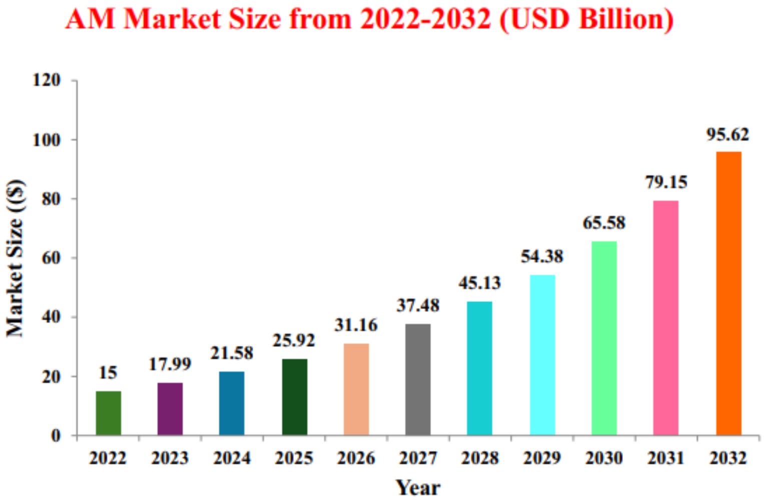

Figure 2.1: Growing trend of AM Market size [6]

This significant increase reflects the expanding adoption of AM technologies across various sectors, including aerospace, healthcare, and automotive. The average annual growth rate suggests increasing industrial reliance on AM for both prototyping and final part production, supported by advancements in materials, machine capabilities, and digital workflows.

This literature review focuses on key aspects of AM, with particular emphasis on fused filament deposition using material extrusion. Particular attention is given to feedstock development for metals, especially the titanium alloy Ti6Al4V. Understanding the rheological behavior of both the feedstock and its binder is essential for screw-based material extrusion, and therefore constitutes a central focus of this review. Additionally, this review will explore the different compositions of feedstock and binder that have already been developed. The review also explores life cycle assessment (LCA) to identify whether comparable studies have previously been conducted. This will aid in assessing the environmental impact of this technology. The chapter concludes with a synthesis and outlines the strategic direction of the research.

2.2 Additive Manufacturing (AM)

2.2.1 Generalities

While 3D printing was initially developed for rapid prototyping, it has progressively evolved into a reliable method for rapid tooling and low-volume manufacturing of functional parts [7]. The AM workflow involves several critical steps, as illustrated in Figure 2.2. The process begins with the creation of a 3D model using computer-aided design (CAD) software.

The design stage—referred to as Design for Additive Manufacturing (DfAM)—is central to the quality and performance of the final part. DfAM principles guide modifications to the CAD model to account for the specific constraints and capabilities of the AM process, including material behavior, anisotropy, and layer-by-layer deposition mechanics. It also promotes the reduction of support structures, minimization of material waste, and facilitation of post-processing steps. This design philosophy fosters innovation by enabling complex geometries and functional integration while optimizing printability, mechanical integrity, and sustainability [8–13].

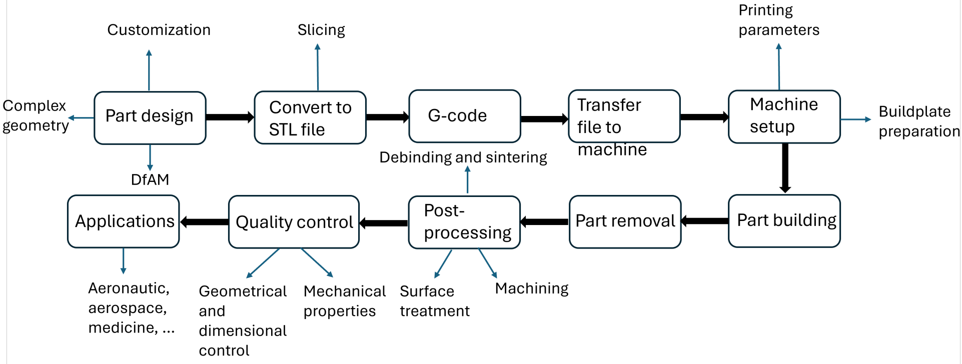

Figure 2.2: Different steps to produce a part by AM

DfAM integrates advanced CAD software like SolidWorks, Siemens NX, and Fusion 360 to create and refine 3D models optimized for printing. Topology optimization tools such as Altair Inspire and ANSYS, alongside slicers like Cura and Simplify3D, enhance part geometries and printing parameters to reduce waste and improve performance. Simulation and material selection software, including Moldex3D and Granta MI, allow for pre-printing analyses and optimal material choices, ensuring parts meet functional and environmental criteria [11].

This model is then exported into the STL (Standard Tessellation Language) format, which represents the geometry using a mesh of triangles. The STL file is subsequently processed using slicing software, which translates the 3D geometry into discrete layers and generates a G-code file. This G-code contains machine-specific instructions that control the motion of the print head or nozzle, material deposition rate, extrusion temperatures, and other key process parameters. The G-code is then uploaded to the 3D printer, initiating the manufacturing phase.

Before printing begins, process settings such as build orientation, layer thickness, infill density, print speed, and temperature profiles must be configured based on the material used and the functional requirements of the part. Once printing is completed, the part is removed from the build platform and undergoes post-processing, which may include surface finishing (e.g., machining, polishing), thermal treatments, or, in the case of metal AM with binders, a debinding and sintering cycle.

In recent years, an important material and process development widened the initial material limitations and enabled the adaptation of SLA and MEX-based printing techniques for the processing of ceramic and metal materials.

FFF and related techniques benefit from the long feedstock development experience in powder injection molding (PIM) for the fabrication of dense and warpage-free metal and ceramic parts according to the following process chain [14]:

1. Feedstock compounding involves the use of suitable binders, additives, and a substantial solid load.

2. Printing via PAM techniques (Figure 2.3).

(a) Ti6Al4V titanium alloy as-printed (HyProPAM)

(b) Tosoh black zirconia (ZrO_2) as-printed (HyProPAM)

Figure 2.3: As-printed watch dials via PAM process during HyProPAM: (a) titanium alloy Ti6Al4V, (b) black Tosoh zirconia ZrO_2.

3. Post-processing (for example, conventional machining and/or laser machining, or other process to improve surface quality) (Figure 2.4).

(a) Ti6Al4V titanium alloy machined (b) Tosoh black zirconia (ZrO_2) machined

Figure 2.4: Watch dials after machining, produced during HyProPAM: (a) titanium alloy Ti6Al4V, (b) black zirconia ZrO_2.

4. Debinding, often a combination of solvant/water debinding and thermal debinding where the part is without any mechanical resistance and very difficult to handle.
5. Sintering with conditions tailored to the filler's properties (Figure 2.5).

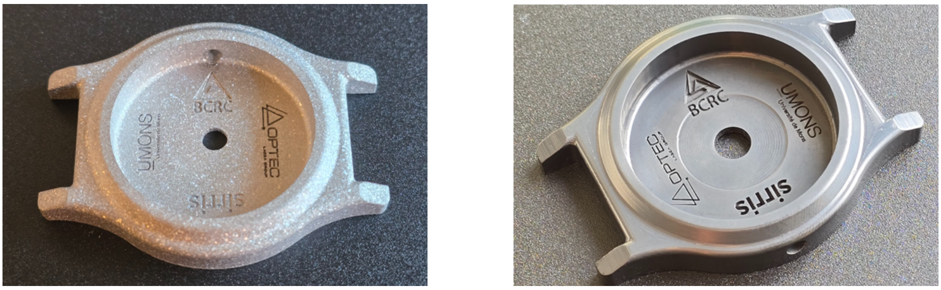

(a) Ti6Al4V titanium alloy as-sintered (b) Tosoh black zirconia (ZrO_2)

Figure 2.5: Watch dials after machining, debinding and sintering, produced during HyProPAM: (a) Ti6Al4V titanium alloy, (b) black zirconia ZrO_2.

These examples illustrate the final stages of part fabrication via Pellets Additive Manufacturing, including machining, debinding, and sintering. While these steps are essential to achieving functional density and mechanical performance, the overall efficiency and applicability of such methods largely depend on the front-end printing process used to shape the initial feedstock. Among the various additive manufacturing techniques, material extrusion processes such as MF^3 (Melted and Formed Filament Fabrication) have gained particular attention due to their low cost, accessibility, and ability to process highly filled feedstocks. The following section introduces the MF^3 process and contextualizes its relevance within the broader landscape of AM technologies [15].

MF^3 is refereeing to Multiplexed Fused Filament Fabrication, which is the group for material extrusion techniques as FDM or PAM.

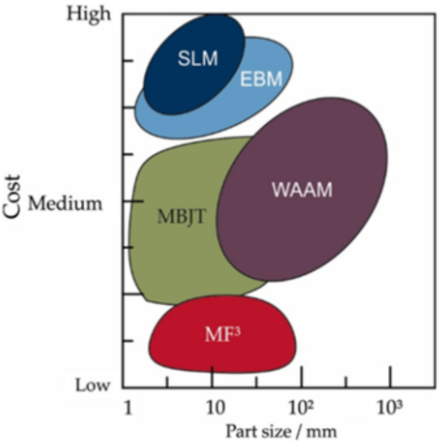

Figure 2.6: Cost of fabrication part depending on the size for different AM techniques [15]

Figure 2.6 shows that MF^3 is the technology with the lowest cost depending on the part size compared to all AM technologies.

2.2.1.1 Evolution of AM in Industry

Figure 2.7 exhibits the numbers of 3D printer manufacturers, software vendors and material suppliers in the AM sector in Europe. It can be observed that polymers and metal machines are the most developed in the industries, due to the cost-effectiveness of both machines and materials, as well as their ease of use [16].

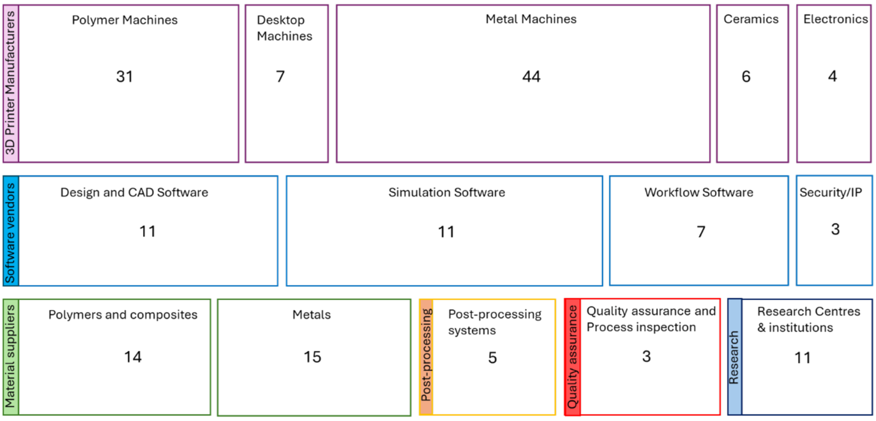

3D Printer Manufacturers	Polymer Machines	31
	Desktop Machines	7
	Metal Machines	44
	Ceramics	6
	Electronics	4
Software vendors	Design and CAD Software	11
	Simulation Software	11
	Workflow Software	7
	Security/IP	3
Material suppliers	Polymers and composites	14
	Metals	15
Post-processing	Post-processing systems	5
Quality assurance	Quality assurance and Process inspection	3
Research	Research Centres & institutions	11

Figure 2.7: Some numbers about AM in the industry (2019) [16]

Machines able to print ceramic materials were developed later due to the difficulty of shaping these materials, which are both brittle and refractory.

CAD and simulation software have become increasingly powerful, enabling a broad range of possiblities to produce complex additively manufactured parts, particularly due to efficient slicing software [17].

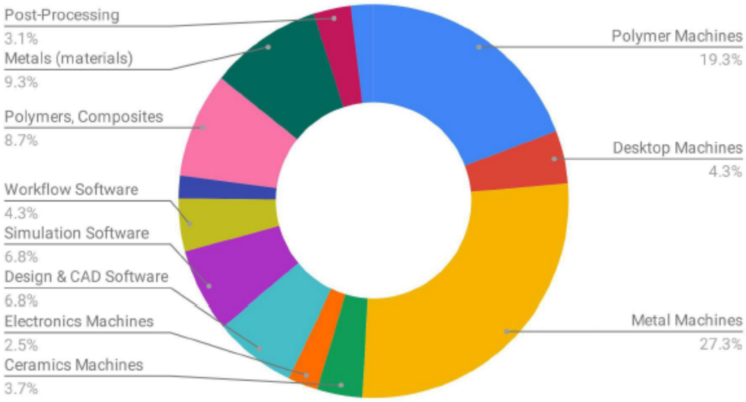

Figure 2.8: Pie chart showing the percentage of presence of each of the domains working in AM [16]

Figure 2.8 represents an AMFG pie chart [16] showing the percentage of each AM machine depending on the material they use and presenting the percentage of each type of material used in AM until 2019.

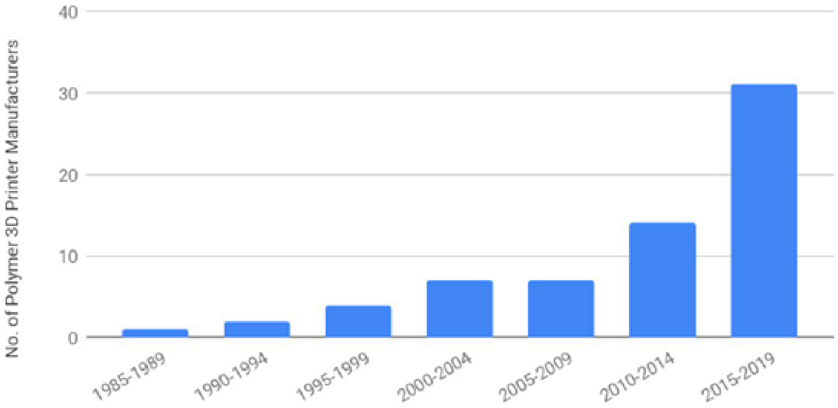

Figure 2.9: Evolution of the number of polymer 3D printer manufacturer from 1985 to 2019 [16]

Figure 2.9 and Figure 2.10 describe the evolution of the number of polymer and metal 3D printer manufacturers. It is possible to see that between 1985 and 2019, the number of 3D printer manufacturers increased considerably and particularly between 2015 and 2019.

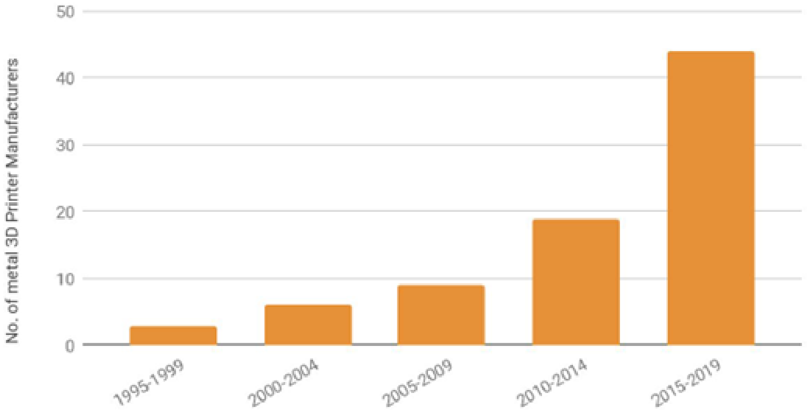

Figure 2.10: Evolution of the number of metal 3D printer manufacturers from 1995 to 2019 [16]

Figure 2.8, Figure 2.9 and Figure 2.10 show that the part of polymer machines is most important in the market followed by metal machines. This can be explained by the massive increasing interest in AM, particularly thanks to FDM-type polymer machines, which are very accessible in terms of both price and ease of use. This can be explained by the possibilities offered by AM technologies such as the versatile type of materials or possible complex geometries and, in some cases (ex: Material Extrusion, FDM,...), the reduction in the cost of the raw material and machine compared to the overall costs of other classic technologies [5, 17].

Although AM is increasingly being adopted by industry, many aspects of these technologies still require improvement, such as surface quality and mechanical properties [18]. Nevertheless, AM offers new opportunities, particularly due to its ability to produce highly complex or customized geometries at reduced costs. As a result, a growing number of research and development studies are currently being conducted in this field, as illustrated in the following subsection.

2.2.1.2 Evolution of research in AM

The earliest scientific publications on AM date back to the 1980s, with an average of 15 to 30 articles published annually during that decade. Since then, AM has become a rapidly expanding research domain, as evidenced by the increasing number of scientific publications indexed in Scopus (Figure 2.11). Since 2010, the annual number of AM-related publications has grown exponentially, surpassing 15,000 in 2024.

This steady increase in the number of publications confirms the growing scientific interest in AM. The technology offers several strategic advantages, such as the ability to fabricate complex geometries, reduce material waste, and enable mass customization at reduced costs.

These capabilities have led to its adoption across various sectors, including aerospace, automotive, and biomedical engineering [19, 20].

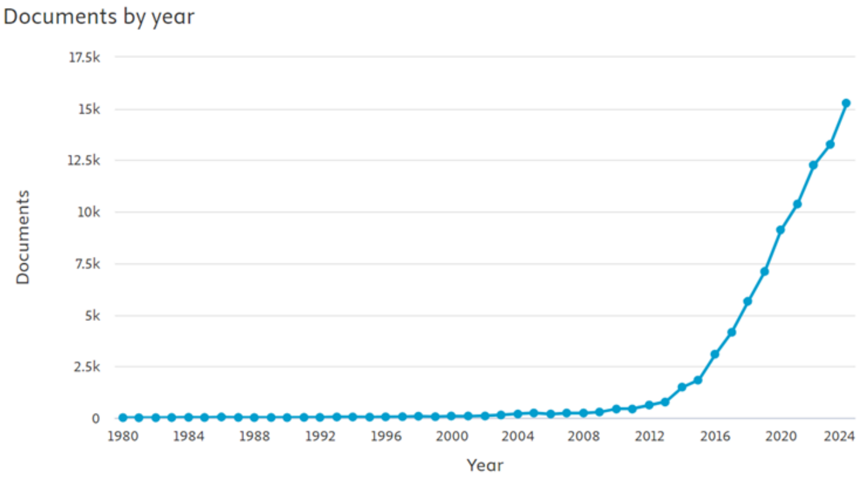

Figure 2.11: Number of publications per year containing the keyword "Additive Manufacturing" from 1980 to 2024 in Scopus.

Despite this growing momentum, AM still faces key challenges that limit its large-scale industrial deployment. Among the most critical limitations are poor surface finish, internal porosity, anisotropic mechanical properties, and restricted material diversity [18, 21]. In response to these issues, hybrid manufacturing technologies have emerged as a promising pathway for overcoming some of AM's intrinsic weaknesses.

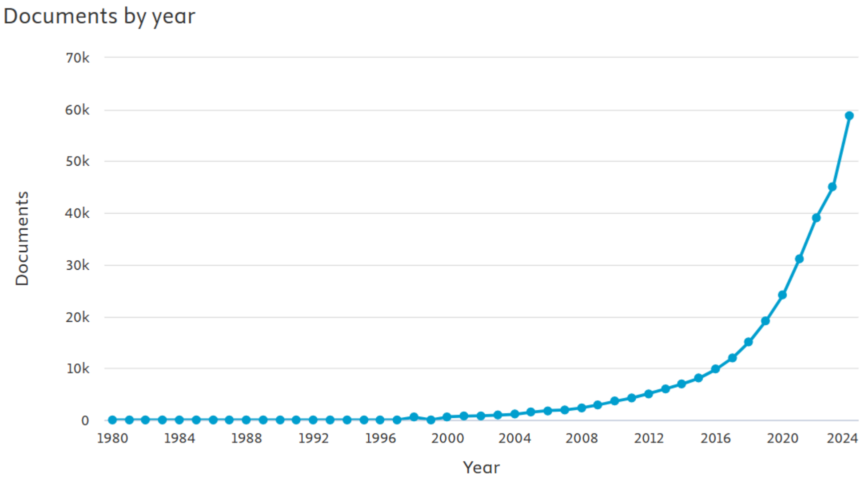

Figure 2.12: Number of publications indexed in Scopus using the keywords "Hybrid", "Techniques", and "Manufacturing" between 1980 and 2024

As shown in Figure 2.12, the scientific interest in hybrid manufacturing has grown in parallel with that of AM, particularly in the last decade. Hybrid manufacturing refers to the integration of additive and subtractive processes—typically combining 3D printing with high-precision machining within a single system.

This dual approach seeks to harness the design freedom of AM while achieving the dimensional accuracy and surface quality offered by subtractive methods [22].

Hybrid manufacturing has been particularly successful in applications requiring both geometric complexity and high-performance mechanical properties, such as aerospace components, injection molds, and patient-specific medical implants. The hybrid approach also enhances material utilization and reduces post-processing needs, contributing to shorter production cycles and lower overall costs [23–25].

In summary, the evolution of AM research, as well as the parallel rise of hybrid manufacturing technologies, reflects the field's dynamic response to the limitations of conventional manufacturing processes and the continuous pursuit of higher-performance, more sustainable production methods.

2.2.1.3 Advantages of AM

AM offers several key advantages that distinguish it from traditional subtractive and formative manufacturing techniques.

- Rapid Prototyping [26]:

  AM enables the fast and cost-effective production of prototypes directly from CAD models. This significantly shortens development cycles and facilitates design iteration, allowing engineers and designers to test and validate concepts more efficiently before committing to mass production.

  For example, General Motors utilizes 3D printing to produce approximately 30,000 prototype parts per year, significantly accelerating product development and iteration cycles [27].

- Design Complexity and Freedom [12]: One of the hallmark benefits of AM is its ability to fabricate highly complex geometries that would be difficult or impossible to achieve using conventional processes. This includes lattice structures, internal channels, and organic forms optimized through topology optimization or generative design. Such capabilities are particularly valuable in industries like aerospace and biomedical engineering where lightweight, performance-optimized components are critical.

- Material Efficiency and Waste Reduction [28]: AM builds components layer-by-layer, using only the material necessary for the part. This reduces material waste compared to subtractive methods, which often generate significant scrap. This feature aligns with sustainable manufacturing goals and reduces overall material costs. Studies indicate that AM can reduce raw material usage by 35% to 80% compared to subtractive methods, contributing to more sustainable production practices [29].

- Customization and On-Demand Manufacturing [30]: AM allows for the easy customization of parts, making it ideal for personalized products such as medical implants or dental devices. Moreover, the digital nature of AM enables decentralized and on-demand production, reducing the need for inventory and long supply chains.

- Tool-less Fabrication [31]: Since AM does not require molds or tooling, it eliminates the costs and lead times associated with tooling production, especially beneficial for low-volume or high-mix manufacturing environments.

- Use of Pellets in Material Extrusion [32]: PAM offers the advantage of using granulated feedstock (generally develop for injection molding process), which is more cost-effective and readily available than filament. Pellets provide higher solid loading, better rheological control, and increased flexibility in binder formulation, making PAM a competitive method for producing metal and ceramic parts.

2.2.1.4 Limitations of AM

Despite its many advantages, AM technologies face several challenges that hinder their broader industrial adoption.

- Surface Quality and Resolution [33]: Parts produced via AM often suffer from poor surface finish due to the layer-by-layer deposition process, leading to visible stair-stepping effects, particularly on curved surfaces. For example,the layer-by-layer FDM process results in visible ridges, and arithmetic surface roughness Ra values can range between 10 to 30 microns, often necessitating post-processing [34].

- Dimensional accuracy [35]: Phenomena like the “sharkskin effect” and anisotropic texture also impact dimensional accuracy and aesthetics, often requiring additional post-processing steps [33]. For instance, Multi Jet Fusion (MJF) exhibits dimensional deviations between 2.1% and 5.2%, while Selective Laser Sintering (SLS) can have errors up to 7% [36].

- Mechanical Properties and Anisotropy [37]: AM parts may exhibit inferior mechanical properties compared to those made through forging or machining. This is especially true in terms of interlayer adhesion and residual porosity, which can lead to anisotropic behavior and lower strength in the build direction.

- Energy Consumption and Environmental Burden [38]: Some AM processes, particularly those involving lasers or high-temperature sintering, are energy-intensive. When post-processing like heat treatment or surface finishing is included, the total energy footprint can exceed that of traditional methods for certain part types and production volumes. Bezzina et al. [39] found that energy consumption for FFF represents 80% of the total environnemental impact of FFF.

- Post-Processing Requirements [33]: Many AM parts require extensive post-processing, including support removal, surface finishing, and heat treatment. These steps can be labor-intensive and time-consuming, diminishing the speed advantage and adding to production costs. These steps can be time-consuming and expensive, sometimes accounting for up to 25% of total production costs [40].

- Material Limitations [41]: Although AM has expanded beyond polymers to include metals, ceramics, and composites, the range of printable materials remains limited compared to conventional manufacturing. Additionally, the feedstock preparation (e.g., powder, pellets, or filament quality) plays a critical role in printability and final part properties. For pellet-based systems, feedstock granule size and binder composition can also impact flow stability and extrusion performance.

2.3 Injection Molding and Material Extrusion processes

2.3.1 Powder Injection Molding PIM

Powder Injection Molding (PIM) is a fabrication process that involves injecting highly filled polymers ($\geqslant$ 50 vol.% solid loading) into a mold using an extrusion screw. The incorporation of polymers—referred to as binders—into the feedstock ensures appropriate flow behavior throughout the process. Binders lower the shaping temperature because they melt at significantly lower temperatures than metallic or ceramic powders. Moreover, due to the abrasiveness of these powders, binders help reduce wear on equipment [42, 43].

PIM comprises four main steps [43–46]:

1. **Feedstock preparation:** Metallic or ceramic powders are mixed with a multi-component binder system to produce a homogeneous mixture called feedstock. Critical parameters at this stage include powder characteristics (e.g., size, shape), binder composition, powder-to-binder ratio, the mixing process, and potential surface treatments. These factors significantly influence all subsequent processing stages. A high powder loading is essential to ensure cohesion of the molded parts. The binder acts as a temporary medium to shape and hold the powder structure until sintering.
2. **Injection molding:** The feedstock is molded using standard plastic injection molding machines (Figure 2.13). The material is melted and conveyed through an Archimedean screw heated by barrel-integrated heaters and injected into a mold. The resulting part, known as the "green part," has the intended geometry but lacks mechanical properties.

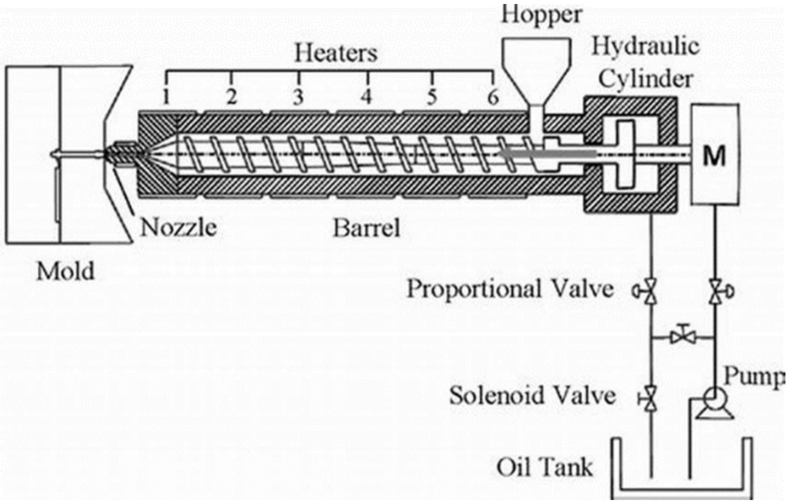

Figure 2.13: Schematical representation of the injection molding process [47]

3. **Debinding:** This step involves removing most of the binder using an appropriate heated solvent (typically around 60°C), without causing defects or deformation. The part at this stage is called the "brown part" and is extremely fragile without significant mechanical properties. Debinding parameters depend on both the binder system and the powder type. It can be carried out through chemical routes (e.g., solvent dissolution, catalytic debinding), thermal routes (e.g., pyrolysis in a controlled atmosphere), or a combination of both. Debinding is often time- and energy-consuming and can lead to defects such as distortion, cracking, or swelling.

4. **Sintering:** The final stage involves thermally bonding the particles by heating the brown part to a temperature close to the melting point of the powder. This densification step eliminates the pores formed by the removed binder and imparts the final mechanical properties to the part. As a result, significant shrinkage occurs, which must be considered during design.

2.3.2 Material Extrusion AM MEX

Extrusion-based fabrication of polymer parts was first patented by S. Scott Crump [48] and commercialized by Stratasys, Ltd. in the early 1990s as the FDM™ process. ASTM in their classification has defined MEX as processes used to fabricate polymer, or polymer composite, parts by depositing a filament or bead of material from an extrusion head“ [49].

In the MEX process, the feedstock composed of ceramic or metal powder (solid loading) and binder (as for MIM) is heated until the material is melted and can be extruded through a nozzle. The filament is then deposited onto a heated build platform to improve adhesion between the part and the bed and to limit the thermal shock. The part is created layer-by-layer following the CAD model [50].

This process can also fabricate multi-material 3D parts, if the printer has more than one printing head or feeding system. Metal MEX processes can be classified into three types depending on the feeding system of the printer as presented in Figure 2.14 which are (a) screw-based, (b) plunger-based and (c) filament-based types [51].

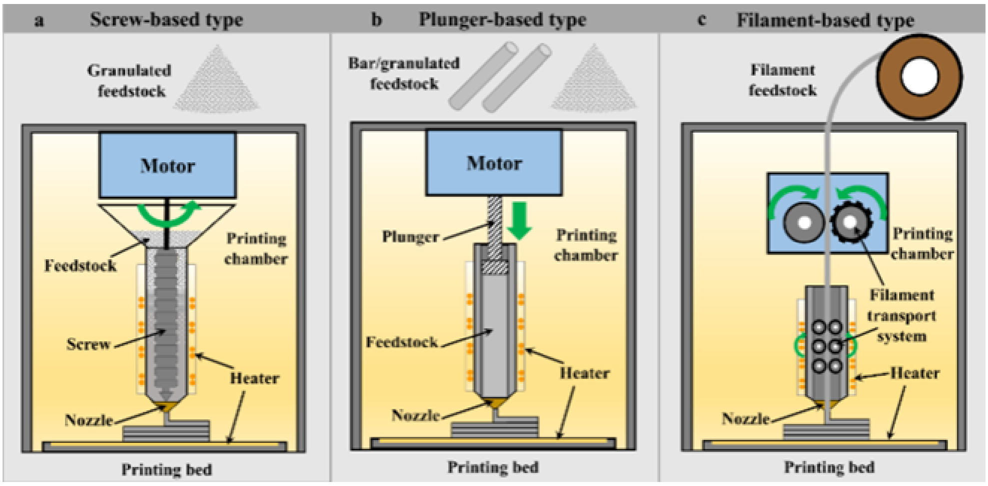

Figure 2.14: Types of MEX classified by feeding system: (a) screw-based, (b) plunger-based and (c) filament-based types [51]

After the printing step, the as-build part needs to be debinded and sintered in a similar way to those in the MIM processing steps, as presented previously.

Screw-based MEX

Screw-based MEX is currently the most versatile material extrusion system in terms of material selection. This method uses granulated feedstock from MIM. In the case of metal MEX, all alloys for MIM feedstocks are applicable but high-quality metal filaments and feedstocks are still limited in alloy selection. The feedstock will be transported by screw rotation and heated simultaneously by heating elements to a temperature above the glass transition temperature Tg of the polymer binder.

Then, the material will be deposited through the nozzle to manufacture the 3D CAD design model on the build platform as presented in Figure 2.14 (a) [51]. This system has some advantages over the other systems (plunger and filament-based), such as high productivity thanks to a continuous filling system. The process does not require an additional filament preparation step, which is necessary in conventional filament-based techniques as FDM. This is particularly advantageous given that solid-loaded filaments containing ceramic or metal fillers are typically brittle and difficult to handle.

In addition, high solid loading rates equivalent to MIM can be used [51]. There are some challenges as the size of the feedstock must be controlled ($<$ 5 mm) to achieve stability during printing and to reduce print defects caused by air entrapment [52].

Singh et al. [53] reported that for copper MIM feedstock (Cu999 from PolyMIM, Germany) with two polymers, namely polyethylene glycol (PEG) and some wax (not precisely specified by the supplier), pellets sized from 3 to 5 mm can lead to a relative sintered density of the final part up to 94.5%.

Similarly, Lieberwirth et al. [54] reported that a size of 3 mm could be easily printed with good appearance. If the feedstock is too large, the feed system will not be able to melt it evenly and properly. Too small feedstock can cause trapping at the hopper. Mono-material green parts with defects or flaws can be easily reused by crushing and screening before returning them to the printer hopper, as for MIM-injected parts.

The stabilization of the screw system is still challenging to fabricate the 3D part, as it is difficult to control the flow rate of the material to be constant due to the trapped air inside the softened material. Moreover, the strength and stability of the printing system are also required during printing due to the high viscosity of the feedstock [20].

Plunger-based MEX

This method uses a plunger or piston mechanism to directly push the material through the extrusion die or a nozzle (Figure 2.14 (b)).

Advantages of Plunger-Based Material Extrusion [55] :

1. Simplicity and reliability: The plunger-based system has fewer moving parts than screw-based systems, which can reduce the likelihood of mechanical failure and make maintenance easier.

2. Precise material control: The direct pressure applied by the plunger provides precise control over the amount of material extruded, which can be beneficial for applications requiring high accuracy and detail.

3. Good for high viscosity materials: Plunger systems can effectively extrude high viscosity materials that can be difficult for screw-based systems to handle due to the direct force applied.

Disadvantages of Plunger-Based Material Extrusion:

1. Limited material capacity: The amount of material that can be extruded is limited by the size of the plunger chamber, requiring frequent refills for large volume prints, which can interrupt the printing process.
2. Potential for inconsistent flow: If the material is not uniformly fed or if there are air bubbles, the flow can become inconsistent, affecting print quality. This is less of an issue in screw-based systems where the screw action can help in homogenizing the material.
3. Slower speeds for large prints: Due to the need for refilling and potential for slower extrusion speeds, plunger-based systems might not be as efficient as screw-based systems for large-scale manufacturing.

Filament-based MEX

Filament-based material extrusion technique is a popular method such as Fused Deposition Modeling (FDM), widely used in 3D printing. In this process, a thermoplastic filament is fed into an extruder, where it is heated to a molten state and then extruded through a nozzle to build objects layer-by-layer on the print bed.

Advantages of Filament-Based Material Extrusion [55]:

1. Ease of use: Filament-based printers are generally easier to use, making them ideal for hobbyists, educators, and professionals alike.
2. Low-cost equipment: Both the printers are typically less expensive than those used in screw or plunger-based systems, making the technology more accessible.
3. Clean and convenient: Filament materials are easy to handle, store, and replace, providing a clean and convenient solution without the need to handle powders or liquids.

Disadvantages of Filament-Based Material Extrusion [56–58]:

1. Material limitations: This process is limited in material choice because of the mechanical properties of certain materials such as ceramics which cannot be shape into filaments due to their fragile nature.
2. Material cost: Filaments are more expensive than pellets
3. Lower throughput and slower production: FDM has limited deposition rates due to filament feeding constraints.

2.4 Materials for AM

To better understand the relevance of titanium in additive manufacturing, it is essential to review its historical background, alloy development, and unique material characteristics.

2.4.1 Titanium and its alloys

2.4.1.1 History

Titanium is a silver-grey metal in group 4 of the periodic table. This useful industrial metal is lightweight, has high strength, and does not corrode easily under normal environmental conditions. Discovered in compound form in 1791 by William Gregor, an English mineralogist and chemist, it was independently rediscovered in 1795 by Martin Heinrich Klaproth, a German chemist. Klaproth gave the element its name. It was first isolated in its pure form in 1910 by Matthew A. Hunter. Titanium is a very common element, making up about 0.57% of the Earth's crust by mass [59].

It is found in almost all sands, clays, soils and rocks. It is also found in biological organisms, natural waters, material dredged from the deep sea, meteorites, and stars. The two most important commercial minerals containing titanium are rutile and ilmenite. Because it is a highly reactive element, the preparation of titanium is challenging. At elevated temperatures, titanium is extremely reactive with nitrogen and oxygen, and conventional oxidative reduction methods do not yield titanium.

Ti6Al4V alloy, also known as Ti6Al4V, is classified as an $\alpha + \beta$ titanium alloy, known for its increased strength, reduced density, remarkable fracture toughness, exceptional corrosion resistance and excellent biocompatibility. Widely recognized as the dominant titanium alloy, Ti6Al4V accounts for nearly half of the global market share for titanium products.

Originally developed in the 1950's [60] for structural applications in aircraft, the alloy's light yet strong composition proves highly advantageous in applications where high strength is required while minimizing weight, such as jet engines, gas turbines and various airframe components.

Although the aerospace industry remains a major user of Ti6Al4V, its popularity has expanded over the past five decades to include the marine, automotive, energy, chemical, and biomedical industries. The alloy's low density, high strength, corrosion resistance and biocompatibility make it attractive for applications such as bridges and implants. In addition, its corrosion resistance to most corrosive acids and alkalis has led to its use in the marine and chemical industries.

The major titanium mines are located in several regions of the world, including Australia, South Africa, Canada, China, India, Norway, Ukraine and Vietnam, mainly in the form of ilmenite FeTiO3 and rutile TiO2. The largest industries exploiting titanium mines are Iluka Resources (Australia), Rio Tinto (South Africa), Tronox (Australia, South Africa etc..) and other industries. The rutile TiO2 is sold in 2024 around 1500 $US/MT [61], ilmenite is sold between 371 and 400 $US/MT depending on the quality [62].

2.4.1.2 Microstructure and properties of Ti6Al4V

The alloy undergoes an allotropic transformation at about 890°C from a hexagonal closed-packed (hcp) structure (α phase) to a stable body-centered cubic (bcc) structure (β phase) as shown in Figure 2.15. The hcp structure has three slip planes: pyramidal, prismatic, and basal with a c/a ratio of 1.587. Titanium alloys exist in α, near α, $\alpha + \beta$, and β microstructures. In the Ti6Al4V alloy, aluminum acts as an α stabilizer by increasing the $\alpha - \beta$ transformation temperature, and vanadium acts as a β stabilizer [63].

Titanium alloy Ti6Al4V generally exists in alpha phase with crystal structure hcp, (SG: P63/mmc) and beta phase with crystal structure bcc, (SG: Im-3m) [64].

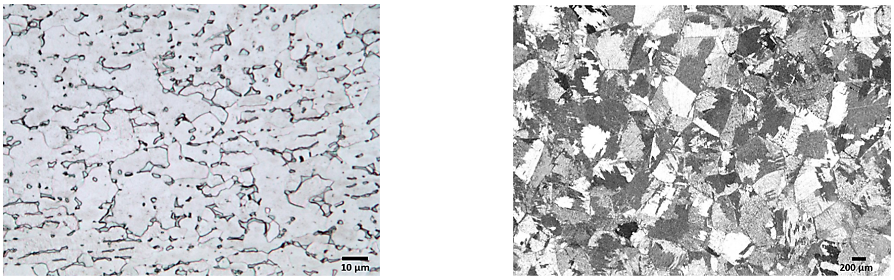

(a) α phase microstructure

(b) α+β phases microstructure

Figure 2.15: Microstructures of Ti6Al4V: (a) α-phase; (b) α+β phases adapted from [64]

Despite high demand, manufacturing Ti6Al4V components remains challenging due to its low thermal conductivity, work hardening, and oxygen reactivity. Conventional methods—such as forging, casting, and rolling followed by machining—lead to significant material waste, high costs, and long lead times. Additive manufacturing (AM), which builds near-net-shape parts directly from CAD models via layer-by-layer deposition, offers a promising alternative, especially for complex geometries.

Ti6Al4V is a dual-phase (α+β) alloy whose microstructure and properties can be tailored by heat treatment. As shown in Figure 2.16, the phase diagram highlights the α+β region in grey.

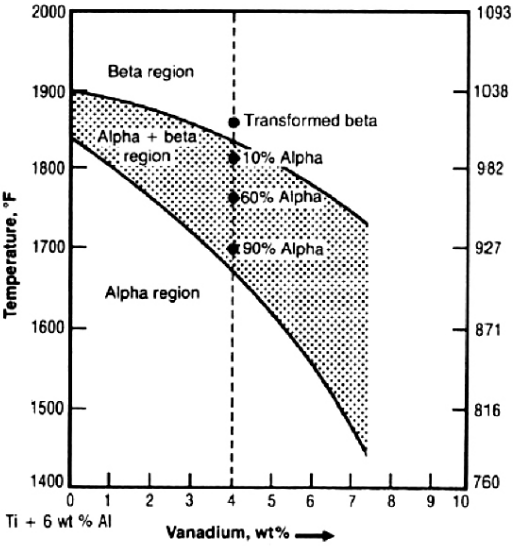

Figure 2.16: Ti6Al4V phases diagram [64]

Above the β-transus, a bcc microstructure with coarse grains forms. In contrast, treatment within the dual-phase region produces varied microstructures, with the α-phase inhibiting β-growth.

As the temperature nears the α/β transition (920°C), the α-phase fraction decreases. Heating to 950°C results in a bimodal structure of primary α grains and acicular transformed β. The resulting phase distribution depends on the initial microstructure, the heating profile, and cooling rate. Rapid quenching from the β region leads to a metastable, diffusionless martensitic α'-phase.

Subsequent heat treatment can be applied to achieve the desired microstructure. However, care must be taken during heat treatment to avoid the formation of a brittle ω phase. The omega ω phase in Ti6Al4V alloys is a metastable phase that can form under certain conditions, such as rapid cooling from high temperatures or aging at intermediate temperatures. This phase is important because it can have a profound effect on the mechanical properties of the alloy, affecting its hardness, strength, and ductility [65].

2.4.1.3 Ti6Al4V Biocompatibility and Applications

Ti6Al4V is widely recognized for its biocompatibility, primarily because it does not elicit a significant immune response upon implantation in the human body. This makes it suitable for long-term biomedical applications.

However, the presence of vanadium and aluminum in the alloy has raised concerns regarding potential long-term cytotoxic and neurotoxic effects. Consequently, recent research has focused on the development of vanadium-free and aluminum-free titanium alloys, including commercially pure grades (Grade 2 and 4) and alternative compositions such as Ti-13Nb-13Zr, Ti-12Mo-6Zr-2Fe, and Ti-15Mo [60].

The alloy's favorable combination of biocompatibility, high mechanical strength, and corrosion resistance makes it one of the most commonly used materials in the biomedical sector. Nevertheless, efforts to improve its long-term safety are ongoing, with particular attention to its alloying elements and their biological interactions [66, 67].

Osteointegration

A key advantage of Ti6Al4V is its ability to promote *osteointegration*, defined as the direct structural and functional connection between living bone and the surface of a load-bearing implant. This property is essential in orthopedic and dental applications, where the implant-bone interface must be mechanically stable and biologically active to ensure long-term success [68].

Potential Issues

Despite its clinical success, Ti6Al4V is not without limitations. The presence of vanadium and aluminum, both of which can release ions over time, has prompted investigation into potential adverse biological effects, particularly for long-term implants.

Applications

Owing to its biocompatibility and mechanical reliability, Ti6Al4V is used in a wide range of medical devices [69, 70], including:

- Joint replacements (hip, knee, shoulder)
- Dental implants (see Figure 2.17)

- Bone fixation devices (screws, plates, rods)
- Cardiovascular implants (e.g., stents, pacemaker housings)

Figure 2.17: dental implants fixation made of Ti6Al4V [71]

The biocompatibility of Ti6Al4V, along with its mechanical strength and corrosion resistance, make it a highly valued material in the biomedical field as shown in Table 2.2. Ongoing research aims to address any concerns related to its alloying elements in order to further improve its safety and efficacy.

Table 2.2: Main properties of Ti6Al4V [65]

Properties	**Values**
Density (g/cm^3)	4.43
Melting point (°C)	1604-1660
Tensile strength (MPa)	880-950
Yield strength (0.2% Offset, MPa)	830-880
Elongation (%)	10-14
Young's modulus (GPa)	114
Hardness (HV)	330-380
Thermal conductivity (W/m.K)	6.7
Coefficient of thermal expansion (10^{-6}/°C)	8.6 (20-100°C)
Corrosion resistance	Excellent
Biocompatibility	Good
Creep resistance	Good at temperature up to 700°C
Fatigue strength	High

Beyond its well-known biocompatibility, the Ti6Al4V alloy exhibits a remarkable combination of mechanical strength, corrosion resistance, and low density, making it attractive for a wide range of applications. While it is extensively used in the biomedical field for implants and prosthetics, its unique properties have also driven widespread adoption in other demanding industries such as aerospace, automotive, and energy.

2.4.1.4 Aeronautic and aerospace industries

Ti6Al4V is widely used in the aerospace industry due to its unique set of properties that make it highly suitable for applications in these demanding fields. Here are the main reasons for its widespread use:

Ti6Al4V has an exceptional strength-to-weight ratio as described in Figure 2.18, which is critical for aerospace applications where weight reduction is essential to improve fuel efficiency and performance. The alloy provides significant strength without the added weight, enabling the design of lighter and more efficient aircraft and spacecraft. The alloy exhibits excellent corrosion resistance, including resistance to a wide range of aggressive environments (Table 2.2). This is particularly important in the aerospace industry, where materials are subjected to high speeds and extreme conditions, including exposure to fuels and oxidizers, which can be highly corrosive. Ti6Al4V's corrosion resistance helps extend the life and reliability of aerospace components.

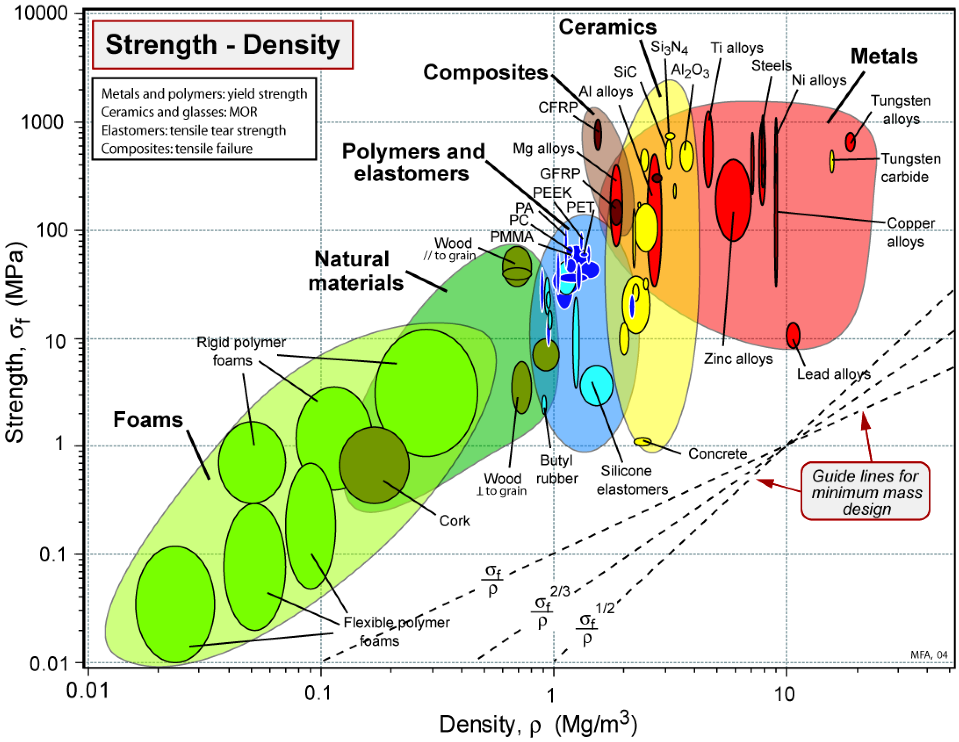

Figure 2.18: Ashby's diagram of the strength (MPa) depending on the density (Mg/m^3) of several materials [72]

Ti6Al4V retains its strength and mechanical properties at elevated temperatures, unlike many other metals that can weaken. This property is essential for parts exposed to the high temperature environments found in jet engines and airframes. The ability to maintain structural integrity at high temperatures contributes to the safety and durability of aerospace components.

Aerospace structures are subject to cyclic loading and stress concentrations that can lead to fatigue and crack propagation. Ti6Al4V has excellent fatigue and crack growth resistance, making it suitable for critical components requiring long life and reliability under cyclic loading conditions.

The alloy has good creep resistance, which means it can withstand long-term exposure to high stresses at elevated temperatures without significant deformation. This property is particularly important for engine components and other high-stress aerospace parts.

Applications in Aerospace and Aeronautics [63]:

Because of these properties, Ti6Al4V is used in a wide range of aerospace applications, including:

- Engine components (compressor blades, disks and casings)
- Airframe structures (bulkheads, wing beams, landing gear)
- Fasteners and critical hardware
- Hydraulic systems

2.4.1.5 Fabrication of Ti6Al4V alloy powder

Titanium alloy Ti6Al4V powder, commonly used in AM processes such as Powder Bed Fusion (PBF), is typically produced by a method called gas atomization.

Gas atomization process for Ti6Al4V powder: The Ti6Al4V alloy consists of 90 wt.% titanium (Ti), 6 wt.% aluminum (Al), and 4 wt.% vanadium (V). The alloy composition is carefully controlled to achieve the desired mechanical and thermal properties.

The alloy is melted in an induction skull furnace or similar high temperature furnace. The molten metal is maintained at a specific temperature to ensure proper alloying. The molten metal is then subjected to high pressure gas atomization as shown in Figure 2.19.

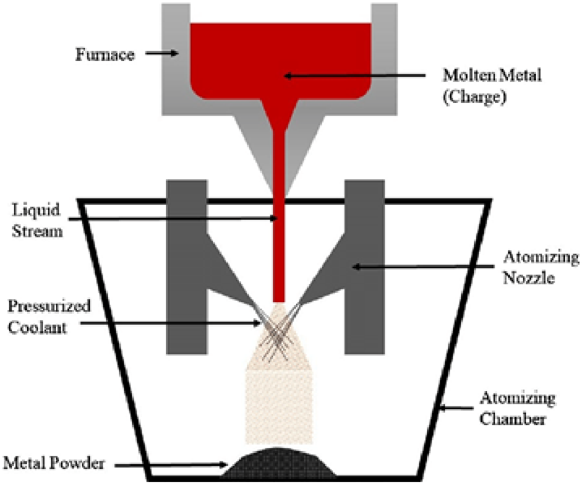

Figure 2.19: schematic representation of the gas atomization system [73]

In this process, the molten metal stream is exposed to a high-speed jet of inert gas (often argon). The high velocity gas breaks the molten metal stream into small droplets. The size and morphology of these droplets are critical to the properties of the resulting powder. The droplets rapidly cool and solidify as they pass through the atomization chamber. The rapid solidification helps maintain the desired microstructure of the Ti6Al4V alloy. The solidified droplets form spherical powder particles. These particles are collected in a chamber or collector.

The collection system is designed to prevent the powder from agglomerating and to maintain its flowability. The resulting powder can have a range of particle sizes. To ensure consistency and to meet the specific requirements of AM processes, the powder is often subjected to size classification processes. This involves separating the powder into different size fractions [74].

The particle size range of Ti6Al4V powder obtained by gas atomization typically varies. However, it's common for the particle size to be in the range of approximately 15 to 150 microns (µm). This range may vary depending on the specific parameters and conditions of the gas atomization process, such as the pressure and type of gas used, temperature, and nozzle design.

Particle size can be classified into several types as shown in Table 2.3:

Table 2.3: Classification of particle size ranges for metallic powders, adapted from [75]

Type of particle	**Diameter range**
Nanopowder	$d < 0.1\ \mu m$
Ultrafine powder	$0.1\ \mu m < d < 10\ \mu m$
Fine powder	$10\ \mu m < d < 100\ \mu m$
Medium powder	$100\ \mu m < d < 250\ \mu m$
Coarse powder	$250\ \mu m < d < 1000\ \mu m$
Granules	$d > 1000\ \mu m$

For MIM, the particle size is typically in the range of 5 to 25 microns. This size range helps achieve a high packing density and ensures smooth flow of the material during the injection process as well as during the sintering phase where the material is densified. Fused Filament Fabrication (FFF) for metals typically uses a metal powder embedded in a plastic binder to form a filament rather than a pellet. The Ti6Al4V powder used in the filament would likely fall within a similar size range as that used in MIM to ensure proper binder distribution and sintering behavior, although the exact size may depend on the specifics of the process and the desired properties of the final product. In metal extrusion, the particle size may be similar to that used in powder bed fusion processes, typically 20 to 45 microns, to ensure good flowability and packing density, but the finer the particle size, the better the density of the final part [73, 75]. The Ti6Al4V powder produced is subjected to rigorous quality control measures to ensure that it meets the desired specifications for particle size distribution, morphology, and chemical composition [3]. The gas atomization process is preferred for producing metal powders for AM due to its ability to produce spherical particles with a relatively narrow size distribution. Spherical particles are advantageous for powder bed fusion processes because they flow more consistently and can be uniformly distributed during layer-by-layer deposition in AM machines [76].

2.4.2 Polymers used for Injection Molding IM and Material Extrusion MEX

In both MEX and MIM, the binder (a blend of polymers) in the feedstock plays a critical role in the processing and forming of the metal parts. The binder acts as a temporary matrix that holds the metal powder particles together, allowing complex shapes to be formed prior to the final sintering step. Here's a breakdown of the binder's role in MEX and MIM: the binder gives the feedstock the viscosity it needs to be easily extruded through a die. Proper viscosity ensures that the material can be formed into the desired shape during the extrusion process [51].

The binder imparts green state strength to the extruded part, allowing it to hold its shape prior to the sintering process [51]. Green state strength is critical for handling and transporting the green (unsintered) parts without deformation or breakage. This is essential for achieving the desired dimensions and properties in the final sintered part.

The binder helps prevent the powder particles from agglomerating during mixing and forming and ensures uniform distribution in the feedstock.

Uniform distribution contributes to the homogeneity of the green part and the final sintered part [77].

Polymers tested in the PhD Thesis

In the context of developing eco-responsible feedstocks for PAM, the selection of suitable polymeric binders is a critical step. The binder system must ensure proper dispersion of metallic powders, adequate flow behavior during extrusion, and clean removal during the debinding stage. This section presents the main polymers investigated during this PhD work, each chosen for its specific physicochemical properties and potential compatibility with highly filled formulations.

Three polymers were selected and tested: Polyethylene Glycol (PEG), a water-soluble synthetic polyether known for its plasticizing effect and thermal stability; Polyvinyl Butyral (PVB), a thermoplastic polymer widely used for its excellent adhesion, flexibility, and toughness; and Methylcellulose (MC), a semi-synthetic cellulose derivative valued for its amphiphilic nature, rheological behavior, and ability to form thermoreversible gels. The following subsections provide a detailed description of their chemical structures, properties, and relevance to the binder system formulation in PAM.

Polyethylene Glycol PEG

Polyethylene Glycol PEG is a synthetic linear polyether with a molar mass $<$ 20 000 g/mol derived from petroleum. The structure of PEG is commonly expressed as $H-(CH_2-CH_2-O)n-OH$.

PEG is made from ethylene glycol and have water-soluble and fat-soluble properties. PEG is soluble in water, toluene, dichloromethane, alcohol and acetone but not in aliphatic carbides such as hexane, cyclohexane. PEG is stable to acids, bases, heat, oxygen, hydrogen peroxide, oxidizers, and reducers. PEG is not biodegradable, but bio-eliminable by renal filtration. Its toxicity is well-known and PEG is not flammable, not volatil et considered by FDA as safe.

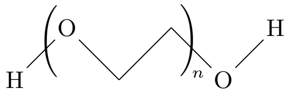

Polyvinyl Butyral PVB

PVB is a synthetic thermoplastic polymer produced by the condensation of butyraldehyde (butanal) with polyvinyl alcohol (PVA) under acidic conditions. It is an amorphous, transparent, and flexible polymer known for its excellent adhesion, optical clarity, toughness, and impact resistance [78]. These properties make PVB particularly suitable for use as an interlayer in laminated safety glass, especially in the automotive and architectural industries, where it enhances shatter resistance and UV protection [78].

Beyond glazing applications, PVB is also used as a binder in ceramic and metallic powder processing, adhesives, inks, paints, and photovoltaic modules [78]. Its hydroxyl and butyral functional groups allow for strong interactions with both polar and non-polar surfaces, making it a versatile matrix in composite systems. In additive manufacturing and powder injection molding, PVB serves as a backbone polymer, providing mechanical integrity during shaping and dimensional stability during debinding and sintering [79].

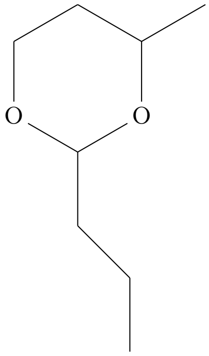

Methylcellulose MC

Methylcellulose (MC) is a semi-synthetic, water-soluble cellulose ether obtained by substituting hydroxyl groups of cellulose with methoxy groups (OCH_3). Its structure provides amphiphilic character, enabling both hydrophilic and hydrophobic interactions. MC is non-ionic, thermoresponsive, and exhibits pseudoplastic (shear-thinning) behavior in solution. It is widely used in ceramics processing, pharmaceuticals, and construction as a thickener, stabilizer, and binder due to its ability to form highly viscous solutions and thermoreversible gels [80–83].

One of the distinctive properties of MC is its thermal gelation in aqueous or polar media. Upon heating, intermolecular hydrophobic interactions between methoxy groups induce the formation of a physical network (gel), which is reversible upon cooling. The gelation temperature varies with the degree of substitution, molecular weight, and concentration. This behavior is beneficial in processing environments where structural support at elevated temperatures is required [84].

In polymer–powder systems (e.g. for MIM or PAM), MC serves as a rheology modifier and structural binder. It increases yield stress and storage modulus (G'), improving the stability of the feedstock at rest and during early solidification stages. This is essential for layer stacking, shape retention, and prevention of collapse or flow during deposition. MC also contributes to elastic recovery after shear, supporting interlayer adhesion and mechanical cohesion [85].

However, high concentrations of MC can induce gelation or excessive viscosity, limiting flowability during extrusion. Therefore, its use requires careful balance with plasticizing agents or lubricants to ensure processability.

In the context of PAM, where feedstocks are subjected to high shear rates during screw extrusion and must retain shape after deposition, MC provides critical rheological control. Its properties supports:

- Shape fidelity upon exiting the nozzle,
- Stabilization during cooling, and
- Resistance to sagging or deformation.

These characteristics make MC a valuable component in binder systems requiring both mechanical integrity and controlled flow, particularly when combined with low-viscosity additives such as fatty acids or waxes.

MC is derived from cellulose, a renewable biopolymer, making it bio-based and non-toxic. Although its biodegradability is limited under standardized aerobic conditions, studies have shown that it can undergo partial degradation over time in natural environments, especially in the presence of adapted microbial communities [86]. Its use can reduce reliance on petroleum-based polymers such as PVB or EVA, aligning with sustainability goals in materials development.

Methylcellulose is a multifunctional, renewable polymer offering valuable rheological properties for highly filled feedstocks in AM. Its thermal gelation, viscoelastic behavior, and ability to enhance structural integrity during and after extrusion make it an effective binder component in PAM. While its high viscosity may require rheological compensation, its bio-based origin and functionality support its use in environmentally conscious formulations.

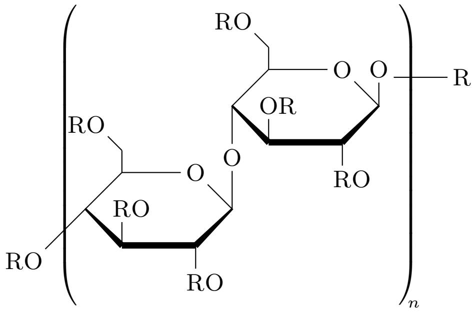

2.4.3 Surfactants

To improve binder properties such as surface wetting, spreading, adsorption, and binder strengthening, a surfactant is often added as an additive to the binder. Generally, the surfactant is a low molecular weight component consisting of a functional group attached to the powder surface and an oriented molecular chain extending into the binder. Therefore, due to its structure, the surfactant acts as a bridge between the binder and the powder and enhances the stabilization of the powders when they are broken apart by mechanical shear during the mixing process [51, 87, 88]. The surfactant is critical to the MIM and MEX processes. As a lubricant,

- it can reduce the frictional force existing between the powder particles as to reduce the viscosity of the feedstock to improve the solid loading [45];

- It can also be used as a dispersant, easing the dispersion of the particles in the binder and improving the homogeneity of the feedstock; or as a plasticizer;
- it can improve the mixing properties among the binder components [51, 89];
- More importantly, the surfactant can effectively increase the adhesion strength between the binder and the powder, which improves the strength of green parts and provides a potential way to eliminate structural defects. Therefore, the surfactant has an important influence on the quality control of the final products.

In MIM and PAM feedstocks, surfactants are added in small quantities (0 to 5 vol.% [51, 90, 91]) to improve powder wetting, enhance binder adhesion, and reduce surface energy. According to Yi-min [89], the surfactant has significant effects for improving the properties of MIM and MEX feedstocks. In fact, it serves as a bridge between the powder and the binder, enhancing the stability of the feedstock. Proper content of the SA can decrease the viscosity of the feedstock and improve the dispersibility of the powder. Moreover, adding surfactant can increase the critical solid loading due to the enhancement of interaction between the powder and the binder. A chemical bonding is found in the mixture of the surfactant and the solid loading after mixing, indicating that chemical adsorption occurs on the powder surface with the help of the surfactant. Thus, chemical adsorption can reinforce the interacting force between the powder and the binder, enhancing the solid loading of the feedstock system.

2.4.3.1 Stearic Acid SA

In the formulation of highly filled feedstocks for AM processes such as PAM and MIM, the use of functional additives is essential to optimize flow behavior and ensure homogeneous dispersion of metallic powders.

Among these additives, stearic acid (SA) plays a prominent role due to its amphiphilic nature and surface-active properties. Commonly employed as a lubricant and dispersant, stearic acid contributes significantly to the rheological performance of polymer–powder mixtures, particularly under extrusion conditions.

This section provides a detailed overview of the chemical, thermal, and rheological characteristics of stearic acid, with a focus on its behavior in PAM-specific processing environments. The discussion highlights its advantages, limitations, and optimal usage conditions within binder systems designed for sustainable and efficient AM.

Chemical Properties

Stearic acid, or octadecanoic acid, is a saturated long-chain fatty acid with the molecular formula $C_{18}H_{36}O_2$ and a molar mass of approximately 284.48 g/mol. It consists of an 18-carbon hydrocarbon chain terminated by a carboxylic acid group. This amphiphilic structure—comprising a polar head and nonpolar tail—confers surface-active properties, allowing stearic acid to adsorb onto particle surfaces and interfaces within multicomponent systems. It is solid at room temperature, insoluble in water, but soluble in many organic solvents, and shows excellent compatibility with polymer matrices [92, 93].

Its melting point lies between 69–72°C, making it thermally accessible during low-temperature processing such as pre-extrusion softening in PAM.

Thermal Behavior

Stearic acid exhibits a well-defined melting transition near 70°C and begins to degrade thermally around 185°C, with continued decomposition up to 300°C [94]. This early degradation must be considered when processing at temperatures above 60–70°C, especially in long-residence-time systems. Nonetheless, its early melting is advantageous in binder systems for enabling initial softening and flow without excessive heating.

In PAM, this property enables smoother screw feeding and onset of melt flow during the early stages of extrusion [95].

Rheological Role in Polymer–Powder Feedstocks

Stearic acid is widely used as a lubricant and dispersant in metal or ceramic-filled feedstocks for processes such as MIM and PAM. It reduces interparticle friction and enhances powder–binder interactions by improving wettability of metallic surfaces [89]. Chan et al. [87] showed that stearic acid significantly improves the injection molding behavior of alumina by lowering viscosity and facilitating better powder dispersion.

Gorjan et al. [95] further demonstrated that incorporating SA into highly filled feedstocks for FFF reduces both complex and apparent viscosity, enhances shear-thinning behavior, and contributes to a smoother flow regime under extrusion-relevant conditions.

At concentrations between 2–3 vol.%, SA typically optimizes rheological performance. At higher levels (e.g., ($\geqslant 5 vol.\%$)), diminishing returns are often observed, with possible phase separation, binder saturation, or surface quality degradation due to accumulation of low-molecular-weight species [87, 95].

Behavior in PAM-Specific Conditions

In PAM, stearic acid facilitates key process steps by enabling:

- Low-viscosity melt flow through the screw and nozzle,
- Reduced extrusion pressure, and
- Improved feeding behavior, especially in pre-melting zones.

However, due to its low thermal stability, care must be taken to avoid premature decomposition during residence in heated zones. Inappropriate processing temperatures may cause volatilization or embrittlement, which could lead to voids, binder burnout, or incomplete layer bonding [87, 94, 95].

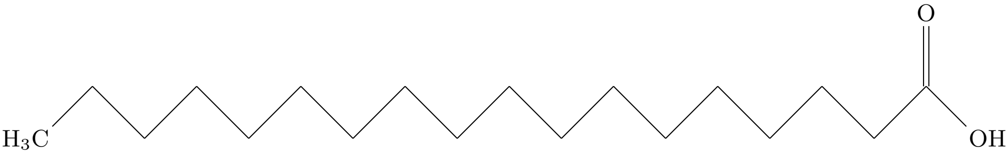

2.4.4 Relations in a highly filled blend of immiscible polymers

In highly filled systems involving immiscible polymers, understanding the morphological interactions between components becomes essential, as these interactions strongly influence the flow behavior and final structure of the feedstock. The following section explores the concept of continuity in such blends.

2.4.4.1 Continuity in blend

In the case of immiscible polymer blends, there are two types of morphologies in polymer blends depending on the proportions of A or B in the mixture (Figure 2.20) [96]:

- Nodular: in the case where the proportions of A in B are low (up to approximately 20% by mass) and vice versa.
- Co-continuous: above 20 wt.%, a co-continuous morphology begins to appear. It is representative of a polymer network which is formed from entangled A and B.

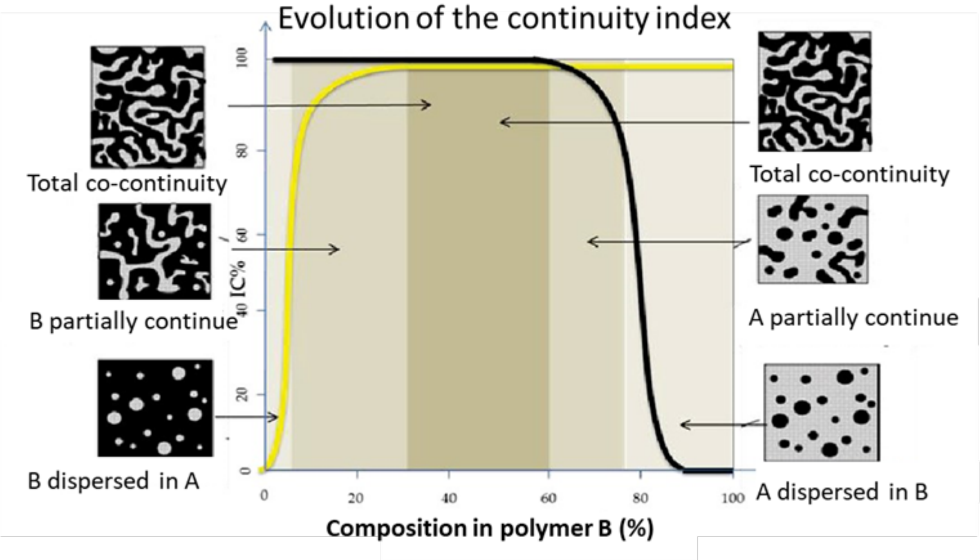

Figure 2.20: Blend of immiscible polymers: evolution of the continuity depending on the polymer content [96]

The parameters influencing the formation of morphologies are temperature, interfacial tension, composition, viscosity ratio of the phases, mixing time, mixing speed and the equipment used [96].

Melt mixing poses two problems:

- The high viscosity prevents diffusion and turbulence of the polymers at the molecular level.
- There is also likely to be degradation of the polymers related to temperature and shear, but the main reason is the lack of intensive mixing between both components. The viscosity, and elasticity of the polymers as well as the interfacial tension and the implementation influence the co-continuity phenomenon. Indeed, the greater the difference in viscosity, the more the repulsive forces will push one of the polymers towards the surface of the material, the proportion of polymer will not be homogeneous throughout the material and the less viscous polymer will coat the one which is the most viscous one.

The interfacial tension also plays a very important role [97]: in fact, if the interfacial tension value for a system is low, the occluded domains presenting stretched shapes will be little affected by interfacial effects, and even very thin filaments will be stable.

On the other hand, for systems with high interfacial tensions, the interfacial effects will be very pronounced and most of the filaments will be destabilized and broken into droplets. Under these conditions, it is difficult to form stable co-continuous morphologies for weak compositions in the dispersed phase. The mixing conditions during the implementation of the polymers have a strong influence on the morphology produced.

For example, the stress experienced by a polymer in an extruder, or a mixer is very different. It is therefore necessary to consider the influence of different processing parameters such as temperature, mixing time, type and rate of shear.

It is important to consider the morphology of the blend in the case of MIM/MEX feedstocks to determine the effect of the binder on solvent debinding and sintering [98].

2.4.4.2 Liquid-solid wetting

In MIM and MEX, particle wettability plays a pivotal role in determining the quality and performance of the feedstock. These processes rely on mixing solid powders (typically metal or ceramic) with an organic binder system. Good wettability between particles and binder is essential to ensure homogeneous dispersion, stable flow during extrusion, and strong interfacial adhesion in the final consolidated part.

In PAM and FDM, poor wettability leads to incomplete coating of powder particles by the binder or polymer melt. This results in agglomeration, poor dispersion, and inconsistent rheology, affecting printability and dimensional accuracy. For example, in a study on oxide dispersion-strengthened steel produced by LPBF [99] (a process with similar feedstock issues), Y_2O_3 particles showed significant agglomeration due to poor wettability with the 316L stainless steel matrix. These agglomerates led to a reduction in tensile elongation and weak mechanical performance, illustrating how critical interfacial bonding is in powder-based systems.

In MIM, the binder system must effectively wet and disperse the metallic or ceramic particles to prevent phase separation during injection. Poor wettability can result in binder migration or powder-binder phase segregation during molding or debinding, leading to part defects and non-uniform shrinkage. According to Yang et al. [100], wettability governs the formation of particle networks and capillary bridges, which strongly influence the rheological properties and stability of dense suspensions.

Furthermore, the rheology of MEX/PAM formulations is greatly affected by the degree of particle wetting. In systems where the polymer acts as a non-Newtonian fluid, the addition of poorly wetted particles leads to erratic shear-thinning behavior, increased yield stress, and potential nozzle clogging during printing. Xia and Krueger [101] showed that both the flow consistency and shear behavior of particle-loaded suspensions depend significantly on the wettability and particle-to-capillary diameter ratio, which directly affects flow stability during extrusion.

Overall, good particle wettability ensures homogeneous mixing, stable flow, better debinding/sintering, and improved mechanical integrity. In contrast, inadequate wettability results in agglomeration, rheological instability, and weak part performance—issues that are especially problematic in high-load systems like MIM and PAM. The liquid-solid wetting characteristics are crucial for AM process, which consists of the wetting behavior between the solid loading and the liquid binder as well as the wetting behavior between the molten system and the previously solidified layer.

The wetting of a solid by a liquid is related to the surface tension of solid-liquid (γ_{sl}), solid-vapor (γ_{sv}), and liquid-vapor (γ_{lv}) interfaces as described in Figure 2.21 [102].

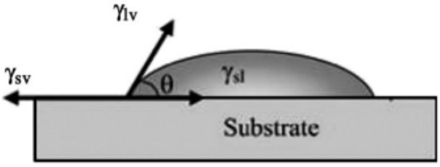

Figure 2.21: Contact angle of a liquid on a solid substrate [102]

If the subtraction of the surface tension of solid-vapor and solid-liquid is higher or equal to the surface tension of liquid-vapor interfaces:

$$\gamma_{\mathrm{sv}} - \gamma_{\mathrm{sl}} \geqslant \gamma_{\mathrm{lv}} \tag{2.1}$$

Thus, the material completely or partially wet the substrate characterized by a contact angle between 0° and 90°. Then, if the solid-liquid surface tension is equal to the solid-vapor interface surface tension, the liquid material is partially non-wetting the substrate:

$$\gamma_{\mathrm{sv}} = \gamma_{\mathrm{sl}} \tag{2.2}$$

In the case where the subtraction of the surface tension of the solid-vapor interface and the solid-liquid surface tension interface is less than the liquid-vapor interface surface tension:

$$\gamma_{\mathrm{sv}} - \gamma_{\mathrm{sl}} \leqslant \gamma_{\mathrm{lv}} \tag{2.3}$$

The material does not wet the substrate as shown in Figure 2.22.

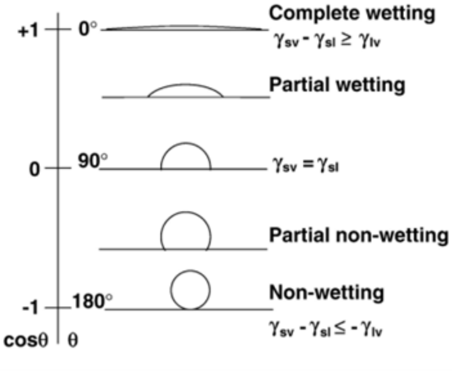

Figure 2.22: types of liquid behavior on a substrate [102]

2.4.4.3 Rheological properties

In the framework of this thesis, the development of a sustainable and high-performance metal AM process based on PAM required a deep understanding of the material-process interactions. Given that commercially available metal feedstocks were originally developed for MIM, it was essential to investigate whether these materials could be directly reused or adapted for use in a continuous layer-by-layer deposition process.

Unlike MIM, which is based on rapid injection cycles into closed molds, PAM relies on continuous and controlled extrusion of highly filled metal-polymer compounds through a heated nozzle. This fundamental shift in process dynamics—particularly in terms of extrusion pressure, screw geometry, and deposition forces—raises critical questions regarding the rheological suitability of conventional MIM feedstocks in additive contexts.

To address this, a detailed review of the rheological properties of highly loaded composites, the principles of screw design in both MIM and PAM systems, and the structural behavior of binders and powders was conducted. Studies such as those by Thavanayagam et al. have shown that the pseudoplastic nature and binder compatibility of MIM feedstocks are highly sensitive to powder loading and composition, especially for Ti6Al4V systems [103]. Furthermore, Widyastuti et al. demonstrated that particle shape—whether spherical or dendritic—has a profound impact on melt viscosity and flow stability, thereby influencing the feedability and extrusion consistency in screw-based systems [104].

Comparative investigations by Ewart et al. further highlighted how conventional MIM characterization tools, such as torque mixers and twin-screw extruders, may not fully reflect the behavior under the low-pressure, low-shear conditions typical of AM [105]. These insights underscore the need for process-specific evaluation techniques when considering MIM-derived materials for PAM applications.

Additionally, the preparation method of MIM feedstock—whether via dry or wet mixing—can significantly alter its flowability, as noted by Jamaluddin et al. [106]. Finally, the work by Karataş and Saritas illustrates how combining gas- and water-atomized powders enables higher solid loadings and better rheological behavior, which is directly relevant to tailoring feedstock for PAM systems [107].

As such, the insights presented in the following sections are not only a literature-based analysis, but also a technical foundation for the experimental implementation of PAM within the HyProPAM project.

Melt-strength

The melt strength refers to the ability of a molten polymer to resist deformation under applied stress. It is a measure of the material's resistance to elongation or stretching when in a molten state. Melt strength is crucial in various processing techniques, such as extrusion and blow molding, where the molten material needs to maintain its shape and resist sagging or drooping. Melt strength is often measured using a rheometer or other testing equipment that applies a controlled force to the molten polymer [108]. For a Ti6Al4V/binder composite, the melt strength needs to be high enough to support the extrusion process, allowing the material to be deposited layer-by-layer without collapsing under its weight. However, it should not be so high that it hinders the flow through the printer's nozzle.

Some key standards for Evaluating Melt Strength exist:

- ISO 1133 / ASTM D1238 – Melt Flow Rate (MFR) and Melt Volume Rate (MVR): these standards define procedures for measuring the flow characteristics of thermoplastic polymers under specified conditions of temperature and load. While primarily used for quality control, MFR and MVR values can provide indirect insights into a polymer's melt strength. Lower MFR values typically indicate higher molecular weight and, consequently, higher melt strength [109].

- ISO 11443 – Determination of Viscosity Using a Capillary Rheometer: this standard outlines methods for determining the viscosity of polymer melts using a capillary rheometer. By analyzing the viscosity at various shear rates, one can infer the melt strength, especially in processes involving high shear conditions [110].

- ISO 6721-1:2019 – Determination of Dynamic Mechanical Properties: these standards describes methods for determining the dynamic mechanical properties of polymers. By measuring storage and loss moduli, insights into the viscoelastic behavior and melt strength of polymers can be obtained [110].

Highly filled polymers, such as those containing significant amounts of mineral fillers, present unique challenges in processing due to altered rheological properties. Studies have shown that increasing filler content can significantly affect the melt strength of the composite. For instance, research on high-density polyethylene (HDPE) filled with natural zeolite demonstrated that while the addition of fillers increased the composite's viscosity, the shear-thinning behavior was maintained, indicating a complex relationship between filler content and melt strength [111].

While there isn't a single standard exclusively dedicated to measuring "melt strength," several standardized rheological tests provide valuable insights into this property. For highly filled polymers, understanding and measuring melt strength is crucial, as fillers can significantly alter the melt behavior, impacting processing and final product performance.

Rheological properties of highly filled melted polymers

For the MIM and PAM process, the raw material called "feedstock" must have certain rheological properties or flow behavior to ensure a good and homogeneous shaping. A thorough study of feedstock flow behavior is essential to balance the conflicting requirements of an ideal feedstock. Achieving a high solid load is essential to minimize the risk of shrinkage and warpage during sintering. However, the solid load must not be too high to ensure good melt flow behavior, which allows defect-free extrusion and filament deposition without voids due to solid overfilling to obtain a dense part.

Highly filled feedstocks with solid loading create a complex system with both elastic (solid) and viscous (polymer) properties in the molten state. According to Thavanayagam et al. [112–114], the binder must have good flow properties, interact well with the metal powder, allow for easy debinding, maintain shape during debinding and sintering, be easy to dispose of, environmentally safe and cost effective. Fluid behavior can be Newtonian or non-Newtonian. The viscosity of a Newtonian fluid is affected by the material, the temperature and the pressure but is independent of the shear rate or shear stress whereas the viscosity of a non-Newtonian fluid is affected by flow conditions.

There are several types of non-Newtonian fluids [115]:

1. Shear-thinning (pseudoplastic) fluids: The viscosity of shear-thinning fluids decreases as the shear rate increases.
2. Shear-thickening (Dilatant) fluids: The viscosity of shear-thickening fluids increases with an increase in shear rate.
3. Bingham plastic (Yield stress) fluids or Thixotropic: Bingham plastic fluids behave like a solid at low stresses but flow like a viscous fluid once a critical stress (yield stress) is exceeded. Below the yield stress, the fluid does not flow and behaves more like an elastic solid. Above the yield stress, the fluid flows and behaves like a viscous fluid.
4. Rheopectic: Viscosity increases with stress over time.

MIM feedstocks are time-independent fluids with either a linear (Bingham plastic) or nonlinear (yield pseudoplastic) relationship between shear stress and shear rate once the minimum yield stress for flow is applied [1, 91].

Viscosity, and others properties

A key determinant of successful shaping in both MIM and PAM is the rheological behavior of the feedstock—a mixture of fine metallic powders and polymeric binders. The feedstock must balance conflicting requirements: a high solid loading to minimize sintering shrinkage and warpage, and sufficient fluidity to enable defect-free flow and extrusion[113].

Highly filled feedstocks exhibit non-Newtonian and viscoelastic behavior due to the interplay between solid particles and polymer matrix. They behave like yield-pseudoplastic or Bingham-type fluids, flowing only when a critical shear stress is exceeded [91, 112, 115].

Definitions and Flow Models

Viscosity is classicaly defined as:

$$\eta = \frac{\tau}{\dot{\gamma}} \tag{2.4}$$

Where:

- η: dynamic viscosity [Pa.s],
- $\dot{\gamma}$: shear rate, which is the rate of change of deformation due to the shear stress (s^{-1}),
- τ: shear stress (Pa or N/m^2), which is the force per unit area applied parallel to the surface of the fluid.

Non-Newtonian behavior is modeled using the power-law (Ostwald-de Waele) equation:

$$\tau = m\dot{\gamma}^n \tag{2.5}$$

With:

- m is the consistency index or coefficient ($Pa.s^n$), a factor that describes the consistency of the fluid. Higher values of m indicate a more viscous fluid.

- n: flow behavior index (typically n $\prec$ 1 for pseudoplastic fluids)

Flow curve The Figure 2.23 illustrates two fundamental rheological concepts: the flow curve (shear stress depending on shear rate) and the viscosity curve (viscosity vs. shear rate), which are essential for understanding the printability of feedstocks in extrusion-based additive manufacturing [116]. The flow curve shows how different material types respond to increasing shear rates. Newtonian fluids exhibit a linear relationship between shear stress and shear rate, maintaining constant viscosity. Pseudoplastic (or shear-thinning) materials, which are highly desirable for 3D printing, show a decreasing viscosity with increasing shear rate—this facilitates smooth extrusion at high flow rates while ensuring stability at rest [117]. In contrast, dilatant (shear-thickening) materials become more viscous as shear rate increases, which can lead to extrusion issues such as nozzle clogging or irregular flow. Bingham plastics, like many yield-stress fluids, do not flow until a critical stress is applied—this property can be advantageous for preserving the shape of deposited layers but must be carefully balanced to avoid under-extrusion. The viscosity curve on the right complements this by directly showing how each material's viscosity responds to varying shear rates. For additive manufacturing, especially PAM and FDM, the ideal behavior is pseudoplastic: low viscosity under high shear (during extrusion) and high viscosity at rest (to maintain part geometry). Understanding these curves allows for better formulation and control of feedstocks, ensuring process stability, dimensional accuracy, and high-quality printed parts [117].

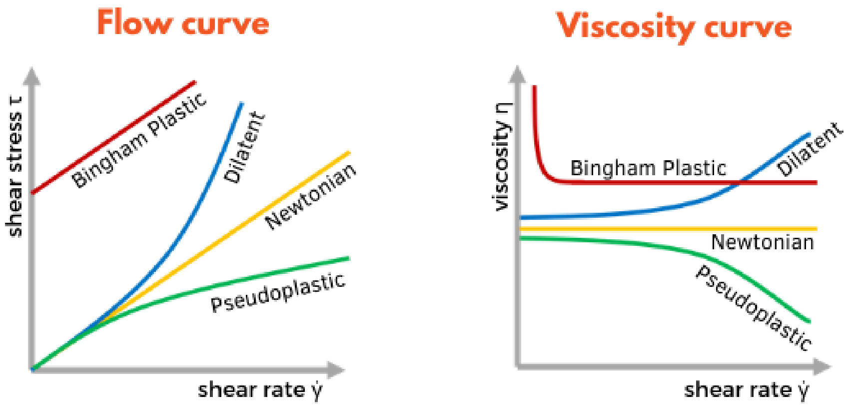

Figure 2.23: Typical flow curve and rheological curve for different type of material [116]

Storage and Loss modulus (G' and G") In oscillatory rheology, two key parameters are used to describe the viscoelastic behavior of materials: the storage modulus (G') and the loss modulus (G"). G' quantifies the elastic response of a material, reflecting the energy stored during deformation and recovered when the stress is released. It characterizes the solid-like behavior of the system. In contrast, G" represents the viscous response, indicating the amount of energy dissipated as heat—hence, the liquid-like behavior. The relative magnitude of G' and G" provides direct insight into the balance between structure (elasticity) and flow (viscosity) within a viscoelastic material [14, 91].

Definition of Storage and Loss Moduli

In small-amplitude oscillatory shear (SAOS), the applied shear stress is defined as:

$$\sigma(t) = \sigma_0 \sin(\omega t), \tag{2.6}$$

where σ_0 is the stress amplitude and ω is the angular frequency. The angular frequency ω (rad/s) is related to the oscillation frequency f (Hz) according to:

$$\omega = 2\pi f \tag{2.7}$$

The resulting strain response is phase-shifted by an angle δ:

$$\gamma(t) = \gamma_0 \sin(\omega t + \delta), \tag{2.8}$$

with γ_0 the strain amplitude. The complex shear modulus is given by:

$$G^*(\omega) = \frac{\sigma_0}{\gamma_0} e^{i\delta} = G'(\omega) + iG''(\omega), \tag{2.9}$$

where:

$$G'(\omega) = \frac{\sigma_0}{\gamma_0} \cos(\delta), \tag{2.10}$$

$$G''(\omega) = \frac{\sigma_0}{\gamma_0} \sin(\delta). \tag{2.11}$$

Here, $G'(\omega)$ is the storage modulus, representing the elastic (energy-storing) component, and $G''(\omega)$ is the loss modulus, representing the viscous (energy-dissipating) component [118, 119].

Small-amplitude oscillatory shear (SAOS) tests are commonly employed to determine the storage modulus G' and the loss modulus G'', as described in international standards for dynamic mechanical analysis. According to [120], G' quantifies the elastic energy stored during deformation, while G'' represents the viscous energy dissipated as heat.

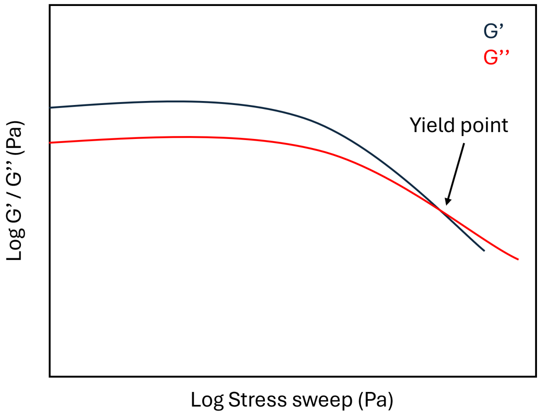

Figure 2.24: Typical stress sweep for viscoelastic material as feedstock for MIM or PAM

The figure 2.24 illustrates a typical result of an amplitude sweep test performed on a viscoelastic material, such as a highly filled feedstock used in extrusion-based additive manufacturing. The storage modulus G' represents the elastic or solid-like behavior of the material, while the loss modulus G" corresponds to its viscous or liquid-like behavior. At low strain or stress amplitudes, both moduli remain relatively constant, defining the Linear Viscoelastic Region (LVE) where the material maintains its internal structure and responds elastically to small deformations.

As the applied shear strain or stress increases beyond a critical point, G' begins to decrease, indicating the onset of structural breakdown. Simultaneously, G" decreases and eventually crosses G', defining the yield point—the transition from elastic-dominated to viscous-dominated behavior. This point is particularly relevant for materials used in 3D printing by extrusion, as it reflects the minimum mechanical input required to initiate flow. Beyond the yield point, both moduli decrease, and the material flows more freely, behaving like a liquid. This type of analysis is crucial for determining the processing window and the balance between flowability and shape retention during printing [121].

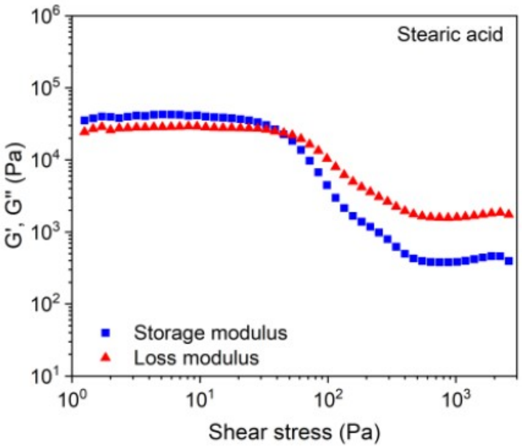

Figure 2.25: Storage (G') and loss modulus (G") of PEG 8000/PVB system containing SA (temperature 160 °C, solid load 60 vol%) via oscillatory test applying amplitude stress sweep [91]

Figure 2.25 shows the stress sweep performed by Eickhoff et al. [91] on a PEG (8000 g/mol) and PVB-based feedstock containing stearic acid (SA). The authors observed a plateau in both G' and G", which they suggested may indicate a phase separation phenomenon. However, this interpretation was not definitively confirmed [91].

To accurately describe melt flow behavior, it is necessary to measure not only the shear-rate dependent viscosity but also the viscoelastic flow through oscillatory measurements using a rotational rheometer. This technique has been applied to various feedstock systems, including recent studies [91].

The complex shear modulus (G^*) is determined, which consists of the storage modulus (G', elastic part) and the loss modulus (G”, viscous part).

Knowing the applied angular frequency, the complex viscosity (η^*) can be estimated.

The direct relationship between the complex shear modulus and the complex viscosity is shown below.

$$G^* = G' + G'' \tag{2.12}$$

$$\eta^* = \eta' + i\eta'' = G'/\omega + i(-G''/\omega) \tag{2.13}$$

$$|\eta^*| = |G^*/\omega| \tag{2.14}$$

Extensive feedstock development and rheological characterization according to the variation of the ratio of binder components allowed to tailor the flow properties of the feedstock. The latter are particularly relevant for 3D printing processes (PAM and FDM), which are characterized by low shear rates and low deposition forces, in contrast to injection molding. Due to their flexibility, material extrusion processes such as PAM, in contrast to FDM, can use a higher solid loading similar to MIM (60 to 65 vol.% vs. 50 to 60 vol.%) [91, 112]. The pseudoplastic flow behavior of the feedstock and a lower print temperature could be exploited due to the higher forces in FDM during printing, which correspond to higher shear stresses. Some materials can solidify rapidly after extrusion. Appropriate cooling mechanisms, such as a heated bed or cooling fans, are used to control the solidification rate and prevent problems such as warping.

Optimizing the flow behavior of the feedstock is critical to achieving high-quality, accurate 3D printed objects. This involves balancing factors such as temperature control, viscosity, and shear thinning to ensure consistent material deposition throughout the printing process. Experimentation and fine-tuning of printing parameters is often required to achieve the desired results with different materials.

Measurement and Application in AM

According to Filip et al. [122], capturing true shear viscosity in PAM or MIM requires not only capillary data but also correction for die entrance pressure losses and velocity profiles. This level of detail is especially vital for low shear rate conditions typical of 3D printing.

Ajinjeru et al. [123] showed that complex viscosity increases significantly when reinforcing PEI feedstock with carbon fibers. This affects extruder torque, requiring higher process temperatures or reduced filler content for stable printing.

In MIM, particle morphology also plays a major role. Spherical, gas-atomized powders flow more easily than dendritic ones, allowing higher solid loadings (e.g. 50–65 vol.%) while maintaining pseudoplastic flow behavior [104].

2.5 Manufacturing Process

This section addresses key parameters like torque, feedstock compositions from literature, 3D printing techniques, and post-processing steps such as debinding and sintering.

2.5.1 Torque parameter

In physics and mechanics, torque is the rotational analogue of linear force. It is also referred to as the moment of force (also abbreviated as moment) [124]. Torque parameters in extrusion are critical to understanding the mechanical forces involved in the extrusion process. During extrusion, a material is pushed or pulled through a die with a desired cross-section. Torque parameters refer to the rotational force applied to the material or machine during the process. These parameters are affected by several factors [14, 91]:

- Material properties: The type of material being extruded (e.g., metals, plastics) significantly affects the torque required. Materials with higher viscosity or shear strength require more torque to be extruded.
- Die design: The complexity and shape of the die also affects torque. Narrower or more complex designs increase resistance and require higher torque.
- Temperature: For materials that are thermally softened or melted prior to extrusion (such as thermoplastics or certain metals), the temperature of the material can affect its viscosity and therefore the torque required.
- Extrusion speed: The speed at which the material is extruded will affect the torque required. Faster extrusion speeds generally require more torque to overcome the increased resistance.
- Lubrication: The presence or absence of lubrication between the material and the die surfaces can change the friction and therefore the torque.
- Extrusion equipment: The specific type of extrusion machine (e.g., single screw, twin screw) and its mechanical condition can also affect torque parameters. For example, twin screw extruders can handle higher torque levels compared to single screw extruders.
- Back pressure: The pressure built up at the die outlet can affect the torque required to push the material through the die.

Quantitatively, torque in extrusion can be measured in Newton-meters (Nm) or pound-force-feet (lbf-ft) and is calculated based on the resistance encountered by the material as it is forced through the die [124]. Monitoring and optimizing torque parameter are critical for efficient extrusion operations, as excessive torque can indicate potential problems such as die blockage, insufficient material heating or equipment overload, while insufficient torque can indicate processing conditions that are inadequate for the material's characteristics [14, 91].

Eickoff et al. [91] did a study on the filament fabrication of composite Ti6Al4V, PEG, PVB and surfactant as SA, PAT-77P or PAT-659CB and a torque measurement around 10 Nm has been measured as shown in Figure 2.26.

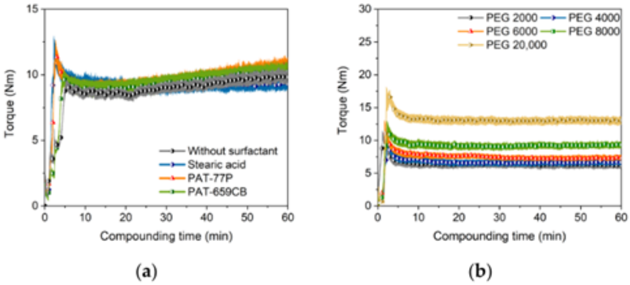

Figure 2.26: Torque recording of different compositions of composite Ti6Al4V, PEG, PVB and surfactant (SA, PAT:77P, PAT-659CB) [91]

A high infill percentage is desirable to enhance the density of the green part and consequently reduce the porosity and the shrinkage of the final part [125].

In the study conducted by Cerejo et al. [125], the maximum powder content in a stainless-steel binder feedstock was defined using a torque rheometer. The method consists of measuring the torque in the mixer while gradually adding the metal powder. The same torque rheometer method was used by Singh et al. [126] to obtain an optimal Ti6Al4V feedstock. The torque increases until it reaches a point of instability, that corresponds to the maximum solid fraction exploitable to ensure printability. Exceeding the maximum limit leads to a viscous filament with worse flowability.

In Figure 2.27, the critical load was registered for 64 vol.% solid content, but it was preferred to use the precautionary percentage of 59 vol.%. The interaction between powder particles is the main responsible for the viscosity increase when excessive solid infill is mixed.

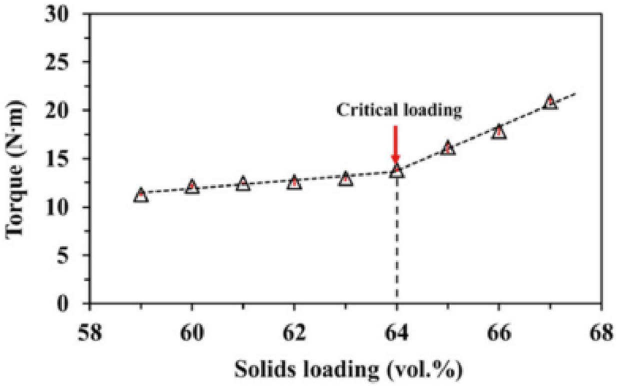

Figure 2.27: torque depending on the solid loading from [126]

According to Gloeckle [127], the filler-filler interaction depends on the powder loading and the particles size. The friction between powder leads to an increase in the minimum extrusion temperature and a lower flow rate. As seen previously, despite injection molding and PAM using similar feedstocks, differences reside in the flow properties that are more important in the case of the MEX process because the part needs to maintain its shape during printing. So, the shear-thinning behavior is more important in the MEX cases.

2.5.2 MIM and MEX feedstocks compositions in the literature

Appendix A give an overview of the composition of MIM and MEX feedstock's compositions found in the literature for ceramics and metals solid loading. These tables different feedstocks compositions found in the literature describing the binder composition, the rate of each component, but already the debinding and sintering conditions and final mechanical properties of build part.

It is possible to see that the rate of solid loading is limited for a certain range corresponding to 50 to 69 vol.%. Below 50 vol.%, the sintered part will have low final mechanical properties and a solid loading content higher than 69 vol.% is not extrudable due to a lack of binder conducting to a too high viscosity of the feedstock.

The global trend in some studies on Ti6Al4V feedstock development for screw-based MEX and MIM processes is the presence in most of the cases, of derivate of PolyEthylene PE as PEG (PolyEthylene Glycol), or LDPE/HDPE (Low- and High-Density PolyEthylene) as main component of the binder and waxes (PW) as backbone polymer. Several reasons can explain these choices as the low cost of these polymers, their compatibility with metallic powders, their flexibility, and rheological properties.

Feedstock fabrication methods

Commonly, the feedstocks for MIM and MEX processes are prepared through the following steps (Figure 2.28):

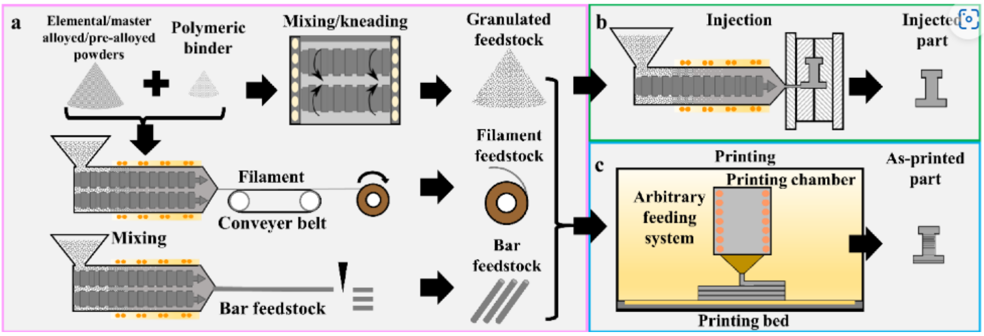

Figure 2.28: Feedstock preparation for MIM, MEX, FFF processes [128]

1. **Powder mixing for pre-impregnation:** the metallic or ceramic powders are dry-blended with a fraction of the binder (typically the surfactant or low-viscosity component) to ensure initial homogenization and wetting of the powder particles [129, 130].

2. **Hot mixing step with a high shear rate mixer:** the remaining binder components are added and the mixture is compounded under high shear in equipment such as a Brabender mixer, sigma blade kneader, or torque rheometer to form a homogeneous feedstock [20, 129, 130].

3. **Extrusion step into filaments with a twin-screw extruder or Granulation:** the compounded feedstock is extruded into strands or filaments using a single- or twin-screw extruder, depending on the target application (pellets production for MEX/PAM or filament for FFF-based metal printing) [131].

2.5.3 Extrusion print head

Print head for MIM and PAM/MEX machines

The extrusion head consists of the feeding zone, the extrusion screw, and the barrel where the material is heated and melted and forced through the nozzle as described in Figure 2.29. The extrusion head (or liquefier) and screw geometry play an important role in the melt behavior. Most current systems use a straight cylindrical tube with a conical section to which the nozzle is attached. The pressure drop in the extrusion head is an important factor affecting the process. Resistive heating is provided by a coiled heating element wrapped around the extrusion head or by cartridge heaters embedded in the head block [51, 132]. The heating elements are controlled by a closed-loop system using thermocouple sensors and controllers to maintain the required temperature for melting, depending on the feedstock properties. In addition, fans can be included into the print head, to prevent overheating and provide further control on the temperature inside the head. The complete print head units are often designed to be replaceable and can be swapped for different materials. The liquefier ends in the print nozzle through which the material exits from the system. The diameter of the nozzle depends on the material being used, and typically ranges from 200–500 µm, but in some cases, it is possible to print with a larger nozzle diameter for faster printing. In the case where a separate material is used for the support structure, a second set of feed system can be used as multi-head printing machine described in Figure 2.29 (e.g PAM Pollen AM) [132].

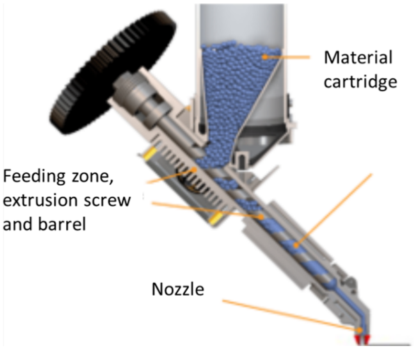

Figure 2.29: Print head of the PAM from Pollen AM [132]

While MIM and PAM both rely on the extrusion of metal-polymer feedstocks, the mechanical and rheological constraints of each process differ significantly. One of the key distinctions lies in the design of the extrusion screw, which affects material melting, flow consistency, and process stability. These differences critically determine the compatibility of MIM granules in PAM systems, often rendering them suboptimal without adaptation.

Screw Design for MIM compared to screw for PAM

1. Metal Injection Molding
   In MIM, the screw design is optimized for short, high-pressure injection cycles, where feedstock composed of finely powdered metal and binder is melted and rapidly injected into a mold cavity. Typical MIM screws are long (L/D $\approx$ 20–24), featuring [133]:

   - Three distinct zones: feed, compression, and metering
   - High shear mixing sections to homogenize the powder-binder mixture
   - A focus on rapid melting and compression to ensure mold filling before solidification

   Such designs prioritize throughput, pressure build-up, and efficient degassing—but not continuous, low-rate, stable extrusion.

2. Pellets Additive Manufacturing

   In contrast, PAM uses shorter screws (e.g., L/D $\approx$ 4.25), designed for continuous, low-pressure deposition of material layer-by-layer. As described by [134], PAM screws typically:

   - Have shallow compression ratios
   - Operate at lower rotational speeds (5–10 RPM)
   - Focus on stable melting and deposition, not rapid injection
   - Are more sensitive to viscosity variation and pellet geometry

   They are engineered to maintain flow consistency over time, which is crucial for dimensional accuracy and print stability [134].

MIM feedstocks

Those feedstocks exhibit the following specific characteristics [53, 135]:

- Highly loaded with metal powder (60–65 vol.%)
- Shaped for compaction and injection, not free flow
- Often have irregular particle geometry, leading to feeding inconsistencies

These characteristics cause problems in PAM systems:

- Poor flowability in the hopper or screw channel
- Inconsistent melt homogeneity
- Risk of nozzle clogging or pressure fluctuations

- Delayed or uneven melting profiles, which degrade print quality

Suwanpreecha and Manonukul [51] highlight that the binder systems and solid loading levels optimized for MIM do not translate well into extrusion-based AM, where smooth layer deposition requires a different thermal and rheological balance.

Engineering Adaptations

To adapt MIM pellets for use in PAM, several modifications are necessary:

- Pellet size and shape must be modified to improve feeding
- Binder systems may need plasticizing agents for better flow
- PAM extruders may require augmented torque or heating control

Some studies suggest designing hybrid screws with variable pitch and compression zones tailored to handle high-viscosity, particle-rich feedstocks like those used in metal AM [134].

Conclusion

The incompatibility of standard MIM pellets with PAM systems originates from fundamental differences in screw design, process dynamics, and material expectations. While MIM relies on short, intense injection cycles, PAM demands steady, low-pressure extrusion. Adapting MIM materials for AM thus requires re-engineering not only the hardware, but also the feedstock composition and pellet geometry.

2.5.4 3D Printing

The AM of metal-filled feedstocks by MEX techniques such as PAM involves a complex interplay between material formulation, process control, and machine configuration. Once the feedstock composition is validated, the printing process must be carefully optimized to ensure successful layer deposition, dimensional stability, and functional integrity. This section focuses on the influence of process parameters during the MEX printing stage and their direct impact on the characteristics of the produced green parts. In particular, parameters such as nozzle temperature, print speed, infill strategy, and build orientation are discussed in relation to mechanical performance, structural homogeneity, and surface quality.

2.5.4.1 Impact of Printing Parameters on Printed Parts

MEX technologies such as PAM construct parts layer-by-layer using thermoplastic or metal-filled filaments. The final properties of printed components—including mechanical performance, dimensional accuracy, and internal structure—are governed by multiple process parameters. Optimizing these parameters is essential to produce dense and defect-free green parts, especially when targeting sintering.

Among the most critical parameters, the nozzle temperature governs the viscosity of the feedstock and the fusion between layers. Increasing the nozzle temperature enhances flow and interlayer bonding; however, excessive temperatures can degrade the polymeric binder, affecting the homogeneity and surface finish of the part [136].

Similarly, the build plate temperature improves adhesion and minimizes warping by ensuring uniform cooling. This temperature typically ranges from 40 to 100°C and is generally set slightly below the binder's glass transition temperature Tg [137].

Printing speed and flow rate multiplier are two interconnected parameters. Slow speeds improve material deposition and bead shape regularity, while faster speeds reduce build time but can introduce flow instabilities and voids if not properly compensated. The flow rate multiplier allows fine control of the volume of material extruded and is often adjusted to compensate for under- or over-extrusion, directly affecting part density and dimensional accuracy [138, 139].

Layer thickness also plays a major role in the quality of the printed surface and the interlayer adhesion. Lower thickness values offer better surface smoothness and mechanical integrity but increase print time. Common values in metal-loaded feedstocks range from 0.05 mm to 0.4 mm depending on feedstock viscosity, printer resolution, and desired finish [51, 131]. In hybrid manufacturing systems combining additive and subtractive steps, thicker layers can be tolerated since surface finishing is performed afterward.

Figure 2.30 illustrates the raft system used to improve first-layer adhesion. This structure, often printed in the same material as the part, can be separated by an intermediate ceramic release layer for ease of removal. This technique is employed by manufacturers such as Desktop Metal and Markforged [140].

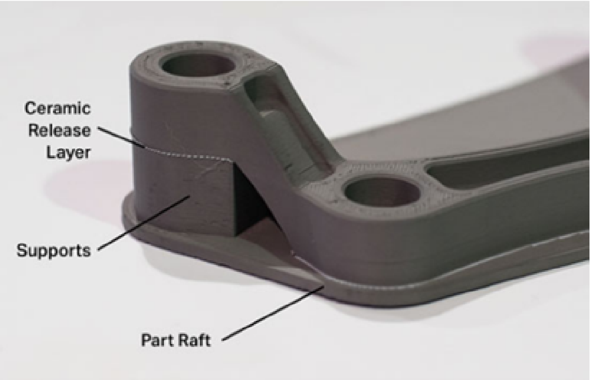

Figure 2.30: Ceramic release layer for support removal [141]

Other parameters include infill density and infill pattern, which influence mechanical performance and internal stress distribution. Denser infills increase tensile strength and reduce porosity. Printing orientation, nozzle diameter, screw speed, and extrusion pressure are also determinant, particularly in PAM where the feeding mechanism involves complex melt dynamics. Each parameter must be calibrated according to the feedstock formulation, machine setup, and desired part geometry [53, 126, 142].

The influence of these parameters on green part properties has been quantified in several studies. For instance, Valean et al. [143] showed that infill density accounted for 43.4% of the tensile strength variation, while the number of outer walls and the layer height also played significant roles. Numerical simulations by Bakrani Balani et al. [144] demonstrated that minor changes in viscosity or inlet velocity affect bead shape and void formation.

Taguchi-based experimental design has further highlighted the sensitivity of mechanical properties to nozzle diameter and layer thickness. Finer layers combined with appropriately sized nozzles result in reduced voids and improved repeatability [145]. Moreover, Zarean et al. [146] found that while print orientation in PEEK did not significantly affect tensile strength, greater variability was observed along the Z-axis due to weaker interlayer bonding.

The cooling system also plays a crucial role in metal extrusion processes. Efficient cooling avoids delamination, uneven shrinkage, or deformation. For metal-filled feedstocks with high viscosity and low thermal diffusivity, poor thermal management can compromise the dimensional fidelity and structural integrity of the part [51, 147].

2.5.4.2 The Staircase Effect

The staircase effect, also known as the stair-stepping effect, is a characteristic artifact of layer-by-layer fabrication methods such as MEX, FDM, or PAM. It manifests as step-like structures visible on inclined or curved surfaces as shown in Figure 2.31, compromising both visual appearance and functional performance [148].

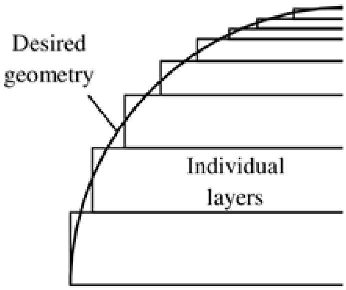

Figure 2.31: Staircase effect in the 3D printing process [149]

This effect results from the discrete vertical stacking of layers that approximate sloped features. The severity of the appearance of the staircase depends on several factors [148]:

- **Layer thickness:** Thicker layers create more pronounced steps.
- **Geometry and orientation:** Surfaces angled relative to the build plate show more visible steps.
- **Nozzle size:** Larger nozzles deposit more material per layer, enhancing the visibility of the stair patterns.

Functionally, the staircase effect can weaken mechanical properties by creating surface stress concentrators and increasing roughness, which may hinder assembly, sliding contact, or sealing behavior. Aesthetically, it reduces part smoothness and may require post-processing to achieve the desired finish.

Mitigation strategies include reducing the layer height, optimizing build orientation, or applying post-processing techniques such as machining, polishing, or chemical smoothing. Additionally, hybrid manufacturing approaches can circumvent this limitation by machining critical surfaces after sintering.

2.6 MIM/MEX debinding process

Debinding, a critical step in MIM and PAM processes, involves the removal of polymer binders from the feedstock loaded with metal powders, such as titanium. This process is typically divided into two main stages: chemical debinding and thermal debinding. Chemical debinding is the initial step, particularly effective for feedstocks containing water-soluble or solvent-soluble binders. It involves immersing the feedstock in a suitable chemical bath (aqueous or organic), allowing selective dissolution of the soluble binder components.

The material flow during this stage is driven by the diffusion of the solvent into interconnected pores formed by the dissolved binder, followed by the extraction of dissolved fragments out of the feedstock. This diffusion process is governed by concentration gradients and the physico-chemical interactions between the solvent, binder, and metallic powder. Once chemical debinding is complete, thermal debinding is employed to remove the remaining binder, particularly the insoluble components.

This step is carried out in a furnace under controlled atmosphere (inert or reducing), where a gradual temperature increase facilitates the thermal decomposition of the residual binder into volatile gases, which are subsequently evacuated through the porous structure. Chemically, this stage involves pyrolysis and, in some cases, oxidation reactions, depending on the binder composition and atmospheric conditions. The aim is to preserve the integrity of the porous framework and avoid defects or collapse, ensuring a uniform distribution of the metallic powder in preparation for the final sintering stage.

Figure 2.32 exhibits typical debinding recommendations from supplier of MIM feedstock.

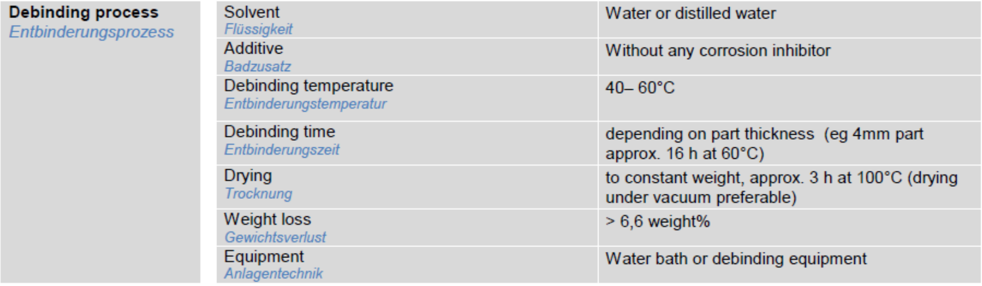

Debinding process *Entbinderungsprozess*	Solvent *Flüssigkeit*	Water or distilled water
	Additive *Badzusatz*	Without any corrosion inhibitor
	Debinding temperature *Entbinderungstemperatur*	40– 60°C
	Debinding time *Entbinderungszeit*	depending on part thickness (eg 4mm part approx. 16 h at 60°C)
	Drying *Trocknung*	to constant weight, approx. 3 h at 100°C (drying under vacuum preferable)
	Weight loss *Gewichtsverlust*	> 6,6 weight%
	Equipment *Anlagentechnik*	Water bath or debinding equipment

Figure 2.32: Debinding recommendations from manufacturer for Ti6Al4V feedstock

The debinding step of metal MEX is the same as for MIM process. This process aims to remove the binder after printing to create a "brown" part. For the conventional multi-component binder, the debinding process can be realized in two steps, which are:

Primary debinding step (or solvent/water debinding) to remove the main polymer component of the binder (low molecular weight polymer). When the main polymer is removed, an interconnected pore path is created so the backbone polymer can be easily removed in the secondary debinding step. Solvent or water debinding can take 15 hours or more depending on the thickness of the part, the type of binder and its rate [80]. As seen in [14, 51, 91, 135] in most of cases, the debinding temperature generally used varies from 40 to 75°C during 4 to 75 hours depending on the main component of the binder.

Secondary debinding step (thermal debinding) to remove the backbone component or other residual polymers and additives of the binder (high molecular weight polymer) in the printed part.

This process is achieved by slowly heating the part (1 to 5°C/min for MIM) to ensure that the backbone or remaining binder will evaporate without creating defects. A multi-holding step may be necessary, depending on the amount of binder remaining in the part after primary debinding. The debinding temperature depends on the type of the backbone polymer, according to the evaporation points of each type. This temperature can be accurately selected by Thermogravimetric analysis (TGA) of the feedstock, filament or binder only, or by Differential Scanning Calorimetry (DSC). The temperature range of 450 to 600°C during 1 to 2 hours for most of cases, but as observed for both MIM and metal MEX parts [44, 51].

In order to reduce the total debinding time, the combination of solvent (acid) and thermal debinding, which is known as catalytic debinding, was introduced by BASF under the name Catamold® [81]. Catalytic debinding was initially developed for the POM-based (polyacetal or polyformaldehyde) binder used in the MIM process. This requires a specially controlled catalytic debinding furnace. Although the part is primarily debinded and requires a secondary thermal debinding step to completely remove all remaining binder components, especially the backbone polymer, by evaporation in a controlled atmosphere, depending on the metallic powders. Typically, catalytic acid vapor, i.e. nitric acid, is used at a temperature of 110 to 120°C.

Figure 2.33 (a) and (b) exhibits C and O content uptake during debinding of Ti6Al4V MIM [150]; After complete binder removal, the carbon content remains relatively stable when the temperature exceeds 600°C and the holding time is longer than one hour. However, the O content continuously increases with increasing debinding temperature and time.

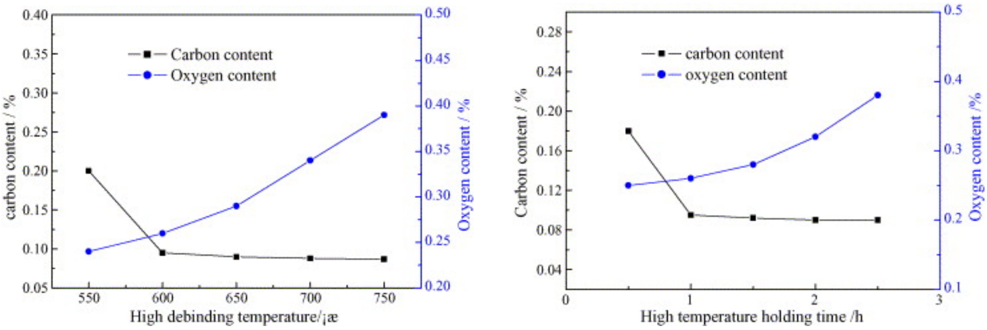

(a) Effect of debinding temperature

(b) Effect of high-temperature holding time

Figure 2.33: Correlation between processing parameters and carbon/oxygen content in Ti6Al4V specimens [150]

As low as possible debinding temperature and time is suggested to avoid O uptake, especially for Ti and its alloys.

In addition, the atmosphere of the furnace should be controlled to avoid any undesirable reaction during debinding. The atmosphere that is commonly used is an inert gas or vacuum depending on the alloys. Ar, N_2, H_2 and vacuum atmosphere are used for stainless steel, while argon or vacuum are used for Ti6Al4V alloy.

Shibo et al. [150] reported that vacuum provides lower O content when compared to the Ar flow atmosphere. On the other hand, MIM Ti alloys can also be successfully debind using the argon flow atmosphere.

2.7 Sintering

Sintering is a key step in the fabrication of metal parts via MEX and MIM. It enables the densification of the printed or molded components through thermal bonding of metal powders. This section explores the mechanisms involved in sintering, the factors influencing shrinkage and final density, and the differences in behavior between MEX and MIM processes. It also discusses the impact of powder characteristics, sintering parameters, and furnace atmosphere on the microstructure and mechanical properties of Ti6Al4V parts. Sintering is a thermal process used to bond metal powders and achieve densified components, with relative densities reaching up to 99% [151].

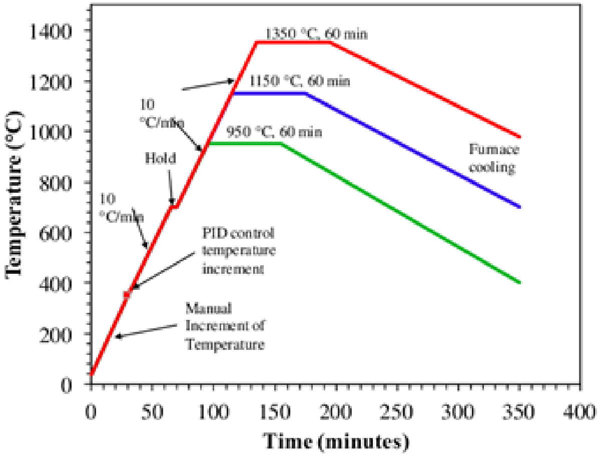

Figure 2.34: Typical sintering cycle for Ti6Al4V alloy [147]

Figure 2.34 describes typical sintering cycles used for Ti6Al4V components. During the initial stages of sintering, mass transport mechanisms such as evaporation and condensation, surface diffusion, and volume diffusion dominate. Once necks are formed between touching powder particles (as shown in Figure 2.35), plastic flow, viscous flow, grain boundary diffusion, and volume diffusion become the dominant mechanisms.

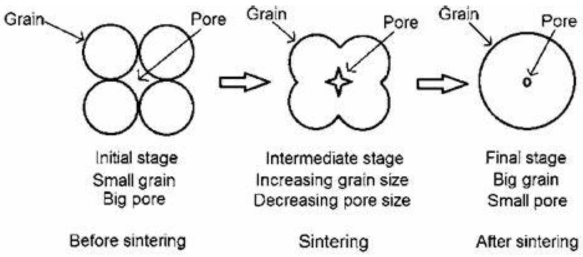

Figure 2.35: Particle diffusion during sintering step [152]

During sintering, shrinkage occurs, typically ranging from 12% to 20% of the part's total volume. This variation depends on several factors, including material type, powder characteristics (size, distribution), solid loading, sintering temperature and time, and the quality of the printed green part [153, 154]. Figure 2.36 shows a comparison between as-printed and as-sintered Ti6Al4V specimens produced via metal MEX, highlighting the dimensional changes due to shrinkage, similar to those observed in MIM.

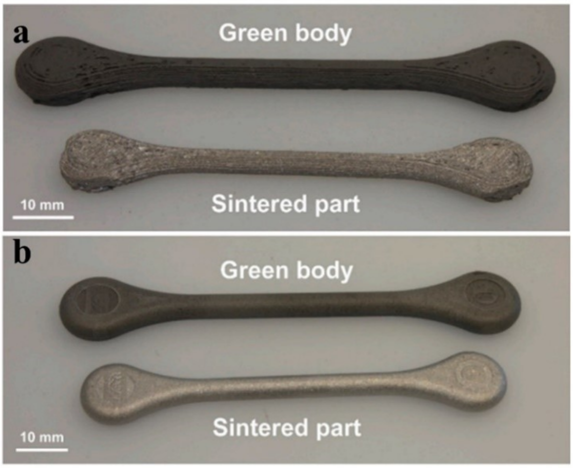

Figure 2.36: Green and sintered Ti6Al4V bending test part (a) made by MEX (b) made by MIM [127]

A typical sintering cycle is shown in Figure 2.37, representing the actual process recommended by the Ti6Al4V feedstock manufacturer PolyMIM GmbH (Germany).

Sintering processs *Sinterprozess*	Sintering atmosphere *Sinteratmosphäre*	Vacuum sintering or under argon 5.0 atmosphere
	Sintering substrata *Sinterunterlage*	Zircon oxide or yttrium oxide plates
	Sintering cycle *Sinterzyklus*	RT - 5K/min – 200°C 200°C – 2,5K/min – 600°C, 1h hold 600°C – 5K/min – 1350°C, 4h hold 1350°C – 15K/min – RT, cooling

Figure 2.37: Sintering recommendations of the manufacturer of Ti6Al4V MIM/MEX feedstock

Compared to MIM, the MEX process generally results in greater linear and volumetric shrinkage after debinding and sintering. This is mainly due to the lower green density obtained via MEX, caused by the layer-by-layer deposition and the presence of voids between adjacent extruded filaments. While MIM enables the fabrication of highly homogeneous and dense green parts, often exceeding 96–98% of the theoretical feedstock density, MEX green parts generally exhibit densities in the range of 85–93%, depending on the extrusion parameters and feedstock formulation.

As a result, linear shrinkage in MIM parts typically falls between 13% and 17% [129, 155], whereas MEX parts may exhibit shrinkage from 16% to over 22% [51, 130, 156], with volumetric shrinkage exceeding 40% in some cases. Shrinkage in MEX-processed parts also tends to be more anisotropic, particularly along the build (Z) axis, due to differences in interlayer bonding and thermal gradients during printing. These variations require careful dimensional compensation at the design stage and highlight the need for process calibration to achieve high dimensional accuracy in MEX-fabricated metal components.

Using fine powders increases diffusion rates and shrinkage, which leads to higher sintered densities—up to 99%. Fine powders also improve mass transport compared to coarser ones. Likewise, elevated sintering temperatures and extended sintering durations enhance shrinkage and part densification [77]. As shown by Bragaglia [50], the relative sintered density of Ti6Al4V produced via metal MEX increases with both temperature and time.

However, excessive sintering conditions can cause significant grain growth, compromising mechanical performance. Therefore, optimizing both temperature and time is crucial to achieve a favorable compromise between high density and acceptable grain size.

In PAM-based processes, part density can also be improved by adjusting key printing parameters, including flow rate, nozzle and extruder temperatures, and layer height. For instance, the HyProPAM process demonstrated sintered densities of up to 99.8% for black zirconia and 98.8% for titanium, underlining the impact of fine-tuning on final part quality.

Although MEX typically uses finer powders than MIM, their sintering temperatures are generally comparable. Ti6Al4V is commonly sintered in the β phase region. However, applying lower sintering temperatures within the α+β region for longer durations—particularly in MIM—has been shown to refine grain size and improve fatigue strength.

Figure 2.38 illustrates Ti6Al4V microstructures obtained via both MIM and MEX under conventional (β region) and low-temperature (α+β region) sintering.

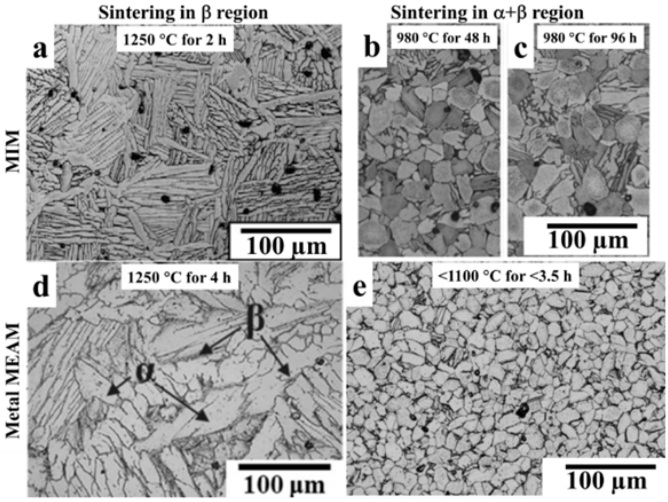

Figure 2.38: Microstructure comparison of Ti6Al4V parts (a) fabricated by MIM process sintered in the β region, (b,c) fabricated by MIM process sintered in the $\alpha + \beta$ region, (d) fabricated by metal MEX process sintered in the β region and (e) fabricated by metal MEX process sintered in the $\alpha + \beta$ region for grain refinement [153]

Grain refinement is clearly visible, and the resulting microstructures are largely similar across both processes and thermal conditions.

The furnace plays a critical role in sintering, particularly for titanium alloys, which are highly reactive with carbon, oxygen, nitrogen, and hydrogen. Excessive impurity pick-up during debinding and sintering reduces elongation owing to the formation of (α)-phase by oxygen pick-up in CP-Ti and the formation of brittle TiC generated by excessive carbon in beta Ti alloys. It has been suggested that Ti sponge material with a high specific area should be placed in the sintering furnace with MIM Ti parts to scavenge any impurities in the furnace atmosphere [151, 153].

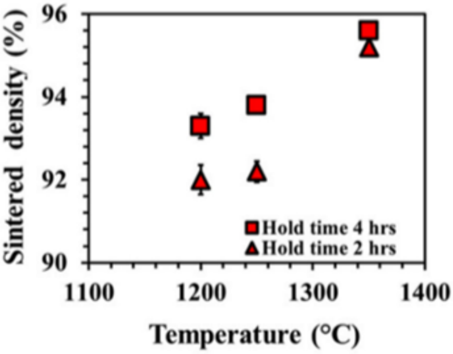

Figure 2.39: Relative sintered density of Ti6Al4V fabricated by metal MEX process sintered using varied sintering temperature and time, demonstrating the dependence of relative sintered density on the sintering temperature and time [153]

The sintering temperature plays a crucial role in the densification of MEX and MIM parts. As shown in Figure 2.39, the sintering temperature for the metal MEX process has an important impact on the sintered density of the part. It was proved by [153] that the sintered density can be improved from 92% to 95% by increasing the sintering temperature from 1200 to 1350°C. In the same way, it clearly appears that a finer particle size leads to a higher relative sintered density [153].

2.8 Qualification of metallic additive manufactured parts

As AM technologies mature, the qualification of metallic parts becomes essential to ensure their reliability, performance, and compliance with industrial standards. Among the various criteria used to qualify metallic parts produced by AM, dimensional accuracy and surface roughness are two fundamental parameters.

2.8.1 Dimensional accuracy and surface roughness

2.8.1.1 Dimensional and geometrical accuracy

Studies often focus on how closely AM parts meet the intended dimensions. Techniques such as X-ray computed tomography (CT), laser scanning, and digital image correlation are frequently used for this purpose.

The dimensional and geometric accuracy of MEX 3D printing systems is often characterized using the ISO 286-1 tolerance interval (IT) [110], which defines standardized limits for acceptable dimensional deviations. While MEX processes such as FDM and PAM generally yield lower precision than subtractive manufacturing, they can still meet industrial tolerances depending on machine quality and process control. According to ISO 286-1, PAM typically achieves tolerances within the IT13 to IT16 range [157]. Spitaels et al. [158] specifically evaluated the dimensional accuracy of the Pollen PAM system and reported an IT grade of 15 to 16, which is higher (i.e., less precise) than the performance of a commercial Ultimaker FDM printer, which achieved an IT13 classification. These results highlight the variability in accuracy among extrusion-based AM systems and underline the importance of calibration and process optimization to approach tighter tolerance classes.

2.8.1.2 Surface roughness

Due to the layered nature of AM processes, surface roughness is a critical parameter. Researchers use profilometers and optical microscopy to quantify surface roughness and understand its impact on part performance. Typical metrics include arithmetic surface roughness Ra (µm) and total surface roughness Rt (µm) [158]. Ra represents the absolute values of the surface deviations from the mean plane within a sample length. It provides a general indication of surface texture and is the most used surface roughness parameter. Ra is measured in micrometers (µm) or microinches. Rt represents the total height from the roughest peak to the deepest valley within a given length. It measures the vertical distance between the highest and lowest points of surface irregularities. Like Ra, Rt is measured in micrometers (µm) or microinches. For AM metal parts, surface roughness standards help ensure part reliability, functionality and compatibility with intended applications. The main standards are:

- ISO 17295:2023: This standard provides terminology for AM – general principles and AM processes [159].
- ASTM F2924: This specification covers AM of Ti6Al4V alloy for powder bed fusion [120].
- ISO/ASTM 52900: Defines terms for AM processes, systems, and their operation as well as the properties of manufactured parts [1].
- NF EN 4288: Defines the rules for evaluating surface roughness using profile methods, specifying how to measure, filter, and assess parameters like R_a or R_z to ensure consistent and repeatable surface texture analysis [160].

2.8.2 Challenges and futures directions

A recurring theme is the need for standardized measurement techniques and benchmarks specific to AM parts to ensure consistency and reliability across the industry. As AM technologies transition from prototyping to full-scale production, scalable quality assurance methods that do not significantly increase time or cost are necessary. Currently, several standardization bodies such as ISO/ASTM are actively developing new guidelines tailored to AM. For instance, the ISO/ASTM 52900 [1] series addresses terminology and classification, while other emerging standards like ISO/ASTM 52908:2023 [1] specifically target mechanical testing of metal AM parts.

Additionally, initiatives like the ASTM F42 committee and ISO/TC 261 are working collaboratively [161] to harmonize global testing protocols, material specifications, and part qualification frameworks. These efforts are crucial to support industrial adoption, regulatory compliance (especially in sectors like aerospace and medical), and to enable reliable comparison of AM part performance across different platforms and processes. The continued evolution of these standards will play a key role in facilitating certification, traceability, and process validation in AM.

2.9 Life Cycle Assessment of PAM process compared to MIM process

2.9.1 Introduction

The environmental impact of the AM process, particularly in the context of PAM , remains underexplored due to a significant lack of research and publications in this domain. This is due to several factors, such as the lack of data provided by machine manufacturers, whether in terms of the manufacture of the machines or their use. Much data is classified as confidential, and therefore it is difficult in most cases to carry out a cycle analysis with a solid database. However, measuring the environmental impact of a process is a challenge that needs to be addressed.

2.9.2 Generalities – Life Cycle Assessment (LCA)

Life Cycle Assessment (LCA) is a standardized and comprehensive methodology used to evaluate the environmental impacts of a product, process, or service throughout its entire life cycle. This includes all stages from raw material extraction, material processing, manufacturing, distribution, use, maintenance, and repair, to end-of-life treatment such as disposal or recycling. The primary objective of LCA is to evaluate the environmental impacts associated with every stage of a product's life cycle. This comprehensive approach is intended to support more informed decision-making by consumers, businesses, policymakers, and other stakeholders, ultimately contributing to the advancement of sustainable development [162].

LCA is especially useful for finding which parts of a process harm the environment the most, comparing different technologies, and helping to design more eco-friendly products. It helps people to quantify resource consumption, emissions, and waste generation, and to assess trade-offs between different environmental impacts.

According to the ISO 14040:2006 [163] and ISO 14044:2006 standards [164], an LCA study is structured into four main phases:

1. Goal and Scope Definition This initial phase sets the foundation of the study. It defines the purpose of the assessment, the intended audience, and the functional unit, which serves as the reference for quantifying environmental impacts. It also establishes the system boundaries (i.e., which processes are included or excluded), the impact categories to be considered (e.g., global warming potential, resource depletion), and the assumptions or limitations that will guide the analysis.

2. Life Cycle Inventory (LCI) This phase involves the collection and quantification of input and output data for each process within the system boundaries. It includes data on energy and material consumption, emissions to air, water, and soil, and waste generation. The accuracy and completeness of the LCI are critical for the reliability of the overall assessment.

3. Life Cycle Impact Assessment (LCIA) In this phase, the inventory data are translated into potential environmental impacts using characterization models. The results are grouped into impact categories such as climate change, acidification, eutrophication, and human toxicity. This step helps to understand the relative significance of different environmental burdens.

4. Interpretation The final phase synthesizes the results of the LCI and LCIA to draw conclusions and make recommendations. It identifies the life cycle stages with the greatest environmental impact, evaluates the robustness of the results through sensitivity analyses, and highlights critical points for improvement. This phase is essential for supporting decision-making and guiding future developments.

By using this step-by-step method, LCA gives a clear and reliable way to measure and improve how products and technologies affect the environment. In the context of this thesis, LCA will be used to compare the environmental impacts of PAM and MIM for the production of Ti6Al4V parts, thereby contributing to the development of more sustainable manufacturing practices.

2.9.3 Life Cycle Assessment of AM Technologies

The application of LCA to AM technologies is essential for understanding their environmental performance and for guiding the development of more sustainable production methods. While AM is often promoted for its potential to reduce material waste and enable localized, on-demand production, its actual environmental impact depends on multiple factors, including energy consumption, material efficiency, and waste generation throughout the product life cycle [39, 165].

2.9.4 Environmental Impact of AM

2.9.4.1 Energy Consumption

AM processes, particularly those involving thermal operations such as extrusion or laser sintering, can be energy-intensive. Compared to traditional manufacturing methods like injection molding or machining, AM often requires longer processing times and continuous heating, which can significantly increase energy demand. Evaluating and optimizing energy consumption is therefore a key aspect of improving the sustainability of AM [38, 166].

2.9.4.2 Material Efficiency

One of the main advantages of AM is its ability to use only the material necessary to build a part, thereby minimizing waste. This is especially true for complex geometries that would otherwise require extensive machining. The efficiency depends on the process and material used. For example, support structures in some AM processes may still generate waste, and not all unused material can be recycled [167, 168].

2.9.4.3 Waste Generation

Although AM generally produces less waste than subtractive methods, it is not waste-free. Failed prints, support materials, and post-processing residues contribute to the overall environmental burden. Strategies to reduce waste include improving process reliability, optimizing part orientation, and developing recyclable or biodegradable materials [167].

2.9.5 Life Cycle Inventory (LCI) for AM

The LCI phase is a critical component of the LCA methodology, as it involves the systematic quantification of all material and energy flows associated with a product or process. This phase provides the foundational data needed to assess environmental impacts in subsequent stages [169]:

- Data Collection Methods: Data for the LCI can be collected through various means, including direct measurements, process simulations, literature reviews, and the use of standardized databases. The inventory phase is where all material and energy flows are quantified. It includes a description of the database used, the inputs of energy and materials, the calculations performed, and the way the system has been modeled.
- Impact Assessment: This phase involves the use of specialized software and calculation methods to convert the quantified flows into environmental impact categories. Through this characterization process, the environmental impact profile of the system under study is established. One of the most commonly used and comprehensive tools for LCA is SimaPro, which supports detailed modeling and analysis. This tool includes a wide range of databases for the LCI phase, with EcoInvent being the most widely used. EcoInvent provides extensive data on energy supply, production processes, transportation, and waste management, all linked to their respective environmental performance indicators.
- LCI for AM Processes: In the context of AM, the LCI includes specific data such as the type and quantity of raw materials, energy consumption during printing, emissions from heating or melting processes, and waste generated from failed prints or support structures.

2.9.6 Life Cycle Impact Assessment (LCIA) for AM

The LCIA phase translates the inventory data into potential environmental impacts using characterization models [39, 170].

- Impact Categories: The environmental impacts are grouped into categories such as Global Warming Potential, Ozone Depletion Potential, Acidification and Eutrophication, and Resource Depletion.

  The characterization of environmental impact categories was carried out using the Product Environmental Footprint (PEF) methodology, a standardized approach developed by the European Commission to provide a consistent framework for assessing environmental performance. This method enables the comparison of products and processes based on a comprehensive set of impact indicators.

  All impact categories defined by the PEF were considered in the assessment, including: Acidification of terrestrial and freshwater ecosystems (AP), Human toxicity – cancer effects (HTP-C), Climate change (GWP), Freshwater ecotoxicity (FETP), Freshwater eutrophication (F-EP), Marine eutrophication (M-EP), Terrestrial eutrophication (T-EP), Ionizing radiation (IRP), Land use (LU), Human toxicity – non-cancer effects (HTP-NC), Ozone depletion (ODP), Photochemical ozone formation (POCP), Fossil resource use (F-RD), Mineral and metal resource use (M-RD), Respiratory effects due to inorganic pollutants (PMF), Water scarcity (W-RD) [170].

  This comprehensive set of indicators ensures a holistic evaluation of the environmental impacts associated with the studied system, supporting more informed and sustainable decision-making.

- Assessment Methods: Several LCIA methods exist, including ReCiPe [170], TRACI [171], and CML [172]. Among these, ReCiPe is particularly well-suited for AM applications due to its comprehensive coverage of midpoint and endpoint indicators, and its compatibility with European environmental policy frameworks.

In LCA, midpoint and endpoint indicators represent two levels of impact assessment. Midpoint indicators quantify environmental mechanisms at an intermediate stage in the cause-effect chain (e.g., climate change in kg CO_2-eq), offering detailed and relatively robust results. Endpoint indicators aggregate these into damage categories affecting areas of protection such as human health (in DALY), ecosystem quality (in $\mathrm{PDF} \cdot \mathrm{m}^2 \cdot \mathrm{yr}$ corresponding to the Potential Disappeared Fraction of species over a certain area and time), and resource depletion (in MJ), providing a more intuitive but more uncertain interpretation [164, 170, 173].

2.9.7 Comparison of AM and Traditional Manufacturing

The environmental performance of AM compared to traditional manufacturing methods has been the subject of increasing attention in recent years. LCA studies provide a robust framework for comparing these technologies across multiple impact categories.

- Environmental Performance [38, 39, 174]
  AM processes often demonstrate advantages in terms of material efficiency and design flexibility, particularly for complex geometries and low-volume production. However, they can also exhibit higher energy consumption, especially in thermally intensive processes like FFF or SLM. Traditional methods such as Injection Molding (IM) tend to be more energy-efficient for large-scale production due to optimized cycle times and economies of scale.

- Case Studies
  Several case studies have been conducted to evaluate the environmental advantages and disadvantages of AM technologies compared to traditional manufacturing methods. These studies provide valuable insights into the contexts in which AM can offer sustainability benefits, as well as the limitations that must be addressed.

  In a study by Kokare [4], AM technologies were found to have a positive environmental impact, particularly in scenarios involving complex geometries and small production batches. The functional unit (FU) was defined as the production of a single mechanical part. The research highlighted that AM can significantly reduce energy consumption and raw material usage compared to conventional manufacturing processes, especially when the design complexity would otherwise require extensive machining or tooling. These results underscore the environmental efficiency of AM when complexity and customization outweigh the advantages of conventional mass production.

  A more detailed analysis was conducted by Ulkir et al. (2023) [38], who performed a LCA of products manufactured using different materials and AM techniques, including Fused Deposition Modeling (FDM) and Stereolithography (SLA). The study followed ISO 14040/44 [163, 164] standards and assessed the environmental impacts from raw material extraction through to end-of-life disposal. The FU in this study was defined as the production of 1 kg of printed material. Materials such as Acrylonitrile Butadiene Styrene (ABS), Polylactic Acid (PLA), Polyethylene Terephthalate (PETG), and Ultraviolet (UV) Resin were evaluated.

> According to Ulkir, UV resin was identified as the most environmentally friendly material based on both midpoint (e.g., global warming potential) and endpoint indicators (e.g., damage to human health and ecosystems), whereas ABS was found to have the highest environmental burden due to its fossil-based composition and high energy demand during processing. This research provides valuable guidance for practitioners in AM by helping them assess the environmental impacts of different materials and make more sustainable choices. It also highlights the critical importance of material selection and process type in determining the overall environmental footprint of AM products.
>
> A study conducted by Bezzina et al. [39] offers a comparative analysis of the environmental and financial impacts of FFF versus IM for the production of cosmetic plastic packaging. The functional unit in this case was the production of 100,000 identical packaging units. The results revealed that FFF has a significantly higher environmental impact, primarily due to its energy consumption, which was approximately five times greater than that of IM. Energy use during the printing process alone accounted for nearly 80% of FFF's total environmental footprint. Although IM required a larger quantity of raw materials, resulting in a slightly higher impact in that area, the overall environmental performance of IM remained superior due to the excessive energy demands of FFF.
>
> From a financial standpoint, FFF was also found to be considerably more expensive. A net present value (NPV) analysis showed that the cost of producing parts via FFF was seventeen times higher than with IM. This disparity was largely attributed to the higher cost of raw materials and the intensive energy consumption associated with FFF. However, a sensitivity analysis indicated that FFF could become more financially viable than IM for production volumes below 20,000 units per year, primarily due to the high initial tooling costs associated with IM from an economic standpoint, rather than an environmental one. In terms of product quality, IM outperformed FFF both aesthetically and functionally. The layer-by-layer nature of FFF led to visible surface defects and structural inconsistencies that were not observed in IM-produced parts.
>
> The study concluded that, under current conditions, IM remains both environmentally and economically more advantageous than FFF for large-scale production of plastic cosmetic packaging. The high energy consumption and associated environmental impact, together with the higher cost of FFF, make it less feasible than IM for high-volume production. Nevertheless, for small production runs, FFF may offer a competitive alternative due to its lower initial investment and its ability to produce complex geometries without additional tooling costs. The authors recommend further exploration of alternative 3D printing technologies that could reduce cycle times and energy consumption, potentially making AM more competitive with traditional manufacturing methods such as IM. Additionally, the use of more environmentally friendly materials and the optimization of part designs specifically for AM could further enhance the sustainability and cost-effectiveness of FFF.

These case studies collectively demonstrate that while AM can offer environmental and economic advantages in specific contexts, particularly for low-volume, high-complexity parts, its sustainability is highly dependent on factors such as material choice, energy efficiency, and production scale. They also underscore the importance of continued research into more energy-efficient AM technologies and the development of eco-friendly materials to enhance the overall sustainability of AM.

2.9.8 Future Directions and Research Gaps

Despite the growing research on AM sustainability, several gaps remain:

2.9.8.1 Emerging Technologies

New AM techniques such as PAM, Cold Spray AM, and Hybrid AM systems offer promising avenues for reducing energy use and improving material efficiency. However, their environmental performance is still poorly documented [167, 175].

2.9.8.2 Sustainability in AM

Sustainability in AM must be evaluated through the lens of the Triple Bottom Line, which considers environmental, economic, and social dimensions:

To improve sustainability, eco-design principles can be applied to AM processes. These include designing parts to minimize support structures and material use, selecting biodegradable or recyclable materials, optimizing print parameters to reduce energy consumption, and considering end-of-life scenarios during the design phase [9].

2.9.8.3 Research Gaps

Most LCA studies focus on established AM methods like FDM or SLA. There is a notable lack of quantitative data for PAM, particularly regarding CO_2 emissions per part, energy consumption per unit of material, and material efficiency and waste rates [175]. In addition, currently available LCA databases are insufficiently populated with process-specific data for PAM, making reliable environmental assessment even more challenging.

Recent research efforts should focus on quantifying these performance metrics under controlled production conditions. This includes conducting sensitivity analyses on key process parameters such as nozzle diameter, extrusion temperature, and binder content, in order to better understand their influence on the environmental and technical performance of AM processes.

2.10 Conclusions and strategy of the research

A comprehensive literature review was conducted to establish the scientific and technological framework of this thesis. It identified several key areas, including general aspects of AM and its growing role in industry, with a particular focus on two technologies: MIM and 3D printing by MEX.

These two processes share notable similarities, especially in the formulation of feedstocks, which consist of a filler (metallic or ceramic) and a polymer binder—often a blend of thermoplastic polymers and surfactants. The non-Newtonian behavior of the binder is essential in both cases: in MIM, it enables homogeneous mixing and injection into complex molds while minimizing defects; in MEX, it ensures stable extrusion and shape retention after deposition.

Despite their similarities, key differences exist, particularly in the required viscosity of the feedstock. MEX typically requires slightly lower viscosities to allow extrusion through small-diameter nozzles. The filler loading rates are comparable, generally between 50% and 69% by volume. Both technologies involve debinding and sintering steps, although MEX presents specific challenges, such as the rapid oxidation of Ti6Al4V during sintering.

The review also highlighted phenomena specific to MEX, such as the staircase effect and the sharkskin effect, which are influenced by molding temperatures and feedstock composition.

Feedstock Formulations and Current Limitations

Feedstock formulations are well-documented for MIM, particularly with ceramic or metallic fillers (e.g., zirconia, 17-4PH, 316L, Ti6Al4V) and various polymer binders (PMMA, PVB, EVA, wax, PEG, Embemould K83). However, for MEX, data remains limited. To date, only three feedstock formulations using Ti6Al4V with a partially water-soluble binder have been developed, all using PEG as the main binder.

The mixing stages are similar: a pre-mixing step using a twin-screw extruder (e.g., Brabender type), followed by filament extrusion at temperatures ranging from 110°C to 190°C. Typical debinding and sintering cycles are described, highlighting the challenges of binder removal and titanium oxidation.

Identified Gaps and Originality of the Thesis

A critical gap identified in the literature is the lack of studies on the environmental impacts of MEX technology and, more broadly, AM by extrusion. Since 2023, only a few publications have addressed these aspects, indicating a growing but still emerging interest.

Comparative studies with MIM show that MEX has a higher environmental impact, mainly due to energy consumption. However, for small production runs, manufacturing costs remain competitive. While MEX is not yet a mature technology, its potential for future development toward more sustainable processes is significant.

Contribution of the Thesis

This thesis positions itself within this context, with its originality based on:

- The development of new feedstock formulations tailored to MEX technology, particularly for metallic alloys like Ti6Al4V.
- An in-depth study of rheological properties and their influence on printed part quality.
- An indirect evaluation of the environmental impacts of MEX, a topic still scarcely explored through a cradle to gate approach.
- A comparative approach between MIM and MEX, providing insights into optimization strategies for more efficient and sustainable AM.

Part II

Experimental Part

Introduction and Global Context of the Experimental Work

This PhD thesis aims to develop a feedstock formulation incorporating fully or partially water-soluble and bio-based binders specifically tailored to the material extrusion process. In addition, a comparative study on energy and material consumption between PAM and MIM will be conducted to compare the potential environmental impact of PAM technology with that of the Metal Injection Molding (MIM) process.

The main objectives of this work are as follows:

- To evaluate the environmental impact of a PAM system in comparison with MIM, focusing on energy and material consumption;
- Identify key areas for improvement to reduce the environmental footprint of PAM;
- To develop a PAM-specific feedstock formulation with optimized viscosity and adhesion properties;
- Design a more eco-friendly titanium feedstock by incorporating water-soluble and/or bio-based components.

An environmental assessment was conducted using a commercial Ti6Al4V feedstock supplied by PolyMIM GmbH within the framework of the HyProPAM project as reference case. The study revealed that the primary source of energy consumption in PAM is its significantly longer per-part manufacturing time, heating elements, and the need to heat during all the process.

A full Life Cycle Assessment (LCA) was not carried out due to the lack of available data in existing databases, which would have required creating a dedicated dataset specifically for this study—a task that would have been too time-consuming.

Volatile Organic Compound (VOC) emissions could not be measured due to a lack of appropriate equipment. However, they are assumed to be low in both processes, particularly in PAM, as long as processing temperatures remain below the degradation thresholds of the binder components.

It is important to note that the commercial feedstock used in the project was not initially developed for PAM, but rather for injection molding. Its formulation is optimized for easy demolding, which results in poor adhesion during extrusion and defects such as shark-skin effects. These lead to open and closed porosities, which are directly related to the feedstock's rheology and the high processing temperatures required.

The development of a more environmentally responsible feedstock, processable at lower temperatures, could represent a significant improvement for PAM. This would help reduce energy consumption (for example, by lowering nozzle temperatures) and improve print quality, dimensional stability, and overall process sustainability.

PAM was chosen because this thesis continues the work initiated in the HyProPAM project, where PAM was already used. PAM allows the production of complex parts and, from a hybrid manufacturing perspective, enables fast printing using a larger nozzle diameter without focusing on surface quality. Indeed, surface finishing is corrected later through green state machining (before debinding and sintering), which is easier than machining sintered Ti6Al4V. Using a high nozzle diameter also helps print faster, reduce the number of interfaces, and potentially improve mechanical properties. Surface quality is not a concern in the comparative study on energy and materials consumption.

CHAPTER 3

Comparative Study of PAM and MIM Processes

The implementation of an energy and material consumption comparative study within this doctoral research is both timely and essential, given the growing emphasis on sustainable manufacturing and the environmental challenges associated with emerging technologies such as PAM. While AM is often promoted for its potential to reduce material waste and enable complex geometries, its actual environmental performance, particularly in metal-based processes like PAM, remains insufficiently documented in the literature.

This thesis, aims to develop a new, eco-responsible feedstock for the AM of Ti6Al4V parts using PAM. However, the environmental implications of this technology, especially when compared to more established processes such as Metal Injection Molding (MIM), are not yet well understood. Therefore, a comparative study between PAM and MIM is necessary to quantify and evaluate the environmental trade-offs associated with each process through energy and material consumption.

3.1 Introduction

In the context of sustainable development, Life Cycle Assessment (LCA) is a widely used tool to evaluate the environmental impact of manufacturing technologies. However, its results can vary significantly depending on the scope and available data, which may lead to biased comparisons between processes.

A full LCA in accordance with ISO 14040/14044 standards [163, 164] was initially considered. However, the absence of PAM-specific data in reference databases such as EcoInvent highlighted a relevant gap. While the creation of a dedicated dataset was beyond the scope and timeframe of this thesis, this limitation underlines the need for future work to develop such data for more comprehensive assessments.

Instead, the study adopts a qualitative approach focused on energy and material consumption during the manufacturing phase, in line with the general principles of LCA. These aspects were previously discussed in the literature review.

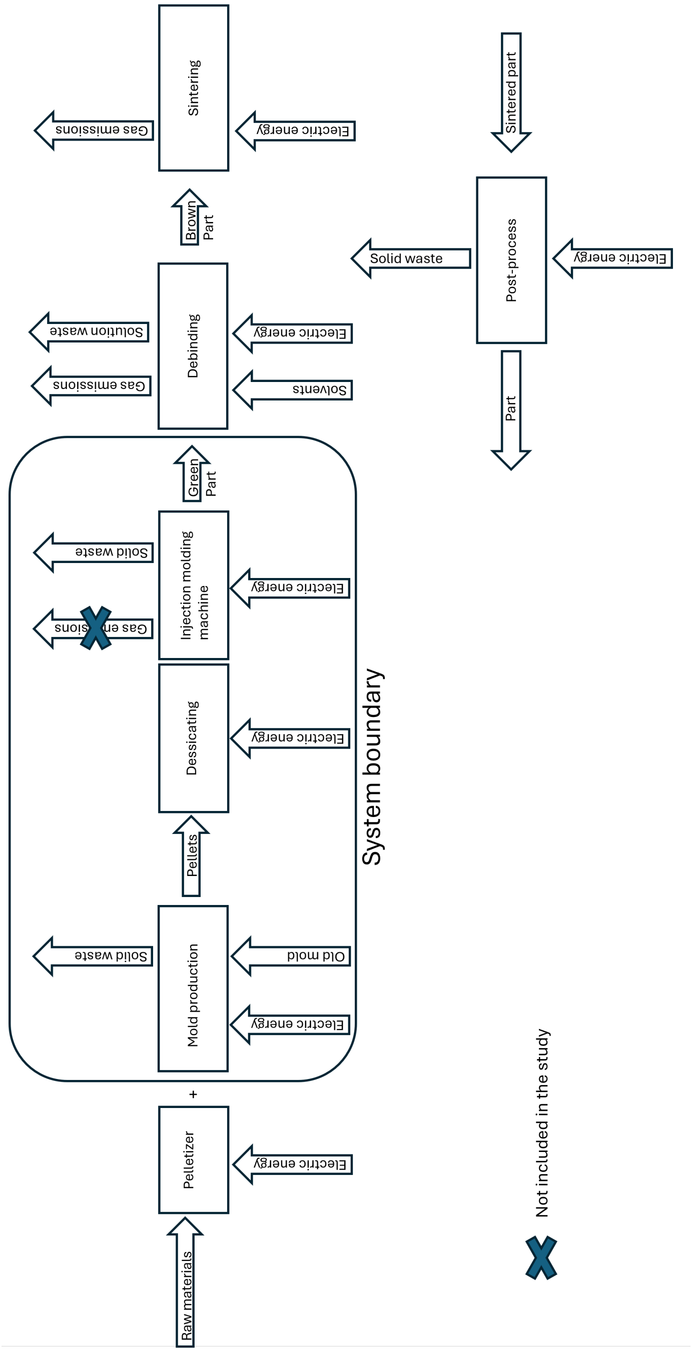

Figure 3.1: System boundary and production system of the MIM process

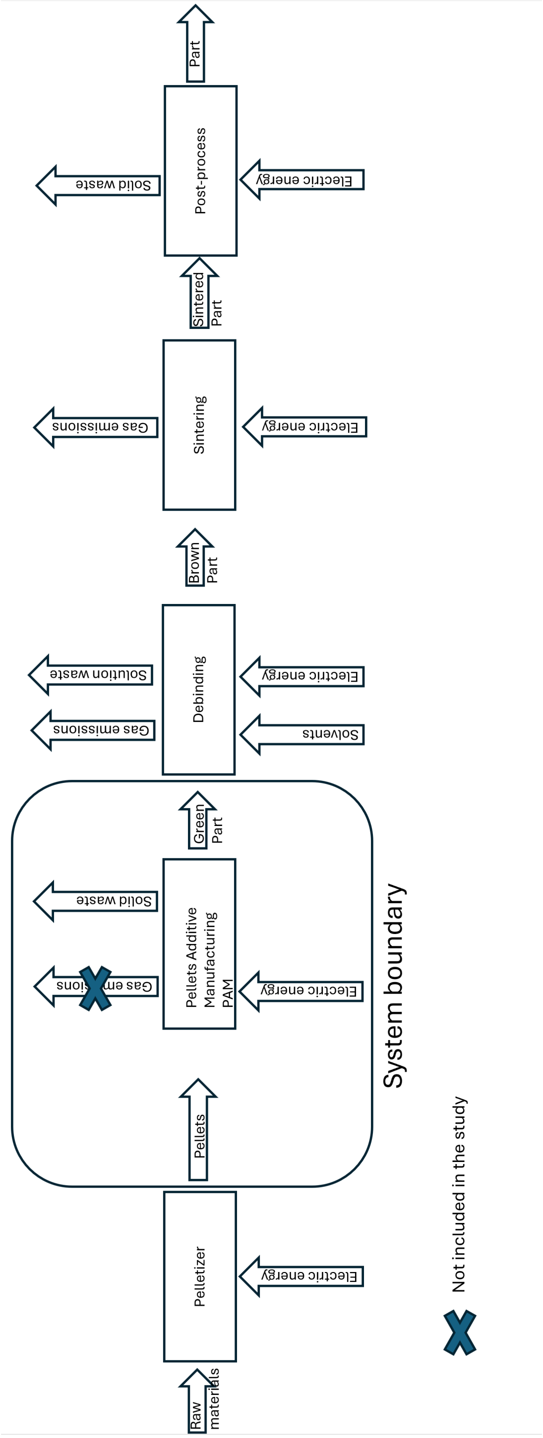

Figure 3.2: System boundary and production system of the PAM process

This work is part of the HyProPAM project, which aims to develop a hybrid manufacturing platform combining PAM with subtractive processes such as milling and laser finishing. The feedstock used is based on a Ti6Al4V formulation originally developed for MIM. While suitable for MIM due to its high viscosity and ease of demolding, it presents challenges in PAM, such as poor interlayer adhesion and instability during printing, mainly due to high processing temperatures (190-195°C).

Due to limited LCA data for PAM, the study draws on research related to Fused Deposition Modeling (FDM), which shares similar extrusion principles. Despite differences—such as mold use in MIM—the overall process flow remains comparable, as shown in Figures 3.1 and 3.2. Both technologies use similar feedstocks and involve common post-processing steps like debinding, sintering, and finishing.

Given the data limitations, specialized LCA tools like SimaPro could not be used. Therefore, this work is presented as a qualitative comparative study rather than a full quantitative LCA.

3.2 Materials and Methods

3.2.1 Case Study – Goal and Scope Definition

To enable a meaningful comparison between PAM and MIM, it is essential to define a functional unit and a representative part geometry. A literature review identified a titanium dental implant as a part compatible with both technologies [16, 127, 168, 176–178]. The selected design, illustrated in Figures 3.3 and 3.4, is sufficiently complex to justify AM, yet remains compatible with MIM fabrication [179, 180].

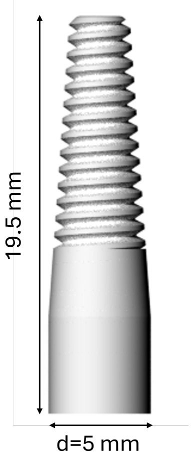

Figure 3.3: Adapted model of the dental implant

The design of the implant was simplified to reduce risks of failure during printing, especially around the connection point for the crown. Implant dimensions vary depending on clinical requirements, patient anatomy, and implant location. For this case study, the dimensions were set at 19.5 mm in length and 5 mm in diameter.

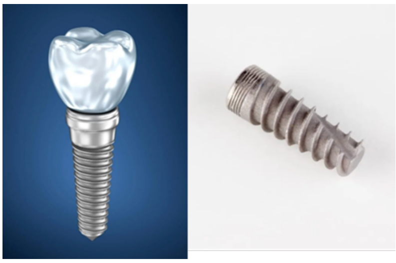

Figure 3.4: Dental implant in Ti6Al4V – case study [177]

The feedstock used in both technologies is a commercial Ti6Al4V-based formulation developed by PolyMIM GmbH, incorporating a partially water-soluble binder.

3.2.2 Assumptions and System Boundaries

To enable a meaningful comparison of the environmental performance between the MIM and PAM processes, several assumptions and system boundaries—previously described—are illustrated in Figures 3.1 and 3.2.

Limitations

- Raw material extraction and feedstock preparation are assumed to be the same for both processes and are therefore excluded from the analysis
- The production of equipment (e.g., machine assembly, electronics) is not considered in the scope of this study
- Debinding and sintering steps are assumed to be identical for both technologies and are thus not included
- Transportation and packaging are also excluded from the analysis

Assumptions

- A production volume of 5.000 parts is considered
- It is assumed that MIM feedstock is stored in a desiccator, based on industrial practices* ("*" = from expert recommendations)
- Four cavities mold fabrication is considered for the MIM process*
- The mold is produce with an old mold*
- 15-20 Tons range micro-injection molding machines as Microplast M2-II from Moiron [181] are considered as model*

- Power consumption is estimated at 3 kW for both machines, based on average equipment specifications [132, 181, 182]
- MIM is assumed to have a production capacity of 500 parts per hour*
- No support structures are required for PAM following DfAm principles as presented in the literature review chapter [9, 13]

To remind, a complete LCA using SimaPro could not be performed.

3.2.3 Environmental Impact Considerations

The scientific literature indicates that during the manufacturing phase, the most significant environmental impacts are primarily due to two key factors:

- Energy consumption during material processing [183];
- Material usage and associated losses throughout production [184].

However, when considering the entire life cycle of the process, including critical post-processing stages such as debinding and sintering, additional environmental burdens emerge. Notably, the release of effluents, such as solvents, volatile organic compounds (VOCs), fine particulate matter, and greenhouse gases like carbon dioxide (CO_2), becomes a substantial contributor to the overall environmental footprint of PAM [185].

This shows the environmental advantage of employing water-soluble binders or those that decompose cleanly, producing minimal toxic emissions. Such alternatives can significantly reduce the ecological impact of the process, particularly during the debinding phase.

Due to the inability to conduct direct MIM experiments, the study relied on data extracted from existing literature and expert insights to simulate and compare the environmental performance of both technologies. While this approach is theoretical, it provides a robust foundation for evaluating and contrasting the sustainability of PAM and MIM processes.

3.2.4 Mold production

To manufacture MIM molds, it is necessary to rely on advanced technologies such as high-precision CNC milling, Electrical Discharge Machining (EDM), and laser techniques. These methods allow for the production of intricate cavities and fine geometrical features with a level of precision that conventional machining cannot achieve. Once fabricated, molds are subjected to strict dimensional and geometric inspections, using coordinate measuring machines (CMMs) or even computed tomography (CT), to avoid potential defects and ensure repeatability.

In the context of this case study, the component considered weighs approximately 2.5 g, which corresponds to a typical application for micro-injection molding machines. The machine selected for this scale would typically be a Microplast or BOY injection press in the 15–20 ton range, commonly used for precision molding in the medical and electronics sectors [181].

For a production volume of 5,000 parts, a four-cavity mold would be used—balancing productivity and cost. A mold of this quality (with underwater injection and integrated cooling channels) would cost between €20,000 and €25,000. Higher cavity numbers would lead to a disproportionate increase in complexity and price of the mold.

Molds are typically produced from high-grade steel, often reusing the body (or “carcass”) of an old mold. Manufacturing lead times are typically around three months. Once in operation, such a setup could yield approximately 500 parts per hour.

An alternative approach involves the use of metal AM to fabricate mold plates via SLM. This method significantly reduces lead times, allowing functional plates to be produced within 1 to 2 weeks.

It is particularly relevant to discuss mold fabrication in this study, as it represents a key contributor to the environmental impact and cost structure of the MIM process—especially when compared with PAM, where no molds are required. However, data regarding mold production (especially for small series or micro-injection use cases) is scarce in the literature. Therefore, expert input from a professional in the mold-making industry was sought to obtain realistic and credible order-of-magnitude estimates. This ensures that the results presented here reflects industrial practice as closely as possible.

3.2.5 Setup

The 3D printing trials were performed using a PAM machine from Pollen AM. To quantify the energy consumption of the printing process, a GreenBlue GB202 power meter was installed directly on the PAM machine. This device measures electrical power with an accuracy of ±1% for both voltage and current.

To record the power usage in real time, a camera was set up to continuously film the power meter display during the entire printing process. Power values were extracted every 30 seconds over a 30-minute printing session. The total energy consumption was then calculated from this discrete dataset.

The data used for the MIM process came from official sources, including manufacturers, industrial suppliers, and expert feedback. According to the data quality levels defined by Ciroth et al. [169], this qualifies as class A data, ensuring high reliability and consistency.

The uncertainty estimates for energy and material consumption in PAM and MIM are grounded in metrological principles—particularly those outlined in the Guide to the Expression of Uncertainty in Measurement (GUM – JCGM 100:2008) [186]. These estimates also take into account the origin and reliability of the data (measured vs. theoretical), as well as insights from scientific literature and industrial practice.

Energy Consumption: estimated uncertainty

PAM (±5–10%)

Energy data for PAM were obtained through direct experimental measurements using a GreenBlue GB202 power meter, which has a stated accuracy of ±1% for both voltage and current. While the method described in the setup section ensures traceability, it introduces moderate uncertainty due to:

- Discrete time sampling (potentially missing transient power peaks),
- Variability in heating cycles,
- Minor manual interventions (e.g., purging or restarts).

According to the JCGM 100:2008 (GUM) guidelines [186], when calculating energy as a sum of discrete products (like E = P x t), the overall uncertainty depends on both the measurement accuracy and the sampling method. Given these factors, an uncertainty range of ± 5–10% is considered reasonable for a well-instrumented but non-continuously monitored experimental setup.

MIM (± 10–15%)

In contrast, energy data for MIM are entirely theoretical, derived from:

- Literature sources,
- Manufacturer specifications,
- Expert assumptions (e.g., press power consumption of 3 kW, cycle times, drying, and mold fabrication energy).

Mold fabrication energy is particularly variable, estimated between 360–432 kWh based on assumed machining durations and machine power ratings. These values are not directly measured and can vary significantly depending on equipment, process optimization, and plant-specific conditions. According to LCA methodology guidelines (e.g., Ciroth et al., 2011) [187], theoretical or expert-based data typically carry uncertainties of ± 10–20%. Given that operational energy is relatively constrained but mold-related data are more speculative, a total uncertainty of ± 10–15% is considered appropriate.

Material Consumption: estimated uncertainty

PAM (± 2–5%)

For PAM, material consumption was determined by directly weighing printed parts. Small recurring losses (e.g., due to purging or support structures) were estimated through repeated observations. These measurements were conducted under controlled laboratory conditions, with high weighing precision (typically $\leqslant$ 1%). As a result, the relative uncertainty in material consumption is estimated at ± 2–5% [167].

MIM (± 10–20%)

In the case of MIM, material consumption per part was reconstructed from theoretical components, including:

- Part mass,
- Excess injected material (sprues, runners),
- Amortized mold machining waste.

The latter was estimated based on the amount of raw material removed during mold fabrication (e.g., 3.5 kg), distributed over a batch of 5000 parts. These assumptions are highly dependent on mold geometry, block dimensions, machining strategies, and reuse policies. Due to the cumulative nature of these uncertainties and the lack of direct measurement, the overall uncertainty in material consumption for MIM is estimated at ± 10–20% [188, 189].

This case study perfectly illustrates the potential of hybrid manufacturing systems such as those developed in the HyProPAM project. The combination of AM (for the rough part) with subtractive operations (milling and laser finishing) enables the production of fully customized components [190]. For example, the screw thread of the dental implant—difficult to print with sufficient precision—can be finalized via post-processing steps to ensure perfect fit and mechanical functionality tailored to the patient.

3.3 Results

3.3.1 3D Printing with PAM

All printing parameters used to realize the part are listed below in Table 3.5a.

Parameter	Value
T_{radian}	200°C
T_{nozzle}	170°C
T_{extruder}	150°C
$T_{\text{buildplate}}$	70°C
Flow rate	160%
Infill density	100%
Printing speed	7 mm/s
Layer height	0.2 mm
Number of walls	1
Nozzle diameter	0.4 mm
Nozzle material	Brass

(a) 3D Printing Parameters for Ti6Al4V Feedstock on PAM

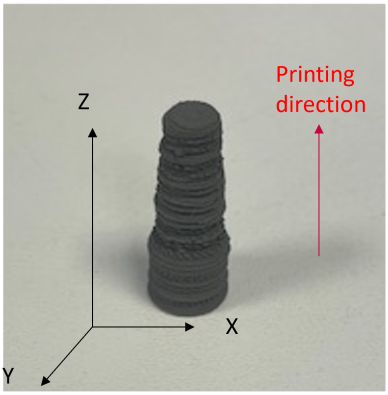

(b) 3D printed Ti6Al4V dental implant produced using PAM

Figure 3.5: Overview of 3D printing parameters (left) and the resulting printed part (right).

Printing the dental implant using the PAM process proved to be particularly challenging, especially regarding the screw thread geometry, which is difficult to reproduce with sufficient fidelity using extrusion-based processes as in Figure 3.5b of the as-printed implant exhibiting poor surface quality.

However, the primary objective of the printing trials was not to obtain a functional or high-quality implant, but rather to quantify the material usage and energy consumption of the process. As such, the quality of the printed part was not a limiting factor for this analysis.

3.3.2 Energy consumption

3.3.2.1 PAM

Energy consumption has been determined from the video of the power meter measurement during printing. The average power measured was 277 W. The printing time was 30 minutes, or 0.5 hours. To calculate the electricity consumption for this print, we use the formula [167]:

$$E = P \times t \tag{3.1}$$

Where:

- E is the energy consumption (in Wh)
- P is the power (in W)
- t is the printing time (in h)

The calculated average energy consumption of the PAM machine to print a dental implant is 139 Wh, which is equivalent to 0.139 kWh per piece. This aligns well with the general energy consumption range for AM (typically 0.05–0.5 kWh depending on volume and technology) [191, 192]. Considering approximately 2,500 hours to produce 5,000 pieces (30 minutes per piece), the total energy consumption can be calculated as follows:

$$E_{Total} = E_{part} \times N \tag{3.2}$$

Where:

- E_{Total} is the total energy consumption (kWh)
- E_{part} is the energy consumption for a part (kWh)
- N is the number of part

$$0.139 \times 5000 = 692.5kWh \tag{3.3}$$

Specific Energy Consumption

The total mass produced is given by:

$$\text{Total mass} = N \times \frac{m}{1000} \tag{3.4}$$

with m being the mass per part in grams (2.5 g):

$$\text{Total mass} = 5000 \times \frac{2.5}{1000} = 12.5 \text{ kg} \tag{3.5}$$

The specific energy consumption per kilogram is then calculated as:

$$E_{specific} = \frac{E}{\text{Total mass}} \tag{3.6}$$

$$E_{specific} = \frac{692.5}{12.5} = 55.4 \text{ kWh/kg} \tag{3.7}$$

These formulas are consistent with energy assessment models used in AM literature [193–195].

3.3.2.2 Injection molding estimations

The injection molding process uses a machine with a power consumption fixed at 3 kW and a production rate of 500 parts per hour. Producing 5,000 parts thus requires 10 hours. The total energy consumption for injection is:

$$E_{\text{injection}} = 3\,\text{kW} \times 10\,\text{h} = 30\,\text{kWh} \tag{3.8}$$

A desiccator is required to eliminate residual moisture in the feedstock, preventing defects such as cracking or injection failure. The energy for drying is estimated at:

$$E_{\text{drying}} = 3\,\text{kWh} \tag{3.9}$$

The total operational energy is:

$$E_{\text{operation}} = E_{\text{injection}} + E_{\text{drying}} = 30 + 3 = 33\,\text{kWh} \tag{3.10}$$

Thus, the energy consumption per part for the operational phase is:

$$E_{\text{operation/part}} = \frac{33}{5{,}000} = 0.0066\,\text{kWh} \tag{3.11}$$

This is consistent with Meekers et al. [196] and [197] for high-throughput scenarios.

The mold fabrication, required due to the complexity of dental implant geometry, involves 72 hours of five-axis CNC machining, channel drilling and milling, EDM, and heat treatment [198]. It consumes between 5 and 6 kW [162, 197], the average has been selected:

$$E_{\text{mold}} = 72\,\text{h} \times 5.5\,\text{kW} = 396\,\text{kWh} \tag{3.12}$$

$$E_{\text{mold/part}} = \frac{396}{5{,}000} = 0{,}0792\,\text{kWh} \tag{3.13}$$

The total energy consumption per part is:

$$E_{\text{total/part}} = E_{\text{operation/part}} + E_{\text{mold/part}} = 0.0066 + 0.0792 = 0.0858\,\text{kWh/part} \tag{3.14}$$

Which gives a total energy consumption of:

$$E_{\text{total}} = E_{\text{total/part}} \times 5{,}000 = 429\,\text{kWh} \tag{3.15}$$

And a specific energy consumption of:

$$E_{\text{specific}} = \frac{E_{\text{total}}}{12.5} = 34.32\,\text{kWh/kg} \tag{3.16}$$

3.3.2.3 Conclusion for energy consumption

The experimental quantification of energy consumption during the production of a dental implant using the PAM process reveals significant insights into its environmental implications.

Table 3.1: Comparison of energy consumption between PAM and injection molding (MIM)

Parameters	**PAM**	**MIM**
Energy per part (kWh)	0.139	0.0858
Specific energy (kWh/kg)	55.6	34.32
Drying	No	Yes
Mold fabrication energy	None	396 kWh
Production rate	2 parts/h	500 parts/h
Total energy (5,000 parts, kWh)	695	429

The PAM printing process consumed an average power of 277 W over a 30-minute print duration, resulting in an energy use of 139 Wh (0.139 kWh) per part as summarized in Table 3.1. This value aligns with typical AM energy consumption ranges, reported between 0.05 and 0.5 kWh per piece depending on technology and geometry.

Scaling up, the production of 5,000 implants using PAM would require approximately 695 kWh, yielding a specific energy consumption of 55.4 kWh per kilogram of printed titanium, assuming a part mass of 2.5 g. This relatively high specific energy reflects the limited production throughput of PAM (2 parts/h), which inherently amplifies the energy footprint per unit mass.

In contrast, the MIM process demonstrates a substantially lower energy demand per part, attributed to higher production rates and energy-efficient bulk processing. The base operational energy, combining injection and drying steps, is estimated at 34 kWh for 5,000 parts. However, when accounting for the significant energy required for mold fabrication—estimated at 396 kWh (based on 72 hours of CNC machining at 5.5 kW)—the total energy per part rises to 0.086 kWh as shown in Figure 3.6.

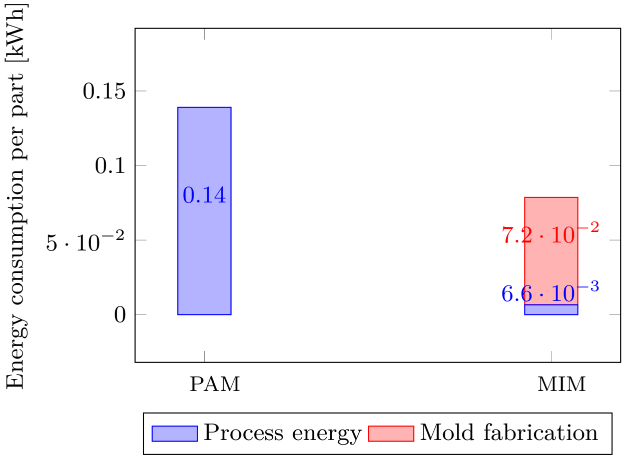

Figure 3.6: Stacked bar chart of energy consumption per part for PAM and MIM

When normalized by mass, the MIM process exhibits an average specific energy consumption around 34 kWh/kg, notably lower than PAM. This difference highlights the advantage of MIM in high-volume production scenarios, where initial tooling energy can be amortized over large batches.

From a qualitative standpoint, Figure 3.5 visually demonstrates one of the key limitations of the PAM process: the fidelity of complex geometries. The dental implant printed with PAM shows notable limitations in reproducing fine features, particularly the screw threads, due to the resolution constraints of extrusion-based deposition. In contrast, MIM offers significantly higher dimensional accuracy and surface finish, enabled by the precision of mold fabrication and the uniformity of high-pressure injection. This makes MIM more suitable for end-use medical components requiring stringent geometric and mechanical tolerances.

Notably, the part in Figure 3.5 (b) was printed using a 0.4 mm diameter nozzle (a). This small nozzle size significantly increased the total production time, as it limits the material deposition rate. Employing a larger nozzle diameter could reduce the printing time by a factor of two to three, depending on the chosen diameter. Consequently, the overall energy consumption during the printing phase could be substantially reduced.

However, this gain in process efficiency comes at the expense of part quality, particularly for geometries with fine details and steep overhangs. Therefore, there exists a trade-off between energy efficiency and geometric fidelity when optimizing the PAM process.

The comparison, clearly illustrates the energy efficiency of MIM, with lower energy use per part and per kilogram. However, this comes at the cost of significant upfront investment in tooling and limited flexibility in part design.

Conversely, PAM offers geometric freedom and tooling-free production, at the expense of higher per-unit energy consumption, lower surface quality, and slower production rates.

3.3.3 Material Consumption

3.3.3.1 PAM

For the PAM process, the material consumption per part is composed of two components: the implant itself and small, recurring process losses. The implant has a mass of:

$$m_{\text{implant}} = 2.5\,\text{g} \tag{3.17}$$

In addition, minor losses occur due to pre-printing adhesion structures and pre-extrusion purging. These losses are estimated at:

$$m_{\text{loss}} = 0.1\,\text{g/part} \tag{3.18}$$

Thus, the total material consumption per part is:

$$m_{\text{total, PAM}} = m_{\text{implant}} + m_{\text{loss}} = 2.6\,\text{g} \tag{3.19}$$

The solid waste for PAM machine represents in this case of study 3.8% of the mass total used to print the part and 4% of the mass of the part.

3.3.3.2 MIM

In the case of injection molding, material waste during part production is higher than PAM . Most losses come from sprues, runners, gate vestiges, and occasional flash, but these are generally considered negligible. Literature indicates that 3D printing performs slightly better in terms of material efficiency than injection molding, but the difference is marginal at the part level.

However, a major contributor to material consumption in injection molding is the mold itself. A typical mold for small implants ($m \approx 2.5g$) weighs between 20 and 50 kg [199], and includes multiple cavities, complex internal cooling channels, and high-precision surfaces. The mold is manufactured over approximately 72 hours of machining [200], and material losses during machining (cutting, drilling, EDM) are estimated between 10% and 20% of the raw mold block mass.

While the mold material is not physically incorporated into each part, its fabrication involves significant material losses during machining. In this analysis, these losses are amortized over the production batch and allocated per part to reflect their environmental burden, in accordance with standard LCA methodology.

Therefore, including this contribution in the total material consumption per part is both methodologically valid and necessary for a fair comparison with tool-less processes like PAM [164]. Assuming a median case of 3.5 kg of material removed during machining (estimation based on the volume of the part (4 cavities) and the runner system), and amortizing this over a batch of 5,000 parts, the material consumption attributable to the mold becomes:

$$m_{\text{mold per part}} = \frac{3{,}5}{5{,}000} = 0.7\,\text{g/part} \tag{3.20}$$

According to [168, 176]. The injection step requires pressurization inside the mold by injecting more material than necessary for the part while filling runners, sprues,... [201]. This generally represents between 5 to 20% of the mass of the part [168]. Here, we will consider 10%.

$$m_{\text{runners}} = 0.1 \times 2.5 = 0.25\,\text{g/part} \tag{3.21}$$

Therefore, the total material consumption per part for the MIM process is:

$$m_{\text{total, MIM}} = m_{\text{implant}} + m_{\text{mold per part}} + m_{\text{runners}} \approx 2.5 + 0.7 + 0.25 = 3.45\,\text{g} \tag{3.22}$$

3.3.3.3 Conclusions for material consumption

This analysis, resumed in Table 3.2 highlights a significant point: the mold fabrication alone contributes more material loss per part (0.7 g) than the total material loss of the entire PAM process (0.1 g). Although injection molding is efficient in direct production, its reliance on heavy, machined tooling results in a higher cumulative material footprint, particularly for small batches or high-precision applications such as dental implants. This reinforces the environmental and material efficiency advantages of PAM over MIM in such contexts [16].

Table 3.2: Material consumption comparison between PAM and MIM

Material category	**PAM**	**MIM**
Useful mass (implant) [g/part]	2.5	2.5
Pre-processing loss [g/part]	0.1 (adhesion, purging)	0.25 (sprue, runners)
Mold fabrication loss [g/part]	–	0.7
Total material consumption [g/part]	2.6	3.45

In the case of injection molding, the material waste represents 28% of the total amount of material used to produce a part and 38% of the mass of the part as shown in Figure 3.7.

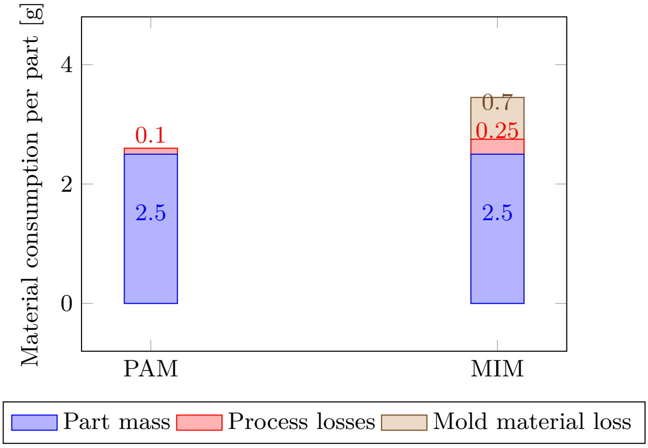

Figure 3.7: Stacked bar chart of material consumption per part for PAM and MIM

This study adopts a simplified cradle-to-gate approach, focusing solely on the quantification of material and energy consumption without proceeding to a full LCIA. While this does not constitute a complete LCA as defined by ISO 14040 and ISO 14044, it aligns with practices observed in early-stage environmental evaluations and design-oriented assessments. Such approaches are commonly used when data availability, time, or resources are limited, and they provide valuable insights into the resource intensity of a system. As highlighted by Tasala Gradin and Björklund [202], this study can serve as effective tools for identifying environmental hotspots and guiding decision-making, provided that their limitations are clearly acknowledged.

In this context, the aggregation of different material inputs—despite their varying nature—is performed for indicative and comparative purposes. This practice is supported in the literature on simplified LCA methodologies, where material flows are often summed to provide a general overview of resource use (e.g. [202, 203]). Although such aggregation does not reflect environmental equivalence, it enables a practical understanding of material demand across processes. This approach is particularly relevant in studies that do not apply characterization models or software tools, and where the primary objective is to highlight material efficiency or compare scenarios. Transparency in reporting and consistency with the study's goal are essential to ensure the validity of this method.

Figure 3.8 shows the total energy consumption (kWh) as a function of the number of parts produced, for PAM and MIM. The x-axis spans production volumes from 500 to 5,000 parts, while the y-axis tracks the total cumulative energy consumption.

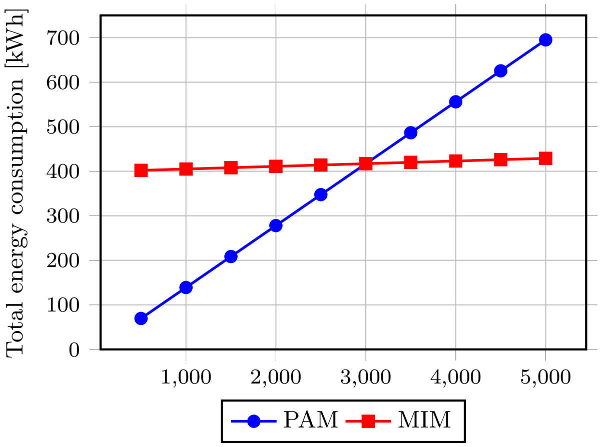

Figure 3.8: Total energy consumption as a function of the number of parts for PAM and MIM processes

The energy consumption curve for PAM (in blue) exhibits a strictly linear growth, with total energy rising proportionally with the number of parts produced. This reflects the constant unit energy cost per part inherent to additive processes like laser sintering or extrusion. Each additional part requires essentially the same amount of energy as the previous one, without any amortization of setup or process energy over time.

This behavior is well-documented in additive manufacturing literature. Baumers et al. [204] found that AM technologies typically have fixed per-part energy requirements, which results in linear total energy curves unless batch optimizations or nesting are applied.

Unlike PAM, the MIM curve (in red) shows a slight but consistent upward slope, indicating that energy consumption does increase with production volume, albeit very slowly. This suggests that MIM involves: a large fixed energy cost, likely for mold creation and setup and a very low marginal energy cost per additional part, allowing for near-constant average consumption as output scales. This pattern aligns with research by Gutierrez-Osorio et al. [205], who emphasized that processes like MIM and injection molding incur high initial energy input but benefit from economies of scale due to minimal per-part energy additions.

The intersection point of the two curves—where PAM's rising energy cost exceeds that of MIM—marks the break-even production quantity. For part volumes below this threshold ($\approx$ 2,500 parts), PAM is more energy-efficient. Beyond this point, MIM becomes the superior choice in terms of energy performance. Watson and al. [206] provided a theoretical model showing that AM processes outperform traditional methods like MIM for low volume fractions, but become less efficient as the production scale grows.

This analysis emphasizes a fundamental manufacturing trade-off:

- PAM is ideal for small-batch, customizable, or complex geometries, where setup energy is negligible and flexibility is prioritized.
- MIM excels in large-scale production, where energy efficiency improves due to dilution of fixed costs and highly optimized per-part energy inputs.

A recent life-cycle energy assessment by Hasan et al. [207] confirms that hybrid or traditional techniques become more efficient than AM once the setup energy is amortized over larger production volumes.

As energy consumption represents approximately 80% of PAM's environmental impact [39], reducing printing time and temperature could make the process more suitable for higher production volumes.

3.4 Cradle to gate diagram

A cradle to gate diagram has been realised in Figure 3.9 to summarize the positive (green) or negative (red) environmental impact of PAM compared to MIM for each step of part production. PAM has a negative impact on the environment during the process of printing than injection because of the printing time which explode the energy consumption.

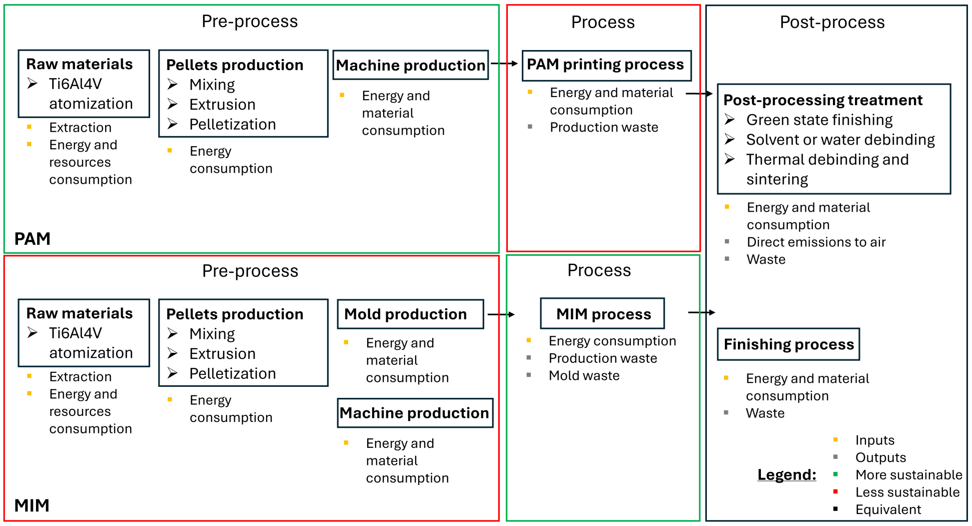

Figure 3.9: Cradle to gate diagram comparing PAM and MIM processes before, during and after the printing/molding step.

3.5 Conclusions and prospects

This comparative environmental analysis focused on the energy and material consumption of two manufacturing processes—PAM and MIM—for producing 5,000 geometrically simplified Ti6Al4V dental implants, using a water-soluble feedstock provided by PolyMIM GmbH. The system boundaries were limited to the core manufacturing stages: printing (for PAM), injection, and mold fabrication (for MIM). Upstream and downstream steps such as feedstock preparation, debinding, and sintering were excluded, as they are essentially identical for both processes.

As expected, PAM consumes significantly more energy—approximately 64% more than MIM for the same production volume. This is mainly due to its longer cycle time: around 30 minutes per part, compared to just 0.12 minutes for MIM. However, it's important to note that mold fabrication in MIM accounts for a substantial portion of its total energy demand. Thanks to its tool-free nature, PAM becomes more energy-efficient than MIM below a certain production volume threshold.

In terms of material consumption, PAM shows a clear advantage. MIM uses 32.7% more material per part, mainly due to:

- Machining waste from mold fabrication,
- Excess feedstock needed to fill runners, gates, and sprues during injection.

Although this excess material can often be recycled, it must first be reprocessed into usable feedstock, which requires additional energy and infrastructure. Moreover, the material used for mold production is not fully amortized over the 5,000 parts.

In summary, while MIM remains highly efficient for large-scale production due to its speed and industrial maturity, PAM offers several compelling advantages for small to medium production runs. Its flexibility, reduced material waste, and elimination of tooling requirements make it a promising alternative — especially for applications requiring design adaptability and moderate volumes. Despite its higher energy consumption, PAM presents a more sustainable profile in specific contexts, and its potential for optimization remains significant.

CHAPTER 4

Context of experimental research

4.1 Introduction and Research Context

AM technologies continue to evolve as viable solutions for the production of complex components, particularly in sectors requiring high-performance materials such as aerospace, biomedical, and energy. Among these, PAM—an extrusion-based process using thermoplastic feedstocks in pellet form—offers promising advantages in terms of cost-efficiency and material flexibility.

However, despite the ability of PAM machines to process materials developed for injection molding, very few feedstocks have been specifically designed for this process. This limitation affects both the technical performance and environmental sustainability of PAM.

4.2 Research Objectives

This PhD thesis aims to address these challenges by developing a feedstock formulation incorporating fully or partially water-soluble and bio-based binders, specifically tailored to the material extrusion process.

The main objectives of this work are as follows:

- Develop a PAM-specific feedstock formulation with optimized viscosity and adhesion properties;
- Design a more eco-friendly titanium feedstock by incorporating water-soluble and/or bio-based components.

4.3 Experimental Framework: The HyProPAM Project

This study was conducted within the framework of the HyProPAM project (Hybrid Production of Pellets-based Additive Manufactured Parts), using a commercial Ti6Al4V feedstock supplied by PolyMIM GmbH referenced as PolyMIM Ti6Al4V.

This feedstock, originally developed for injection molding, was optimized for easy unmolding rather than extrusion. This type of feedstock is not inherently suited for additive processes where layer and build plate adhesion is necessary.

As a result, several issues were observed when used in PAM:

- Inadequate interlayer cohesion
- Poor adhesion to the print bed
- Formation of open and closed porosity
- Shark-skin effects due to high shaping temperature

These defects are directly related to the feedstock's rheology and compromise the mechanical integrity of the printed parts.

4.4 Environmental Assessment and Challenges

In this thesis, a comparative environmental analysis was conducted to evaluate the performance of PAM relative to MIM (chapter 5). As anticipated, PAM shows higher energy consumption, primarily due to its significantly longer per-part manufacturing time. Additional energy is also required to heat the nozzle and extrusion head, though this remains a secondary factor.

This elevated energy demand is closely linked to the low printing speeds (typically 8–10 mm/s) imposed by current feedstock formulations. These limitations highlight the need for next-generation feedstocks offering:

- Improved rheological behavior,
- Higher printing speeds (e.g., up to 20 mm/s, the machine's maximum),
- Lower processing temperatures,
- Compatibility with aqueous debinding methods.

Such improvements could significantly reduce energy consumption and enhance the overall sustainability of PAM, making it more competitive for broader production scenarios.

4.5 Toward Sustainable Feedstock Development

From a materials perspective, traditional binders used in PAM/MIM are often petroleum-based and require organic solvents for debinding—substances that are hazardous and environmentally harmful. This has led to growing interest in:

- Bio-based or partially bio-based binders,
- Water-soluble systems that eliminate the need for toxic solvents and simplify post-processing.

Such feedstocks would also be more compatible with the hybrid manufacturing approach envisioned by the HyProPAM project.

4.6 Research Vision and Expected Outcomes

This research aims to develop a PAM-specific feedstock that satisfies multiple criteria:

- Partially water-soluble, enabling safe and efficient aqueous debinding;
- Incorporates bio-sourced polymers to minimize environmental impact;
- Offers enhanced printability for improved surface finish and mechanical performance;
- Enables low-temperature processing to reduce energy demand during fabrication.

These objectives reflect an integrated approach to sustainable, high-quality additive manufacturing of metallic parts, positioning PAM as a competitive and environmentally responsible alternative for small to medium-scale production.

CHAPTER 5

Materials, Methods and Characterizations

5.1 Materials

Prior to developing sustainable feedstock formulations, a commercial material was used to identify key parameters affecting part production via PAM. A Ti6Al4V feedstock from PolyMIM GmbH, originally developed for MIM, was selected for this purpose. It was also employed in the HyProPAM project to demonstrate the technical feasibility of hybrid manufacturing, as discussed in Chapter 4. Although based on a water-soluble primary binder, this feedstock presents several limitations when adapted to PAM. In addition, its exact binder composition is proprietary and undisclosed by the manufacturer. The main technical and environmental drawbacks identified during PAM processing are summarized in Table 5.1:

Table 5.1: Limitations of the commercial PolyMIM feedstock for PAM and their environmental or technical impacts (adapted from HyProPAM)

Limitation	**Impact**
Poor surface quality Ra $\geqslant$ 25 µm	Requires post-processing like machining, raising energy use and material loss
Low interlayer adhesion	Causes delamination and rejects, increasing waste and inefficiency
High cooling rate (radiant heating)	Needs radiant and heated buildplate, raising energy demand and carbon footprint
Poor green strength	Leads to part failure and reprints, consuming more energy and material
High shaping temperature (170–180°C)	Requires high thermal input, lowering process efficiency
Long heating time (45–60 min) before printing	Sustains energy demand, delays productivity
High viscosity	Requires higher torque and energy, accelerates wear and surface defects
Low wettability or chemical incompatibility	Causes warping, deformation, poor debinding and sintering (e.g. +0.47/0.29 µm std. dev. on printed cylinders)
Degradation residues	Potentially toxic gases (CO, CO_2) (thermal degradation)

In this study, more sustainable feedstock formulations specifically tailored for PAM were developed by combining metallic powders with thermoplastic binders. The formulation strategy focused on using PEG as the primary water-soluble phase, polyvinyl butyral (PVB) as the structural backbone polymer, stearic acid (SA) as a dispersant and plasticizer, and methylcellulose (MC) as a bio-based viscosity modifier.

- The metallic powder used was a Ti-6Al-4V-ELI (Grade 23) gas-atomized alloy (Osprey®) supplied by Sandvik. Its chemical composition complied with the ASTM F3001-14 specification [208], with measured contents of Aluminum (Al): 6.14 wt.%, Vanadium (V): 4.01 wt.%, Oxygen (O): 0.13 wt.%, Nitrogen (N): 0.01 wt.%, Carbon (C): 0.01 wt.%, Hydrogen (H): 0.001 wt.%, and Iron (Fe): 0.18 wt.%. The particle size distribution was tailored for powder injection moulding applications, with a D_{10} of 4.0 µm, D_{50} of 10.5 µm, and D_{90} of 22.0 µm.

- Polyethylene glycol (PEG 12,000), purchased in flake form from Sigma-Aldrich, was employed as the main water-soluble binder. Although previous studies by Eickhoff [91] demonstrated improved printability in Fused Deposition Modeling (FDM) using higher molecular weight PEGs (e.g., PEG 20,000 g/mol), such grades were found unsuitable for MEX due to phase separation at elevated nozzle temperatures (e.g., 230°C). PEG 12,000 was therefore chosen as a compromise, offering a balance between solubility, thermal stability, and extrusion compatibility.

- Polyvinyl butyral (PVB), Mowital B30H, supplied by Kuraray, was used as the backbone polymer to enhance structural integrity during filament extrusion and printing. PVB was selected for its excellent film-forming properties, good flexibility, and strong adhesion to metallic particles, which contribute to mechanical cohesion of the green body. Its thermoplastic behavior supports shape retention during extrusion and layer stacking, while its compatibility with PEG ensures homogeneous blending and stable flow during processing.

- Methylcellulose MC, solid with 2% solubilization exhibiting a viscosity of 1,500 cP, obtained from Sigma-Aldrich, was incorporated as an additional binder and rheological modifier. MC is commonly used in ceramic and metallic feedstocks as a water-soluble polymer with a viscosity of 1,500 cP [82, 85], offering benefits such as enhanced viscosity, improved flow stability, reduced tooling wear, and smoother surface finish. It is also known to increase green strength and facilitate the extrusion of fine or thin-walled features in aqueous-based systems [80]. However, in the present study, MC was applied in an organic-based feedstock, which differs from the typical aqueous systems.

- Finally, stearic acid (SA), supplied by Sigma-Aldrich, was added as a plasticizer and dispersing agent to improve powder dispersion and reduce internal friction during mixing and extrusion [93].

Several compositions were evaluated, and Table 5.2 presents the nomenclature used to identify each formulation along with their respective chemical compositions. The Ti6Al4V content was fixed at 55 vol.%, and the proportions of PEG and PVB were held constant during the optimization of SA and MC. A detailed discussion on the selection of these concentrations is provided in Chapter 7.

Table 5.2: Composition and nomenclature of each feedstock formulation

Composition	**Ti6Al4V**	**PEG**	**PVB**	**SA**	**MC**
	[vol. %]	[vol. %]	[vol. %]	[vol. %]	[vol. %]
F0SA0MC	55	22.5	22.5	0	0
F1SA	55	22.0	22.0	1	0
F2SA	55	21.5	21.5	2	0
F3SA	55	21.0	21.0	3	0
F4SA	55	20.5	20.5	4	0
F5SA	55	20.0	20.0	5	0
F1MC	55	22.0	22.0	0	1
F2MC	55	21.5	21.5	0	2
F3MC	55	21.0	21.0	0	3
F4MC	55	20.5	20.5	0	4
F5MC	55	20.0	20.0	0	5
F3SA3MC	55	18.0	21.0	3	3

The first group of formulations, containing SA from 0 to 5 vol.%, was tested to evaluate its influence on the rheological properties of the feedstock and to determine the optimal SA content for future formulations.

The second group, incorporating varying amounts of MC, aimed to assess its effect as a solidening agent in a water-free organic binder system, with a particular focus on its impact on viscosity.

The final formulation, incorporating 3 vol.% SA and 3 vol.% MC, was developed based on prior optimization results to enhance the feedstock's flow behavior during PAM processing while improving its overall sustainability. To preserve a balanced 50/50 ratio between water-soluble and non-water-soluble components, the 3 vol.% of MC was deducted from the PEG content, thereby maintaining a consistent hydrophilic/hydrophobic fraction in the formulation.

5.2 Feedstock preparation

5.2.1 Mixing of the powders

The initial stage of pellet production involves blending the powders that will form the final composite material. A high shear rate corotational twin screw mixer manufactured by Brabender (Brabender measuring mixer 30 EHT) was used to realize the blending step as described in Figure 5.1. The volume capacity of the machine is about 30 cm^3 and double roller blades were used to blend the melted composition. It is important to note that these blades were developed by Brabender especially for thermoplastics.

First, the powders are added one by one into a container, starting with Ti6Al4V, followed by PEG, PVB, and finally SA and/or MC. The container is then sealed and manually shaken to pre-mix the powders. The resulting blend is subsequently transferred into the Brabender mixer for compounding.

The blending of the feedstocks was carried out in a temperature range of 100°C to 150°C (except in the case of commercial feedstock which requires a higher mixing temperature), with 10°C increments, in order to determine the torque response at each temperature. This allowed for the identification of a suitable processing window and ensured a homogeneous and stable mixture.

This step also served as a screening method to eliminate formulations in which powders failed to mix effectively. Repeated trials indicated that a minimum blending time of 15–20 minutes was necessary to achieve adequate homogenization and torque stabilization. Each formulation was therefore mixed for 15 minutes, and this process was repeated across a range of temperatures (100, 110, 120, 130, 140, and 150 °C) to assess temperature sensitivity.

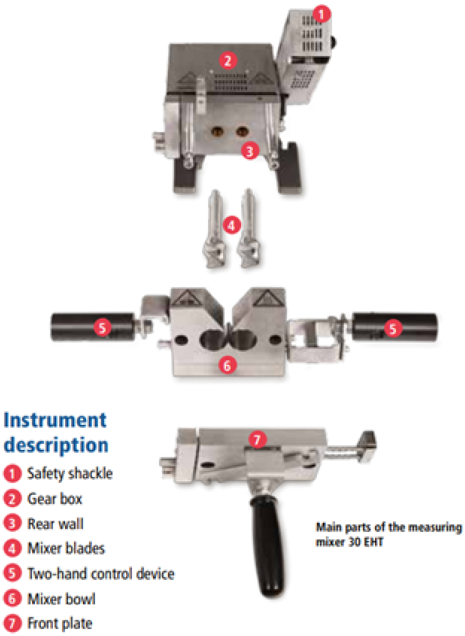

Figure 5.1: Presentation of the Brabender mixer 30 EHT used in the thesis [209]

This temperature range was selected based on the thermal properties of the base polymers: the melting point of PEG ($T_f = 60–65°C$) [210] and the glass transition temperature of PVB ($T_g \approx 68°C$) [211]. The addition of Ti6Al4V powder is known to significantly increase these transition temperatures due to its high thermal mass and interaction with the matrix. Furthermore, the presence of SA and/or MC is expected to further alter the thermal behavior of the blend.

Therefore, a broad temperature range was investigated to ensure adequate flow and dispersion under varying conditions. But also based on trial-and-error approach to obtain good mixing, facilitate cleaning (not too fluid after opening the machine).

To assess the mixing behavior and flow resistance of the various feedstock formulations, torque monitoring was employed as a key rheological indicator during compounding. The concept of torque is therefore briefly introduced below. Torque, also known as moment of force, is a measure of the rotational force applied to an object around an axis, pivot, or fulcrum. It determines how effectively a force can cause an object to rotate [124].

Mathematically, torque $\boldsymbol{\tau}$ is defined as the vector product of the position vector $\mathbf{r}$ (from the axis of rotation to the point of force application) and the force vector $\mathbf{F}$ [212, 213]:

$$\boldsymbol{\tau} = \mathbf{r} \times \mathbf{F} \tag{5.1}$$

The magnitude of the torque is given by:

$$|\boldsymbol{\tau}| = rF\sin(\theta) \tag{5.2}$$

Where:

- r = distance from the axis of rotation to the point of force application (lever arm),
- F = magnitude of the applied force,
- θ = angle between $\mathbf{r}$ and $\mathbf{F}$.

Torque is measured in newton-meters ($\mathrm{N} \cdot \mathrm{m}$) in the SI system using a high shear mixer (Brabender) to identify a suitable processing window and ensure a homogeneous and stable mixture [214].

For feedstocks containing SA, torque measurements stabilized after approximately 15 minutes of mixing, as shown in Figure 5.2. However, in the case of feedstocks containing MC and no SA, the torque had not yet stabilized after 15 minutes (see Figure 5.3), indicating incomplete homogenization. As a result, an additional 15-minute mixing cycle was performed to promote further dispersion. This second mixing step led to stable torque values, confirming improved homogeneity, as shown in Figures 5.4.

Figure 5.2 presents the torque profile recorded during the mixing of F1SA over a period of 15 minutes at 60 RPM and a temperature of 130°C. The diagram shows a sharp increase in torque, peaking at approximately 10.5 Nm, which corresponds to the addition of powders into the mixing chamber. This is followed by a gradual decrease in torque as the mixing progresses. From the 12th minute onward, the torque stabilizes around 5 Nm, indicating that the mixture has reached a homogeneous state. The selected torque value is the one measured at the end of the mixing process, once stabilization has been achieved.

Considering that filament extrusion using the DSM system (described in the following subsection) involves an additional 15-minute mixing phase, the total mixing time was deemed sufficient to ensure complete feedstock homogenization.

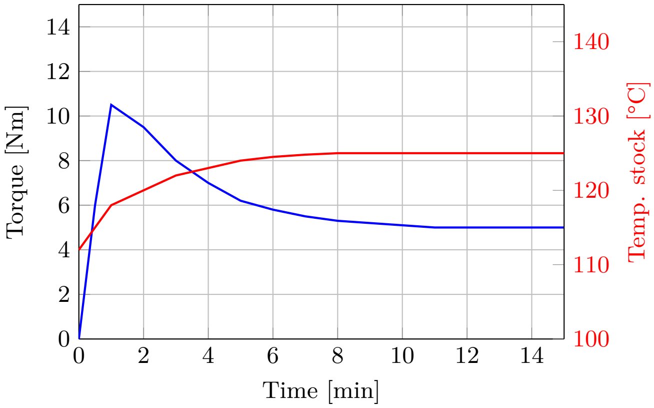

Figure 5.2: Torque (Nm) and stock temperature (°C) as a function of time (min.) over 15 min for F1SA at 130°C showing stabilization around 12 minutes

Unlike the blends containing SA, those formulated with MC do not exhibit torque stabilization after 15 minutes, as shown in Figure 5.3, which illustrates the torque evolution of the F2MC blend at 130°C. Consequently, these initial torque values are not meaningful, as the mixture has not yet reached homogeneity. To ensure proper homogenization of the powders and to obtain a stabilized torque measurement for each blend, a second mixing step lasting 15 minutes was performed.

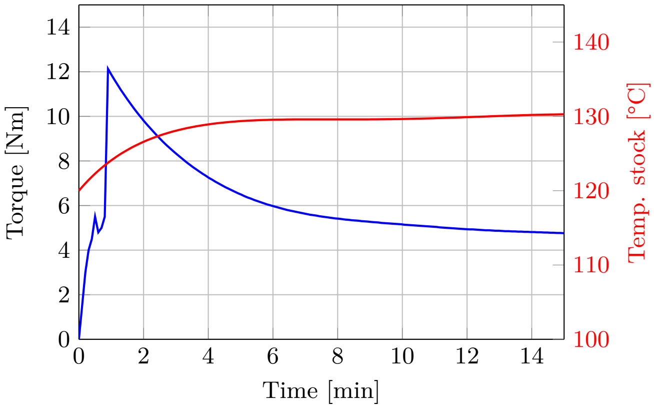

Figure 5.3: Torque (Nm) and temperature of the stock (°C) as a function of time (min.) for F2MC during 15 min. at 130°C

The resulting torque values reported for the MC-based blends correspond to those measured after this second mixing phase, i.e., after a total of 30 minutes, as presented in Figure 5.4.

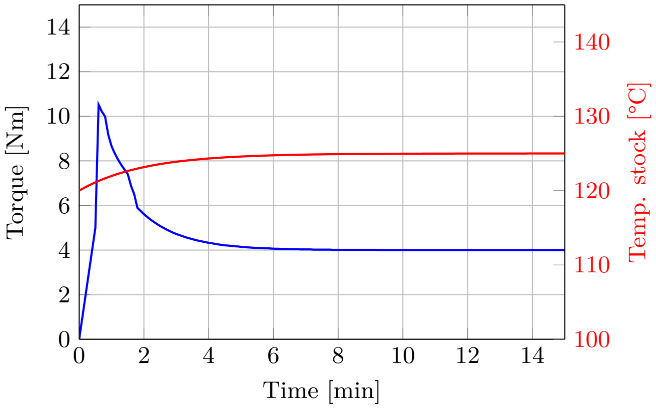

Figure 5.4: Torque (Nm) and temperature of the stock (°C) as a function of time (min.) for F5MC after 30 min.

5.2.2 Filament Extrusion

Filament extrusion consists of the extrusion of the blended composite obtained by the Brabender mixer into filaments. The equipment used is a twin-screws micro-compounder (DSM) manufactured by Xplore represented in Figure 5.5. The DSM is a machine using twin-screws to melt the composite and extrudate it through an extrusion die into filaments of 2 mm with a volume of 15 cm^3. This machine has a recirculating channel that allows the melt to be recirculated to the screws to improve the homogeneity of the feedstock.

Figure 5.5: Xplore DSM twin screws micro-compounder MC 15EHT [215]

The DSM micro-compounder was used to evaluate the extrudability of various compositions and to determine the corresponding processing temperatures. It also enabled assessment of the mechanical integrity of the extruded filaments. If a filament broke under its own weight, this indicated either excessive viscosity or insufficient particle bonding, leading to brittleness or non-extrudability. Conversely, if the material was too fluid, the filament lacked shape retention, meaning that any part printed with such a composition would not be able to maintain its shape.

The extrusion parameters are summarized in Table 5.3. These were selected based on a combination of literature guidance and empirical observations, particularly mixing torque measurements, which helped to define an appropriate processing window. The processing temperature was set at 110°C for feedstocks containing SA, following the protocol reported by Eickhoff et al. [91]. Then, temperatures has been adjusted depending on results from trials-and-error preliminary tests to obtain filaments with properties adapted to extrusion (not too viscous or fluid).

Table 5.3: Set of extrusion parameters used on DSM

Parameters	F1 to F5SA	F1 to F5MC	F3SA3MC
Temperature (°C)	110	120	120
Screws speed (RPM)	60	60	60
Time (min.)	15	15	15

Although Eickhoff et al. originally employed a screw speed of 30 RPM, a more detailed literature analysis suggests that a higher speed—specifically 60 RPM—is more effective for highly viscous, powder-rich feedstocks. At lower speeds such as 30 RPM, shear forces are insufficient to achieve adequate dispersion, often leading to powder agglomeration and internal temperature gradients. In contrast, operating at 60 RPM offers an optimal trade-off between mechanical shear, thermal input, and residence time, enhancing homogeneity without causing thermal degradation. This observation is consistent with findings by Das et al. [216], who reported minimum torque and better mixing performance at 60 RPM, and by Gunning et al. [217], who demonstrated improved dispersion of solid fillers at higher screw speeds, while cautioning against speeds above 80 RPM due to the risk of thermal degradation.

Thus, 60 RPM was selected as a robust compromise, offering efficient powder dispersion and energy input control suitable for PAM feedstock preparation.

5.3 Feedstocks analysis

Given the number of different materials involved, and consequently the large number of analyses required—which are time-consuming, material-intensive, and laborious—only one measurement was performed for each analysis and each material.

5.3.1 Kofler bench

The methodology used to assess the rheological behavior of feedstocks for PAM was initially developed by Dr. Cathy Delmotte from BCRC during the HyProPAM project. The rheological measurements presented in this work were carried out by Dr. Delmotte and analysed by the author, following the same protocol established within the project.

To characterize the thermal behavior of the individual feedstock components, each material was first tested using a Kofler heating bench. This device consists of a metal plate featuring a fixed, linear temperature gradient ranging from room temperature up to 260°C. When a small amount of a material is placed across this gradient, it is possible to directly observe its softening, melting, or decomposition as a function of position, which corresponds to a specific temperature. In this study, the Kofler bench was used to identify key thermal transitions such as the glass transition temperature (T_g) or melting point (T_f) of each component. These results, summarized in Table 5.4, serve to complement technical datasheets and inform later processing steps including compounding, extrusion, and 3D printing.

The same technique was also applied to feedstock pellets (PAM and MIM) to qualitatively evaluate their global softening behavior. When placed along the temperature gradient, the pellets visibly soften and deform within a certain temperature range. By noting the onset of deformation and the range of flowability, the temperature at which the binder system becomes sufficiently mobile for extrusion can be estimated. This visual method is especially valuable when comparing different formulations or assessing the influence of certain additives on the activation temperature of the binder. Although qualitative, the Kofler bench offers a quick and intuitive screening of thermal behavior in multi-component systems and helps define relevant temperature windows for rheological testing and printing trials. In this context, it acts as a complementary tool alongside TGA and dynamic rheometry.

Table 5.4: Malleability and fusion temperatures of raw materials as determined by Kofler bench analysis

Product	**Malleability Temperature (°C)**	**Fusion Temperature (°C)**
PEG	N.D.	56
PVB	88	116
MC	220	>260
SA	N.D.	66

For PEG, only the fusion temperature was identified, at 56°C, while the malleability temperature was not determined—likely because PEG transitions rapidly from solid to liquid without a distinct softening phase.

PVB shows a malleability temperature of 88°C and a fusion temperature of 116°C, indicating a gradual softening before melting, which is typical of thermoplastics that provide structural support during heating.

MC exhibits a much higher malleability temperature of 220°C and a fusion point above 260°C, suggesting it remains rigid over a wide temperature range and is suitable for maintaining shape at elevated temperatures.

Finally, SA has a fusion temperature of 66°C, with no malleability temperature reported, implying it melts quickly without a significant softening phase. These thermal characteristics help clarify the functional roles of each component in the binder system and guide the selection of appropriate processing temperatures for the PAM process.

Kofler bench tests were also performed on the commercial Ti6Al4V PolyMIM feedstock during HyProPAM. Pellets were maintained at defined temperatures for 30 minutes and visually inspected to determine their respective processing temperature ranges. The Kofler bench test thus provided a preliminary estimation of the processing temperature range.

5.3.2 Thermogravimetric analysis TGA

Thermogravimetric analysis was employed to characterize the thermal stability of the formulated feedstocks and to quantify the degradation behavior of individual binder components. The thermal stability of a feedstock is influenced by multiple parameters, including the nature of the carrier gas, the molecular weight distribution of the polymers, and the specific chemical interactions between constituents.

All analyses were performed using a TA Instruments Q500 thermobalance under an inert nitrogen atmosphere. A constant heating rate of 10°C/min was applied, with nitrogen flow rates set to either 40 mL/min and 60 mL/min.

The TGA profiles were used to identify the onset of thermal degradation, the number and position of decomposition steps, and the total mass loss associated with each formulation. These data are critical for determining suitable debinding parameters and for defining safe processing windows that prevent premature decomposition or uncontrolled oxidation of the metal powder during heat treatment.

5.3.3 Rheological analysis

Viscosity measurements were conducted by Dr. Cathy Delmotte at BCRC using a HAAKE Mars III rheometer equipped with a parallel-plate configuration (20 mm diameter, 1 mm gap, P20TiL). The selected gap corresponds to the nozzle geometry used in the PAM printing trials, ensuring a relevant approximation of shear conditions during extrusion.

The feedstock samples were preheated and tested at controlled temperatures depending on the formulation and the results of Kofler bench, reflecting the typical processing window observed during filament extrusion. Each measurement was preceded by a temperature equilibration stage to eliminate transient thermal effects.

Shear rate-dependent viscosity (η) was recorded in order to capture the pseudoplastic (shear-thinning) behavior of the formulations. Complex viscosity η^* and storage/loss moduli (G', G") were also evaluated under oscillatory tests to assess the viscoelastic nature of the feedstocks at low strain amplitudes.

The rheological data were used to compare the influence of formulation parameters (e.g., SA and MC content) on processability, predict extrusion behavior.

Parameters used for each type of measures are available below:

Time sweep oscillation: controlled stress (CS) τ = 10 Pa, f = 1 Hz, t = 900 s, 90 points, $T = x$°C.

Frequency sweep oscillation: CS τ = 10 Pa, f = 100–0.1 Hz, 5 points per decade, $T = x$°C.

Strain sweep oscillation: CS τ = 10–1000 Pa, f = 1 Hz, 20 points, $T = x$°C.

Steady shear (rotation) test: CS τ = 1–200 Pa, linear ramp, 10 points, $T = x$°C.

Steady shear (rotation) test: CS $\tau = 250\text{–}1 \times 10^5$ Pa, linear ramp, 200 points, $T = x$°C.

5.3.4 Thermal camera analysis

The challenges encountered in determining an optimal range of printing parameters led us to perform thermal measurements both on the outer surface and within the printing nozzle. A dedicated experimental campaign was carried out using a thermal camera (Optris PI), which was positioned directly facing the nozzle at a fixed location (Figure 5.6). The feedstock was extruded through a brass nozzle (1 mm diameter).

The thermal camera's Optris PI software allows users to define measurement "spots," corresponding to specific pixels within the thermal image where temperature readings are desired as shown in Figure 5.7.

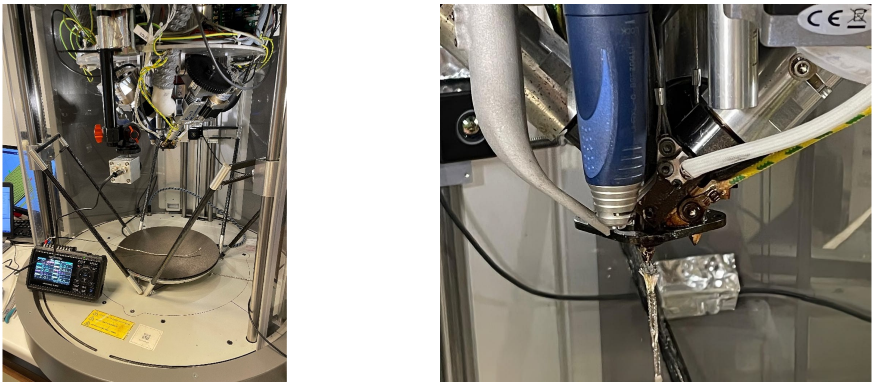

(a) Thermal camera setup on PAM

(b) Thermocouple inserted in a 1 mm brass nozzle

Figure 5.6: Instrumentation on the PAM printer: (a) thermal camera setup; (b) thermocouple placement inside the brass nozzle.

Five spots were positioned on the captured image: one spot located on the nozzle, a second spot placed directly at the nozzle exit, and a third spot slightly below along the same axis, enabling an assessment of the filament's cooling behavior. A fourth spot was positioned on the nozzle holder, and the final spot was placed on the extruder block, precisely at the location of the thermocouple responsible for heating the nozzle. The nozzle used is a brass nozzle of 1 mm diameter from Luter.

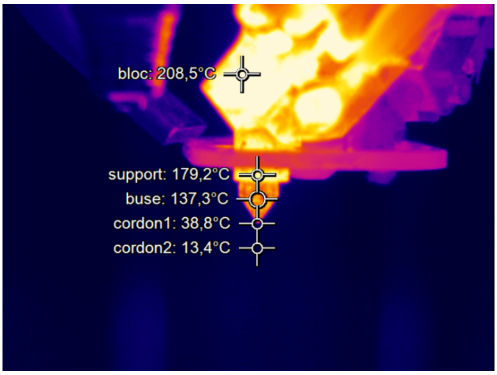

Figure 5.7: Setup use in the Optris PI software during thermal camera analysis

Emissivity calibration

The emissivity of each feedstock was calibrated using a thermocouple as a reference. The feedstock was heated until melting occurred, and the corresponding temperature was recorded by the thermocouple inside the nozzle as shown in Figure 5.6b.

Simultaneously, thermal data were acquired using the Optris PI camera. The emissivity parameter in the Optris PI software was iteratively adjusted until the temperature measured by the camera matched the thermocouple measurement at the melting point.

5.4 Pellets Additive Manufacturing PAM 3D printing

All of the printed parts produced during the HyProPAM project and this thesis were printed using a PAM HT series machine, as shown in Figure 5.8, based on a linear vertical delta system from Pollen AM [132] with four printing heads and a moving build plate. The geometry of the extrusion screw is not disclosed by the manufacturer. The maximum printing speed is 20 mm/s.

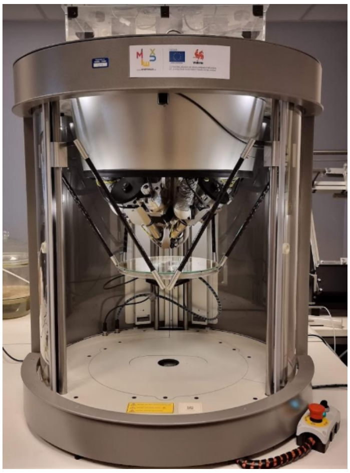

Figure 5.8: Pellets Additive Manufacturing PAM HT series from Pollen AM photography

CAM/CAD softwares as Rhinoceros and SolidWorks were used to realize 3D models and the slicer Cura has been used to develop the G-code. G-code (short for Geometric Code) is the numerical control programming language used to instruct the printer on how to create an object layer-by-layer. It defines the movement and actions of the printer's hardware—such as the print head, bed, extruder, and temperature control systems.

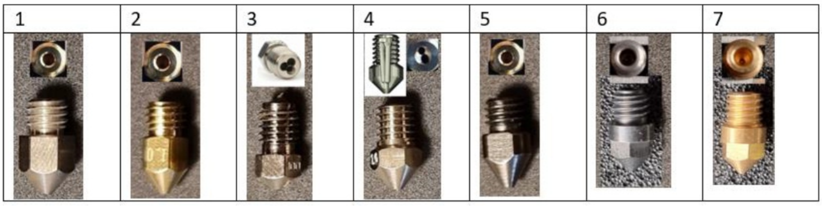

Figure 5.9: Different types of nozzle tested during HyProPAM to determine the most adapted nozzle

Different nozzle types were tested during the HyProPAM project, including nozzles with various inlet diameters, different angles, inserts, coatings (e.g., tungsten), and materials (stainless steel, brass), in order to determine which type best suited our application in terms of service life, nozzle clogging, printing quality, and dimensional accuracy. The nozzle selected after this study was the brass nozzle shown as No. 1 and No. 2 in Figure 5.9, as brass offers better thermal conductivity and heats the filament more quickly, which also helps to smooth the surface and achieve better surface quality. Nozzle No. 2, with a cost of € 1 per unit, was chosen for both the HyProPAM project and this PhD work.

Parts geometries

The geometries presented below were selected during the HyProPAM project to ensure a consistent basis for comparing the commercial PolyMIM feedstock with the newly developed formulations. The same shapes were retained across all tests.

The first geometry, shown in Figure 5.10a, corresponds to a three-point bending specimen defined by the EN843-1 standard size B [218]. Although originally intended for testing ceramic materials, this geometry was not used for bending tests on titanium. Instead, it was selected as a reference "simple" geometry due to its standardization and dimensional stability.

Similarly, the geometry shown in Figure 5.10b—a basic combination of a cube and a cylinder—was used for green machining evaluations. This shape was chosen to highlight common printing defects in dense parts, particularly during longer print durations, while remaining geometrically simple and easy to produce.

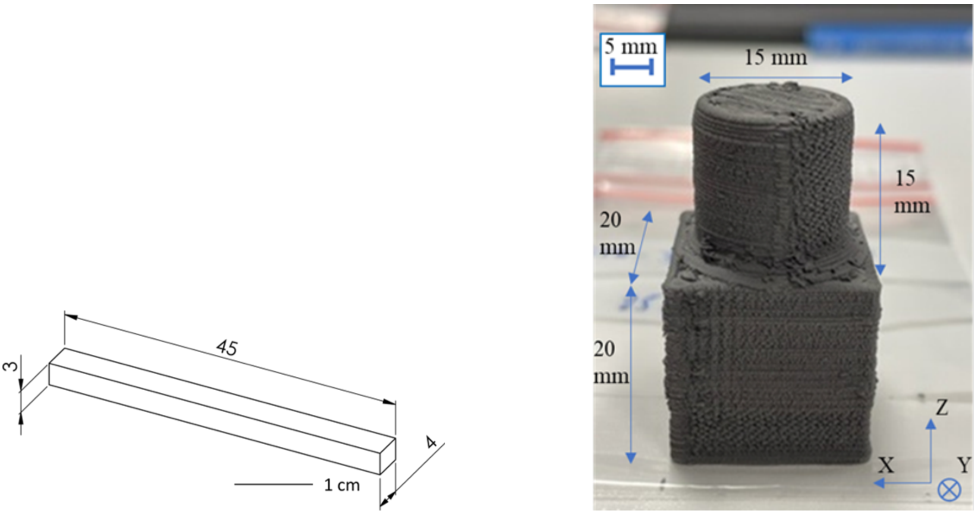

(a) Bending test design according to standard EN843-1

(b) Simple geometry used for green machining tests (HyProPAM project)

Figure 5.10: Test geometries used for bending (a) and green machining (b).

Tensile test specimens will also be produced (Figure 5.11 with the objective of evaluating the mechanical strength of the printed parts following ASTM E8/E8M standard [219]. However, these tests are planned beyond the scope of this thesis, as the debinding and sintering processes must first be fully optimized for the developed feedstock. Therefore, in this work, the evaluation of tensile parts remains purely qualitative.

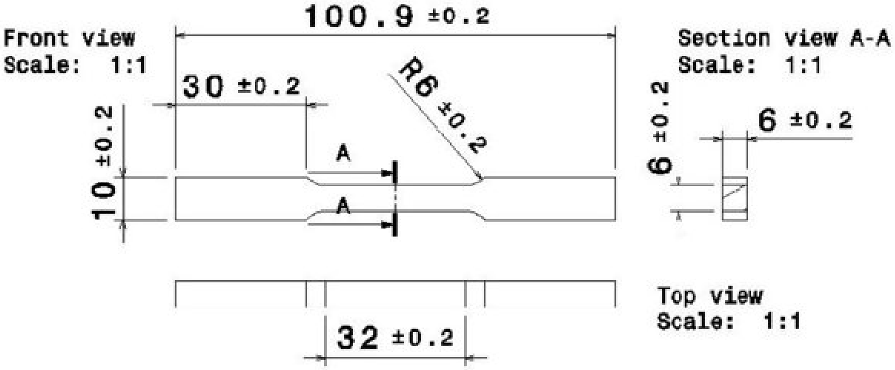

Figure 5.11: Tensile test design adapted from ASTM E8:E8M standard [220] units: mm

All parts were intentionally designed with slightly oversized dimensions to compensate the shrinkage that occurs during the debinding and sintering stages. Based on prior observations and literature values, a dimensional reduction of approximately 20–25% was anticipated. This oversizing also accounts for post-sintering finishing operations such as machining, which are required to meet the dimensional tolerances defined in the relevant standards, particularly for mechanical testing specimens.

CHAPTER 6

Commercial Ti6Al4V feedstock for PAM process

Before developing a suitable feedstock formulation tailored for PAM technology, it is essential to first understand the fundamental properties that such feedstocks must possess. To establish a reference point, a commercial feedstock was selected and its properties thoroughly evaluated.

Currently, there is no titanium-based feedstock specifically designed for PAM. This technology, which shares similarities with Fused Deposition Modelling (FDM) in terms of layer-by-layer deposition, differs in that it uses injection molding pellets as raw material, extruded through an Archimedean screw. In the absence of a dedicated PAM-compatible titanium feedstock, users typically rely on PolyMIM feedstock—originally developed for MIM—to produce PAM parts.

The aim of this chapter is to investigate the PolyMIM feedstock not only in terms of its intrinsic properties, but also with the objective of identifying the appropriate processing parameters for the production of parts using PAM technology. Since this feedstock was originally developed for MIM and not specifically tailored for PAM, a thorough evaluation is necessary to assess its suitability and performance throughout the PAM process.

To this end, several complementary analyses were carried out. Torque monitoring was used during mixing to evaluate the consistency and flow resistance of the material. The feedstock was then extruded and regranulated into pellets to simulate its preparation for PAM. Thermogravimetric analysis was performed to study the thermal stability and decomposition behavior of the binder system. Rheological characterization provided insight into the flow behavior of the feedstock under shear, which is critical for extrusion-based processes. Finally, 3D printing trials were conducted to validate the material's performance in real PAM conditions and to fine-tune the printing parameters.

6.1 Mixing step and torque recording analysis

Figure 6.1 from the Brabender mixing analysis illustrates how torque varies with temperature for a commercial PolyMIM feedstock. As the temperature increases from 140°C to 190°C, the torque steadily decreases, indicating a reduction in the material's viscosity.

This behavior is typical during thermal processing, where higher temperatures facilitate the softening or melting of the material, making it easier to mix.

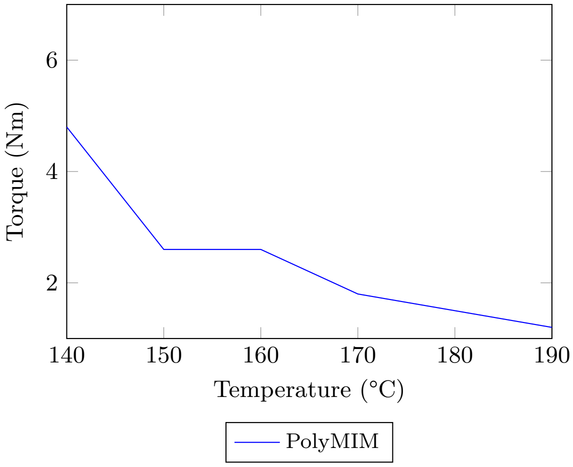

Figure 6.1: Torque of commercial PolyMIM feedstock depending on the temperature

The PolyMIM feedstock required a relatively long heating time, approximately 25 minutes, inside the Brabender mixer to reach a workable state. Temperatures below 140°C were not tested, as the introduction of the pellets at 140°C led to a brief spike in torque, reaching nearly the measurable limit of the equipment (50 Nm). This initial spike suggests that the material was still too solid and resistant to mixing at that point.

This trend is crucial for identifying a suitable processing window. At lower temperatures, the high torque indicates that the material is more resistant to mixing, likely due to its higher viscosity or incomplete melting. However, starting at around 170°C, the torque levels off and remains relatively stable at up to 190°C. This plateau indicates that the material has reached a state where it can be processed efficiently, with minimal resistance and without risking mechanical stress on the equipment.

However, at 190°C, visible signs of degradation were observed, including vapor emission, suggesting the onset of thermal degradation. This observation sets an upper limit for the processing temperature, as further heating could compromise the material's integrity.

Moreover, the stability of the torque curve in the 170–185°C range suggests that the mixture is homogeneous and stable. There are no abrupt changes or fluctuations in torque, which would otherwise signal issues like phase separation or inconsistent mixing.

Therefore, this analysis defines the optimal temperature range for processing, likely between 170°C and just below 190°C, and confirms the stability and uniformity of the mixture under those conditions.

6.2 Kofler bench

The results, shown in Figure 6.2, revealed that degradation begins at approximately 200–210°C as evidenced by a distinct change in the pellet's appearance. At this point, the material loses its malleability and disintegrates into powder.

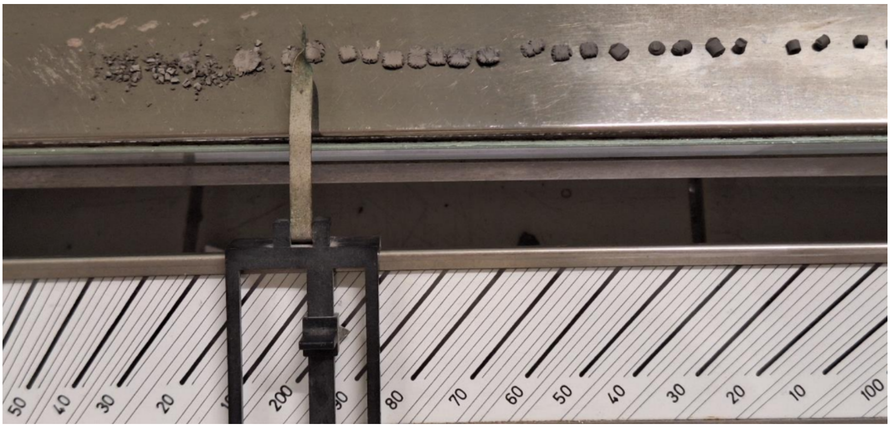

Figure 6.2: Kofler bench test of the commercial Ti6Al4V PolyMIM feedstock (HyProPAM).

The different thermal behavior zones identified through this test are summarized as follows in Table 6.1.

Table 6.1: Thermal behavior zones of the pellets based on temperature

Temperature Range	**Behavior Description**
$< 115°$C	Cold zone — pellets remain hard and cannot be crushed
$115 - 135°$C	Transition zone — pellets are difficult to crush
$135 - 150°$C	Malleable zone — pellets can be crushed but are not sticky
$> 150°$C	Sticky zone — pellets are malleable and adhesive
$\approx 200°$C	Degradation onset

Based on these results, the temperature interval selected for rheological testing was narrowed to 150–200°C for the PolyMIM feedstock, minimizing the number of required measurements while avoiding thermal degradation and preventing potential damage to the rheological testing equipment.

6.3 Extrusion behavior analysis

The extrusion behavior of the commercial PolyMIM was evaluated using a micro-compounder under various temperature conditions, while maintaining constant screw speed (60 RPM) and mixing time (15 minutes).

As reported in Table 6.2, the material remains non-extrudable at temperatures below 160°C, where the pellets retain their hardness and cannot flow through the die. This marks a threshold below which the feedstock is unsuitable for deposition.

Table 6.2: Summary table of Fused Filament Fabrication of commercial Ti6Al4V PolyMIM feedstock on DSM

Temperature (°C)	**Screw speed (RPM)**	**Time (min.)**	**Extrudable (Y/N)**	**Brittleness**
150	60	15	N	N.D.
160	60	15	Y	Brittle
170	60	15	Y	Brittle
180	60	15	Y	Malleable
190	60	15	Y	Malleable

At 160°C and 170°C, the material becomes extrudable, indicating that the binder phase softens sufficiently to allow flow. However, the filaments remain brittle (Figure 6.3a) throughout this range, exhibiting poor flexibility and high susceptibility to fracture upon minimal deformation at this range of temperature.

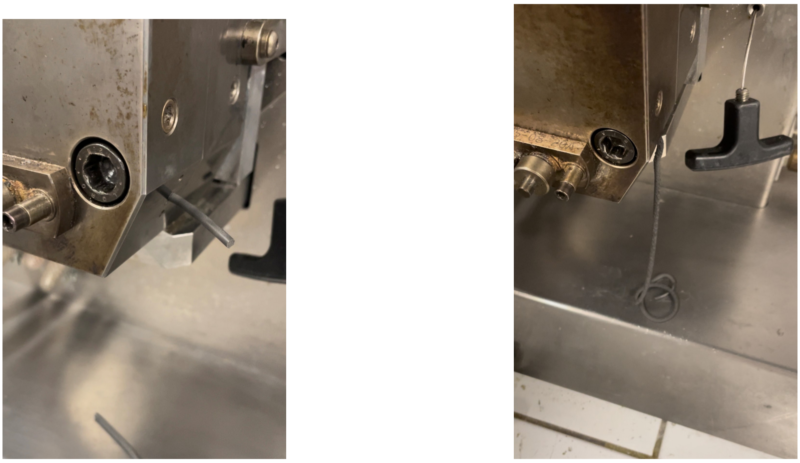

(a) Extrusion at 160°C of PolyMIM feedstock showing its brittleness

(b) Extrusion at 180°C of PolyMIM feedstock malleable showing visible sharkskin effect

Figure 6.3: Extrusion of the PolyMIM feedstock using DSM extruder at 160 and 180°C

At 180°C, the feedstock enters a malleable regime. In this state, the extruded material displays enhanced ductility and cohesion, making it suitable for shape retention and interlayer adhesion—two critical criteria in pellet-based extrusion systems like PAM. Therefore, 180°C is identified as the optimal processing temperature for this feedstock, balancing flowability with mechanical workability. The flowability of the feedstock at 180°C is described Figure 6.3b.

These results delineate a critical thermal processing window, a key parameter for successful PAM implementation. Below this range, the pellets are unprintable due to excessive stiffness; within the range, they begin to flow but remain too brittle; and above this range, malleability is achieved, enabling viable 3D printing. This thermal transition correlates with the softening of the binder matrix and marks the onset of acceptable viscoelastic behavior for extrusion.

6.4 Thermogravimetric analysis TGA

Thermogravimetric analysis was conducted to investigate the thermal degradation behavior of the commercial Ti6Al4V PolyMIM feedstock. This material consists of titanium alloy powder and a binder system comprising multiple polymers with distinct thermal and functional roles. The TGA profile, shown in Figure 6.4, reveals two major weight loss events, indicating the presence of at least two polymeric constituents in the formulation.

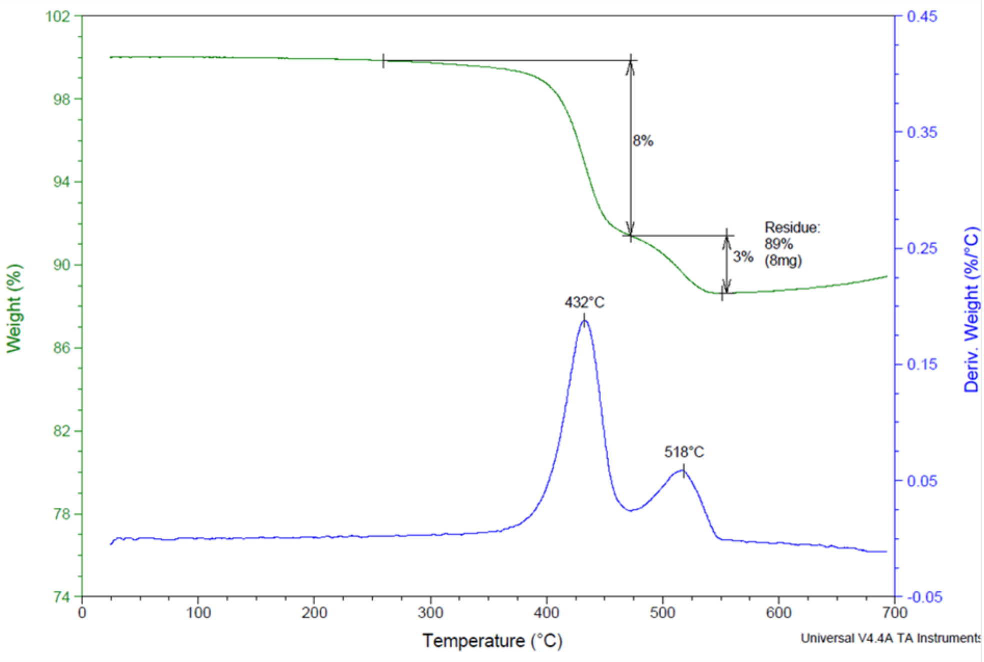

Figure 6.4: TGA of PolyMIM Ti6Al4V granules using TGA Q500 presenting two weight loss of 8 wt.% at 432°C and 3 wt.% at 518°C

The first significant weight loss occurs at approximately 432°C and corresponds to an 8 wt.% reduction in mass. This loss is attributed to the decomposition of the main polymer, which is typically designed to be water-soluble and easily removable during the early stages of the debinding process. These polymers are chosen for their ability to dissolve in water, allowing for a controlled and environmentally friendly pre-debinding stage. Their relatively low molecular weights and thermal thresholds make them suitable for facilitating flow during extrusion while still being easy to remove post-printing (e.g. PEG, PVA, ...).

The second weight loss, recorded at around 518°C and accounting for an additional 3 wt.% of the feedstock mass, is associated with the degradation of the backbone polymer. This component remains intact after the initial solvent debinding phase and serves to maintain the structural integrity of the part during the subsequent thermal debinding and early sintering stages. Based on its higher degradation temperature and common use in MIM technologies, the backbone polymer in this case is likely to be PVB or Other commonly used backbone polymers include polymethyl methacrylate (PMMA) and polyolefins such as polypropylene (PP) or polyethylene (PE). These polymers exhibit higher thermal stability and are generally not water-soluble, ensuring that the green part retains sufficient mechanical strength during handling and during the ramp-up to sintering.

The rationale for employing a two-component binder system lies in the complementary functionalities of the main and backbone polymers. The main polymer facilitates early flowability during extrusion and enables easy solvent debinding. It typically possesses a lower molecular weight and thermal degradation point, which allows it to be removed efficiently without causing damage to the printed part [221, 222]. In contrast, the backbone polymer, which is more thermally stable and mechanically robust, ensures dimensional stability and cohesive strength of the printed part throughout the post-processing steps [221]. This sequential degradation strategy is essential for producing defect-free, dense sintered parts [221].

Altogether, the total binder content in the PolyMIM Ti6Al4V feedstock is approximately 11 wt.%, which aligns with conventional formulations used in MIM. The remaining 89 wt.% (in mass) is composed of the Ti6Al4V metallic powder. The TGA curve also shows that thermal degradation initiates slightly above 225°C, indicating the upper limit for safe processing during extrusion and printing. Exceeding this temperature can trigger premature binder breakdown, leading to viscosity loss, gas evolution, and possible print failure. This observation highlights the importance of maintaining a controlled thermal window during PAM processing.

In conclusion, the TGA analysis confirms the presence and function of two distinct polymeric phases within the binder system. The main polymer enables solvent debinding and early flow, while the backbone polymer preserves mechanical strength during thermal debinding and sintering. Their respective degradation behaviors define the thermal boundaries for safe and effective processing in PAM. Understanding this thermal profile is crucial for optimizing extrusion conditions and ensuring successful downstream processing without compromising part integrity.

While thermogravimetric analysis provides insight into the thermal stability and degradation profile of the binder system, it does not fully capture the material's behavior under shear. To complement this thermal analysis and better understand the flow dynamics during extrusion, rheological testing was conducted. These tests offer critical information on viscosity evolution, flow resistance, and viscoelasticity, which are essential for defining a stable and safe processing window in PAM applications.

6.5 Rheological analysis

6.5.1 Shear Stress Response under Steady-State Flow Conditions

As part of the optimization study conducted during the HyProPAM project, rheological analyses were carried out on the commercial Ti6Al4V feedstock from PolyMIM GmbHto investigate the causes of the poor print quality observed. This characterization aims to more precisely define a suitable processing window in terms of temperature and flow rate for this material, with the objective of improving the final part quality—both visually and mechanically.

Figure 6.5 illustrates the flow curves of PolyMIM feedstock by plotting shear stress (τ) as a function of shear rate ($\dot{\gamma}$) across several processing temperatures (170–200°C). These controlled shear experiments are used to determine the yield stress and to analyze the flow regime, indicating whether the material exhibits pseudo-plastic (shear-thinning) behavior — a prerequisite for successful extrusion in PAM. The curve morphology offers insights into flow initiation, stress overshoot, and potential flow instabilities. A plateau or drop at higher shear rates may suggest structural breakdown, wall slip, or phase separation. This data informs the choice of temperature and shear rate settings in PAM to ensure smooth flow without flow instabilities or nozzle clogging [223, 224].

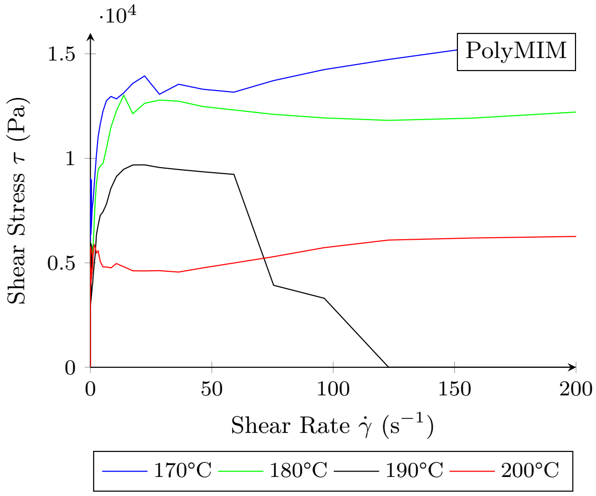

Figure 6.5: Shear stress τ as a function of shear rate $\dot{\gamma}$ for PolyMIM at 150, 160, 170, 180, 190 and 200°C.

Across all temperatures, the PolyMIM feedstock exhibits shear-thinning behavior—where the shear stress increases with shear rate at a decreasing rate. This is typical for highly filled systems where polymer chains and solid particles form transient structures that resist flow at low shear but progressively align and disentangle as the shear rate increases. The curves at 170°C and 180°C show a consistent increase in τ with $\dot{\gamma}$, reaching a plateau-like region, indicative of steady, controlled flow, which is desirable for extrusion-based printing applications [225, 226].

Temperature significantly affects the flow behavior of the feedstock. At 170°C, the shear stress is the highest among the measured temperatures, reflecting a high viscosity and strong internal network. As the temperature increases to 180°C, the material becomes easier to flow—τ values decrease slightly but remain stable, suggesting this is the optimal temperature range for PAM processing. However, at 190°C, a sharp decrease in shear stress is observed beyond $\dot{\gamma} \approx 70 \text{ s}^{-1}$, followed by an abrupt drop to nearly zero. This anomaly is associated with material ejection from the rheometer, likely caused by thermal degradation, where the polymer matrix loses structural cohesion and can no longer support shear. At 200°C, the shear stress remains consistently low, pointing to a significant loss of integrity and possibly irreversible degradation of the feedstock structure [227, 228].

The rheological behavior observed here has direct consequences for PAM. The stable response at 170°C–180°C suggests that the feedstock maintains sufficient resistance to deformation while being flowable enough for extrusion, ensuring smooth deposition and adequate filament shape retention. In contrast, the instability at 190°C and degradation at 200°C could lead to extrusion failures, such as strand discontinuities, weak interfilament bonding, or poor adhesion to the build platform. The sudden drop in shear stress may result in uncontrolled flow, ultimately compromising print quality and mechanical performance of the final part. Such conditions could also induce residual stresses during cooling and shrinkage, affecting sintering behavior [225].

Although the exact binder formulation of PolyMIM is not disclosed, the rheological transitions suggest significant thermo-mechanical changes in the material. At lower temperatures, polymer chain entanglements and filler interactions dominate, leading to higher stress values. As temperature rises, increased chain mobility and possible filler–matrix debonding reduce internal resistance. The drastic flow loss at high temperatures may also reflect interfacial instabilities between the organic phase and metallic powders, leading to material separation or foaming, which would explain the ejection observed at high shear [229–231].

In summary, Figure 6.5 confirms that PolyMIM feedstock exhibits stable and controlled flow behavior between 170°C and 180°C, making this the recommended PAM processing window. Above this range, the material undergoes thermal softening followed by degradation, leading to flow instability and potential extrusion failure. These findings underscore the need for tight thermal control during PAM, especially when repurposing MIM feedstocks for AM where shear rates and residence times differ substantially.

6.5.2 Time-Dependent Stability under Oscillatory Shear

Figure 6.6 illustrates the time-dependent evolution of the complex viscosity (η^*) of the PolyMIM feedstock at 180°C, under oscillatory shear conditions. The test is conducted at a fixed shear stress of 10 Pa and a constant frequency of 1 Hz. This type of time sweep test is crucial for evaluating the thermal stability and rheological consistency of a feedstock during isothermal processing—an essential consideration for AM processes like PAM, where the material remains molten over prolonged periods [232, 233].

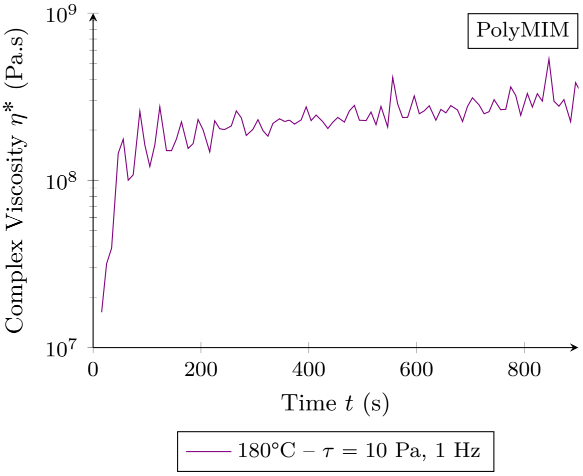

Figure 6.6: Evolution of complex viscosity η^* as a function of time at τ = 10 Pa and f = 1 Hz at 180°C for PolyMIM feedstock.

The curve exhibits a sharp rise in complex viscosity during the initial seconds, followed by a steady-state plateau that persists for over 800 seconds. Initial fluctuations are visible, likely due to thermal equilibration or instrumentation response. Beyond this transient phase, η^* stabilizes around 10^8 Pa.s, reflecting the material's resistance to deformation under combined elastic and viscous contributions [234].

Complex viscosity η^* is defined as [223]:

$$\eta^* = \frac{\sqrt{G'^2 + G''^2}}{\omega} \tag{6.1}$$

where G' is the storage modulus (elastic behavior), G" the loss modulus (viscous behavior), and ω the angular frequency $\omega = 2\pi f$.

The stabilization of η^* over time indicates that no significant molecular degradation or crosslinking occurs at 180°C over the duration of the test. This suggests that the polymer chains remain chemically stable and physically entangled, maintaining a uniform viscoelastic response [223].

This time sweep result supports the feasibility of using PolyMIM in PAM at 180°C, as the rheological stability over time ensures consistent flow behavior during extrusion. Stable complex viscosity is crucial for ensuring layer uniformity, preventing clogging, and minimizing fluctuations in extrusion pressure.

However, while this figure alone suggests good thermal stability at this temperature, it must be correlated with other factors such as interlayer adhesion, shrinkage, and post-processing behavior (e.g., debinding and sintering) [235].

Despite the apparent thermal stability, the high viscosity $\approx 10^8$ Pa.s may hinder flow under low shear, potentially affecting wettability on the print bed and interlayer fusion—key requirements in PAM. Moreover, the initial fluctuation could still hint at minor structural rearrangements, such as filler migration, minor solvent evaporation, or partial dewetting. These could introduce local inconsistencies during the early extrusion phases [236, 237].

In conclusion, Figure 6.6 demonstrates that PolyMIM exhibits time-stable complex viscosity at 180°C under mild dynamic loading. This rheological consistency is favorable for PAM, confirming thermal robustness. However, the relatively high viscosity may contribute to poor bed adhesion and weak interlayer bonding, which are critical challenges noted in experimental trials of PolyMIM in PAM applications.

6.5.3 Frequency-Dependent Viscoelastic Properties

Figure 6.7 presents the evolution of the complex viscosity η^* as a function of frequency f, measured at a constant shear stress $\tau = 10$ Pa, for PolyMIM feedstock at temperatures from 150°C to 200°C. In oscillatory shear rheology, frequency sweeps provide critical insight into the viscoelastic time-dependent behavior of materials, particularly how polymer chains and particle interactions respond across a range of deformation timescales [235, 238, 239].

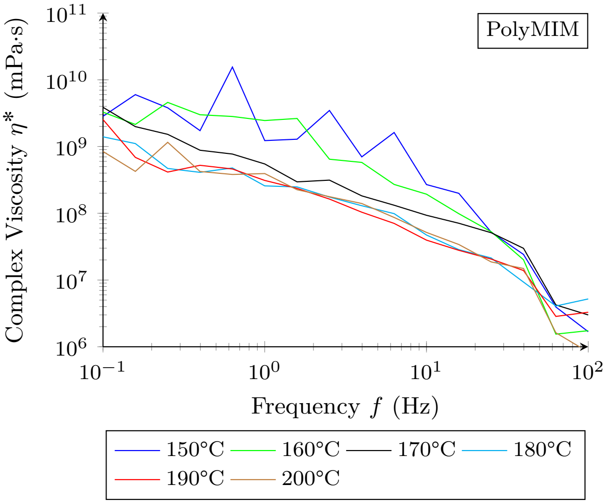

Figure 6.7: Complex viscosity η^* as a function of frequency f at fixed shear stress $\tau = 10$ Pa for PolyMIM feedstock ranging from 150 to 200°C.

All curves demonstrate a decrease in viscosity with increasing frequency, characteristic of shear-thinning (or frequency-thinning) behavior [236]. This indicates that under fast deformations (high frequencies), the material flows more easily, as the polymer chains have less time to entangle or relax. At lower frequencies (longer timescales), the structure is more preserved, resulting in higher complex viscosity.

At low frequencies, the complex viscosity clearly increases as the processing temperature decreases. This is most pronounced at 150°C and 160°C, where the viscosity reaches $10^{\mathbf{10}}$ mPa.s, suggesting significant resistance to flow and dominant elastic-like behavior. This is likely due to limited polymer chain mobility and possible incomplete melting of the binder system, which reinforces the material structure [240].

In contrast, at 180°C and above, the viscosity remains consistently lower throughout the frequency spectrum, signifying greater molecular mobility and a transition toward more viscous-dominated behavior. This aligns well with a softening of the polymer matrix and partial relaxation of internal interactions (e.g., van der Waals, hydrogen bonds) [230, 237].

Between 170°C and 180°C, the curves show both moderate viscosity values and a smooth, predictable frequency response. This behavior is ideal for PAM, where the material must be fluid enough to flow through a nozzle while retaining enough structure to support successive layers [241]. This region thus defines a rheological sweet spot, balancing viscosity, structural recovery, and interlayer adhesion.

The curve at 160°C appears jagged and unstable, particularly at mid-range frequencies, potentially due to partial yield events or phase transitions (e.g., microphase separation or incomplete melt homogenization). Conversely, the 200°C data shows lower overall viscosity and slightly accelerated thinning, suggesting the binder system might be degrading or over-softening—consistent with observations from other figures such as the shear rate dependence and steady-state curves [242].

The frequency-dependent complex viscosity profile of PolyMIM can be can be summarized as follows:

- Below 170°C, viscosity is too high for stable extrusion, and the feedstock may resist flow or create internal stresses during deposition.
- Above 190°C, excessive softening or degradation may lead to poor layer cohesion, low mechanical strength, or even binder volatilization.
- Frequencies corresponding to typical print head actuation rates (around 1–10 Hz) fall in the range where optimal flow and moderate η^* are observed for 170–180°C, marking this as the most favorable operational window.

These findings have significant implications for PAM processing:

- The optimal processing window for PAM is between 170 and 180°C: the viscosity is sufficiently low for extrusion, while the thermal stability of the feedstock remains intact.
- Below 170°C, the feedstock may be too viscous, potentially causing under-extrusion or incomplete bonding.
- At 190°C, the degradation not only compromises rheological consistency but could also result in poor filament adhesion, void formation, and inferior mechanical properties due to thermal damage and gas evolution.

The rheological profile reveals a viscosity softening threshold around 170°C and more particularly at 180°C, marking the lower bound for efficient processing, while 190°C crosses into thermal degradation territory. These insights affirm the necessity of tight thermal control during PAM processing and highlight the mismatch between MIM-formulated binders and the extrusion demands of AM [139].

6.5.4 Stress-Dependent Viscoelastic Properties and Yield Behavior

Figure 6.8 presents the variation of the storage modulus (G') and the loss modulus (G") as a function of applied shear stress (τ) in a log-log scale for the PolyMIM feedstock at 180°C. These dynamic oscillatory measurements are crucial for evaluating the viscoelastic behavior of the material under small-amplitude deformation. G' quantifies the elastic (energy-storing) response, while G" reflects the viscous (energy-dissipating) behavior. In the context of PAM, a balanced viscoelastic profile is essential: sufficient elasticity (high G') maintains structural fidelity post-deposition, while adequate viscosity (G") ensures flow and interlayer adhesion. This test helps identify the linear viscoelastic region (LVR) and assesses the dominance of solid- or liquid-like behavior, which influences layer bonding and internal stress accumulation in printed parts [243].

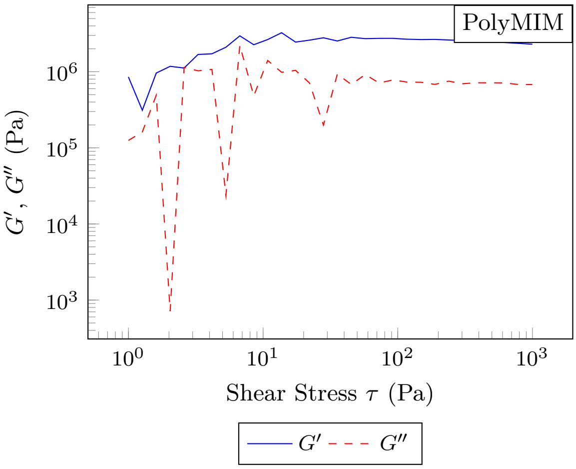

Figure 6.8: Log-log plot of storage modulus (G') and loss modulus (G'') as a function of shear stress τ for PolyMIM at 180°C.

At low shear stresses, both G' and more particularly G" exhibit significant fluctuations, reflecting an unstable viscoelastic regime. These oscillations likely result from microstructural rearrangements and poor filler-polymer wetting, particularly at low stresses where the feedstock is not fully mobilized [244].

As τ increases, G' stabilizes and dominates G", indicating a solid-like behavior where energy is predominantly stored elastically. This is consistent with a highly structured system where the polymer chains and solid particles (metal powders) are entangled or physically bonded, resisting deformation. However, in the context of PAM, this high elasticity (high G'/G") ratio can be detrimental. It implies that the material resists flow and tends to store mechanical energy rather than dissipate it as heat. Such behavior may induce internal stresses during printing and cooling, which could manifest as defects or mechanical weaknesses during debinding or sintering [118].

The PolyMIM feedstock likely forms a rigid structure upon melting due to strong physical interactions within the binder system and/or dense packing of solid particles, leading to a markedly high G'. This reflects a quasi-solid behavior under small deformations.

The extremely low values of G" indicate minimal viscous flow and energy loss, suggesting either a rigid polymer matrix or a high solid loading that hinders polymer chain mobility.

The sharp decreases observed in G" particularly those exceeding three orders of magnitude below G' could also be due to the instrument's detection limit at low shear stress, where the torque signal may fall below the reliable measurement threshold.

6.6 Thermal camera analysis

During the HyProPAM project, thermal analysis using infrared (IR) imaging was performed to investigate the thermal behavior of the commercial PolyMIM feedstock during PAM printing. This analysis aimed to diagnose printing defects, particularly poor adhesion to the build plate, by comparing theoretical extrusion temperatures with actual measured values.

The targeted setpoints were 165°C for the extruder and 192°C for the nozzle. However, thermal measurements revealed significant discrepancies between these setpoints and the actual temperatures observed, especially at the filament level. These differences are summarized in Table 6.3.

Table 6.3: Thermal measurements of the PolyMIM feedstock during extrusion at 192°C nozzle setpoint

	$T_{\textbf{Extruder}}$	$T_{\textbf{Nozzle}}$	$T_{\textbf{Filament}}$
Theoretical setpoints	165°C	192°C	192°C
Measured (Thermocouple)	–	–	167°C
Measured (Thermal Camera)	157°C	180°C	148°C

Thermal imaging (Figure 6.9) revealed surface temperatures of 180°C at the nozzle, 157°C at the extruded filament (Cordon1) and 148°C for Cordon2, indicating a consistent 15–25°C thermal gap between internal settings and actual material output. These results were consistent across different trials and confirmed the presence of substantial heat loss after material exits the nozzle.

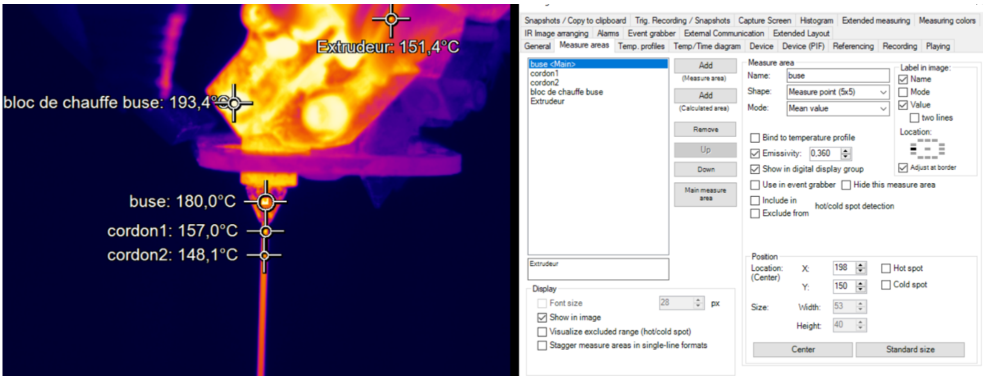

buse <Main>
cordon1
cordon2
bloc de chauffe buse
Extrudeur

Extrudeur

Measure area
Name: buse
Shape: Measure point (5x5)
Mode: Mean value
☐ Bind to temperature profile
☑ Emissivity: 0,360
☑ Show in digital display group
☐ Use in event grabber ☐ Hide this measure area
☐ Include in / ☐ Exclude from hot/cold spot detection

Label in image:
☑ Name
☐ Mode
☑ Value
☐ two lines
Location:
☑ Adjust at border

Display
☐ Font size 28 px
☑ Show in image
☐ Visualize excluded range (hot/cold spot)
☐ Stagger measure areas in single-line formats

Position
Location: (Center) X: 198 Y: 150
☐ Hot spot
☐ Cold spot
Size: Width: 53 Height: 40

Figure 6.9: Thermal camera view using Optris PI software showing PolyMIM extrusion at 192°C nozzle setpoint.

To validate these findings, a thermocouple was inserted directly into the nozzle to measure the internal temperature of the filament (Figure 6.10). This approach provided more accurate readings at the core of the extruded material and enabled proper calibration of the IR camera's emissivity. The thermocouple recorded a temperature of 167°C, which remains significantly lower than the setpoint of 192°C, confirming substantial heat loss during extrusion.

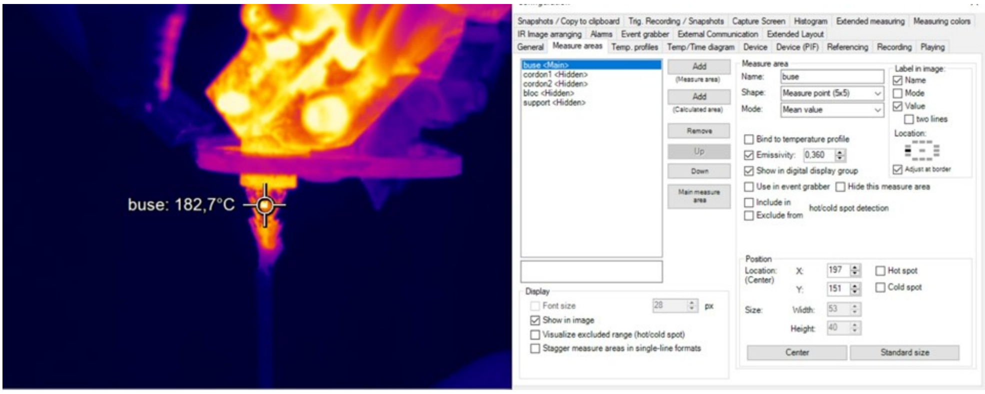

buse <Main>
cordon1 <Hidden>
cordon2 <Hidden>
bloc <Hidden>
support <Hidden>

Measure area
Name: buse
Shape: Measure point (5x5)
Mode: Mean value
☐ Bind to temperature profile
☑ Emissivity: 0,360
☑ Show in digital display group
☐ Use in event grabber ☐ Hide this measure area
☐ Include in hot/cold spot detection
☐ Exclude from hot/cold spot detection

Label in image:
☑ Name
☐ Mode
☑ Value
☐ two lines
Location:
☑ Adjust at border

Position
Location: (Center) X: 197 Y: 151
☐ Hot spot
☐ Cold spot
Size: Width: 53 Height: 40

Display
☐ Font size 28 px
☑ Show in image
☐ Visualize excluded range (hot/cold spot)
☐ Stagger measure areas in single-line formats

Figure 6.10: Thermal image and thermocouple setup used to calibrate emissivity and validate filament core temperature.

These findings suggest that in order to reach a real extrusion temperature of 175–180°C—identified as optimal through rheological analysis—the nozzle setpoint must be increased by approximately 15–25°C. The thermal drop observed from the internal system to the extruded filament is critical to understand and manage for consistent print quality.

Several causes may explain this loss of heat:

- Ambient cooling: The filament rapidly loses heat upon exiting the nozzle due to convection and radiation.
- Insufficient residence time: Fast throughput prevents the feedstock from reaching equilibrium temperature inside the heated zones.
- Nozzle inefficiency: Poor insulation and thermal transfer between the heater block and nozzle tip can hinder temperature consistency.
- IR measurement limitations: Composite materials like PolyMIM have complex emissivity, affecting the accuracy of thermal imaging if not properly calibrated.

While absolute values from IR cameras should be treated with caution, the consistent relative temperature gap across multiple setups reveals a systemic limitation in heat transfer control within the extrusion system.

This discrepancy has significant implications: underheated filament may adhere poorly to the build surface or previously deposited layers, leading to delamination, warping, or structural defects. To address this, several improvements are proposed:

- Enhance nozzle temperature

- Slow down extrusion speed to increase heating time
- Calibrate IR emissivity settings precisely using internal thermocouples
- Employ radiant heaters or enclosures to reduce ambient cooling
- Integrate real-time temperature monitoring near the nozzle exit

This study underscores the need for precise thermal control in PAM to ensure stable extrusion, proper interlayer adhesion, and high part quality.

6.7 3D printing

Printing parameters

A study was carried out to identify suitable printing parameters to produce parts with properties comparable to those obtained through MIM.

Initially, these parameters were based on specifications provided by the feedstock manufacturer. Although originally intended for MIM, the manufacturer also promotes PolyMIM as compatible with material extrusion. The recommended parameters initially used in PAM are summarized in Table 6.4.

Table 6.4: Printing parameters giving by the feedstock manufacturer for MIM technique employed for PAM

MIM temperatures	Values	Adapted printing temperatures	Values
Zone 1	180°C	Nozzle temperature	194°C
Zone 2	185°C	Extruder temperature	155°C
zone 3	190°C	Coldpoint temperature	45°C
zone 4	195°C	Buildplate temperature	70°C

As shown in Figures 6.11 to 6.13, the resulting printed parts exhibited multiple defects. Figure 6.11 highlights significant warping during bending tests, indicating insufficient layer adhesion and thermal gradients during printing.

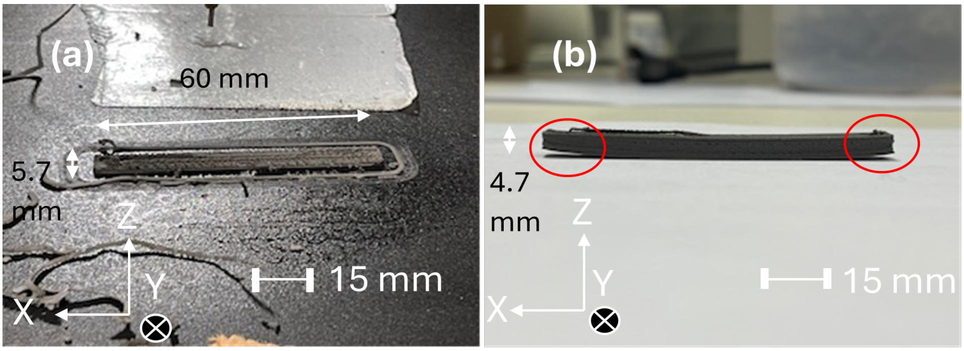

Figure 6.11: Bending test as-printed part showing warping

Figure 6.12 shows a severe porosity defect located at the center of the part, suggesting localized under-extrusion or poor material deposition, possibly due to low flow or temperature inconsistency.

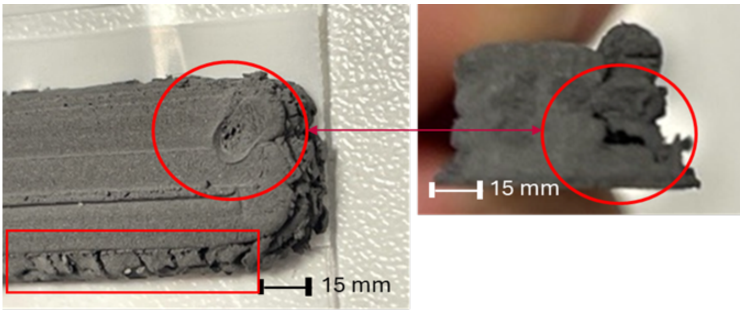

Figure 6.12: High porosity due to defect inside the as-printed part

Finally, Figure 6.13 illustrates the occurrence of a pronounced sharkskin effect on the surface of parts intended for machining trials. This surface irregularity is typically associated with excessive shear stress and insufficient melt homogeneity. These observations indicate that the initial parameter set—particularly the nozzle and extruder temperatures—was not suitable for stable PAM processing, and optimization was therefore required to improve part quality, interlayer bonding, and surface finish.

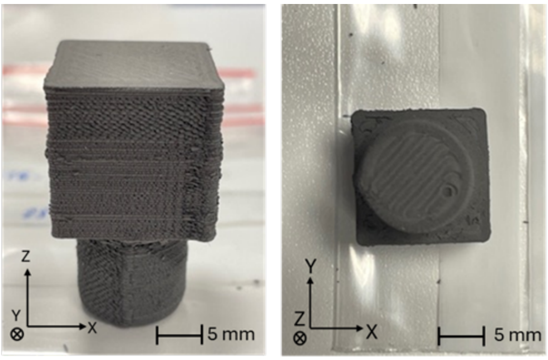

Figure 6.13: Part for machining test presenting high sharkskin effect

Subsequently, the printing parameters were adjusted by increasing the nozzle temperature, infill density, and flow rate.

Final parts produced as part of the HyProPAM project

During the HyProPAM project, parts with enhanced density (up to 98%) and significantly reduced porosity (as low as 0.4%) were successfully produced, showing virtually no geometric deviations. These density and porosity values were measured by BCRC.

The printing parameters that led to these improved results were optimized based on results from Kofler bench testing, rheological analysis, and thermal imaging (see Table 6.5).

Table 6.5: Optimized 3D Printing parameters

Printing Parameters	**Values**
Nozzle diameter	1 mm
Layer height	mm
Initial layer height	mm
Infill density	105%
Infill pattern	Lines
Extruder printing temperature	165°C
Nozzle temperature	200°C
Cold printing temperature	45°C
Build plate temperature	85°C
Flow	68%
Initial layer flow	110%
Radiant temperature	200°C
Print speed	15 mm/s

As illustrated in Figure 6.14, the printed plate exhibits relatively good surface quality compared to previous prints, with a significantly reduced sharkskin effect. This observation confirms that optimizing the processing temperature can effectively minimize surface defects in polymer-based additive manufacturing [245].Moreover, the use of radiant heating to maintain the filaments at an elevated temperature not only improves surface quality by reducing thermal gradients and solidification defects, but also enhances interlayer adhesion. As a result, the final printed part exhibits enhanced mechanical properties.

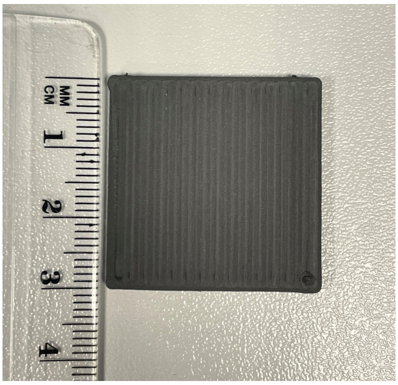

Figure 6.14: Plate made of Ti6Al4V PolyMIM of 30*30*3 mm with optimized parameters

Figure 6.15 highlights the advantages of the hybrid process combined with green-state machining, which constitutes the core focus of the project. This approach enabled coarser printing using a larger nozzle diameter and higher material flow to ensure high part density.

The excess material was then removed while the part was still in the green state—i.e., before acquiring its final mechanical properties—thereby facilitating both machining and surface finishing.

Figure 6.15: Watch dials after sintering: without machining (left) and with green-state machining (right)

Finally, the project demonstrated that the debinding and sintering steps do not alter the surface finish of parts machined in the green state.

6.8 Conclusions for commercial feedstock

The comprehensive analysis of the PolyMIM feedstock within the HyProPAM project has defined an optimal thermal processing window between 170°C and 190°C, ensuring material stability, controlled viscosity, and effective extrusion without thermal degradation.

Kofler bench testing helped narrow the temperature range for rheological evaluation to 150–200°C. Extrusion behavior analysis revealed a critical thermal transition: below 170°C, the material is too stiff for printing; within the range, it begins to flow but remains brittle; and above 190°C, it becomes malleable enough for successful 3D printing.

TGA results confirmed the presence of two distinct polymeric phases in the binder system—one enabling solvent debinding and early flow, and the other maintaining mechanical integrity during thermal debinding and sintering.

Rheological analysis showed stable flow behavior between 170°C and 180°C, making this the recommended PAM processing window. However, high viscosity may hinder bed adhesion and interlayer bonding, highlighting the importance of precise thermal control, especially when adapting MIM feedstocks to additive manufacturing.

Thermal camera analysis revealed significant heat losses during extrusion, with actual filament temperatures 20–25°C lower than expected. This discrepancy explains poor build plate adhesion and reduced mechanical performance observed in earlier trials.

Based on those results, the project successfully produced parts with improved density, reduced porosity, and minimal geometric deviations, with thermal parameters tightly controlled.

However, the HyProPAM project also demonstrated that, although high-quality sintered parts (up to 98% density) could be achieved through careful parameter optimization (thermal analysis, rheology, print tuning), PolyMIM remains suboptimal for PAM. Its high processing temperature, rapid cooling, and difficulty extruding through fine nozzles led to limited surface quality, increased energy demand (e.g., radiant heaters), and the need for post-processing, ultimately reducing both process efficiency and environmental performance. These findings underscore the need to develop PAM-specific feedstocks with improved thermal processability, better flow behavior, and optimized printability to reduce energy consumption, enhance surface finish, and minimize material waste.

CHAPTER 7

Sustainable Ti6Al4V feedstock optimized for PAM

7.1 Introduction

In the literature, similar feedstocks based on Ti6Al4V alloy combined with PEG, PVB, and SA were explored by Eickhoff et al. [91]. These formulations, intended to be partially water-soluble and suitable for PAM, experienced issues of phase separation. They performed effectively in filament-based FDM processes but failed under MEX conditions, highlighting the sensitivity of these systems to process variations.

PEG remains a reliable choice in water-soluble binder systems due to its proven effectiveness across numerous studies. PVB provides beneficial thermoplastic properties, including compatibility with inorganic fillers, favorable melting temperatures between 160–190°C, robust green-part mechanical cohesion, moisture resistance, and compatibility with various organic compounds. SA is frequently utilized as an additive for lubrication and dispersion enhancement but, by itself, is insufficient for ensuring structural integrity and shape retention in PAM processes.

Despite maintaining an equivalent titanium loading (55 vol.%), these existing formulations require further refinement and optimization tailored specifically to the operational requirements of the PAM method.

This chapter presents the progressive development of an eco-designed feedstock for PAM, through a structured optimization of the binder system. The experimental approach was conceived to sequentially assess the individual and combined effects of specific additives on the processability, rheology, and thermal behavior of the formulations.

The study begins with the investigation of SA, a well-known dispersant and lubricant widely used in metal-polymer systems. SA was tested at concentrations ranging from 0 to 5 vol.% to evaluate its effect on extrusion torque, softening behavior, and flow properties. This initial step was crucial to define the formulation window beyond which SA becomes detrimental, and to establish a reference binder with enhanced flowability and reduced processing temperatures. This formulation had previously been explored for MEX by Eickhoff et al. [91], where phase separation was reported as a critical limitation. The goal here was to determine whether a similar issue arises in PAM, and if so, to identify a strategy to mitigate it.

Following this, the role of MC was investigated as a bio-based viscosity modifier. Unlike SA, MC acts as a solidener and network stabilizer. Its addition is tested here in a water-free binder matrix to examine its influence on viscosity, print fidelity, and thermal behavior. PEG and PVB contents were kept constant in this campaign to isolate the specific contribution of MC. This stage aimed to overcome the phase separation previously identified and to reinforce the cohesion of the system under thermal stress.

Lastly, a hybrid formulation was designed by combining 3 vol.% SA and 3 vol.% MC, leveraging their complementary effects: lubrication and dispersion from SA, and structural stabilization from MC. To maintain the water-soluble polymer fraction constant, PEG was substituted proportionally for MC. This final composition was selected based on a balance between rheological stability, flow efficiency, printability, and environmental considerations.

The relevance of the analyses carried out in this chapter lies in their ability to quantify and correlate key formulation parameters with process performance. Torque measurements, Kofler bench observations, thermogravimetric analysis, and capillary rheometry were combined to provide a comprehensive understanding of the thermal transitions, flow behavior, and printability of each feedstock. These multi-scale evaluations not only validate the compatibility of the binder components, but also guide the design of a composition that satisfies both functional (printability, homogeneity, extrusion behavior) and environmental (bio-based content, process energy) criteria. Altogether, this approach contributes to bridging the gap between material formulation and process integration in the specific context of PAM with metallic powders.

7.2 Highly filled PEG/PVB based binder

7.2.1 Ti6Al4V content

In PAM, the solid loading of the feedstock plays a critical role in determining both sintering efficiency and mechanical performance. A solid content between 55 and 65 vol.% is generally recommended to ensure sufficient densification and acceptable final part properties [51, 246]. Higher solid loadings typically lead to increased sintered densities—often achieved in the range of 60 to 65 vol.% [51]. However, beyond 55 vol.%, the feedstock tends to exhibit increased brittleness and a more pronounced fracture-prone behavior, especially during extrusion or filament shaping [130]. Excessively high loadings also cause rheological challenges, such as high viscosity and loss of shear-thinning, and accelerate wear of processing tools and extrusion equipment. Moreover, a solid loading of 55 vol.% is sufficient to ensure that all Ti6Al4V particles are in contact after sintering.

For these reasons, a conservative solid loading of 55 vol.% was selected in this study to minimize the risk of embrittlement and to maintain a processable feedstock. Nevertheless, future work may explore the use of higher powder contents to potentially enhance the sintered density and final mechanical properties, provided that the rheological behavior remains compatible with PAM processing.

7.2.2 Ratio PEG/PVB

The first step of this study was to define an appropriate PEG and PVB ratio to ensure good processability. To reduce the number of experimental variables and isolate the effects of SA and MC addition, the PEG and PVB content was maintained constant at a 50:50 vol.% ratio throughout the formulation screening, except in the case of hybrid compositions with SA and MC, where adjustments were made to maintain a consistent water-soluble fraction.

In previous work by Eickhoff et al. [91], a PEG:PVB ratio of approximately 2:1 was successfully used in FFF. However, when transitioning to PAM processing, this ratio proved unsuitable due to significant phase separation issues during extrusion. In their study, only PEG with a molecular weight of 20,000 g/mol allowed stable filament fabrication, likely due to its higher melt strength and reduced diffusivity. In the present work, PEG with a lower molecular weight (12,000 g/mol) was selected for its balance between processability, degradation stability, and environmental impact. However, its reduced chain entanglement and mechanical integrity in the molten state require reinforcement through increased PVB content.

PVB, being a thermoplastic with good film-forming properties and high adhesion, plays a crucial role in enhancing filament cohesion, layer bonding during extrusion, and overall green part strength. These properties are particularly critical in PAM, where the extruded filament must support its own weight and maintain shape before complete solidification. Additionally, increasing the PVB fraction improves the mechanical stability of the printed parts after aqueous debinding, by forming a robust backbone once PEG is extracted. This helps prevent part collapse or deformation before the thermal debinding stage.

Overall, the choice to increase the PVB content in PAM feedstocks, especially when using a lower Mw PEG, is well justified based on both rheological behavior and mechanical performance requirements.

Following the formulation design, the next step involved characterizing the rheological behavior of the PEG/PVB-based binder in order to evaluate its potential suitability for 3D printing compared to the commercial feedstock. In particular, this was assessed through measurements of viscosity and flow properties, which directly impact print quality. To avoid redundancy with numerous rheological plots, the detailed results for the base binder formulation are provided in Appendix B. These results confirmed the promising characteristics of the PEG/PVB binder, which exhibited lower viscosity and enhanced flow behavior, both of which are advantageous for material extrusion processes. However, analysis of the storage modulus (G') and loss modulus (G") for the F0SA0MC formulation also indicated a lower structural rigidity compared to the commercial feedstock, potentially affecting shape retention during printing.

7.2.3 Conclusion on PEG/PVB based binder

The rheological analysis of the F0SA0MC feedstock reveals a promising profile for extrusion-based AM. It displays stable complex viscosity over time, clear shear-thinning behavior, and a well-defined viscoelastic transition, all of which are desirable traits for reliable printing. Compared to PolyMIM, which exhibits strong elastic dominance (high) and limited flow behavior (low), F0SA0MC is more adaptable under shear and exhibits a smoother viscosity response. PolyMIM's predominantly elastic nature may hinder interlayer adhesion and lead to stress accumulation during printing and debinding, potentially causing delamination or cracking. Additionally, the PolyMIM feedstock shows signs of material ejection and instability under high shear, likely tied to early-stage thermal degradation.

In contrast, F0SA0MC maintains mechanical stability and consistent rheological profiles across a range of temperatures, with optimal processing suggested between 140–160 °C. These findings validate its suitability as a base formulation, offering a more controlled and tunable behavior than PolyMIM, particularly important before introducing surfactants or rheological modifiers for advanced feedstock formulations.

7.3 Selection of the surfactant

The objective of this work is to develop a feedstock formulation better suited for PAM, as opposed to commercial formulations like PolyMIM, which were originally designed for MIM. A composition based on Ti6Al4V, PEG, PVB, and SA has already shown promising results in MIM, and has also been studied for AM applications by Eickhoff et al. [91]. This formulation is particularly interesting because it enables shaping at lower temperatures and includes a binder that is partially water-soluble, which facilitates debinding.

In the study by Eickhoff et al., the PEG/PVB-based feedstock worked well in fused filament fabrication (FFF), but encountered phase separation issues when used in MEX from pellets. As a result, no printable parts were obtained in PAM using granules. However, an alternative formulation based on PMMA and proprietary additives (PAT-77 P and PAT-659/CB) proved compatible with both FFF and MEX, and yielded high-quality sintered parts with final densities between 94% and 96%.

In contrast, for the PEG/PVB system, parts produced from filament achieved similar densities ($\approx$ 96%) when using high-molecular-weight PEG (20,000 g/mol), whereas lower densities ($\approx$ 75%) were reported with PEG 8000 g/mol. This suggests that PEG molecular weight (Mw) significantly influences the densification behavior of printed parts.

In this study, PEG with a molecular weight of 12,000 g/mol was selected as an optimal compromise between processability, thermal stability, and environmental considerations. Higher molecular weight PEGs, such as PEG 20,000 g/mol, not only approach the degradation temperature of PVB, complicating thermal debinding, but also require longer polymerization times and greater energy input, increasing their environmental footprint. Furthermore, their combination with methylcellulose has been reported to produce excessively high viscosities, making them less suitable for PAM.

The feedstock formulation is adapted from the composition proposed by Eickhoff et al. [91], with several modifications. Although the Ti6Al4V powder remains Grade 23, it was procured from a different supplier. The same Mowital-grade PVB was employed, while SA originated from an alternative manufacturer. In particular, the PEG used in this work (12,000 g/mol) was not included in the original study, resulting in a novel feedstock composition with distinct rheological and processing characteristics. While PEG is petroleum-based, its water solubility contrasts with the hydrophobic nature of PVB and SA, offering potential advantages during the debinding phase.

It is important to highlight that, as widely reported in the literature, the incorporation of a plasticizer is considered almost mandatory to ensure appropriate viscosity for PAM. Plasticizers enhance powder dispersion and promote adequate coating of metal particles, thereby facilitating particle mobility and improving the shear flow behavior of the feedstock. Among the available options, SA is the most commonly used bio-based plasticizer due to its effectiveness, availability, and compatibility with metal-polymer systems. Therefore, SA was selected as the primary plasticizer for this study.

However, determining the optimal SA content is crucial, as excessive amounts can lead to undesirable effects. Literature reports indicate that an overly high concentration of plasticizer results in a feedstock that is overly soft and fluid, ultimately increasing the risk of phase separation during the printing process [87, 92, 95].

To investigate this, several feedstocks were prepared with a constant solid loading of 55 vol.% Ti6Al4V and a 50/50 PEG/PVB binder system as described in Table 7.1. The SA content was varied from 0 to 5 vol.% in order to evaluate its influence on mixing behavior and rheological performance.

As explained previously, the mixing process was carried out in a heated Brabender mixer, allowing for real-time monitoring of the torque.

Table 7.1: Composition and nomenclature of feedstock formulations with SA from 0 to 5 vol.%

Composition	**Ti6Al4V**	**PEG**	**PVB**	**SA**	**MC**
	[vol.%]	[vol.%]	[vol.%]	[vol.%]	[vol.%]
F0SA0MC	55	22.5	22.5	0	0
F1SA	55	22.0	22.0	1	0
F2SA	55	21.5	21.5	2	0
F3SA	55	21.0	21.0	3	0
F4SA	55	20.5	20.5	4	0
F5SA	55	20.0	20.0	5	0

7.3.1 Impact of SA rate on the mixing torque

Torque measurements provide valuable insights into the homogeneity and rheological characteristics of the blend. A stabilization phase in the torque profile typically indicates that a homogeneous mixture has been achieved. Moreover, torque can be used as a preliminary indicator of the feedstock's viscosity. According to the literature, increasing the SA content should result in a gradual decrease in torque, reflecting reduced viscosity and easier mixing due to enhanced lubrication and reduced interparticle friction.

Figure 7.1 presents the torque as a function of temperature for various Ti6Al4V, PEG and PVB formulations with increasing contents of SA from 0 to 5 vol.%.

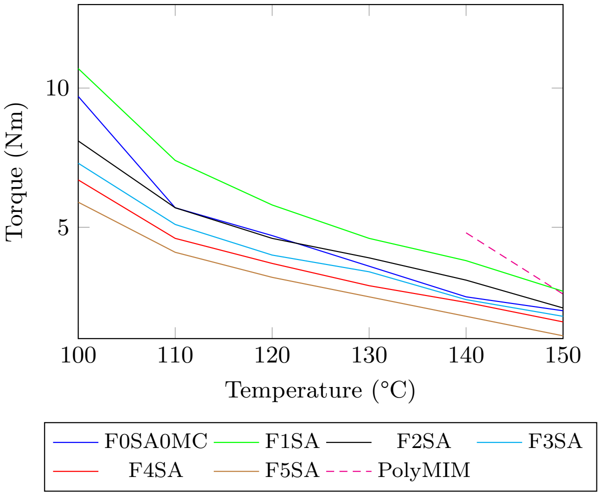

Figure 7.1: Torque of feedstocks with SA depending on the temperature and SA rate (from 0 to 5 vol.%)

The commercial PolyMIM feedstock is included as a reference, but only from 140 to 150°C due to its much higher viscosity at lower temperatures, which prevented stable measurements.

All experimental formulations show a continuous decrease in torque with increasing temperature, which is characteristic of thermoplastic binder systems: the viscosity of the polymer matrix decreases as it softens, leading to lower resistance to shear. This trend is particularly evident in the 100–130°C range, where the melting of PEG and softening of PVB occur, resulting in improved chain mobility.

Interestingly, the F1SA formulation (1 vol.% SA) exhibits a higher torque than F0SA0MC, which contains no stearic acid. This unexpected result can be explained by the dual role of SA in powder-based feedstocks. At low concentrations, SA can improve the wetting and dispersion of metal particles within the polymeric binder. This enhanced dispersion leads to increased particle–matrix interactions, which in turn results in higher internal resistance during mixing, and thus, a higher torque [87, 247]. In contrast, in the absence of SA, poor dispersion may result in a lower torque despite insufficient homogenization. Beyond a certain threshold (typically around 2 vol.% in this study), SA acts predominantly as a lubricant, forming a layer around the particles and reducing interparticle friction, which translates into a lower torque.

The PolyMIM feedstock, although only measured from 140°C onward due to its high viscosity, exhibits a higher torque than all SA-containing formulations (excepting F1SA) at both 140 and 150°C. This suggests that the experimental PEG:PVB-based formulations, especially those with 4–5 vol.% SA, exhibit significantly higher flow behavior at elevated temperatures. Despite PolyMIM being a commercial benchmark, its high torque may be linked to its more viscous binder system and lack of optimization for the lower-temperature PAM process.

This torque analysis demonstrates the key role of SA in enhancing feedstock processability for PAM. A content of 3–5 vol.% leads to substantial reductions in mixing resistance, especially in the critical temperature window for extrusion (100–140°C). Additionally, the fact that these formulations outperform PolyMIM in torque performance at high temperatures reinforces their relevance for energy-efficient and low-force printing.

7.3.2 Effect of SA rate on processability temperature range

To assess thermal behavior, all feedstocks with SA contents ranging from 0 to 5 vol.% were subjected to Kofler bench testing. Pellets were placed at 1 cm intervals on the bench and left for 45 minutes prior to evaluation.

The results in Figure 7.2 show a clear trend: as the stearic acid content increased, the fusion temperature of the feedstock decreased. Feedstock with SA have very low thermal stability at elevated temperatures and a range of working temperature has been determined by curshing all pellets to identify where pellets are still too hard and where pellets are degraded.

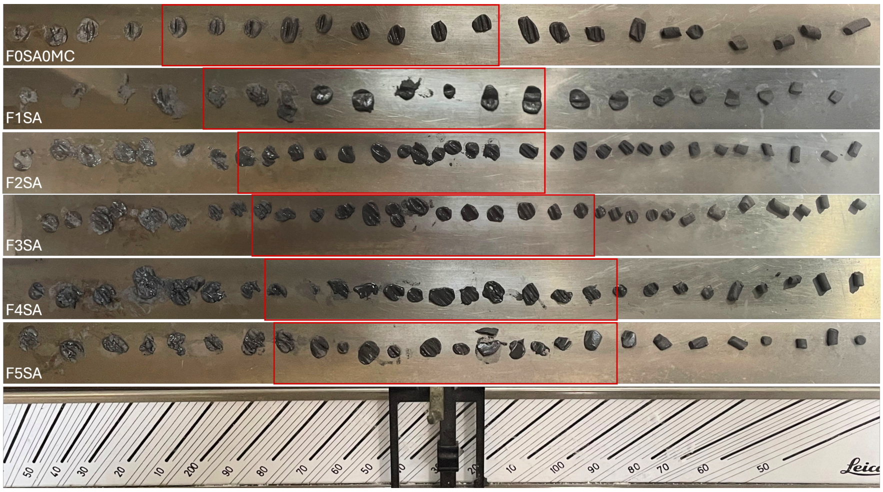

Figure 7.2: Working range (red) of pellets with varying SA contents from 0 to 5 vol.% determined on Kofler Bench (from 50 to 260°C).

Kofler bench results for 0 to 5 vol.% of SA content are summarized in Table 7.2. These results confirm that the processing temperature range for the experimental formulation is significantly lower than that of the commercial PolyMIM feedstock.

Table 7.2: Fusion temperatures of SA compositions determine by Kofler bench

Composition	**SA**	$T_{\mathrm{malleability}}$	T_{fusion}	T_{NoSticky}	T_{sticky}	$T_{\mathrm{degradation}}$
	[vol.%]	[°C]	[°C]	[°C]	[°C]	[°C]
F0SA0MC	0	x < 60	60 < x < 80	80 < x < 130	130 < x < 175	x > 175
F1SA	1	x < 65	65 < x < 78	78 < x < 130	130 < x < 178	x > 178
F2SA	2	X < 64	64 < X < 76	76 < x < 116	116 < x < 180	x > 180
F3SA	3	x < 55	55 < x < 70	70 < x < 110	110 < x < 180	x > 182
F4SA	4	x < 60	60 < x < 80	80 < x < 94	94 < x < 182	x > 182
F5SA	5	x < 50	50 < x < 75	75 < x < 110	110 < x < 185	x > 185
PolyMIM	-	x < 115	115 < x < 135	135 < x < 150	150 < x < 200	x > 200

This behavior is attributed to the use of binder components with lower melting temperatures, as shown in Table 5.4. The lower melting points are primarily related to the shorter molecular chain lengths of the polymers used, which reduce thermal resistance and facilitate earlier softening and flow onset during heating.

7.3.2.1 Extrusion and Pellets fabrication depending on the SA rate

A series of feedstocks with varying SA content (0 to 5 vol.%) were tested for extrudability using a DSM micro-compounder. All compositions were processed at 110°C, 60 RPM, for 15 minutes.

Table 7.3: Summary table of Fused Filament Fabrication on DSM of feedstock with 0 to 5 vol.% of SA at 110°C, 60 RPM during 15 minutes (Y/N= Yes/No)

Composition	**SA**	**Extrudable**	**Informations**
	[vol.%]	[Y/N]	
F0SA0MC	0	Y	Fluid
F1SA	1	Y	Too fluid
F2SA	2	Y	Too fluid
F3SA	3	Y	Too fluid
F4SA	4	Y	Too fluid
F5SA	5	Y	Too fluid

As summarized in Table 7.3, every formulation was successfully extruded; however, all blends were described as overly fluid, particularly those containing SA concentrations from 1 to 5 vol.%. This high fluidity negatively affects the shape retention of the extrudate and indicates that formulation lacks sufficient structural consistency for 3D printing despite being extrudable at 110°C.

Figure 7.3a shows the extrusion behavior of the F5SA filament at 110°C and 60 RPM. The extrudate appears highly fluid and fails to retain its filament shape, instead collapsing under its own weight compared to PolyMIM feedstock at 180°C (Figure 7.3b).

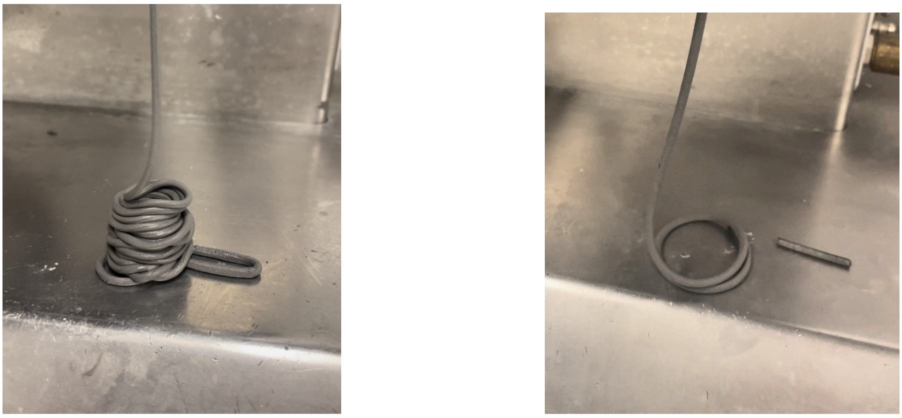

(a) F5SA at 110°C and 60 RPM: filament deforms under its own weight.

(b) PolyMIM at 180°C and 60 RPM: filament retains its shape.

Figure 7.3: Comparison of extruded filaments obtained with the DSM extruder: effect of formulation and processing temperature on shape retention.

This loss of dimensional stability is problematic for 3D printing applications, where consistent strand geometry is essential. Beyond 3 vol.% SA, the extruded filaments become too soft and deformable, indicating that 3 vol.% SA is the upper limit for maintaining sufficient shape retention in this formulation. In particular, the feedstock remains slightly malleable even at room temperature, which could be advantageous for filament fabrication in FDM-like systems, where continuous spooling and flexibility are beneficial. However, in pressure-assisted microextrusion (PAM) systems, this softness may hinder shape retention after extrusion and compromise dimensional accuracy, especially in unsupported sections or fine features.

7.3.3 Thermogravimetric analysis TGA

Thermogravimetric analysis was performed on the feedstock containing SA to assess whether the degradation temperature decreases with increasing SA content, as observed on the Kofler bench. The TGA results for the F5SA formulation are presented in Figure 7.4.

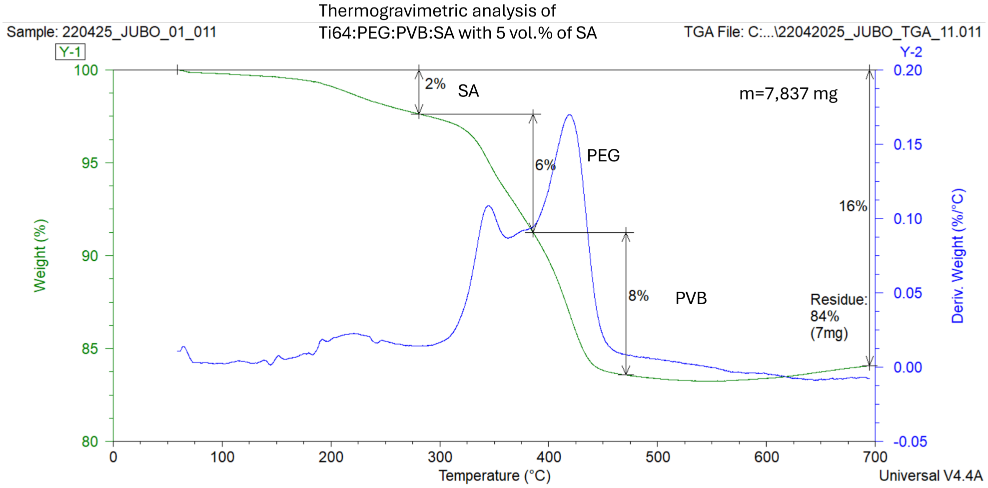

Figure 7.4: Themogravimetric analysis of F5SA

Stearic acid appears to degrade very rapidly, similarly to its behavior when analyzed individually (Appendix C), starting around 60–75°C. Likewise, PEG and PVB also seem to initiate degradation at temperatures consistent with their individual thermal profiles, approximately 300°C for PEG and around 380–390°C for PVB. The early degradation of stearic acid at such relatively low temperatures presents a significant challenge for the PAM process, as operational temperatures must exceed 60°C to ensure proper extrusion. Consequently, the onset of SA degradation at these working temperatures could compromise feedstock stability and overall print quality.

7.3.4 Selection of the optimal temperature for experimental tests

To reduce the number of experimental tests required for each feedstock formulation, the optimal testing temperature was determined based on rheological measurements. Specifically, stress versus shear rate curves were analyzed to simulate the flow conditions encountered during extrusion.

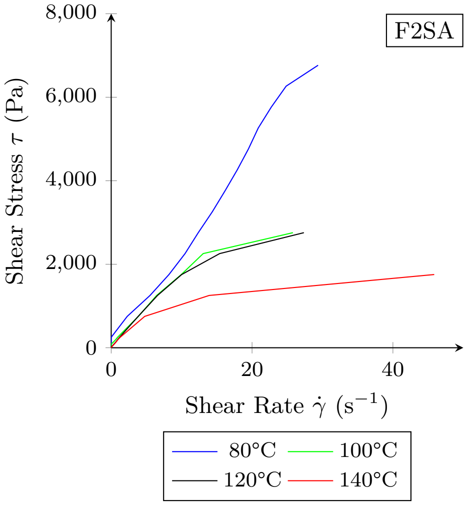

Figure 7.5: Shear stress τ vs shear rate $\dot{\gamma}$ for F2SA at 80, 100, 120, and 140°C.

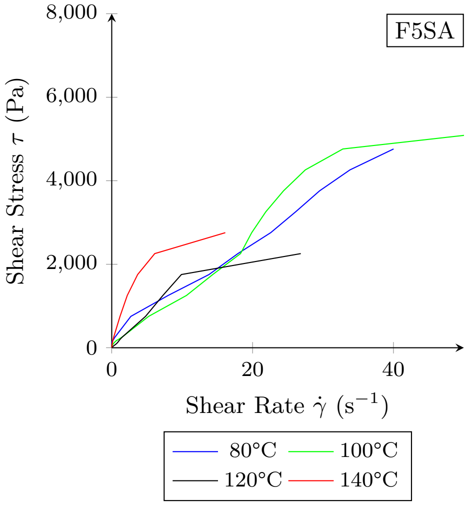

Figure 7.6: Shear stress τ vs shear rate $\dot{\gamma}$ for F5SA at 80, 100, 120, and 140°C

The rheological behavior of the F2SA and F5SA feedstocks, as illustrated in Figures 7.5 and 7.6, reveals a typical shear-thinning response, where shear stress increases non-linearly with shear rate. This behavior is consistent with polymer-based systems containing solid fillers and lubricants such as SA [230]. Interestingly, despite SA's well-known lubricating effect at low concentrations, F5SA exhibits higher shear stress than F2SA across all temperatures. This counterintuitive result can be explained by the saturation of interfacial sites at higher SA content, leading to the formation of a semi-crystalline or continuous phase that increases internal resistance to flow [95]. Consequently, the SA no longer acts purely as a lubricant but contributes to a more cohesive and viscous structure.

Temperature also plays a critical role in modulating flow behavior. As temperature increases from 80°C to 140°C, both feedstocks show a marked decrease in shear stress, indicating reduced viscosity. However, 120°C appears to be the optimal processing temperature, offering a balance between sufficient flowability and structural stability. At this temperature, the material exhibits manageable shear stress without signs of thermal degradation or excessive fluidity, which aligns with processing windows reported in powder injection molding literature [129]. Therefore, 120°C will be used as the reference temperature for all subsequent rheological analyses of SA-based feedstocks, ensuring consistency and relevance to practical processing conditions.

7.3.5 Effect of the addition of SA on rheological properties

In this section, the rheological behavior of various feedstocks composed of PEG/PVB (50/50) binder with different contents of SA at 120°C compared to commercial PolyMIM at 180°C reference. The objectif is to assess the impact of the addition of SA as plasticizer in the feedstock and determine the most adapted ratio of SA.

7.3.5.1 Shear Stress Response under Steady-State Flow Conditions

Figure 7.7 plots the shear stress as a function of shear rate for the same set of materials. This analysis is key for evaluating how feedstocks respond to deformation, with direct relevance to flow control during extrusion.

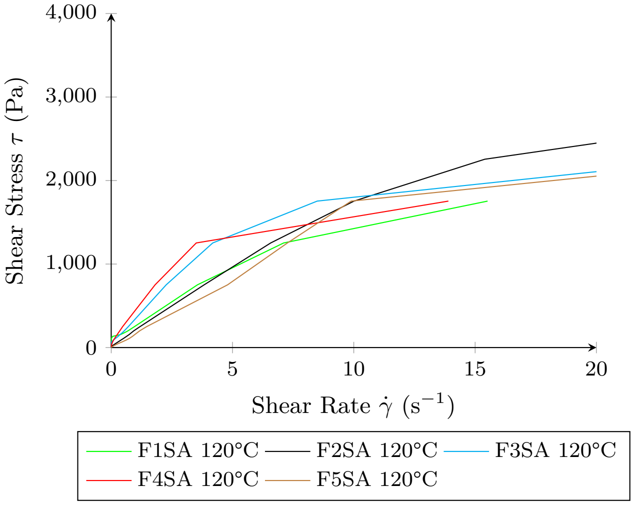

Figure 7.7: Zoomed view of shear stress τ vs shear rate $\dot{\gamma}$ for F1SA, F2SA, F3SA, F4SA, and F5SA at 120°C

All formulations presenting a pseudoplastic behavior as seen previously in Chapter 2, Figure 2.23. A typical nonlinear relationship is observed for all formulations, confirming their non-Newtonian nature. Most curves show increasing stress with increasing shear rate, though some, such as PolyMIM, exhibit a plateau or slight decrease at higher rates, possibly due to material ejection or degradation under testing. The elevated stress levels of PolyMIM compared to other samples reinforce its high viscosity and limited printability. The similar trends for F1SA to F5SA indicate that while SA improves dispersion, excessive content does not drastically alter the flow resistance beyond a threshold.

While steady shear analysis provides insights into flow resistance during extrusion, it does not capture time-dependent structural evolution under small deformations. To complement these results, oscillatory tests were performed to evaluate the stability of the internal structure over time and detect potential degradation or phase separation.

7.3.5.2 Time-Dependent Stability under Oscillatory Shear

Figure 7.8 presents the time evolution of complex viscosity under oscillatory conditions (τ= 10 Pa, f= 1 Hz) at 120°C for all SA-containing feedstocks and the PolyMIM control. This test assesses structural stability and possible degradation or rearrangement over time.

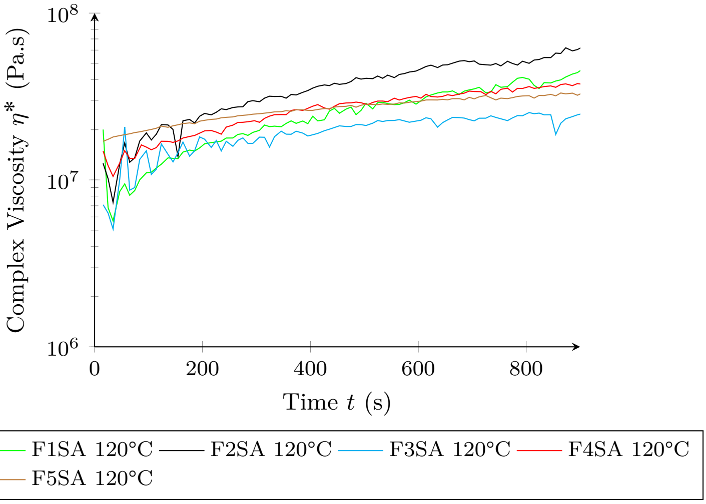

Figure 7.8: Evolution of complex viscosity η^* as a function of time at τ = 10 Pa and f = 1 Hz for F1SA, F2SA, F3SA, F4SA, and F5SA at 120°C

Viscosity trends show a rapid increase initially, followed by stabilization. The absence of significant downward drift suggests minimal thermal degradation or phase separation during the test window. PolyMIM displays the highest and most stable viscosity, which while advantageous for shape retention, may hinder extrusion. Among the PEG/PVB formulations, F5SA shows higher final viscosities, indicating strong network interactions. However, excessively high or low viscosities may compromise performance, highlighting the importance of balancing these interactions.

While time-resolved measurements assess structural stability under constant deformation, evaluating the response under increasing shear stress is equally important to understand the material's flow dynamics. For this purpose, complex viscosity was plotted as a function of shear stress to investigate shear-thinning behavior and flow adaptability under dynamic conditions.

7.3.5.3 Shear-Thinning Behavior and Flow Adaptability

Figure 7.9 presents the complex viscosity (η^*) as a function of shear stress (τ) at a fixed frequency of 1 Hz. This measurement provides insight into the feedstocks' shear-thinning behavior and their structural integrity under increasing deformation forces.

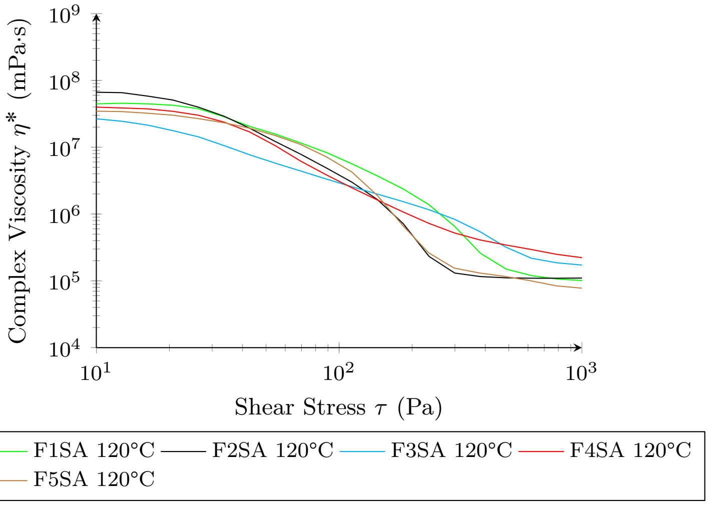

Figure 7.9: Complex viscosity η^* as a function of shear stress τ at $f = 1$ Hz for F1SA, F2SA, F3SA, F4SA, F5SA at 120°C

All curves demonstrate shear-thinning behavior, with viscosity decreasing as shear stress increases. This is a typical characteristic of viscoelastic polymer composites and is beneficial for material extrusion processes, as it allows easier flow under pressure. Among the formulations, PolyMIM exhibits significantly higher viscosity across all stress levels, indicative of its stronger interparticle and polymer-polymer interactions. The F0SA0MC and F5SA formulations also show relatively high viscosities, likely due to insufficient lubrication or poor particle wetting, which can impact processability and layer adhesion. Conversely, intermediate formulations like F1SA and F2SA maintain moderate viscosities, potentially offering a balance between flowability and mechanical cohesion.

To complement the steady-state shear measurements, oscillatory tests were conducted under varying frequencies to assess the dynamic viscoelastic properties of the formulations.

7.3.5.4 Frequency-Dependent Viscoelastic Properties

The frequency sweep at constant shear stress (10 Pa) in Figure 7.10 investigates the time-dependent deformation behavior (viscoelasticity) of the feedstocks. Complex viscosity is plotted against frequency (f) on a log-log scale.

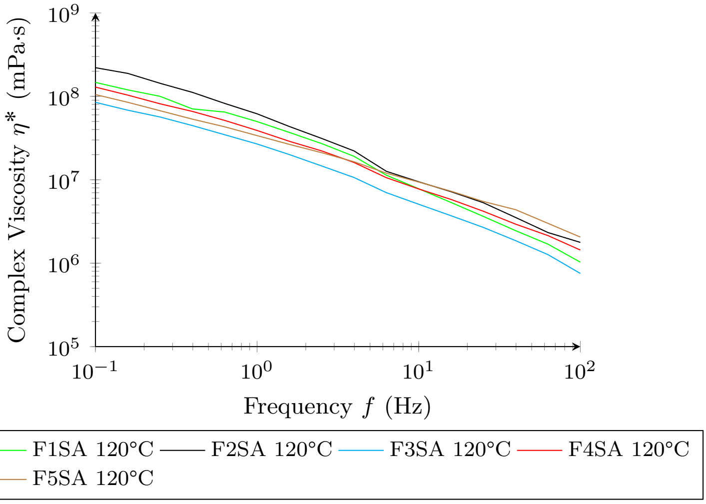

Figure 7.10: Complex viscosity η^* as a function of frequency f at fixed shear stress $\tau = 10$ Pa for F1SA, F2SA, F3SA, F4SA, and F5SA at 120°C

All formulations exhibit decreasing viscosity with increasing frequency, characteristic of shear-thinning and polymer relaxation mechanisms. At low frequencies, the polymer chains are more entangled and resist deformation, resulting in higher viscosities. At higher frequencies, the chains align with the deformation, reducing resistance. PolyMIM remains consistently more viscous across the frequency range, suggesting a more entangled or less mobile network. Among SA-containing samples, F2SA and F3SA appear to offer a good compromise between flexibility and cohesion, showing moderate and stable viscosity profiles.

In addition to frequency-dependent viscoelasticity, understanding how the feedstocks behave under varying shear rates is essential to evaluate their processability. For this purpose, the apparent viscosity η was plotted as a function of shear rate, providing further insight into flow resistance under extrusion-relevant conditions.

7.3.5.5 Apparent Viscosity Behavior under Varying Shear Rates

The log-log plot in Figure 7.11 illustrates the apparent viscosity (η) as a function of shear rate ($\dot{\gamma}$).

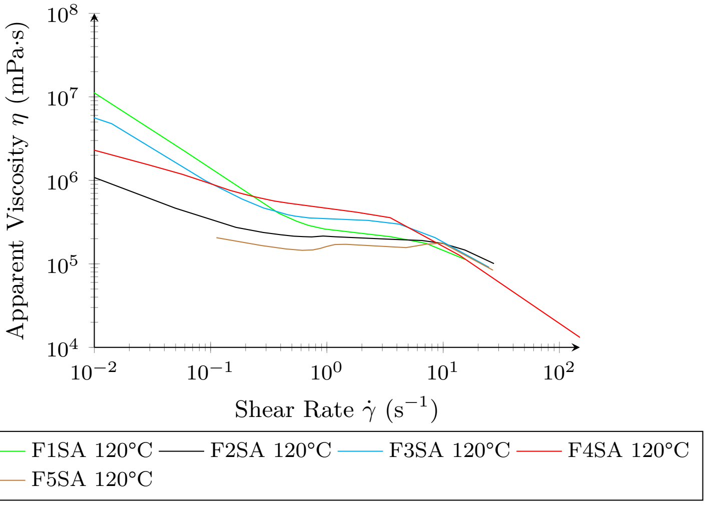

Figure 7.11: Log-log plot of apparent viscosity η as a function of shear rate $\dot{\gamma}$ for F1SA, F2SA, F3SA, F4SA, and F5SA at 120°C

All materials demonstrate pronounced shear-thinning behavior, confirming that higher shear rates during extrusion will ease material flow confirming their applicatbility for extrusion 3D printing as seen in Chapter 2 Figure 2.23. PolyMIM maintains significantly higher viscosities across the range, affirming its poor extrusion compatibility. F1SA to F4SA display increasingly favorable viscosities with more SA, suggesting improved dispersion or reduced interfacial friction. F5SA, however, reaches a lower viscosity plateau, implying over-lubrication or potential particle demixing.

While apparent viscosity provides a macroscopic view of shear-thinning behavior, it does not fully capture the material's viscoelastic character under stress. To further assess the balance between elastic and viscous responses, stress sweep tests were performed to determine storage (G') and loss (G") moduli and identify yielding points

7.3.5.6 Stress-Dependent Viscoelastic Properties and Yield Behavior

Figures 7.12 evaluate viscoelastic properties using stress sweeps. Storage modulus (G') reflects elastic behavior (solid-like response), while loss modulus (G") reflects viscous behavior (fluid-like response). The crossover point where G" surpasses G' indicates yielding and the onset of flow.

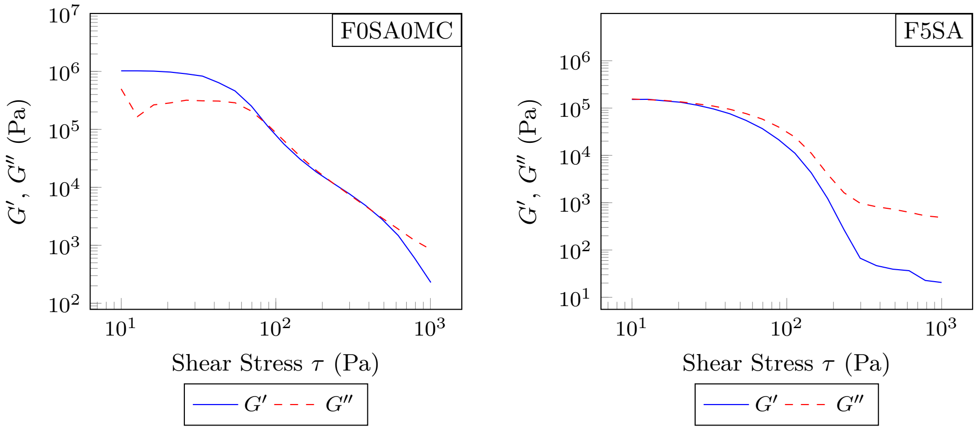

(a) F0SA0MC at 120°C

(b) F5SA at 120°C

Figure 7.12: Comparison of storage (G') and loss (G'') moduli as a function of shear stress for (a) F0SA0MC and (b) F5SA at 120°C.

All formulations exhibit typical viscoelastic transitions, as illustrated in the figures provided in Appendix D. F0SA0MC and F1SA maintain high storage modulus (G') at low shear stress, indicating a predominantly solid-like behavior. As the SA content increases, G' decreases and the loss modulus (G") becomes dominant at lower stress levels, reflecting a reduction in structural rigidity and a facilitated onset of flow. These observations are consistent with previously reported viscosity trends. Therefore, the analysis of G'/G" crossover provides valuable insight into the internal structure of each formulation and highlights the role of SA in modulating the mechanical relaxation behavior of the feedstocks. For F5SA the second plateau may indicates phase separation suggesting a too high content of SA as seen in the literature [91].

7.3.5.7 Conclusion of the addition of SA on rheological properties

The rheological characterization of PEG/PVB-based feedstocks with varying SA content (1 to 5 vol.%) has revealed critical insights into their flow behavior, viscoelasticity, and processing suitability. Through a combination of shear rate-dependent viscosity, oscillatory testing, and modulus analysis, it becomes evident that SA acts as both a plasticizer and a dispersion aid, modulating polymer-particle and particle-particle interactions.

At low SA content (F1SA, 1 vol.%), improvements in flowability and moderate viscosity were observed, contributing to enhanced extrudability without compromising too much on cohesion. As the SA content increases to F2SA and F3SA (2–3 vol.%), a viscosity optimum appears: these formulations demonstrate balanced shear-thinning behavior, favorable viscoelastic transitions, and stable complex viscosity over time.

This suggests efficient particle lubrication and reduced interfacial friction, essential for print fidelity and green body integrity.

However, beyond 3 vol.% SA (F4SA, F5SA), viscosity becomes excessively low and viscoelastic moduli decrease significantly, indicating potential over-lubrication or phase separation. These effects may lead to mechanical weakness, poor filament cohesion, or demixing during processing.

Therefore, formulations around 2–3 vol.% SA (F2SA, F3SA) appear optimal, offering a trade-off between printability, shape retention, and mechanical robustness. Compared to PolyMIM, which shows significantly higher viscosity and elastic dominance, these optimized PEG/PVB formulations exhibit superior rheological profiles for PAM, especially in terms of shear-thinning behavior and time-stable viscosity.

7.3.6 Selection of the SA content for 3D printing tests

The present feedstock design builds upon the formulation proposed by Eickhoff et al. [91], which encountered difficulties with MEX due to phase separation issues. In their study, 5 wt.% of SA relative to the total binder content was incorporated, replacing an equivalent mass fraction of PEG. This corresponds to approximately 6.4 vol.% of SA—likely contributing to the instability observed during processing. Furthermore, their extrusion trials were conducted at nozzle temperatures ranging from 180°C to 230°C, a range that exceeds the degradation onset temperature measured here ($\approx$ 185°C) and results in excessive fluidity, as confirmed during our DSM extrusion tests. These conditions are unsuitable for MEX, which requires a more controlled rheological profile.

To address these limitations, the current study explores a PEG with a molecular weight of 12,000 g/mol and optimizes the SA content. The formulation selected for 3D printing trials contains 3 vol.% SA. Rheological measurements revealed no substantial differences between the 2 and 3 vol.% SA formulations. However, complementary Kofler bench assessments indicated that F3SA formulation demonstrated slightly greater softness at lower temperatures. This enhanced low-temperature deformability is advantageous for low-temperature printing, potentially improving process reliability and energy efficiency.

Moreover, given that MC—a known solidening agent—will be introduced in the final formulation, selecting a slightly more lubricated system (i.e., 3 vol.% SA) provides a safer rheological baseline. It helps ensure that the overall viscosity remains within a printable range once MC is added. Thus, the 3 vol.% SA formulation appears to strike the best balance between flowability, structural integrity, and MEX compatibility.

7.3.7 3D Printing

3D printing trials were conducted using the feedstock containing 3 vol.% of stearic acid (F3SA) to evaluate its printability and determine whether successful part fabrication could be achieved, in contrast to the findings reported by Eickhoff et al. [91].

Multiple tests were performed at varying nozzle and bed temperatures to identify optimal processing conditions. These experiments aimed to assess the material's flow behavior, layer adhesion, and dimensional stability during deposition. The results provide insights into the feasibility of using F3SA in PAM and contribute to understand the influence of formulation on printability.

It proved impossible to obtain a complete and undeformed printed part (Figures 7.13 and 7.14) due to the excessive softness and rapid melting of the filament, even at the lowest tested extruder and nozzle temperatures of 60°C and 90°C, respectively. Under these conditions, the extrusion screw appeared to shear the material rather than effectively pushing it forward.

Figure 7.13: First try to print bending part with Ti6:PEG:PVB:SA 3 vol.% feedstock

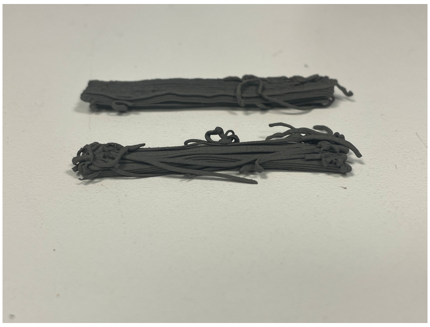

Figure 7.14: Printing test of TiPEGPVBSA with 3 vol.% of SA

These outcomes were anticipated based on previous thermogravimetric analysis, Kofler bench tests, and rheological measurements, all of which indicated the formulation's inadequate mechanical stability and excessive fluidity at low temperatures. Although lowering the SA content from 3 vol.% to 2 vol.% might marginally enhance printing behavior, such a slight adjustment is unlikely to produce significant improvements, given the minimal differences observed in preliminary rheological evaluations.

7.3.8 Conclusions for SA content

The feedstock containing only SA proved to be too soft for 3D printing. With an extruder operating at a minimum temperature of 60°C, the material was too fluid to be properly sheared and pushed through the system. As a result, the printed part failed to retain its shape. Even at a reduced SA content of 2 vol.%, the behavior remained unchanged. This was confirmed by the shear stress versus shear rate graph, which showed values too low to support adequate material cohesion.

Kofler bench tests revealed that the individual components—PEG, PVB, and SA—melt at relatively low temperatures, which further explains the lack of mechanical integrity. No thermal imaging measurements were conducted on this formulation, as the material was quickly deemed unsuitable for PAM due to its inability to solidify and maintain structure. Moreover, TGA exhibits that SA has a degradation temperature very low (60-75°C) which is incompatible with PAM machine.

To address these limitations, a material with a significantly higher melting point is required—one that can reinforce the blend by increasing its viscosity at processing temperatures. Methylcellulose was introduced for this purpose, as it begins to soften only around 240–250°C, providing the necessary thermal and mechanical stability for effective extrusion and shape retention.

The following section aims to evaluate, similarly to the case of stearic acid, the effect of MC addition on the Ti6Al4V, PEG and PVB feedstock formulation in the absence of any surfactant. The objective is to assess how MC influences the rheological and mechanical behavior of the feedstock, and to determine whether an optimal concentration exists for AM via PAM.

Although the optimal concentration of SA was previously determined to improve flowability and dispersion, initial formulations involving MC were intentionally prepared without SA to isolate and better understand the specific rheological contribution of MC.

This approach allows for a clear evaluation of how MC, a known thickening agent and rheology modifier, alters the viscoelastic properties, yield behavior, and shear response of the PEG/PVB-based feedstock. Including SA at this stage could have masked or interfered with the characterization of MC's effects due to their potentially opposing roles—SA being a plasticizer and MC a thickener.

Therefore, SA was temporarily excluded to:

- Avoid confounding effects between SA and MC on viscosity and flow.
- Clarify MC's independent impact on the feedstock's printability and shape retention.
- Establish a baseline for MC-containing systems prior to co-formulating with SA in the final optimization phase.

7.4 Addition of Methylcellulose Impact Assessment

The new composition used a binder composed of PEG, PVB and Methylcellulose MC as shown in Table 7.4. MC supposed to be a solidener agent, stabiliser in solution. No study has been made for MC with organic polymer without water. One of the objectives is to determine if MC have the same behavior than in solution.

Table 7.4: Composition and nomenclature of each feedstock formulations with SA or MC content

Composition	**Ti6Al4V**	**PEG**	**PVB**	**MC**
	[vol.%]	[vol.%]	[vol.%]	[vol.%]
F0SA0MC	55	22.5	22.5	0
F1MC	55	22.0	22.0	1
F2MC	55	21.5	21.5	2
F3MC	55	21.0	21.0	3
F4MC	55	20.5	20.5	4
F5MC	55	20.0	20.0	5

The formulations described in this section maintain the same contents of Ti6Al4V, PEG, and PVB as in the previous batches. The only variation lies in the absence of SA and the progressive addition of MC from 0 to 5 vol.%.

The first objective is to verify whether, despite the absence of SA and the presence of MC, the mixing process still proceeds correctly and reaches a stable state over time. It is also essential to assess whether the metallic particles are adequately mixed and fully coated by the binder matrix, ensuring homogeneous dispersion and proper wetting of the Ti6Al4V particles.

7.4.1 Impact of MC rate on mixing torque

Figure 7.15 shows the evolution of mixing torque for formulations containing MC as a function of temperature and MC content, ranging from 0 to 5 vol.%. MC acts as a solidening agent, as evidenced by the consistent increase in torque with higher MC concentrations. This trend can be attributed to the intrinsic properties of MC, a high molecular weight, water-soluble cellulose derivative. MC is known to form extensive hydrogen-bonding networks within polymer matrices [80, 82, 85], which enhance intermolecular cohesion and increase the system's resistance to shear. As a result, the addition of MC raises the viscosity of the molten feedstock and reinforces its structural integrity during mixing.

The temperature range of 110–120°C appears optimal for processing these formulations. In this window, the feedstock exhibits favorable rheological characteristics: it mixes uniformly, stabilizes rapidly, and maintains a workable viscosity that is neither too high (causing excessive torque) nor too low (resulting in poor structural definition). Additionally, cleaning the mixing chamber remains manageable in this range.

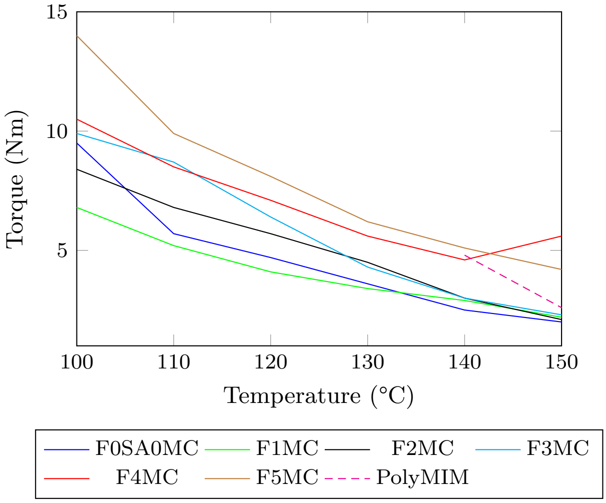

Figure 7.15: Torque of feedstocks with MC (0 to 5 vol.%) formulations depending on the temperature

Above 150°C, the feedstock becomes overly fluid, which may be due to partial thermal degradation or excessive plasticization of the binder components—particularly PEG—leading to phase separation and residue buildup. Below 110°C, torque increases sharply due to insufficient softening of the binder matrix, making the mixture more resistant to shear and harder to homogenize. This higher resistance can hinder downstream extrusion by promoting irregular flow or incomplete filler dispersion.

After assessing the impact of MC addition on hot powder mixing through torque measurements (where an increase in torque indicated a thickening of the feedstock without reaching the high values observed for the commercial PolyMIM formulation, which is reassuring) and verifying that the powder mixing remained homogeneous (i.e., titanium particles remained fully coated by the binder), the next objective was to evaluate whether MC addition negatively affects feedstock extrudability.

In particular, the aim was to determine the maximum MC content that maintains sufficient viscosity for extrusion without inducing brittleness in the material.

7.4.2 Impact of MC on thermal stability and processability of the feedstock

Figure 7.16 presents a visual comparison of the thermal behavior of feedstocks containing either 5 vol.% MC (a) or 5 vol.% SA (b), as assessed using the Kofler bench method. The pellets containing MC exhibited significantly higher resistance to thermal deformation compared to those with SA alone. Even at elevated temperatures, the MC-based pellets retained their structural integrity, whereas the SA-based pellets began to soften and collapse.

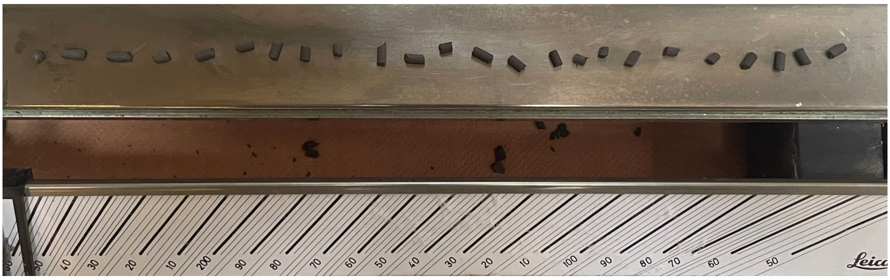

(a) MC 5 vol.% before crushing pellets

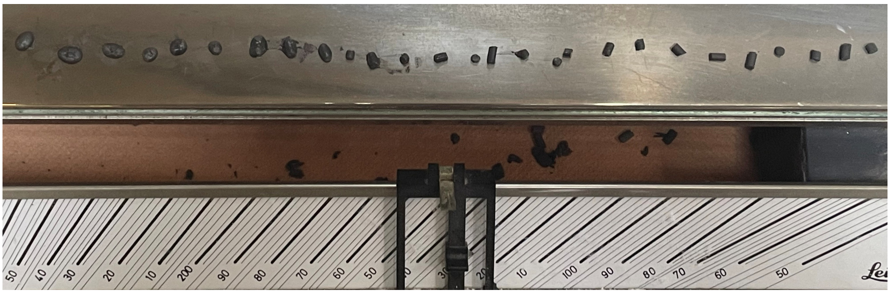

(b) SA 5 vol.% before crushing pellets

Figure 7.16: Kofler bench comparison of feedstocks containing 5 vol.% methylcellulose (left) and 5 vol.% stearic acid (right) before crushing

This behavior can be attributed to the presence of MC, which acts as a thermally resistant structural additive. As the MC content increases, the softening and fusion temperature of the feedstock also increase, indicating enhanced thermal stability. MC's polymeric network—formed through hydrogen bonding—contributes to a stiffer matrix, which delays melting and inhibits deformation under heat.

Among the different MC concentrations tested, formulations containing 1–3 vol.% MC provided the broadest processing temperature windows. These compositions were soft enough to allow for adequate shaping yet resistant to premature flow or collapse. Additionally, MC appears to slightly raise the onset of thermal degradation, further extending the safe thermal processing range of the feedstock.

These results highlight the dual benefit of MC in PAM feedstock formulations: improved mechanical integrity at elevated temperatures and an expanded thermal processing window, both of which are advantageous for stable extrusion and print quality.

Methylcellulose is known to exhibit thermogelling behavior, meaning it undergoes a sol–gel transition upon heating. In aqueous or partially solvated systems, MC initially behaves as a viscous liquid but forms a gel network when heated beyond a critical temperature, typically between 50 and 80°C, depending on molecular weight and concentration [81, 248].

In the context of thermoplastic feedstocks, this property can contribute to the formation of a pseudo-network structure at elevated temperatures, which improves dimensional stability and resistance to deformation[80].

The thermal processing window of MC feedstocks was assessed using the Kofler bench, as shown in Figure 7.17.

Figure 7.17: Working range (red) of pellets with varying MC content from 0 to 5 vol.% determined on Kofler Bench

With increasing MC content (from 0 to 5 vol.%), the softening and flowing zones of the pellets shifted progressively toward higher temperatures. This indicates that MC increases the thermal resistance of the feedstock without significantly narrowing the workable range. Up to 3 vol.% MC, the pellets exhibited homogeneous softening and sufficient cohesion across a stable temperature interval, suggesting adapted behavior for printing.

At 4 and 5 vol.%, the material began to show signs of partial fragmentation or uneven flow within the softened zone, which may be attributed to local stiffening or excessive viscosity. Nevertheless, a working range was still observable even at 5 vol.%, although at elevated temperatures.

The results obtained from the Kofler bench test are summarized in Table 7.5.

Table 7.5: Fusion temperatures of MC compositions determine by Kofler bench

Composition	**MC**	$T_{\text{malleability}}$	T_{fusion}	T_{NoSticky}	T_{sticky}	$T_{\text{degradation}}$
	[vol.%]	[°C]	[°C]	[°C]	[°C]	[°C]
F0MC	0	$x < 60$	$60 < x < 80$	$80 < x < 130$	$130 < x < 175$	$x > 175$
F1MC	1	$x < 55$	$55 < x < 76$	$76 < x < 142$	$142 < x < 210$	$x > 210$
F2MC	2	$x < 66$	$66 < x < 94$	$94 < x < 140$	$140 < x < 212$	$x > 212$
F3MC	3	$x < 72$	$72 < x < 106$	$106 < x < 135$	$135 < x < 210$	$x > 210$
F4MC	4	$x < 86$	$86 < x < 126$	$126 < x < 164$	$164 < x < 220$	$x > 220$
F5MC	5	$x < 100$	$100 < x < 130$	$130 < x < 185$	$185 < x < 230$	$x > 230$

As previously done for stearic acid, the feedstocks developed in this section are subjected to rheological measurements to assess the influence of MC addition on their behavior. If the rheological properties indicate a beneficial effect of MC for PAM processing, then the optimal MC content will also be identified accordingly.

The next section investigates the influence of MC content on the rheological behavior of PEG/PVB-based feedstocks, with the goal of identifying the impact of MC on the flow behavior of the feedstock and the optimal MC concentration adapted for extrusion-based AM (PAM). Unlike SA, which acts as a lubricant and typically reduces viscosity, MC is known to act as a solidening agent. Understanding the impact of varying MC content (from 0 to 5 vol.%) on viscosity, viscoelasticity, and structural stability is critical to ensuring a suitable flow behavior for 3D printing.

7.4.3 Extrusion behavior depending on the MC rate

The extrusion temperature for feedstocks with MC (contents ranging from 0 to 5 vol.%) was fixed at 120°C, with a screw speed of 60 RPM. This temperature was selected based on torque analysis and direct visual inspection of the mixture inside the Brabender mixer, both of which indicated effective and homogeneous dispersion of the metallic powder within the binder system at this processing condition.

Table 7.6: Summary table of Fused Filament Fabrication on DSM of feedstocks with 0 to 5 vol.% of MC at 120°C, 60 RPM during 15 minutes (Y/N = Yes/No)

Composition	**MC**	**Extrudable**	**Informations**
	[vol.%]	[Y/N]	
F0SA0MC	0	Y	Too fluid
F1MC	1	Y	good
F2MC	2	Y	good
F3MC	3	Y	good
F4MC	4	Y	Brittle
F5MC	5	Y	Brittle

Feedstocks containing from 0 to 5 vol.% MC were all extrudable at a temperature of 120°C and a screw speed of 60 RPM. However, blends with higher MC concentrations (4 and 5 vol.%) exhibited brittleness (Table 7.6), breaking under their own weight at this extrusion temperature.

Additionally, formulations containing between 4 and 5 vol.% MC were noticeably more challenging to pelletize, indicating that methylcellulose not only increases viscosity but also significantly hardens the feedstock, making it substantially less malleable.

Figure 7.18: Extruded filament with 3 vol.% of MC

The formulation with 3 vol.% MC appears particularly promising, offering a favorable balance between extrusion viscosity and mechanical robustness during handling (Figure 7.18).

7.4.4 Thermogravimetric analysis TGA

Figure 7.19 presents the thermogravimetric analysis of F5MC. The green curve shows the weight loss as a function of temperature, while the blue curve corresponds to the derivative weight loss (DTG). Two main degradation steps are observed.

The first mass loss occurs between approximately 200°C and 320°C and accounts for about 9% of the initial mass. This step can be attributed to the decomposition of PEG and MC. Based on the initial formulation—55 vol.% Ti6Al4V, 20 vol.% PEG, 20 vol.% PVB, and 5 vol.% MC—the calculated mass fractions are approximately 7.7% PEG and 2.2% MC, totaling 9.9%, which is in good agreement with the measured value. PEG is known to degrade around 250–320°C, and MC typically decomposes in a similar range, justifying their overlapping thermal events.

The second degradation step, starting near 320°C and ending around 470°C, leads to a further 7% mass loss and is attributed to the decomposition of PVB. This aligns closely with the theoretical PVB content of 7.3%. PVB generally decomposes in the range of 350–450°C, which matches the observed event in the DTG curve.

The final residue at 600°C is approximately 84%, which corresponds well with the calculated Ti6Al4V mass fraction of 82.8%. The slight difference could be due to incomplete degradation of organics or minor carbonaceous residue formation.

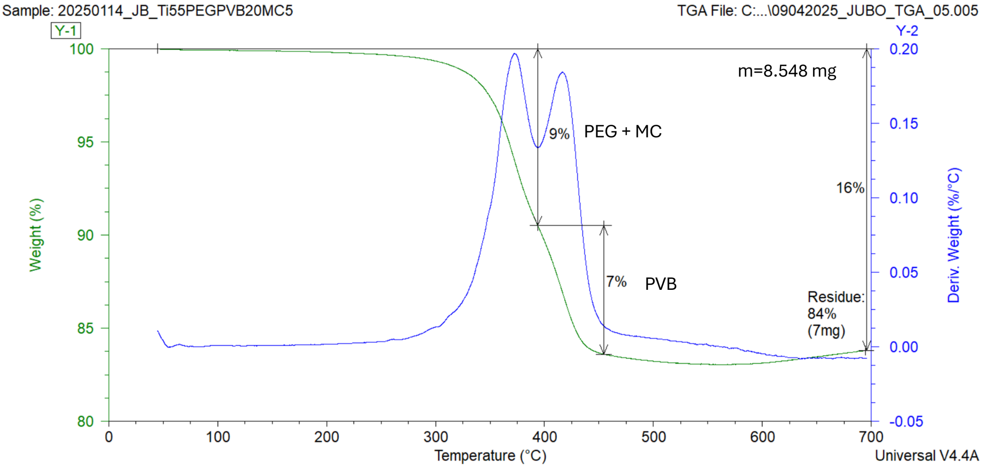

Figure 7.19: TGA of F5MC from 0 to 700°C at 10°C/min.

7.4.5 Selection of the optimal temperature for experimental tests

The same methodology as for SA was followed to determine the ideal temperature for feedstocks with MC.

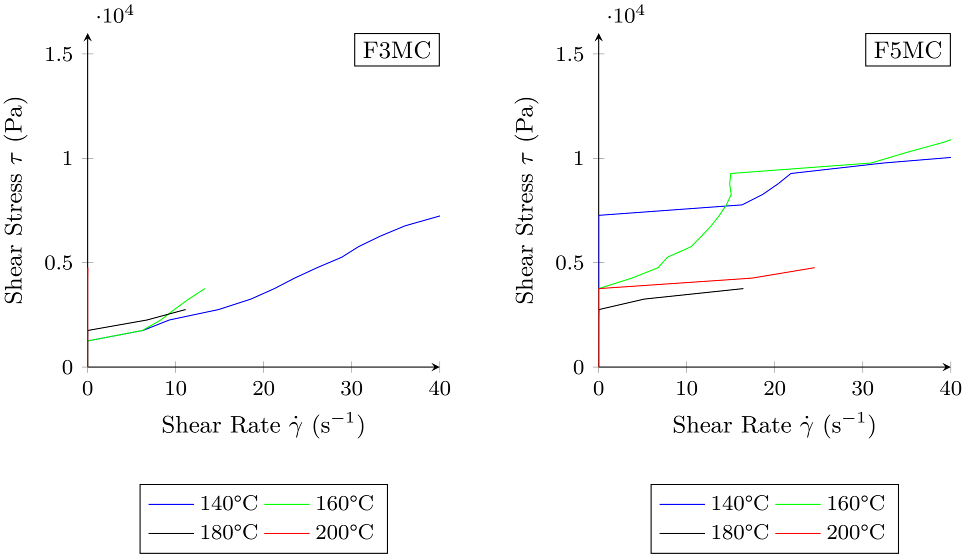

Figure 7.20: Shear stress τ as a function of shear rate $\dot{\gamma}$ for F3MC (left) and F5MC (right) at 140, 160, 180 and 200°C.

Figure 7.20 illustrates the shear stress τ as a function of shear rate $\dot{\gamma}$ for the F3MC (left) and F5MC (right) formulations at 140°C, 160°C, 180°C, and 200°C. As previously conducted for the SA-based formulations, the same rheological methodology was employed to identify the optimal processing temperature range for MC-based feedstocks.

It is important to note that the F3MC curve at 200°C does not appear in Figure 7.20 (left). This omission is due to a rapid increase in shear rate beyond 0.03 s^{-1}, which triggered a safety protocol in the rheometer, thereby halting data acquisition.

The data show that increasing temperature generally leads to a reduction in shear stress at a given shear rate, indicating improved flow behavior. However, above 180°C, the reduction in viscosity becomes marginal or may lead to early signs of degradation or instabilities, especially visible in the low-shear regions.

The Kofler bench test results were also considered in selecting the optimal temperature. These provided complementary thermal insights that helped to confirm the onset of softening and flow initiation under controlled thermal gradients.

For the most promising binder volume fractions (i.e., 2 and 3 vol.% MC), the shear stress profiles indicate that 180°C offers the best compromise between adequate flowability and thermal stability, making it the most appropriate temperature for comparative rheological analysis. The lower concentrations (1 and 2 vol.%) also display acceptable flow behavior at this temperature, although 1 vol.% begins to approach the lower limit of acceptable viscosity for extrusion.

In conclusion, 180°C was selected as the reference temperature for further rheological comparison of MC-containing formulations, in line with the approach used for other binder systems.

Once the reference temperature was established, the next step involved assessing the influence of MC content on the rheological properties of the feedstocks. Since MC is known for enhancing structural stability and modifying flow resistance, its addition can significantly impact the processability and print quality of highly filled formulations. Therefore, a detailed rheological study was conducted to evaluate how varying MC volume fractions—from 0 to 5 vol.%—affect the steady-state and dynamic flow behavior. The following analyses aim to identify an optimal MC concentration that ensures both low flow resistance during extrusion and sufficient cohesion for shape retention post-deposition. The results are presented through shear stress, viscosity, and viscoelastic moduli profiles under processing-relevant conditions.

7.4.6 Effect of MC addition on rheological properties

7.4.6.1 Shear Stress Response under Steady-State Flow Conditions

Figure 7.21 below characterizes the flow behavior of each formulation with a methylcellulose content ranging from 0 to 5 vol.% by plotting the shear stress (τ) depending on the shear rate ($\dot{\gamma}$). The goal is to determine whether the materials exhibit Newtonian, shear-thinning, or shear-solidening behavior to assess the flow initiation (yield stress) and the overall resistance of the feedstocks to deformation under increasing shear rates — crucial parameters for extrusion-based 3D printing.

All feedstocks show typical non-Newtonian behavior, with increasing stress at rising shear rates, reflecting shear-thinning rheology. Compared to the high shear resistance of PolyMIM (almost constant shear stress of $\approx$ 10,000 Pa), the formulations containing MC exhibit much lower stress values, indicating significantly improved flowability — a desirable trait for 3D printing. For instance, F3MC and F5MC maintain stress levels below 5,000 Pa across the shear rate range.

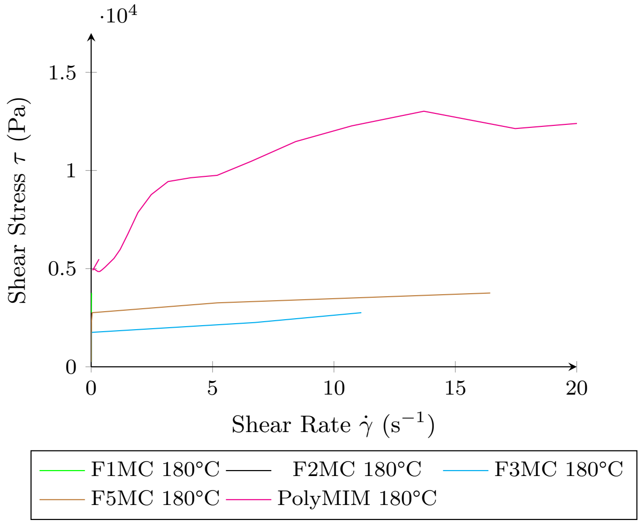

Figure 7.21: Shear stress τ as a function of shear rate $\dot{\gamma}$ for F1MC, F2MC, F3MC, F5MC, and PolyMIM at 180°C.

It is important to highlight two key points regarding Figure 7.21.

Firstly, the F1MC and F2MC samples are not visible in the plotted data due to an accelerated shear rate ramp, which increased from 0.01 s^{-1} to over 200 s^{-1} too quickly. As a result, insufficient data was captured at lower shear rates, preventing meaningful analysis of their flow behavior.

Secondly, the F4MC sample displays anomalous behavior, characterized by a sharp rise in stress—reaching approximately 44,000 Pa at very low shear rates (0.001 $\dot{\gamma}$)—followed by a plateau. This profile is uncharacteristic and inconsistent with general rheological trends. It likely indicates a preparation defect, such as poor dispersion of MC or binder agglomeration, rather than an intrinsic property of the formulation. In contrast, the F5MC sample returns to expected stress levels, supporting the hypothesis of a localized processing error in F4MC.

Therefore, due to significant issues encountered during testing—such as material instability and the production of unusable results—the F4MC formulation will be excluded from the subsequent figures and analyses.

7.4.6.2 Time-Dependent Stability under Oscillatory Shear

Figure 7.22 exhibits the time sweep of MC feedstocks, conducted at constant stress and frequency. Tracking the stability of the formulations over a fixed duration helps determine whether structural relaxation, polymer network rearrangement, or thermal degradation occurs under processing conditions. This is crucial for assessing whether MC incorporation promotes time-dependent rheological instability or contributes to a stable extrusion window.

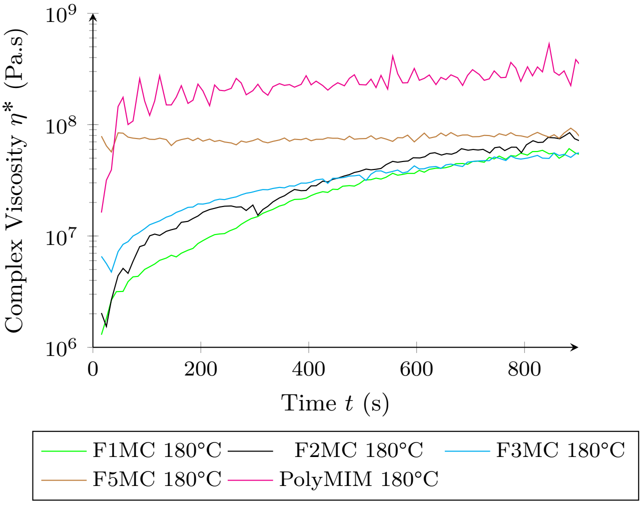

Figure 7.22: Evolution of complex viscosity η^* as a function of time at $\tau = 10$ Pa and $f = 1$ Hz for F1MC, F2MC, F3MC, F5MC, and PolyMIM at 180°C.

The F3MC (cyan), F2MC (black), and F5MC (brown) formulations display moderate and progressive increases in viscosity over time, reflecting gradual microstructural development. F1MC (green) and F0SA0MC (blue), particularly the latter tested at 140°C, show the lowest viscosities with limited time evolution. This highlights the influence of both formulation composition and temperature on the viscoelastic behavior. The PolyMIM feedstock (magenta curve) shows a stable and high viscosity around 10^8 Pa·s, indicating a well-established internal network and excellent time stability.

7.4.6.3 Shear-Thinning Behavior and Flow Adaptability

The graph presented in Figure 7.23 shows the complex viscosity (η^*) of formulations with varying MC contents as a function of applied shear stress at 120°C. The aim is to evaluate the evolution of viscosity under increasing mechanical solicitation and to assess whether a yield point can be identified. Detecting such a point is critical for understanding the transition from a solid-like to a flowable state, particularly relevant for extrusion-based 3D printing where controlled yield behavior ensures dimensional fidelity.

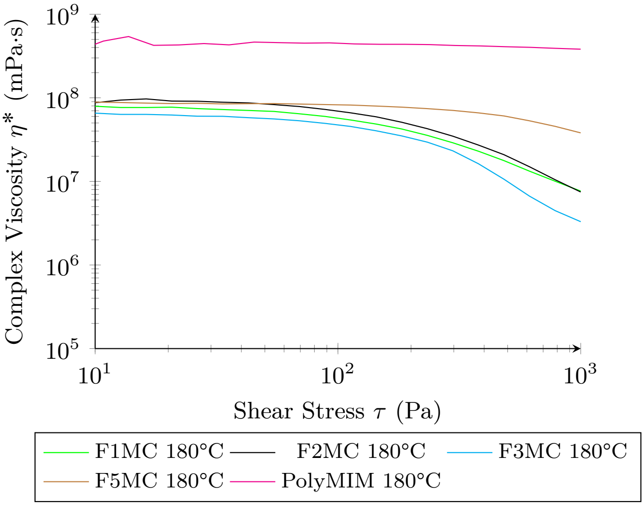

Figure 7.23: Complex viscosity η^* as a function of shear stress τ at $f = 1$ Hz for F1MC, F2MC, F3MC, F4MC, F5MC at 180°C and PolyMIM at 180°C.

The feedstock F0SA0MC, measured at 140°C, exhibits a significantly lower viscosity than the other formulations and a pronounced shear-thinning behavior, indicating limited structural integrity at this temperature. In contrast, the formulations F1MC, F2MC, and F3MC display nearly identical rheological behavior over the entire shear stress range, suggesting that increasing the MC content from 1% to 3% has a limited effect on viscosity under these conditions. Interestingly, F5MC presents a similar viscosity to F1MC–F3MC up to approximately 10^2Pa, but then maintains a more stable viscosity at higher shear stresses. This plateau suggests a more robust network structure or increased resistance to shear-induced breakdown at higher MC content [122]. As expected, the PolyMIM reference shows a much higher and almost constant viscosity across the entire range, reflecting its highly filled and industrially optimized composition. Overall, F1MC to F3MC offer equivalent rheological performance, while F5MC may provide added stability under high shear conditions [249].

7.4.6.4 Frequency-Dependent Viscoelastic Properties

By plotting the viscoelastic properties against frequency (Figure 7.24), it is possible to discern whether the feedstock behaves more like a liquid—dominated by viscous (loss modulus) behavior—or more like a solid—dominated by elastic (storage modulus) behavior. This distinction is particularly valuable for optimizing interlayer adhesion and minimizing print defects during material deposition, as a balanced viscoelastic response can enhance both flowability and shape retention during printing.

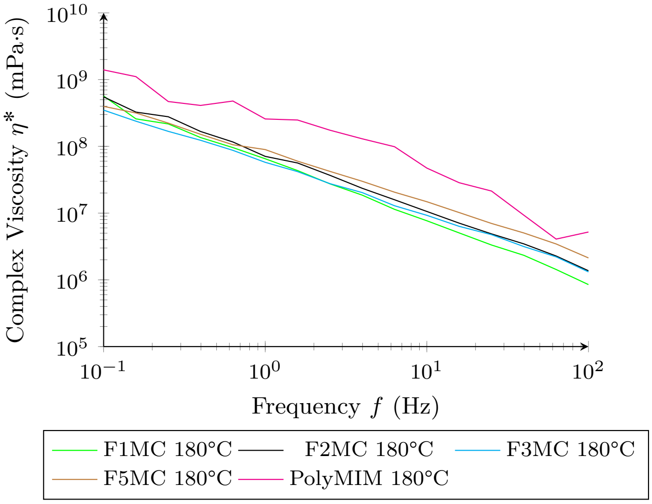

Figure 7.24: Complex viscosity η^* as a function of frequency f at fixed shear stress $\tau = 10$ Pa for F1MC, F2MC, F3MC, F5MC and PolyMIM at 180°C.

As shown in Figure 7.24, viscosity decreases with increasing frequency, reflecting the relaxation behavior of the polymer chains. Research on highly filled materials (such as metal or ceramic composites) shows that the complex viscosity (η^*) decreases with increasing frequency, due to polymer relaxation. However, the viscosity remains elevated when the filler content is high. This indicates that a well-entangled polymer network is essential to maintain cohesion both during and after extrusion [250].

Among the tested formulations, those with high filler content consistently exhibit elevated complex viscosity (η^*) across the frequency spectrum, indicating excellent dimensional stability and shape retention during deposition. In contrast, formulations with lower filler content display increased fluidity at high frequencies compared to PolyMIM, while maintaining a relatively constant η^*. This suggests a favorable balance between flowability and print fidelity. The optimal compromise between ease of processing and mechanical integrity is typically observed at intermediate filler loadings, aligning with literature on moderately filled feedstocks designed to enhance processability without compromising strength.

7.4.6.5 Apparent Viscosity Behavior under Varying Shear Rates

The log-log plot in Figure 7.25 illustrates the apparent viscosity (η) response to increasing shear rates, simulating the flow conditions encountered during extrusion. This analysis is used to assess the degree of shear-thinning behavior and to evaluate how the MC content influences flow resistance under dynamic conditions. Lower viscosities at high shear rates are generally favorable for extrusion, as they facilitate material flow; however, excessively low viscosities may compromise shape retention and dimensional stability during printing.

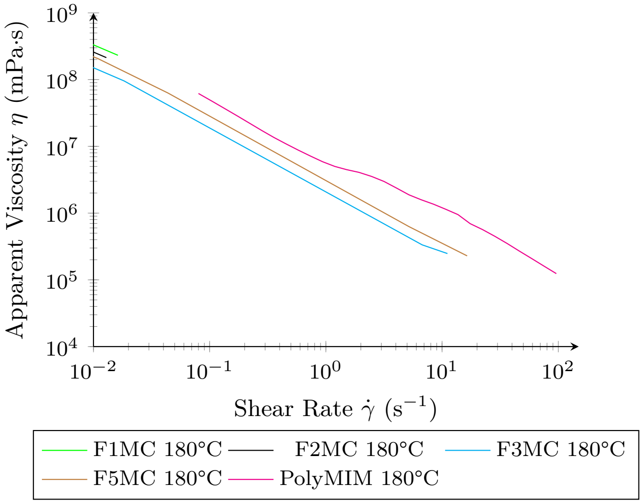

Figure 7.25: Log-log plot of apparent viscosity η as a function of shear rate $\dot{\gamma}$ for F1MC, F2MC, F3MC, F5MC and PolyMIM at 180°C.

Steady-shear data reinforce prior trends: all feedstocks shear-thin, but apparent viscosity scales with MC concentration. F0SA0MC (without MC) shows the lowest viscosity, while F5MC reaches levels potentially unsuitable for extrusion. F3MC and F5MC demonstrate optimal flow behavior with moderate apparent viscosities, suggesting sufficient cohesion and ease of deposition.

7.4.6.6 Stress-Dependent Viscoelastic Properties and Yield Behavior

The stress sweep in Figure 7.26 provides an in-depth analysis of the viscoelastic regime for F1MC (a) and F5MC (b) at 180°C. The crossover point between G' (elastic modulus) and G" (viscous modulus) defines the material's yield stress. This test allows quantifying structural rigidity and flow onset, which are directly tied to dimensional stability post-extrusion. A formulation with a clearly defined yield point and balanced moduli is preferred for 3D printing.

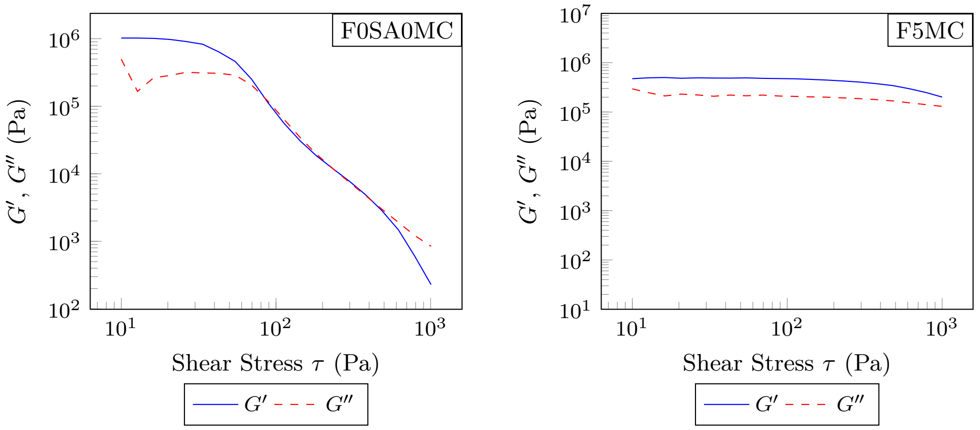

(a) F0SA0MC at 120°C

(b) F5MC at 180°C

Figure 7.26: Comparison of storage (G') and loss (G'') moduli as a function of shear stress for (a) F0SA0MC 120°C and (b) F5MC at 180°C.

The viscoelastic moduli provide insight into the elastic (G') and viscous (G'') responses of the materials under oscillatory shear. For all formulations containing MC, G' remains higher than G'' at low shear stresses, indicating a predominantly solid-like behavior. As the applied stress increases, G' gradually decreases while G'' rises, and the point at which G'' surpasses G' marks the yield point of the material. This transition reflects a shift from elastic to viscous-dominated behavior. In particular, as the MC content increases, the crossover point between G' and G'' shifts toward higher stress values, suggesting the formation of more structurally robust internal networks. Among these formulations, F3MC exhibits a well-balanced viscoelastic profile, offering sufficient rigidity for dimensional stability while remaining within a processable range. The complete rheological analysis for F2MC, F3MC, and F4MC is provided in the Appendix D.

7.4.7 Conclusions on the addition of MC

No printing trials were performed using formulations without SA, as preliminary rheological tests revealed poor flowability and a high risk of equipment malfunction, including excessive torque or screw jamming. Therefore, the role of MC was evaluated only in formulations containing SA, with the objective of optimizing binder composition for PAM.

Table 7.7 summarizes the influence of MC content on the rheological behavior and printability of Ti6Al4V feedstocks. An increase in MC content systematically enhanced the viscoelastic response and shape fidelity during extrusion. At low to moderate concentrations (1–3 vol.%), MC contributed to improved cohesion and strand stability, while maintaining acceptable flow properties. A content of 3 vol.% emerged as the optimal compromise, offering excellent geometrical stability without impairing processability.

Table 7.7: Effect of MC content on the rheological and mechanical behavior of Ti6Al4V-based feedstocks, and their suitability for PAM

MC Content	**Rheological and Mechanical Behavior**	**Suitability for PAM**
0 vol.%	Baseline viscosity, good flowability, but poor shape retention after extrusion	Acceptable
1 vol.%	Slightly increased viscosity, stable flow, improved cohesion and geometry retention	Good
2 vol.%	Noticeable thickening, very cohesive strand, stable during deposition	Very good
3 vol.%	**High but manageable viscosity, excellent shape stability, good flow regularity**	**Optimal**
4 vol.%	Very high viscosity, irregular torque response, difficult extrusion, risk of clogging	unsuitable
5 vol.%	Excessive viscosity, brittle behavior during flow, unstable extrusion	Unsuitable

Beyond 3 vol.%, the viscosity increased sharply, leading to erratic extrusion behavior and torque instabilities. Formulations containing 4 vol.% and above exhibited excessive resistance to flow, increased risk of nozzle clogging, and in some cases, brittle strand failure during deposition. These effects rendered high-MC formulations unsuitable for stable PAM processing.

It is important to note that the test corresponding to the 4 vol.% formulation (F4MC) showed unexpectedly poor results compared to F3MC and F5MC, suggesting a potential issue during feedstock preparation or compounding. This formulation should be re-evaluated in future work to confirm its true behavior under controlled conditions.

Overall, these results highlight the critical role of MC as a rheological modifier: its judicious incorporation enhances printability and shape retention, but excessive amounts severely compromise extrusion reliability. The 3 vol.% threshold is thus recommended for optimal binder formulation in SA-based systems.

In addition, further analyses are needed to more fully characterize the impact of MC addition on other critical parameters, such as the microstructure of green and sintered parts, interlayer bonding, and mechanical properties after densification. Such investigations will help establish a comprehensive understanding of how MC influences both processing and final part performance in PAM.

7.5 Feedstock with MC and SA content optimized for sustainability and PAM

To further enhance the printability of the PEG/PVB-based feedstock for PAM, a final formulation was tested that included 3 vol.% of SA and 3 vol.% of MC. This combination was chosen based on previous findings: SA helped reduce viscosity and improve flowability, while MC acted as a solidifying agent, enhancing mechanical cohesion and network structure.

Due to time constraints, additional experiments involving alternative SA and MC contents could not be conducted. Up to this point, all feedstocks were formulated with equivalent volume fractions of PEG and PVB. However, in this specific formulation, the PEG content was deliberately reduced to accommodate the addition of MC, given that PEG is water-soluble. The aim was to maintain a constant total volume of water-soluble components, thereby enabling the incorporation of MC without increasing the overall water-soluble fraction of the feedstock.

As previously discussed and shown in Table 7.8, the selected formulation contains 3 vol.% of SA and 3 vol.% of MC.

Table 7.8: Composition and nomenclature of each feedstock formulation

Composition	**Ti6Al4V**	**PEG**	**PVB**	**SA**	**MC**
	[vol. %]	[vol. %]	[vol. %]	[vol. %]	[vol. %]
F0SA0MC	55	22.5	22.5	0	0
F1SA	55	22.0	22.0	1	0
F2SA	55	21.5	21.5	2	0
F3SA	55	21.0	21.0	3	0
F4SA	55	20.5	20.5	4	0
F5SA	55	20.0	20.0	5	0
F1MC	55	22.0	22.0	0	1
F2MC	55	21.5	21.5	0	2
F3MC	55	21.0	21.0	0	3
F4MC	55	20.5	20.5	0	4
F5MC	55	20.0	20.0	0	5
F3SA3MC	55	18.0	21.0	3	3

7.5.1 Effect of temperature on the mixing torque

The first step, as previously described, involves mixing the powders at elevated temperatures using a Brabender mixer. Throughout the mixing process, the torque is continuously recorded to monitor the evolution of the feedstock's rheological behavior. The torque measurement offers an initial indication of the rheological characteristics of the formulation—in this case, F3SA3MC.

The torque profile serves as a useful indicator of when homogeneity is achieved, with stabilization over time typically reflecting a uniform distribution of particles within the binder matrix. Additionally, it provides preliminary insights into the processability of the feedstock, such as the quality of particle dispersion, the time required to reach a stable blend, and how its viscosity compares to previously developed formulations.

The corresponding results are presented in Figure 7.27.

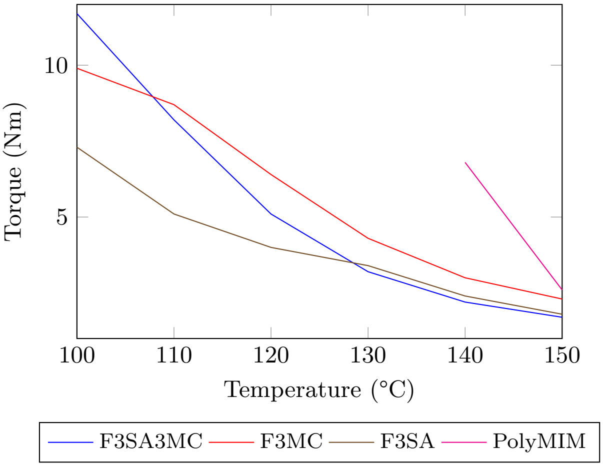

Figure 7.27: Torque of F3SA3MC feedstock depending on the temperature compared to F3MC, F3SA and commercial PolyMIM

As already said before, the commercial PolyMIM feedstock exhibited higher torque at 140–150°C, indicating more resistance to mixing. This observation correlates with its high complex viscosity and confirms that it requires higher temperatures—above 160–170°C—to be properly processable.

By contrast, the formulation containing 3 vol.% of SA and 3 vol.% of MC (F3SA3MC) presents a significantly lower torque, even lower than F3SA or F3MC alone. At 120°C, this blend appears to offer an optimal balance between the two additives, combining fluidity with thermal stability. Moreover, the torque variation across the temperature range is much smaller, highlighting the robustness and processing consistency of the formulation.

7.5.2 Thermal behavior assessment

The Kofler bench was used to qualitatively assess the thermal behavior of the hybrid feedstock composed of Ti6Al4V, PEG, PVB, MC, and SA. As previously mentioned, this method allows rapid visual identification of key temperature intervals, including the onset of malleability, fusion, tackiness, and degradation.

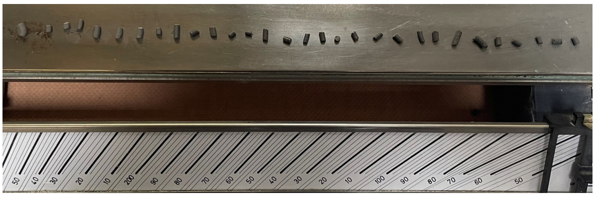

Figure 7.28: Shape retention of the Ti6Al4V-based hybrid feedstock up to 260 °C on the Kofler bench, with no signs of swelling or collapse

As shown in Figure 7.28, the feedstock retains its shape up to 260 °C without deformation, similar to the behavior observed for the reference material containing 3 vol.% MC. This indicates excellent thermal dimensional stability, which is essential for layer stacking during deposition.

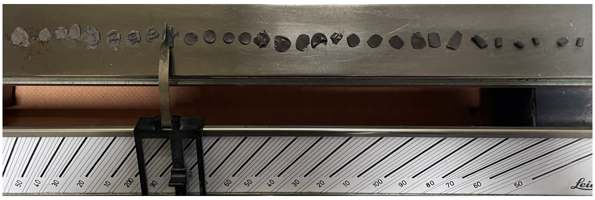

Figure 7.29: Thermal behavior of the hybrid feedstock across the Kofler temperature gradient, indicating different operational thresholds

Figure 7.29 highlights the transition zones identified by tactile and visual inspection. The material becomes malleable below 60 °C, begins to fuse between 60 and 80 °C, and remains tack-free up to 115 °C. Beyond this, a sticky window extends from 115 to 180 °C, with degradation observed above 180 °C.

Table 7.9: Thermal processing windows of F3SA3MC feedstock derived from Kofler bench observations

Composition	**MC**	**SA**	$T_{\textbf{malleability}}$	$T_{\textbf{fusion}}$	$T_{\textbf{NoSticky}}$	$T_{\textbf{sticky}}$	$T_{\textbf{degradation}}$
	[vol.%]	[vol.%]	[°C]	[°C]	[°C]	[°C]	[°C]
PolyMIM	-	-	< 120	115-135	135-150	150–200	> 200
F3SA	0	3	$\prec 55$	55-70	70-110	110-180	$\succ 182$
F3MC	3	0	$\prec 72$	72-106	106-135	135-210	$\succ 210$
F3SA3MC	3	3	< 60	60–80	80–115	115–180	> 180

The combination of MC and SA offers a well-balanced compromise as shown in Table 7.9. While the SA component helps lower the malleability and fusion temperatures, the presence of MC ensures shape retention and mechanical stability up to high temperatures. The resulting operational window (115–180°C) is similar to that of feedstocks containing only SA as an additive (without MC). However, it is more favorable from a sustainability perspective than formulations containing only MC (without SA), as it reduces the overall processing temperature range. This hybrid formulation thus facilitates controlled extrusion and deposition, with minimal risk of filament sagging or thermal degradation during printing.

7.5.3 Filament extrusion

This set of compositions presents good flow properties to be extruded. The strength of the machine during mixing was low for each SA rate as seen in Table 6.2, and there is no problem during extrusion. The filament surface was smooth, with few defects, and it did not break under the effect of its own weight. This mesure helps to determine the range of heating temperature for each compositions on PAM.

The results of all compositions are synthetize in Table 7.2 and Table 7.5. It clearly appears that MC increase the fusion temperature of the composite which is explain by its own fusion temperature (≻ 220°C) (Figure 7.30).

Figure 7.30: Extruded filament of F3SA3MC presenting good extrudability

7.5.4 Thermogravimetric analysis TGA

The thermogravimetric analysis of the F3SA3MC formulation is presented in Figure 7.31.

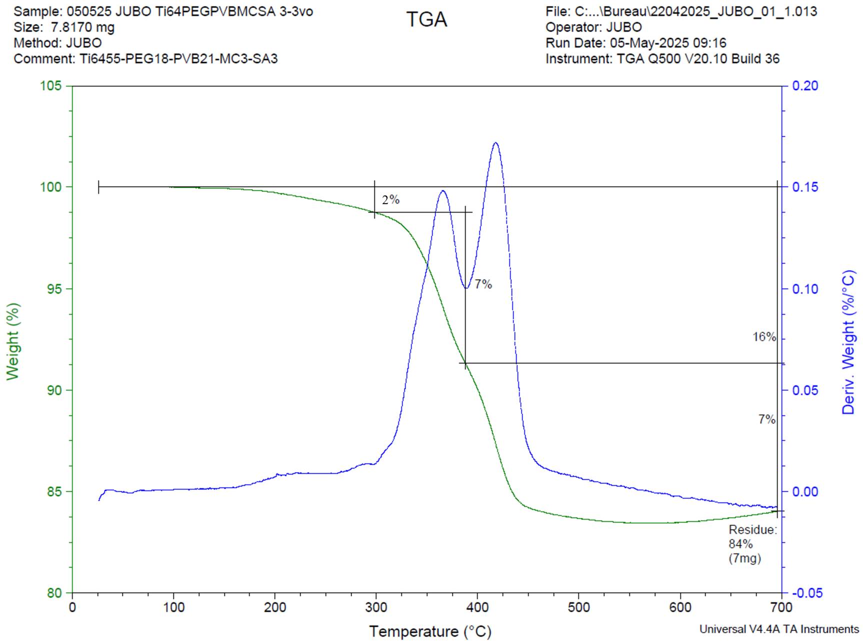

Sample: 050525 JUBO Ti64PEGPVBMCSA 3-3vo
Size: 7.8170 mg
Method: JUBO
Comment: Ti6455-PEG18-PVB21-MC3-SA3

File: C:...\Bureau\22042025_JUBO_01_1.013
Operator: JUBO
Run Date: 05-May-2025 09:16
Instrument: TGA Q500 V20.10 Build 36

Figure 7.31: Thermogravimetric analysis TGA of F3SA3MC from 0 to 700°C at 10°C/min

As observed previously with the formulation containing 5 vol.% MC (Figure 7.19), PEG and MC appear to degrade at similar temperatures. This could indicate either simultaneous degradation of these two components or the formation of a mixed PEG-MC phase. Further investigation, such as SEM imaging or FTIR analysis, would be required to confirm the precise nature of these possible interactions.

7.5.5 Rheological properties assessment

The following analyses aim to determine whether the inclusion of both additives results in a balanced rheological profile suitable for 3D printing [223, 251, 252].

7.5.5.1 Shear Stress Response under Steady-State Flow Conditions

Figure 7.32 shows the flow initiation characteristics and yield point. As mentioned before, the curvature reveals whether the feedstock maintains cohesion under shear and how it transitions from solid-like to fluid-like behavior [223, 252].

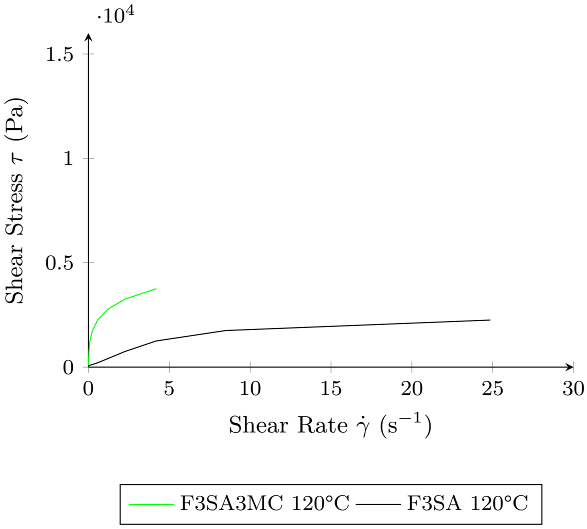

Figure 7.32: Shear stress τ as a function of shear rate $\dot{\gamma}$ for F3SA3MC and F3SA at 120°C

F3SA3MC shows a nonlinear trend typical of viscoplastic materials, with a smoother transition into flow compared to PolyMIM. This supports stable extrusion without the high stress required for PolyMIM, which would challenge nozzle-driven systems. The F3SA3MC maintains higher stress than F3SA alone, suggesting MC reinforces structural integrity under deformation [253, 254].

Following the steady-state shear analysis, attention was next directed toward the time-dependent viscoelastic response, using the same oscillatory framework introduced earlier. This aims to evaluate the internal structural stability of MC-enhanced feedstocks under prolonged stress.

7.5.5.2 Time-Dependent Stability under Oscillatory Shear

Figure 7.33 illustrates the time sweep of the F3SA3MC formulation under constant stress (10 Pa) and frequency (1 Hz), allowing the assessment of its structural stability during prolonged oscillatory deformation.

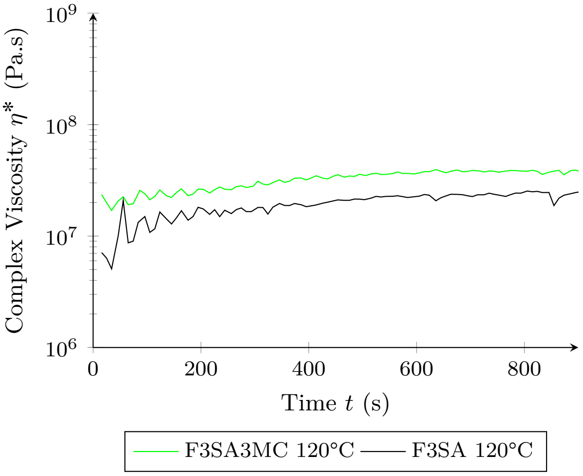

Figure 7.33: Evolution of complex viscosity η^* as a function of time at $\tau = 10$ Pa and $f = 1$ Hz for F3SA3MC and F3SA at 120°C

The F3SA3MC formulation exhibits a gradual increase in viscosity followed by stabilization, indicating the formation of a structural network that reaches equilibrium. Its final viscosity is higher than that of F3SA and F0SA0MC, but remains lower than F3MC and PolyMIM. These results support the conclusion that MC contributes to solidification and structural stabilization, while SA facilitates manageable flow. The time-independent plateau indicates thermal and mechanical stability over printing durations [255].

While time sweep analysis provided insight into the formulation's stability under constant stress, it is equally important to evaluate its rheological behavior under increasing deformation. For this purpose, stress sweep tests were conducted to assess the shear-thinning behavior and determine the formulation's adaptability to dynamic loading conditions.

7.5.5.3 Shear-Thinning Behavior and Flow Adaptability

Figure 7.34 presents the viscoelastic response of the F3SA3MC formulation under increasing shear stress at a constant frequency of 1 Hz. This analysis aims to evaluate the material's stress-thinning behavior and assess its structural resilience under dynamic loading conditions.

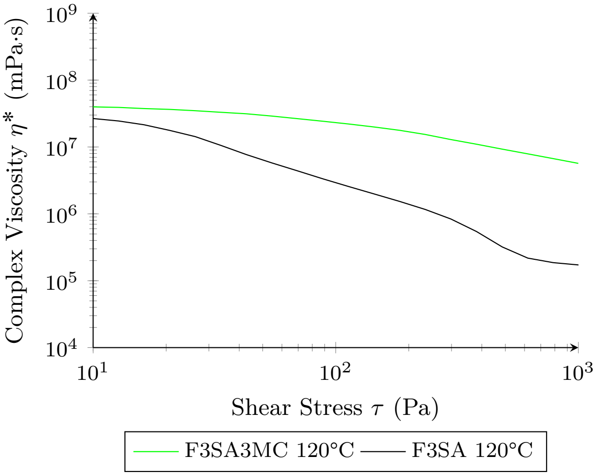

Figure 7.34: Complex viscosity η^* as a function of shear stress τ at $f = 1$ Hz for F3SA3MC and F3SA at 120°C

The F3SA3MC formulation exhibits a gradual decrease in complex viscosity as shear stress increases, indicating a smooth stress-thinning behavior. This transition is more gradual compared to F3MC, which starts with a higher initial viscosity but shows a sharper decline. In comparison to F3SA, F3SA3MC maintains a higher viscosity across most of the stress range, suggesting that the solidifying effect of MC predominates in the formulation. PolyMIM remains the most viscous, validating its higher internal cohesion but inferior extrudability. These results suggest that adding MC helps F3SA formulations retain network integrity under shear, supporting layer fidelity during printing [256, 257].

As previously explained, stress sweep tests provided insight into flow initiation and layer fidelity. To complement these results, frequency sweep analysis was conducted to assess the material's viscoelastic response over a wide range of deformation rates.

7.5.5.4 Frequency-Dependent Viscoelastic Properties

The frequency sweep data presented in Figure 7.35 reveals the material's time-dependent mechanical response. At high frequencies, the response indicates rapid structural relaxation, while low-frequency viscosity reflects resistance to long-term deformation.

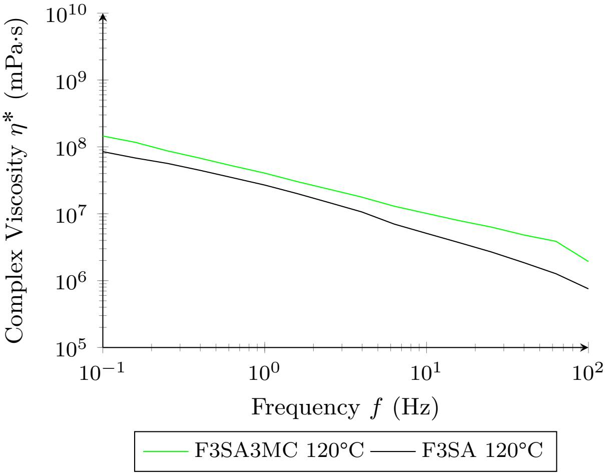

Figure 7.35: Complex viscosity η^* as a function of frequency f at fixed shear stress $\tau = 10$ Pa for F3SA3MC and F3SA at 120°C.

The F3SA3MC formulation exhibits a viscosity profile that lies between those of F3SA and F3MC. At low frequencies, it is more viscous than F3SA but less than F3MC, indicating that MC enhances structural cohesion. At high frequencies, all formulations show a decrease in viscosity, reflecting the influence of relaxation dynamics. PolyMIM stays the most viscous across all frequencies. These trends indicate that F3SA3MC has enhanced resistance to structural breakdown under prolonged loading [256].

With the frequency sweep confirming structural stability, it became essential to isolate and compare the flow behavior of individual and combined binder components. The following analysis focuses on the apparent viscosity trends of FS3AMC, FS3A, FS3MC, and their references.

7.5.5.5 Apparent Viscosity Behavior under Varying Shear Rates

The log-log plot in Figure 7.36 illustrates the flow behavior of the F3SA3MC feedstock compared to its base components: F3SA (stearic acid at 3 vol.%), F3MC (methylcellulose at 3 vol.%), the base F0SA0MC, and a PolyMIM reference. The aim is to assess whether combining SA and MC results in synergistic or antagonistic effects on shear-thinning and flowability.

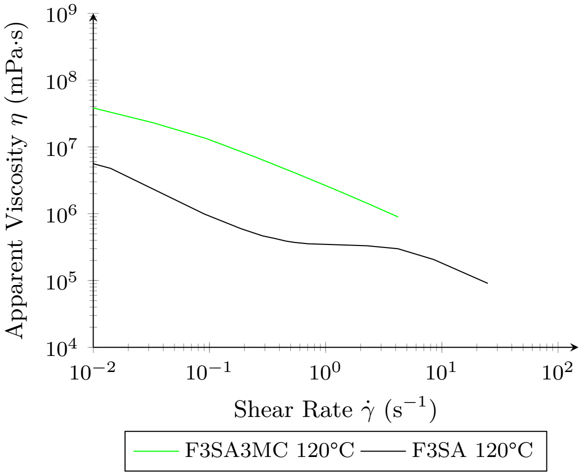

Figure 7.36: Log-log plot of apparent viscosity η as a function of shear rate $\dot{\gamma}$ for F3SA3MC and F3SA at 120°C.

As shown in 7.36, the F3SA3MC formulation exhibits an intermediate viscosity between F3SA and F3MC, suggesting a partial additive effect of both SA and MC. The viscosity remains lower than that of PolyMIM, confirming improved processability [51]. Especially, the shear-thinning behavior is retained, which is desirable for extrusion-based 3D printing. Compared to F3MC alone, the lower viscosity of F3SA3MC implies better flow, possibly due to SA's lubrication effect offsetting MC's solidening influence.

The following analysis presents the stress-dependent viscoelastic moduli of the FS3AMC formulation, focusing on the evolution of G' and G" under increasing stress and the identification of the yield point.

7.5.5.6 Stress-Dependent Viscoelastic Properties and Yield Behavior

The stress sweep shown in Figure 7.37 compares the elastic (G') and viscous (G") moduli of the F3SA3MC feedstock. The crossover point between G' and G" marks the yield point, indicating the transition from solid-like to liquid-like behavior.

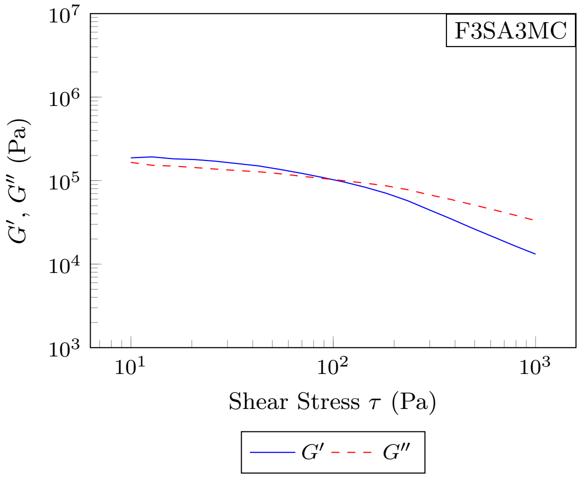

Figure 7.37: Log-log plot of storage modulus (G') and loss modulus (G'') as a function of shear stress τ for F3SA3MC at 120°C.

The F3SA3MC formulation shows a G' > G" regime at low stress, transitioning at moderate stress levels—indicating good elastic storage. Its yield point is slightly higher than that of F3SA, confirming the reinforcing effect of MC. However, it still transitions earlier than F3MC, validating the role of SA in promoting printability. The balance of moduli suggests optimized viscoelastic behavior for extrusion, which is consistent with the pseudoplastic-like response previously reported (Figure 2.24 in Chapter 2) for polymer-based feedstocks in extrusion-based 3D printing [255].

7.5.5.7 Conclusions on rheological behavior of the new feedstock

The rheological analysis of F3SA3MC reveals that combining 3 vol.% SA with 3 vol.% MC successfully integrates the desirable traits of each additive. SA reduces viscosity and improves flow, while MC enhances elastic integrity and long-term stability.

Compared to their individual use, the combined system offers a balanced profile: moderate yield stress, stable viscosity over time, and sufficient structural rigidity. Importantly, F3SA3MC achieves better printability than F3MC and better cohesion than F3SA, while remaining more processable than PolyMIM. These findings position F3SA3MC as a promising candidate for extrusion-based AM of highly filled feedstocks.

7.5.6 Thermal camera analysis

The same experimental setup as for the PolyMIM feedstock was used on F3SA3MC feedstock. The nozzle, along with other measured areas, was painted black to ensure accurate and reliable infrared thermography measurements.

The extruder temperature was set to 130°C, and the external surface temperature of the extruder body was maintained at 90°C.

These conditions were applied to enable a consistent comparison of the thermal behavior between the tested formulation and the commercial feedstock.

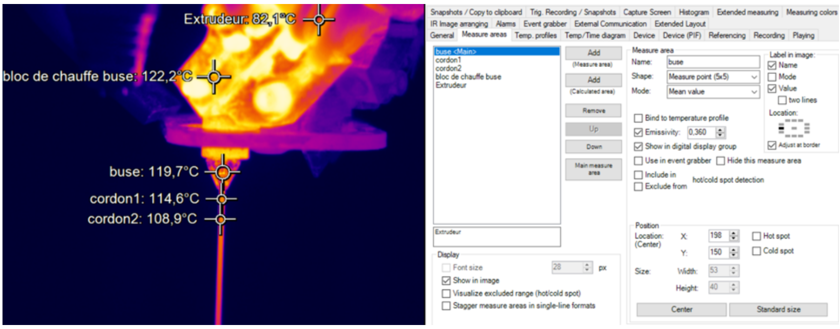

buse <Main>
cordon1
cordon2
bloc de chauffe buse
Extrudeur

Extrudeur

Measure area
Name: buse
Shape: Measure point (5x5)
Mode: Mean value
☐ Bind to temperature profile
☑ Emissivity: 0,360
☑ Show in digital display group
☐ Use in event grabber ☐ Hide this measure area
☐ Include in
☐ Exclude from
hot/cold spot detection

Label in image:
☑ Name
☐ Mode
☑ Value
☐ two lines
Location:
☑ Adjust at border

Display
☐ Font size 28 px
☑ Show in image
☐ Visualize excluded range (hot/cold spot)
☐ Stagger measure areas in single-line formats

Position
Location: (Center) X: 198 Y: 150
☐ Hot spot
☐ Cold spot
Size: Width: 53 Height: 40

Figure 7.38: Thermal measurements for F3SA3MC using IR camera at nozzle temperature 130°C

Thermal imaging, as shown in Figure 7.38, revealed a trend similar to that observed for PolyMIM, with a consistent temperature gap of 15–25°C between the set nozzle temperature and the actual filament temperature. As a result, it is necessary to apply a temperature 15–25°C higher than the target in order to achieve the desired processing temperature within the filament.

Based on the previous analyses, the F3SA3MC feedstock—identified as highly promising for 3D printing—was selected for printing trials using the PAM system. The objective was to validate whether its printability aligns with the favorable rheological and structural characteristics previously observed, and to compare its performance against the commercial feedstock. Key criteria included visual quality, ease of printing, and the robustness of parameter optimization. The results of these trials are presented in the following section.

7.5.7 3D Printing

Despite limited optimization of printing parameters (Figure 7.10 due to time and materials constraints, the initial trials clearly demonstrated the excellent printability of the feedstock. From the very first attempt, parts with good visual quality were successfully produced.

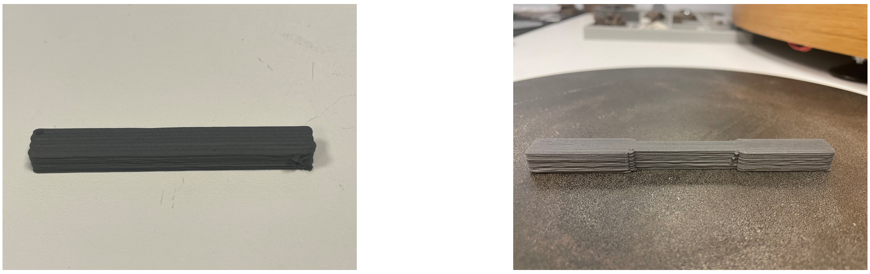

(a) F3SA3MC bending test part

(b) F3SA3MC printed tensile part

Figure 7.39: F3SA3MC 3D printed parts: (a) Bending (EN843-1) and (b) Tensile specimen (ASTM E8/E8M)

Table 7.10 exhibits parameters used for F3SA3MC printing tests. These parameters are significantly different than for PolyMIM.

Table 7.10: Optimized 3D Printing parameters

Printing Parameters	**Values**
Nozzle diameter	1 mm
Layer height	0.34 mm
Initial layer height	0.34 mm
Infill density	100%
Infill pattern	Lines
Extruder printing temperature	90°C
Nozzle temperature	125°C
Cold printing temperature	45°C
Build plate temperature	35°C
Flow	100%
Initial layer flow	100%
Print speed	20 mm/s

Several advantages emerged from this study:

- Lower printing temperatures: The feedstock F3SA3MC allowed printing at 120°C, compared to 200°C for the commercial PolyMIM feedstock, contributing to reduced energy consumption.
- Higher printing speed: A speed of 20 mm/s was achieved with F3SA3MC, versus 15 mm/s for PolyMIM, indicating potential for faster production.
- Improved adhesion: The material adhered well to the build plate without the need for adhesive spray.

- Ease of shaping and robustness: The feedstock was easier to handle and showed significantly less brittleness, making it more suitable for post-processing.

- Better surface finish: A smoother appearance was observed (Figure 7.39), although further measurements are needed to confirm this quantitatively.

While these results are promising, further investigations are needed to fully assess the quality of printed parts. Future work should include porosity analysis, density and hardness measurements, and microstructural characterization via scanning electron microscopy (SEM). Additionally, evaluating debinding and sintering behavior under controlled thermal conditions will be essential to confirm compatibility with industrial post-processing. Complementary techniques such as Fourier-transform infrared spectroscopy (FTIR) and mechanical testing (e.g., tensile, flexural, or impact strength) could help establish correlations between binder composition, processing conditions, and final part performance.

These aspects, beyond the scope of the present study, could form the basis for future research focused on the full qualification of PAM-printed titanium components.

7.5.8 Debinding and sintering

Although debinding and sintering were not the primary objectives of this thesis, preliminary trials were conducted at BCRC using the F3SA3MC feedstock, specifically developed for PAM applications. These tests were based on thermal debinding and sintering parameters initially optimized for the commercial PolyMIM feedstock. While not tailored to the thermal behavior of the new formulation, they provided a useful baseline.

The F3SA3MC feedstock underwent water debinding followed by thermal debinding and sintering. The resulting parts showed apparent density values ranging from 3.32 to 4.01 g/cm^3, with an average of 3.59 g/cm^3. Real density varied between 75.1% and 90.6%, averaging 81.2%, confirming the feedstock's ability to produce sinterable parts. However, relatively high open porosity (mean: 17.3%, max: 23.8%) was observed, indicating that the sintering protocol was not yet optimized for this formulation. Closed porosity remained low (average: 1.8%), suggesting that most residual porosity was interconnected.

To further improve densification and reduce residual porosity, several optimization pathways can be considered. The feedstock formulation itself could be refined by adjusting the PEG/PVB ratio or the content of surfactants such as stearic acid or methylcellulose, in order to enhance powder packing and reduce residue formation during debinding. In parallel, printing parameters—including layer height, extrusion temperature, and build plate temperature—should be optimized to minimize internal defects in the green body. Water debinding efficiency could benefit from improved diffusion conditions, such as extended immersion time or agitation. The thermal debinding schedule may also be revised to more closely match the decomposition profile of the custom binder system, thereby avoiding premature structure collapse. Finally, sintering temperature, dwell time, and atmosphere should be tailored to the feedstock to ensure maximum densification while preventing defects such as grain growth or oxidation.

These initial trials validate the overall processability of F3SA3MC and demonstrate its potential for producing sinterable titanium parts. They also emphasize the need for end-to-end optimization to reach densification levels above 98%, required for high-performance applications.

7.5.9 Conclusions for feedstock optimisation

The formulation combining 3 vol.% SA and 3 vol.% MC has emerged as a particularly promising candidate for PAM of highly filled feedstocks. This hybrid system successfully integrates the complementary properties of its components: SA enhances flowability by reducing viscosity and interparticle friction, while MC contributes to structural integrity through increased yield stress and viscoelasticity. Together, they create a formulation that exhibits stable rheological behavior across a moderate temperature range (80–120°C), significantly lower than that required for conventional PolyMIM systems (190°C).

Rheological analysis confirms that F3SA3MC maintains a moderate and consistent torque profile, indicating robust processability and thermal stability. Unlike formulations with higher MC content, which tend to suffer from phase separation and torque instability, this balanced blend ensures smooth extrusion and reliable deposition. The formulation also demonstrates excellent printability, requiring no adhesion aids, and produces parts with improved ductility and surface finish—key advantages for post-processing and end-use performance.

Initial sintering trials further validate the material's potential, with densification levels averaging over 81% and low closed porosity. However, the presence of open porosity suggests that further optimization of the debinding and sintering protocols is necessary to reach the $>$ 98% density target for high-performance applications. Adjustments to binder composition, printing parameters, and thermal treatment schedules are recommended to enhance powder packing and minimize residual porosity.

In addition to its technical merits, the F3SA3MC formulation offers environmental benefits, as both SA and MC are bio-based, reducing reliance on petroleum-derived binders.

In conclusion, this study highlights the F3SA3MC blend as a reliable, efficient, and sustainable solution for PAM, with strong potential for further development and industrial application.

7.6 Conclusions and prospects

All the objectives set for this work have been successfully achieved. The PAM process has proven to be particularly relevant for the production of small series, especially when paired with a feedstock tailored to its specific requirements. A new partially water-soluble feedstock has been developed, improving both processability and sustainability. While PEG, a petroleum-based compound, was maintained for its well-known performance in such applications, the addition of 3 vol.% of bio-based methylcellulose marks a step forward in the formulation of more environmentally conscious materials. This progress opens the door for future improvements, such as replacing the non-water-soluble PVB with a bio-based thermoplastic alternative like PLA, to further increase the renewable content without compromising the mechanical or thermal integrity of the green parts.

Torque analysis during powder mixing, extrusion behavior, and Kofler bench testing appear to be the most discriminating and time-efficient methods for quickly assessing the material's behavior. The recommended order for performing these analyses is as follows:

1. Mixing (torque measurement)
2. Extrusion
3. Kofler bench test

The new feedstock offers clear advantages over the commercial PolyMIM material. It is more compatible with PAM, exhibiting enhanced printability, significantly better adhesion to the build platform (eliminating the need for adhesive sprays), and improved part quality from the first print attempts. Additionally, it enables processing at lower temperatures than PolyMIM, reducing energy consumption and minimizing the risk of premature degradation.

Perspectives for this work include the exploration of fully bio-based, non-water-soluble binder systems, the refinement of the methylcellulose content to optimize mechanical performance, and the expansion of thermal and rheological studies to predict long-term stability and behavior during the debinding and sintering steps. Furthermore, the implementation of the feedstock in more complex geometries and its validation across multiple machines and printing conditions would solidify its industrial potential.

CHAPTER 8

General Conclusion and Perspectives

This thesis developed and characterized a novel feedstock based on the titanium alloy Ti6Al4V specifically tailored for Pellet Additive Manufacturing (PAM). Motivated by a comprehensive Cradle to Gate comparative analysis of energy and material consumption of PAM against MIM machine performed early in the research, significant environmental advantages of PAM were identified over traditional MIM. These advantages justified the formulation of a more environmentally friendly hybrid binder system, enabling lower processing temperatures and reducing the overall environmental impact of the manufacturing process.

Addressing the limitations inherent in commercial feedstocks initially developed for MIM, this study innovatively used PEG, PVB, SA, and MC. A distinctive and original contribution of this research is the integration of MC as a biosourced rheological modifier within an organic solvent-based environment, rather than the aqueous environments typically used. This addition significantly improved the sustainability profile of the formulation and enhanced rheological stability during extrusion, thereby increasing the repeatability and precision of printed components.

Extensive experimentation determined the optimal concentration of stearic acid to be around 3 vol.%, as this provided essential lubrication, improved rheological stability, and significantly enhanced inter-layer adhesion. The specific choice of 3 vol.% was supported by oscillatory rheology and printing trials showing a balance between flowability and shape retention.

Detailed rheological studies revealed that incorporating MC at a 3 vol.% ratio markedly optimized the viscosity profile, significantly enhancing printability and inter-layer bonding. The use of MC in an organic binder matrix—uncommon in the literature—also opens new possibilities for bio-based additives beyond aqueous systems. The synergistic combination of PEG and PVB was thoroughly investigated, and preliminary results indicated substantial potential for further optimization of their relative proportions. Fine-tuning these ratios could lead to improved printability, mechanical properties, and ecological performance.

Experimental results demonstrated that the newly formulated feedstocks exhibited superior dimensional stability, more homogeneous extrusion profiles, and significantly improved layer adhesion compared to benchmarked commercial feedstocks such as PolyMIM.

In particular, feedstocks like F3SA3MC showed intermediate viscosity between SA- and MC-only systems, suggesting an additive effect that favors both flowability and stability.

Thermal analysis conducted using TGA and Kofler bench tests validated suitable processing windows for extrusion and thermal debinding, fully compatible with industrial-scale applications. The Kofler bench results in particular guided the selection of the effective temperature window for extrusion.

The combined use of thermal cameras and thermocouples allowed precise identification of real-time filament temperatures during extrusion. This approach revealed a temperature discrepancy between 15 and 25°C compared to the targeted nozzle temperature, further exacerbated by rapid cooling upon contact with ambient air. As a result, the actual temperature of the extruded filament can be significantly lower than expected. Such temperature discrepancies, particularly noticeable in the commercial PolyMIM feedstock, caused adhesion issues requiring additional adhesive sprays, increased material waste, and environmental concerns. Remarkably, the developed feedstock overcame these challenges, eliminating the need for adhesive sprays, significantly reducing unsuccessful trials, conserving material, and enhancing environmental performance. Furthermore, due to the identified temperature discrepancies, it became evident that significantly higher nozzle temperatures are required to achieve the optimal processing temperatures determined through Kofler bench and rheological analyses.

A comparative evaluation of PAM against MIM highlighted PAM's distinct advantages for small to medium batch production scenarios. PAM demonstrated lower energy consumption, enhanced material utilization efficiency, and significantly reduced production waste. The early integration of environmental considerations via this methodology reinforced the importance and viability of eco-design principles in additive manufacturing.

Despite these achievements, some limitations remain. For instance, the microstructure and possible phase formation during debinding and sintering of feedstocks with MC remain unexplored. Likewise, long-term stability and sensitivity to environmental conditions such as humidity should be further investigated.

Perspectives

Short-term research avenues include:

- Increasing the Ti6Al4V content in formulations to enhance printability, structural integrity, and mechanical performance after sintering.
- Reproducing the analysis with an optimized blend.
- Conducting a complete LCA of PAM using the F3SA3MC feedstock, in line with recommended standards, to identify potential improvements through reduced printing temperature and time.
- Further increasing proportions of hydrosoluble and biosourced polymers to minimize environmental impacts while maintaining mechanical integrity and dimensional accuracy.
- Refining debinding processes tailored specifically to new feedstock formulations, ensuring dimensional accuracy and mechanical robustness of printed parts.
- Further optimization of SA content and PEG/PVB ratios to enhance stability, printing quality, and sustainability of feedstocks.

- Evaluating the resulting microstructures through Scanning Electron Microscopy (SEM) to identify structural features and phases formed due to MC incorporation.

Medium-term prospects should focus on:

- Detailed characterization of mechanical properties and microstructural evolution of printed and sintered components to validate their applicability in demanding sectors such as biomedical implants and aerospace components.
- Developing intelligent and automatic process control systems integrating advanced thermal sensors and machine learning algorithms for dynamic, real-time adjustment of printing parameters, ensuring consistent high-quality outputs.
- Exploring fully bio-based feedstock formulations aimed at achieving fully sustainable and circular metallic additive manufacturing processes.

Finally, conducting a comprehensive techno-economic evaluation comparing PAM and MIM across various production scales would provide valuable insights supporting strategic decisions and broader industrial adoption.

Bibliography

[1] *ISO/ASTM 52900:2021(en), Additive manufacturing — General principles — Fundamentals and vocabulary*. [Online]. Available: `https://www.iso.org/obp/ui/#iso:std:iso-astm:52900:ed-2:v1:en` (visited on 01/17/2025).

[2] S. Saleh Alghamdi, S. John, N. Roy Choudhury, and N. K. Dutta, "Additive Manufacturing of Polymer Materials: Progress, Promise and Challenges," *Polymers*, vol. 13, no. 5, Jan. 2021. DOI: `10.3390/polym13050753`.

[3] W. E. Frazier, "Metal Additive Manufacturing: A Review," *J. of Materi Eng and Perform*, vol. 23, no. 6, pp. 1917–1928, Jun. 2014. DOI: `10.1007/s11665-014-0958-z`.

[4] S. Kokare, J. P. Oliveira, and R. Godina, "Life cycle assessment of additive manufacturing processes: A review," vol. 68, pp. 536–559, Jun. 2023, ISSN: 0278-6125. DOI: `10.1016/j.jmsy.2023.05.007`.

[5] R. Ranjan, D. Kumar, M. Kundu, and S. Chandra Moi, "A critical review on Classification of materials used in 3D printing process," *Materials Today: Proceedings*, International Conference on Thermo-Fluids and System Design, vol. 61, pp. 43–49, Jan. 2022. DOI: `10.1016/j.matpr.2022.03.308`.

[6] S. Kumar and R. Kumar, "A Comprehensive Study on Additive Manufacturing Techniques, Machine Learning Integration, and Internet of Things-Driven Sustainability Opportunities," *J. of Materi Eng and Perform*, Mar. 2025. DOI: `10.1007/s11665-025-10757-x`.

[7] E. O. Ezugwu and Z. M. Wang, "Titanium alloys and their machinability—a review," *Journal of Materials Processing Technology*, Superplasticity and Superplastic Technology in Japan, vol. 68, no. 3, pp. 262–274, Aug. 1997. DOI: `10.1016/S0924-0136(96)00030-1`.

[8] G. Liu, Y. Xiong, and D. Rosen, "Multidisciplinary design optimization in design for additive manufacturing," *Journal of Computational Design and Engineering*, vol. 9, pp. 1–16, Dec. 2021. DOI: `10.1093/jcde/qwab073`.

[9] I. Gibson, D. Rosen, and B. Stucker, “Design for Additive Manufacturing,” in *Additive Manufacturing Technologies: 3D Printing, Rapid Prototyping, and Direct Digital Manufacturing*, I. Gibson, D. Rosen, and B. Stucker, Eds., New York, NY: Springer, 2015, pp. 399–435. DOI: `10.1007/978-1-4939-2113-3_17`.

[10] G. Boothroyd, P. Dewhurst, and W. A. Knight, *Product Design for Manufacture and Assembly*, 3rd ed. Boca Raton, Dec. 2010. DOI: `10.1201/9781420089288`.

[11] K. Kanishka and B. Acherjee, “Revolutionizing manufacturing: A comprehensive overview of additive manufacturing processes, materials, developments, and challenges,” *Journal of Manufacturing Processes*, vol. 107, pp. 574–619, Dec. 2023. DOI: `10.1016/j.jmapro.2023.10.024`.

[12] M. Dinar and D. W. Rosen, “A Design for Additive Manufacturing Ontology,” *Journal of Computing and Information Science in Engineering*, vol. 17, no. 021013, Feb. 2017. DOI: `10.1115/1.4035787`.

[13] J.-y. Hascoet, “Environmental performance modeling for additive manufacturing processes,” *HAL (Le Centre pour la Communication Scientifique Directe)*, Jan. 2015. DOI: `10.1504/15.74812`.

[14] R. Eickhoff, S. Antusch, S. Baumgärtner, D. Nötzel, and T. Hanemann, “Feedstock Development for Material Extrusion-Based Printing of Ti6Al4V Parts,” *Materials*, vol. 15, no. 18, p. 6442, Jan. 2022, Number: 18 Publisher: Multidisciplinary Digital Publishing Institute. DOI: `10.3390/ma15186442`.

[15] Y. Thompson, “Fused Filament Fabrication-Based Additive Manufacturing of Commercially Pure Titanium,” *Advanced Engineering Materials*, vol. 23, no. 12, 2021. DOI: `10.1002/adem.202100380`.

[16] *The Additive Manufacturing Industry Landscape 2019: 171 Companies Driving the Industry Forward [Updated] - AMFG*, Feb. 2019. [Online]. Available: `https://amfg.ai/2019/02/27/additive-manufacturing-industry-landscape-2019/` (visited on 01/17/2025).

[17] Y. Lakhdar, C. Tuck, J. Binner, A. Terry, and R. Goodridge, “Additive manufacturing of advanced ceramic materials,” *Progress in Materials Science*, vol. 116, p. 100 736, Feb. 2021. DOI: `10.1016/j.pmatsci.2020.100736`.

[18] S. Singh, G. Singh, C. Prakash, and S. Ramakrishna, “Current status and future directions of fused filament fabrication,” *Journal of Manufacturing Processes*, vol. 55, pp. 288–306, Jul. 2020. DOI: `10.1016/J.JMAPRO.2020.04.049`.

[19] I. Gibson, D. W. Rosen, and B. Stucker, *Additive Manufacturing Technologies: Rapid Prototyping to Direct Digital Manufacturing*. Boston, MA: Springer US, 2010. DOI: `10.1007/978-1-4419-1120-9`.

[20] T. D. Ngo, A. Kashani, G. Imbalzano, K. T. Q. Nguyen, and D. Hui, “Additive manufacturing (3D printing): A review of materials, methods, applications and challenges,” *Composites Part B: Engineering*, vol. 143, pp. 172–196, Jun. 2018. DOI: `10.1016/j.compositesb.2018.02.012`.

[21] K. Thrimurthulu, P. M. Pandey, and N. Venkata Reddy, “Optimum part deposition orientation in fused deposition modeling,” *International Journal of Machine Tools and Manufacture*, vol. 44, no. 6, pp. 585–594, May 2004. DOI: `10.1016/j.ijmachtools.2003.12.004`.

[22] R. Alfattani, *Hybrid Manufacturing Systems: Integrating Additive and Subtractive Techniques for Precision and Versatility*, Nov. 2024. DOI: `10.21203/rs.3.rs-5141947/v1`.

[23] M. Rabalo, A. García Domínguez, E. Rubio, M. Marin, and B. Agustina, "Last Trends in the Application of the Hybrid Additive and Subtractive Manufacturing in the Aeronautic Industry," *Advances in Science and Technology*, vol. 132, pp. 353–362, Oct. 2023. DOI: `10.4028/p-M9Diuh`.

[24] X. Duan, R. Cui, H. Yang, and X. Yang, "Hybrid Additive and Subtractive Manufacturing Method Using Pulsed Arc Plasma," *Materials*, vol. 16, p. 4561, Jun. 2023. DOI: `10.3390/ma16134561`.

[25] W. Grzesik, "Hybrid manufacturing of metallic parts integrated additive and subtractive processes," *Mechanik*, no. 7, pp. 468–475, Jul. 2018. DOI: `10.17814/mechanik.2018.7.58`.

[26] N. Nys, M. König, P. Neugebauer, M. J. Jones, and H. Gruber-Woelfler, "Additive Manufacturing as a Rapid Prototyping and Fabrication Tool for Laboratory CrystallizersA Proof-of-Concept Study," *Organic Process Research and Development*, vol. 27, no. 8, pp. 1455–1462, Aug. 2023. DOI: `10.1021/acs.oprd.3c00126`.

[27] A. Marshall, "GM's 3-D Printed Seat Bracket and a Future of Cheaper, Better Cars," *Wired*, Section: tags, ISSN: 1059-1028.

[28] *Maximizing Sustainability in Additive Manufacturing: Strategies for Efficiency & Circular Design*, Jan. 2025. [Online]. Available: `https://insidemetaladditivemanufacturing.com/2025/01/15/maximizing-sustainability-in-additive-manufacturing-strategies-for-material-efficiency-and-circular-design/` (visited on 05/27/2025).

[29] S. Jung, L. B. Kara, Z. Nie, T. W. Simpson, and K. S. Whitefoot, "Is Additive Manufacturing an Environmentally and Economically Preferred Alternative for Mass Production?" *Environmental Science & Technology*, vol. 57, no. 16, pp. 6373–6386, Apr. 2023. DOI: `10.1021/acs.est.2c04927`.

[30] S. Dehghan, S. Sattarpanah Karganroudi, S. Echchakoui, and N. Barka, "The Integration of Additive Manufacturing into Industry 4.0 and Industry 5.0: A Bibliometric Analysis (Trends, Opportunities, and Challenges)," *Machines*, vol. 13, no. 1, p. 62, Jan. 2025, Number: 1 Publisher: Multidisciplinary Digital Publishing Institute. DOI: `10.3390/machines13010062`.

[31] kimeditor, *Large-scale AM drives tool-less manufacturing of FRP parts*, Sep. 2022. [Online]. Available: `https://www.massivit3d.com/blog/large-scale-am-drives-tool-less-manufacturing-of-frp-parts/` (visited on 05/27/2025).

[32] *Fabrication additive de granulés avec des imprimantes 3D par Pollen AM*, Section: Imprimante 3D, Jan. 2024. [Online]. Available: `https://mondeadditif.com/fabrication-additive-de-granules-avec-des-imprimantes-3d-par-pollen-am/` (visited on 05/20/2025).

[33] L. Spitaels, "Enabling the Hybrid Manufacturing of Ceramic Parts by Additive Manufacturing and Milling," Oct. 2024, Publisher: UMONS - Université de Mons [Polytechnique], Mons, Belgium.

[34] N. A. Sukindar, A. S. H. Md Yasir, M. D. Azhar, M. A. Md Azhar, N. F. H. Abd Halim, M. H. Sulaiman, A. S. H. Ahmad Sabli, and M. K. A. Mohd Ariffin, "Evaluation of the surface roughness and dimensional accuracy of low-cost 3D-printed parts made of PLA–aluminum," *Heliyon*, vol. 10, no. 4, e25508, Feb. 2024. DOI: `10.1016/j.heliyon.2024.e25508`.

[35] P. Minetola, M. Galati, F. Calignano, L. Iuliano, G. Rizza, and L. Fontana, "Comparison of dimensional tolerance grades for metal AM processes," *Procedia CIRP*, 13th CIRP Conference on Intelligent Computation in Manufacturing Engineering, 17-19 July 2019, Gulf of Naples, Italy, vol. 88, pp. 399–404, Jan. 2020. DOI: `10.1016/j.procir.2020.05.069`.

[36] *How to Get the Perfect Build Plate Adhesion Settings & Improve Bed Adhesion - 3D Printerly.* [Online]. Available: `https://3dprinterly.com/how-to-get-the-perfect-build-plate-adhesion-settings/` (visited on 01/17/2025).

[37] S. Dai, K. Zhu, S. Wang, and Z. Deng, "Additively manufactured materials: A critical review on their anisotropic mechanical properties and modeling methods," *Journal of Manufacturing Processes*, vol. 141, pp. 789–814, May 2025, ISSN: 1526-6125. DOI: `10.1016/j.jmapro.2025.02.038`.

[38] O. Ulkir, "Energy-Consumption-Based Life Cycle Assessment of Additive-Manufactured Product with Different Types of Materials," *Polymers*, vol. 15, no. 6, p. 1466, Jan. 2023, Number: 6 Publisher: Multidisciplinary Digital Publishing Institute. DOI: `10.3390/polym15061466`.

[39] C. M. Bezzina and P. Refalo, "Fused Filament Fabrication and Injection Moulding of Plastic Packaging: An Environmental and Financial Comparative Assessment," *Machines*, vol. 11, no. 6, p. 634, Jun. 2023, Number: 6 Publisher: Multidisciplinary Digital Publishing Institute. DOI: `10.3390/machines11060634`.

[40] *3D Printing Trends Report: Additive Post-Processing Survey Results.* [Online]. Available: `https://www.postprocess.com/trends-report/` (visited on 05/27/2025).

[41] C. Scott, *Challenges and Future Trends in Additive Manufacturing*, Oct. 2023. [Online]. Available: `https://wohlersassociates.com/uncategorized/challenges-and-future-trends-in-additive-manufacturing/` (visited on 05/27/2025).

[42] J. Adames, "Characterization of polymeric binders for Metal Injection Molding (MIM) process," Jan. 2007.

[43] S. Cano, J. Gonzalez-Gutierrez, J. Sapkota, M. Spoerk, F. Arbeiter, S. Schuschnigg, C. Holzer, and C. Kukla, "Additive manufacturing of zirconia parts by fused filament fabrication and solvent debinding: Selection of binder formulation," *Additive Manufacturing*, vol. 26, pp. 117–128, Mar. 2019. DOI: `10.1016/j.addma.2019.01.001`.

[44] M. D. Hayat, G. Wen, M. F. Zulkifli, and P. Cao, "Effect of PEG molecular weight on rheological properties of Ti-MIM feedstocks and water debinding behaviour," *Powder Technology*, vol. 270, pp. 296–301, Jan. 2015. DOI: `10.1016/j.powtec.2014.10.035`.

[45] M. D. Hayat, A. Goswami, S. Matthews, T. Li, X. Yuan, and P. Cao, "Modification of PEG/PMMA binder by PVP for titanium metal injection moulding," *Powder Technology*, vol. 315, pp. 243–249, Jun. 2017. DOI: `10.1016/j.powtec.2017.04.004`.

[46] M.-S. Huang and H.-C. Hsu, "Effect of backbone polymer on properties of 316L stainless steel MIM compact," *Journal of Materials Processing Technology*, vol. 209, no. 15, pp. 5527–5535, Aug. 2009. DOI: `10.1016/j.jmatprotec.2009.05.011`.

[47] T. Liu, K. Yao, and F. Gao, “Identification and Autotuning of Temperature-Control System With Application to Injection Molding,” *IEEE Transactions on Control Systems Technology*, vol. 17, no. 6, pp. 1282–1294, Nov. 2009, Conference Name: IEEE Transactions on Control Systems Technology. DOI: `10.1109/TCST.2008.2006746`.

[48] S. S. Crump, “Apparatus and method for creating three-dimensional objects,” US5121329A, Jun. 1992. [Online]. Available: `https://patents.google.com/patent/US5121329A/en` (visited on 05/22/2025).

[49] *New Partially Water-Soluble Feedstocks for Additive Manufacturing of Ti6Al4V Parts by Material Extrusion.* [Online]. Available: `https://www.mdpi.com/1996-1944/16/8/3162` (visited on 01/17/2025).

[50] M. Bragaglia, M. Mariani, C. Sergi, F. Sarasini, J. Tirillò, and F. Nanni, “Polylactic acid as biobased binder for the production of 3D printing filaments for Ti6Al4V alloy manufacturing via bound metal deposition,” *Journal of Materials Research and Technology*, vol. 27, pp. 168–181, Nov. 2023. DOI: `10.1016/j.jmrt.2023.09.227`.

[51] C. Suwanpreecha and A. Manonukul, “A Review on Material Extrusion Additive Manufacturing of Metal and How It Compares with Metal Injection Moulding,” *Metals*, vol. 12, no. 3, p. 429, Mar. 2022, Number: 3 Publisher: Multidisciplinary Digital Publishing Institute. DOI: `10.3390/met12030429`.

[52] A. Bellini, L. Shor, and S. I. Guceri, “New developments in fused deposition modeling of ceramics,” *Rapid Prototyping Journal*, vol. 11, no. 4, pp. 214–220, Jan. 2005, Publisher: Emerald Group Publishing Limited. DOI: `10.1108/13552540510612901`.

[53] G. Singh, J.-M. Missiaen, D. Bouvard, and J.-M. Chaix, “Copper extrusion 3D printing using metal injection moulding feedstock: Analysis of process parameters for green density and surface roughness optimization,” *Additive Manufacturing*, vol. 38, p. 101 778, Feb. 2021. DOI: `10.1016/j.addma.2020.101778`.

[54] C. Lieberwirth, A. Harder, and H. Seitz, “Extrusion Based Additive Manufacturing of Metal Parts,” *Journal of Mechanics Engineering and Automation*, vol. 7, Feb. 2017. DOI: `10.17265/2159-5275/2017.02.004`.

[55] O. Miclette, R. Côté, V. Demers, and V. Brailovski, “Material extrusion additive manufacturing of low-viscosity metallic feedstocks: Performances of the plunger-based approach,” *Additive Manufacturing*, vol. 60, p. 103 252, Dec. 2022. DOI: `10.1016/j.addma.2022.103252`.

[56] A. La Gala, D. V. A. Ceretti, R. Fiorio, L. Cardon, and D. R. D’hooge, “Comparing pellet- and filament-based additive manufacturing with conventional processing for ABS and PLA parts,” *Journal of Applied Polymer Science*, vol. 139, no. 44, e53089, 2022, _eprint: https://onlinelibrary.wiley.com/doi/pdf/10.1002/app.53089. DOI: `10.1002/app.53089`.

[57] A. Pagés-Llobet, F. X. Espinach, F. Julián, H. Oliver-Ortega, and J. A. Méndez, “Effect of Extruder Type in the Interface of PLA Layers in FDM Printers: Filament Extruder Versus Direct Pellet Extruder,” *Polymers*, vol. 15, no. 9, p. 2019, Jan. 2023, Number: 9 Publisher: Multidisciplinary Digital Publishing Institute. DOI: `10.3390/polym15092019`.

[58] M. Fabrizio, M. Strano, D. Farioli, and H. Giberti, “Extrusion Additive Manufacturing of PEI Pellets,” *Journal of Manufacturing and Materials Processing*, vol. 6, no. 6, p. 157, Dec. 2022, Number: 6 Publisher: Multidisciplinary Digital Publishing Institute. DOI: `10.3390/jmmp6060157`.

[59] Gerd Lütjering , James C. Williams, *Titanium* (Engineering Materials, Processes). Berlin, Heidelberg: Springer, 2007. DOI: `10.1007/978-3-540-73036-1`.

[60] C. Cui, B. Hu, L. Zhao, and S. Liu, "Titanium alloy production technology, market prospects and industry development," *Materials & Design*, vol. 32, no. 3, pp. 1684–1691, Mar. 2011, ISSN: 0261-3069. DOI: `10.1016/j.matdes.2010.09.011`.

[61] *Current Rutile Price , Historical Prices, USA, China, Europe, Asia, Australia Prices.* [Online]. Available: `https://www.scrapmonster.com/metal-prices/minor-metals/rutile/771` (visited on 01/17/2025).

[62] *Current Ilmenite Price , Historical Prices, USA, China, Europe, Asia, Australia Prices.* [Online]. Available: `https://www.scrapmonster.com/metal-prices/minor-metals/ilmenite/700` (visited on 01/17/2025).

[63] P. Singh, H. Pungotra, and N. S. Kalsi, "On the characteristics of titanium alloys for the aircraft applications," *Materials Today: Proceedings*, International Conference on Advancements in Aeromechanical Materials for Manufacturing (ICAAMM-2016): Organized by MLR Institute of Technology, Hyderabad, Telangana, India, vol. 4, no. 8, pp. 8971–8982, Jan. 2017. DOI: `10.1016/j.matpr.2017.07.249`.

[64] T. Shrestha, *Microstructural evolution, its effect on Ti6Al4V alloy | Thermal Processing Magazine*, Oct. 2019. [Online]. Available: `https://thermalprocessing.com/microstructural-evolution-its-effect-on-ti6al4v-alloy/`.

[65] *ASM Material Data Sheet.* [Online]. Available: `https://asm.matweb.com/search/SpecificMaterial.asp?bassnum=MTP641` (visited on 01/17/2025).

[66] F. Trevisan, F. Calignano, A. Aversa, G. Marchese, M. Lombardi, S. Biamino, D. Ugues, and D. Manfredi, "Additive manufacturing of titanium alloys in the biomedical field: Processes, properties and applications," *Journal of Applied Biomaterials & Functional Materials*, vol. 16, no. 2, pp. 57–67, Apr. 2018, Publisher: SAGE Publications. DOI: `10.5301/jabfm.5000371`.

[67] J. P. Li, P. Habibovic, M. van den Doel, C. E. Wilson, J. R. de Wijn, C. A. van Blitterswijk, and K. de Groot, "Bone ingrowth in porous titanium implants produced by 3D fiber deposition," *Biomaterials*, vol. 28, no. 18, pp. 2810–2820, 2007. DOI: `10.1016/J.BIOMATERIALS.2007.02.020`.

[68] S. Mukherjee, S. Dhara, and P. Saha, "Enhancing the biocompatibility of Ti6Al4V implants by laser surface microtexturing: An in vitro study," *The International Journal of Advanced Manufacturing Technology*, vol. 76, no. 1, pp. 5–15, Jan. 2015. DOI: `10.1007/s00170-013-5277-2`.

[69] P. K. Srivas, K. Kapat, S. K. Chaitanya, S. Koley, B. Su, and S. Dhara, "Net shape forming of Ti6Al4V implants via green machining," *Journal of Materials Research*, vol. 36, 2021. DOI: `10.1557/s43578-021-00360-w`.

[70] X. Wang, Q. Guo, Y. He, X. Geng, C. Wang, Y. Li, Z. Li, C. Wang, D. Qiu, and H. Tian, "A pH-neutral bioactive glass coated 3D-printed porous Ti6Al4V scaffold with enhanced osseointegration," *Journal of Materials Chemistry B*, vol. 11, no. 6, pp. 1203–1212, Feb. 2023, Publisher: The Royal Society of Chemistry. DOI: `10.1039/D2TB02129C`.

[71] *Can dental implants be removed? Dental Implant Learning Center.* [Online]. Available: `https://www.lewisdentistry.com/dental-implants/learning-center/dental-implant-function/removal/` (visited on 01/17/2025).

[72] M. Ashby, *Material Selection Charts*, Oct. 2020. [Online]. Available: `https://proxom.net/material-selection/` (visited on 01/17/2025).

[73] Y. A. Alshataif, S. Sivasankaran, F. A. Al-Mufadi, A. S. Alaboodi, and H. R. Ammar, "Manufacturing Methods, Microstructural and Mechanical Properties Evolutions of High-Entropy Alloys: A Review," *Met. Mater. Int.*, vol. 26, no. 8, pp. 1099–1133, Aug. 2020, ISSN: 2005-4149. DOI: `10.1007/s12540-019-00565-z`.

[74] O. D. Neikov, "Chapter 5 - Atomization and Granulation," in *Handbook of Non-Ferrous Metal Powders*, O. D. Neikov, S. S. Naboychenko, I. V. Murashova, V. G. Gopienko, I. V. Frishberg, and D. V. Lotsko, Eds., Oxford: Elsevier, Jan. 2009, pp. 102–142. DOI: `10.1016/B978-1-85617-422-0.00005-7`.

[75] R. M. German, *Powder metallurgy and particulate materials processing: the processes, materials, products, properties and applications.* Princeton, New Jersey: Metal Powder Industries Federation, 2005, Open Library ID: OL3439416M, ISBN: 978-0-9762057-1-5.

[76] T. Tingskog, *An introduction to metal powders for Additive Manufacturing*, Jun. 2018. [Online]. Available: `https://www.metal-am.com/articles/metal-powders-for-3d-printing-manufacturing-processes-and-properties/`.

[77] A. Mostafaei, P. Rodriguez De Vecchis, I. Nettleship, and M. Chmielus, "Effect of powder size distribution on densification and microstructural evolution of binder-jet 3D-printed alloy 625," *Materials & Design*, vol. 162, pp. 375–383, Jan. 2019. DOI: `10.1016/j.matdes.2018.11.051`.

[78] E. Baştürk, E. Çakmakçi, S. Madakbaş, and M. V. Kahraman, "Surface and proton conductivity properties of electrospun poly(vinyl butyral)/polyaniline nanofibers," *Advances in Polymer Technology*, vol. 37, no. 6, pp. 1774–1781, Oct. 2018. DOI: `10.1002/ADV.21836`.

[79] I. A. Novakov, S. V. Borisov, A. B. Kochnov, and M. A. Vaniev, "Investigation of Rheological Properties of Poly(Vinyl Butyral) Solutions in Methacrylic Monomers," *Polymer Science, Series D*, vol. 11, no. 3, pp. 22–27, 2018. DOI: `10.1134/S1995421218030139`.

[80] T. Ahlfeld, V. Guduric, S. Duin, A. R. Akkineni, K. Schütz, D. Kilian, J. Emmermacher, N. Cubo-Mateo, S. Dani, M. V. Witzleben, J. Spangenberg, R. Abdelgaber, R. F. Richter, A. Lode, and M. Gelinsky, "Methylcellulose – a versatile printing material that enables biofabrication of tissue equivalents with high shape fidelity," *Biomaterials Science*, vol. 8, no. 8, pp. 2102–2110, 2020. DOI: `10.1039/D0BM00027B`.

[81] M. Fahad, M. A. Khan, and M. Gilbert, "Investigation of Thermal Gel Formation of Methylcellulose in Glycols Using DSC and XRD," *Gels*, vol. 7, no. 4, p. 205, Dec. 2021, Number: 4 Publisher: Multidisciplinary Digital Publishing Institute. DOI: `10.3390/gels7040205`.

[82] P. Polamaplly, Y. Cheng, X. Shi, K. Manikandan, X. Zhang, G. E. Kremer, and H. Qin, "3D printing and characterization of hydroxypropyl methylcellulose and methylcellulose for biodegradable support structures," *Polymer*, vol. 173, pp. 119–126, May 2019. DOI: `10.1016/j.polymer.2019.04.013`.

[83] A. Z. Nelson, Y. Wang, Y. Wang, A. S. Margotta, R. L. Sammler, A. Izmitli, J. S. Katz, J. Curtis-Fisk, Y. Li, and R. H. Ewoldt, “Gelation under stress: Impact of shear flow on the formation and mechanical properties of methylcellulose hydrogels,” *Soft Matter*, vol. 18, no. 7, pp. 1554–1565, Feb. 2022, Publisher: The Royal Society of Chemistry. DOI: `10.1039/D1SM01711J`.

[84] J. Desbrieres, M. Hirrien, and S. Ross-Murphy, “Thermogelation of methylcellulose: Rheological considerations,” *Polymer*, vol. 41, pp. 2451–2461, Mar. 2000. DOI: `10.1016/S0032-3861(99)00413-9`.

[85] *Ceramics Processing with METHOCEL™ Details - Industrial Cellulosics by.* [Online]. Available: `https://www.industrialcellulosics.com/insights/ceramics-processing-with-methocel` (visited on 04/08/2025).

[86] M. Bading, O. Olsson, and K. Kümmerer, “Analysis of environmental biodegradability of cellulose-based pharmaceutical excipients in aqueous media,” *Chemosphere*, vol. 352, p. 141 298, Mar. 2024. DOI: `10.1016/j.chemosphere.2024.141298`.

[87] T.-Y. Chan and S.-T. Lin, “Effects of Stearic Acid on the Injection Molding of Alumina,” *Journal of the American Ceramic Society*, vol. 78, pp. 2746–2752, Apr. 2005. DOI: `10.1111/j.1151-2916.1995.tb08050.x`.

[88] R. J. Pugh and L. Bergstrom, Eds., *Surface and Colloid Chemistry in Advanced Ceramics Processing*. Boca Raton: CRC Press, Jul. 2017. DOI: `10.1201/9780203737842`.

[89] Y.-m. Li, X.-q. Liu, F.-h. Luo, and J.-l. Yue, “Effects of surfactant on properties of MIM feedstock,” *Transactions of Nonferrous Metals Society of China*, vol. 17, no. 1, pp. 1–8, Jan. 2007. DOI: `10.1016/S1003-6326(07)60039-9`.

[90] V. Momeni, S. Luca, J. Gonzalez-Gutierrez, S. Cano, E. Sueur, Z. Shahroodi, S. Schuschnigg, C. Kukla, and C. Holzer, “Binder System Composition on the Rheological and Magnetic Properties of Nd-Fe-B Feedstocks for Metal Injection Molding,” *Applied Sciences*, vol. 14, no. 13, p. 5638, Jan. 2024, Number: 13 Publisher: Multidisciplinary Digital Publishing Institute, ISSN: 2076-3417. DOI: `10.3390/app14135638`. [Online]. Available: `https://www.mdpi.com/2076-3417/14/13/5638` (visited on 07/22/2025).

[91] R. Eickhoff, S. Antusch, D. Nötzel, and T. Hanemann, “New Partially Water-Soluble Feedstocks for Additive Manufacturing of Ti6Al4V Parts by Material Extrusion,” *Materials*, vol. 16, no. 8, p. 3162, Jan. 2023, Number: 8 Publisher: Multidisciplinary Digital Publishing Institute. DOI: `10.3390/ma16083162`.

[92] *Stearic acid for synthesis 57-11-4*. [Online]. Available: `https://www.sigmaaldrich.com/BE/en/product/mm/800673` (visited on 05/26/2025).

[93] L. S.-T. Chan T.-Y., *Effects of Stearic Acid on the Injection Molding of Alumina*, 1995. DOI: `10.1111/j.1151-2916.1995.tb08050.x`.

[94] K.-S. Jaw, C.-K. Hsu, and J.-S. Lee, “The thermal decomposition behaviors of stearic acid, paraffin wax and polyvinyl butyral,” *Thermochimica Acta*, Material Chaaracterization by Thermal Analytical Methods, vol. 367-368, pp. 165–168, Mar. 2001. DOI: `10.1016/S0040-6031(00)00680-8`.

[95] L. Gorjan, C. Galusca, M. Sami, T. Sebastian, and F. Clemens, “Effect of stearic acid on rheological properties and printability of ethylene vinyl acetate based feedstocks for fused filament fabrication of alumina,” *Additive Manufacturing*, vol. 36, p. 101 391, Dec. 2020. DOI: `10.1016/j.addma.2020.101391`.

[96] F. Khalil, “Mélanges de polymères biodégradables immiscibles : Influence de la morphologie sur le contrôle de la libération de substances actives ou modèles,” Ph.D. dissertation, Université Claude Bernard - Lyon I, Jul. 2015.

[97] R. C. Willemse, A. Posthuma de Boer, J. van Dam, and A. D. Gotsis, “Co-continuous morphologies in polymer blends: The influence of the interfacial tension,” *Polymer*, vol. 40, no. 4, pp. 827–834, Feb. 1999. DOI: `10.1016/S0032-3861(98)00307-3`.

[98] M. A. Wagner, A. Hadian, T. Sebastian, F. Clemens, T. Schweizer, M. Rodriguez-Arbaizar, E. Carreño-Morelli, and R. Spolenak, “Fused filament fabrication of stainless steel structures - from binder development to sintered properties,” *Additive Manufacturing*, vol. 49, p. 102 472, Jan. 2022. DOI: `10.1016/j.addma.2021.102472`.

[99] W. Zhai, W. Zhou, and S. M. L. Nai, “Effect of Interface Wettability on Additively Manufactured Metal Matrix Composites: A Case Study of 316L-Y2O3 Oxide Dispersion-Strengthened Steel,” *Metals*, vol. 14, no. 2, p. 170, Feb. 2024, Number: 2 Publisher: Multidisciplinary Digital Publishing Institute. DOI: `10.3390/met14020170`.

[100] J. Yang, N. Heinichen, and S. S. Velankar, “The effect of particle wettability on the of rheology particulate suspensions with capillary force,” vol. 558, pp. 164–170, Dec. 2018. DOI: `10.1016/j.colsurfa.2018.08.062`.

[101] B. Xia and P. S. Krueger, “Rheology of particulate suspensions with non-Newtonian fluids in capillaries,” *Proceedings of the Royal Society A: Mathematical, Physical and Engineering Sciences*, vol. 478, no. 2262, p. 20 210 615, Jun. 2022, Publisher: Royal Society. DOI: `10.1098/rspa.2021.0615`.

[102] G. Kumar and K. N. Prabhu, “Review of non-reactive and reactive wetting of liquids on surfaces,” *Advances in Colloid and Interface Science*, vol. 133, no. 2, pp. 61–89, Jun. 2007. DOI: `10.1016/j.cis.2007.04.009`.

[103] G. Thavanayagam, D. L. Zhang, K. L. Pickering, and P. Cao, “Rheological Properties of Feedstock Composed of Titanium Alloy Powder and Polyethylene Glycol Based Binder System for Metal Injection Moulding,” in *Proceedings of the 8th Pacific Rim International Congress on Advanced Materials and Processing*, F. Marquis, Ed., Cham: Springer International Publishing, 2016, pp. 2363–2373. DOI: `10.1007/978-3-319-48764-9_293`.

[104] W. Widyastuti, B. A. Kurniawan, A. P. Wibowo, E. N. Falah, S. P. Wijaya, A. A. Pratama, N. Safrida, and F. Ali, “Rheology Investigation of Metal Injection Molding Feedstock Based on Powder Particle Shape and Solid Loading,” *Applied Mechanics and Materials*, vol. 918, pp. 27–33, 2024, Publisher: Trans Tech Publications Ltd. DOI: `10.4028/p-me6SpX`.

[105] P. D. Ewart, C. J. Verbeek, and S. Y. Ahn, “Comparative Rheology Techniques for Assessment of MIM Titanium Metal Powder Feedstocks,” *Key Engineering Materials*, vol. 770, pp. 195–205, 2018, Publisher: Trans Tech Publications Ltd. DOI: `10.4028/www.scientific.net/KEM.770.195`.

[106] S. Ami, “Metal Injection Moulding (MIM) feedstock preparation with dry and wet mixing: A rheological behaviour investigation,” Jan. 2008.

[107] Ç. Karataş and S. Sarıtaş, “Rheological properties of mixed gas and water atomized stainless steel powder MIM feedstock,” *International Journal of Powder Metallurgy (Princeton, New Jersey)*, vol. 37, pp. 39–44, Nov. 2001.

[108] *Extrusion: Where's the Data? The Importance of Melt Strength in Extrusion*, Jan. 2025. [Online]. Available: `https://www.ptonline.com/articles/what-about-melt-strength` (visited on 01/17/2025).

[109] *A guide to performing an accurate melt flow test.* [Online]. Available: `https://www.prestogroup.com/blog/a-guide-to-performing-an-accurate-melt-flow-test/` (visited on 05/27/2025).

[110] *ISO 286-1:2010.* [Online]. Available: `https://www.iso.org/fr/standard/45975.html` (visited on 01/17/2025).

[111] O. W. Atieno and G. Czél, "Strength evaluation and melt rheology of highly mineral filled polymer composites," *Multidiszciplináris Tudományok*, vol. 14, no. 4, pp. 149–166, Dec. 2024, Number: 4. DOI: `10.35925/j.multi.2024.4.13`.

[112] G. Thavanayagam, D. Zhang, K. Pickering, and S. Raynova, "A Study of Polyvinyl Butyryl Based Binder System in Titanium Based Metal Injection Moulding," *Key Engineering Materials*, vol. 520, pp. 167–173, Aug. 2012. DOI: `10.4028/www.scientific.net/KEM.520.167`.

[113] G. Thavanayagam, K. L. Pickering, J. E. Swan, and P. Cao, "Analysis of rheological behaviour of titanium feedstocks formulated with a water-soluble binder system for powder injection moulding," *Powder Technology*, vol. 269, pp. 227–232, Jan. 2015. DOI: `10.1016/j.powtec.2014.09.020`.

[114] G. Thavanayagam and J. E. Swan, "Optimizing hydride-dehydride Ti-6Al-4V feedstock composition for titanium powder injection moulding," *Powder Technology*, vol. 355, pp. 688–699, Oct. 2019. DOI: `10.1016/j.powtec.2019.07.091`.

[115] R. P. Chhabra, "Non-Newtonian Fluids: An Introduction," in *Rheology of Complex Fluids*, J. M. Krishnan, A. P. Deshpande, and P. B. S. Kumar, Eds., New York, NY: Springer New York, 2010, pp. 3–34. DOI: `10.1007/978-1-4419-6494-6_1`.

[116] *An introduction to rheological additives for coatings.* [Online]. Available: `https://www.l-i.co.uk/knowledge-centre/an-introduction-to-rheological-additives-for-coatings/` (visited on 07/15/2025).

[117] N. D. Polychronopoulos and J. Vlachopoulos, "Polymer Processing and Rheology," in *Functional Polymers*, ISSN: 2510-3466, Springer, Cham, 2019, pp. 133–180, ISBN: 978-3-319-95987-0. DOI: `10.1007/978-3-319-95987-0_4`. [Online]. Available: `https://link.springer.com/rwe/10.1007/978-3-319-95987-0_4` (visited on 08/08/2025).

[118] *G-Values: G', G" and tan | Practical Rheology Science | Prof Steven Abbott.* [Online]. Available: `https://www.stevenabbott.co.uk/practical-rheology/G-Values.php` (visited on 06/06/2025).

[119] R. G. Ricarte and S. Shanbhag, "A tutorial review of linear rheology for polymer chemists: Basics and best practices for covalent adaptable networks," *Polymer Chemistry*, vol. 15, no. 9, pp. 815–846, 2024, ISSN: 1759-9954, 1759-9962. DOI: `10.1039/D3PY01367G`. [Online]. Available: `https://xlink.rsc.org/?DOI=D3PY01367G` (visited on 08/17/2025).

[120] *Standard Specification for Additive Manufacturing Titanium-6 Aluminum-4 Vanadium with Powder Bed Fusion.* [Online]. Available: `https://www.astm.org/f2924-14r21.html` (visited on 01/17/2025).

[121] Y. M. Than, S. Suriyarak, and V. Titapiwatanakun, "Rheological Investigation of Hydroxypropyl Cellulose–Based Filaments for Material Extrusion 3D Printing," *Polymers*, vol. 14, no. 6, p. 1108, Jan. 2022, Publisher: Multidisciplinary Digital Publishing Institute, ISSN: 2073-4360. DOI: `10.3390/polym14061108`. [Online]. Available: `https://www.mdpi.com/2073-4360/14/6/1108` (visited on 08/10/2025).

[122] P. Filip, B. Hausnerova, and E. Hnatkova, "Continuous rheological description of highly filled polymer melts for material extrusion," vol. 20, p. 100 754, Sep. 2020. DOI: `10.1016/j.apmt.2020.100754`.

[123] C. Ajinjeru, V. Kishore, J. Lindahl, Z. Sudbury, A. A. Hassen, B. Post, L. Love, V. Kunc, and C. Duty, "The influence of dynamic rheological properties on carbon fiber-reinforced polyetherimide for large-scale extrusion-based additive manufacturing," *The International Journal of Advanced Manufacturing Technology*, vol. 99, no. 1, pp. 411–418, Oct. 2018. DOI: `10.1007/s00170-018-2510-z`.

[124] *Torque | Equation, Definition, & Units | Britannica*, Jan. 2025. [Online]. Available: `https://www.britannica.com/science/torque` (visited on 01/17/2025).

[125] F. Cerejo, D. Gatões, and M. T. Vieira, "Optimization of metallic powder filaments for additive manufacturing extrusion (MEX)," *Int J Adv Manuf Technol*, vol. 115, no. 7, pp. 2449–2464, Aug. 2021. DOI: `10.1007/s00170-021-07043-0`.

[126] P. Singh, V. K. Balla, A. Gokce, S. V. Atre, and K. H. Kate, "Additive manufacturing of Ti-6Al-4V alloy by metal fused filament fabrication (MF3): Producing parts comparable to that of metal injection molding," *Prog Addit Manuf*, vol. 6, no. 4, pp. 593–606, Dec. 2021. DOI: `10.1007/s40964-021-00167-5`.

[127] C. Gloeckle, T. Konkol, O. Jacobs, W. Limberg, T. Ebel, and U. A. Handge, "Processing of Highly Filled Polymer–Metal Feedstocks for Fused Filament Fabrication and the Production of Metallic Implants," *Materials*, vol. 13, no. 19, p. 4413, Jan. 2020, Number: 19 Publisher: Multidisciplinary Digital Publishing Institute. DOI: `10.3390/ma13194413`.

[128] *Material Extrusion Additive Manufacturing of Metal.* [Online]. Available: `https://encyclopedia.pub/entry/23676` (visited on 05/27/2025).

[129] R. M. German and A. Bose, *Injection Molding of Metals and Ceramics.* Metal Powder Industries Federation, 1997, Google-Books-ID: jXINAAAACAAJ, ISBN: 978-1-878954-61-9.

[130] J. Gonzalez-Gutierrez, S. Cano, S. Schuschnigg, C. Kukla, J. Sapkota, and C. Holzer, "Additive Manufacturing of Metallic and Ceramic Components by the Material Extrusion of Highly-Filled Polymers: A Review and Future Perspectives," *Materials 2018, Vol. 11, Page 840*, vol. 11, no. 5, p. 840, May 2018. DOI: `10.3390/MA11050840`.

[131] I. Zein, D. W. Hutmacher, K. C. Tan, and S. H. Teoh, "Fused deposition modeling of novel scaffold architectures for tissue engineering applications," *Biomaterials*, vol. 23, no. 4, pp. 1169–1185, Feb. 2002. DOI: `10.1016/S0142-9612(01)00232-0`.

[132] *Pollen AM | Pellet Additive Manufacturing.* [Online]. Available: `https://pollen.am/` (visited on 01/17/2025).

[133] K. A. McCullough, "Screw design and method for metal injection molding," US20080217817A1, Sep. 2008. [Online]. Available: `https://patents.google.com/patent/US20080217817A1/en` (visited on 05/26/2025).

[134] A. Curmi and A. Rochman, "From Theory to Practice: Development and Calibration of Micro Pellet Extruder for Additive Manufacturing," *Key Engineering Materials*, vol. 926, pp. 34–45, 2022, Conference Name: The 25th International Conference on Material Forming Publisher: Trans Tech Publications Ltd. DOI: `10.4028/p-b22a9a`.

[135] Q. He, J. Jiang, X. Yang, L. Zhang, Z. Zhou, Y. Zhong, and Z. Shen, "Additive manufacturing of dense zirconia ceramics by fused deposition modeling via screw extrusion," *Journal of the European Ceramic Society*, vol. 41, no. 1, pp. 1033–1040, Jan. 2021. DOI: `10.1016/j.jeurceramsoc.2020.09.018`.

[136] A. Moetazedian, J. Allum, A. Gleadall, and V. V. Silberschmidt, "Bulk-Material Bond Strength Exists in Extrusion Additive Manufacturing for a Wide Range of Temperatures, Speeds, and Layer Times," *3D Printing and Additive Manufacturing*, vol. 10, no. 3, pp. 514–523, Jun. 2023. DOI: `10.1089/3dp.2021.0112`.

[137] F. M. Mwema and E. T. Akinlabi, "Basics of Fused Deposition Modelling (FDM)," in *Fused Deposition Modeling: Strategies for Quality Enhancement*, F. M. Mwema and E. T. Akinlabi, Eds., Cham: Springer International Publishing, 2020, pp. 1–15. DOI: `10.1007/978-3-030-48259-6_1`.

[138] T. D'Amico and A. M. Peterson, "Bead parameterization of desktop and room-scale material extrusion additive manufacturing: How print speed and thermal properties affect heat transfer," *Additive Manufacturing*, vol. 34, p. 101 239, Aug. 2020. DOI: `10.1016/j.addma.2020.101239`.

[139] F. Lambiase, F. Pace, E. Andreucci, and A. Paoletti, "Flow rate-dependent interlayer adhesion in FDM: A thermal and mechanical analysis," *The International Journal of Advanced Manufacturing Technology*, vol. 136, no. 3, pp. 1703–1716, Jan. 2025. DOI: `10.1007/s00170-024-14943-4`.

[140] *3D Printing Raft: When Should You Use It?* Aug. 2024. [Online]. Available: `https://all3dp.com/2/3d-printing-raft-when-should-you-use-it/` (visited on 01/17/2025).

[141] S. Joshi, R. P. Martukanitz, A. R. Nassar, and P. Michaleris, *Additive Manufacturing with Metals: Design, Processes, Materials, Quality Assurance, and Applications*. Cham: Springer International Publishing, 2023. DOI: `10.1007/978-3-031-37069-4`.

[142] S. Santosh, M. S. S. Muthiah, and K. S. Nishad, "Influence of infill density on the mechanical properties and fracture behavior of 3D-printed PLA + components," *Macromolecular Research*, May 2025. DOI: `10.1007/s13233-025-00415-5`.

[143] C. Vălean, M. Baban, D. K. Rajak, and E. Linul, "Effect of multiple process parameters on optimizing tensile properties for material extrusion-based additive manufacturing," vol. 414, p. 135 015, Feb. 2024. DOI: `10.1016/j.conbuildmat.2024.135015`.

[144] S. Bakrani Balani, H. Mokhtarian, T. Salmi, and E. Coatanéa, "An Investigation of the Influence of Viscosity and Printing Parameters on the Extrudate Geometry in the Material Extrusion Process," *Polymers*, vol. 15, no. 9, p. 2202, Jan. 2023, Number: 9 Publisher: Multidisciplinary Digital Publishing Institute. DOI: `10.3390/polym15092202`.

[145] M. Faizaan, S. Shenoy Baloor, S. Nunna, R. Mallya, S. Rao Udupi, C. Ramanath Kini, S. R. Kada, and C. Creighton, “A study on the overall variance and void architecture on MEX-PLA tensile properties through printing parameter optimisation,” *Scientific Reports*, vol. 15, no. 1, p. 3103, Jan. 2025, Publisher: Nature Publishing Group. DOI: `10.1038/s41598-025-87348-2`.

[146] P. Zarean, P. Malgaroli, P. Zarean, D. Seiler, M. de Wild, F. M. Thieringer, and N. Sharma, “Effect of Printing Parameters on Mechanical Performance of Material-Extrusion 3D-Printed PEEK Specimens at the Point-of-Care,” *Applied Sciences*, vol. 13, no. 3, p. 1230, Jan. 2023, Number: 3 Publisher: Multidisciplinary Digital Publishing Institute. DOI: `10.3390/app13031230`.

[147] D. Singh, A. Rana, P. Sharma, P. M. Pandey, and D. Kalyanasundaram, “Microwave Sintering of Ti6Al4V: Optimization of Processing Parameters for Maximal Tensile Strength and Minimal Pore Size,” *Metals*, vol. 8, no. 12, p. 1086, Dec. 2018, Number: 12 Publisher: Multidisciplinary Digital Publishing Institute. DOI: `10.3390/met8121086`.

[148] *Why 3D Printed Objects Showing Stair-Stepping Effect? | Printing It 3D*. [Online]. Available: `https://printingit3d.com/why-3d-printed-objects-showing-stair-stepping-effect/` (visited on 01/17/2025).

[149] H. Brooks, A. Rennie, T. Abram, J. McGovern, and F. Caron, “Variable Fused Deposition Modelling - analysis of benefits, concept design and tool path generation,” in Sep. 2011, pp. 511–517. DOI: `10.1201/b11341-83`.

[150] G. Shibo, Q. Xuanhui, H. Xinbo, Z. Ting, and D. Bohua, “Powder injection molding of Ti–6Al–4V alloy,” *Journal of Materials Processing Technology*, vol. 173, no. 3, pp. 310–314, Apr. 2006. DOI: `10.1016/j.jmatprotec.2005.12.001`.

[151] R. M. German, *Sintering Theory and Practice*. Wiley, Jan. 1996, Google-Books-ID: yHpuQgAACAAJ, ISBN: 978-0-471-05786-4.

[152] *WHAT IS THE PROCESS OF MAKING CERAMICS?* [Online]. Available: `https://materialbehavior.blogspot.com/2020/05/what-is-process-of-making-ceramics.html` (visited on 05/21/2025).

[153] C. Suwanpreecha and A. Manonukul, “On the build orientation effect in as-printed and as-sintered bending properties of 17-4PH alloy fabricated by metal fused filament fabrication,” *Rapid Prototyping Journal*, vol. ahead-of-print, Jan. 2022. DOI: `10.1108/RPJ-07-2021-0174`.

[154] Z.-p. Xie, J.-s. Luo, X. Wang, J.-b. Li, and Y. Huang, “The effect of organic vehicle on the injection molding of ultra-fine zirconia powders,” *Materials & Design*, vol. 26, no. 1, pp. 79–82, Feb. 2005. DOI: `10.1016/j.matdes.2004.03.011`.

[155] D. F. Heaney and R. Spina, “Numerical analysis of debinding and sintering of MIM parts,” *Journal of Materials Processing Technology*, Advances in Materials and Processing Technologies, July 30th - August 3rd 2006, Las Vegas, Nevada, vol. 191, no. 1, pp. 385–389, Aug. 2007. DOI: `10.1016/j.jmatprotec.2007.03.080`.

[156] M. Sadaf, S. Cano, M. Bragaglia, S. Schuschnigg, C. Kukla, C. Holzer, L. Vály, M. Kitzmantel, F. Nanni, and J. Gonzalez-Gutierrez, “Comparative analysis of binder systems in copper feedstocks for metal extrusion additive manufacturing and metal injection moulding,” *Journal of Materials Research and Technology*, vol. 29, pp. 4433–4444, Mar. 2024. DOI: `10.1016/j.jmrt.2024.02.163`.

[157] I. Gibson, D. Rosen, B. Stucker, and M. Khorasani, *Additive Manufacturing Technologies*. Cham: Springer International Publishing, 2021. DOI: `10.1007/978-3-030-56127-7`.

[158] L. Spitaels, E. Riviere, A. Demarbaix, and F. Ducobu, "Adaptive Benchmarking Design for Additive Manufacturing Processes," *Measurement Science and Technology*, vol. 33, Mar. 2022. DOI: `10.1088/1361-6501/ac5877`.

[159] *ISO 17295:2023*. [Online]. Available: `https://www.iso.org/standard/76471.html` (visited on 01/17/2025).

[160] *NF EN ISO 4288*. [Online]. Available: `https://www.boutique.afnor.org/fr-fr/norme/nf-en-iso-4288/specification-geometrique-des-produits-gps-etat-de-surface-methode-du-profi/fa044881/6757` (visited on 06/05/2025).

[161] *Cross-Committee Collaboration: ISO/TC 261, ASTM F42 and ISO/TC 44/SC 14/WG 1*. [Online]. Available: `https://committee.iso.org/sites/tc261/home/news/content-left-area/Posted%20news/cross-committee-collaboration-is.html` (visited on 05/27/2025).

[162] P. Peças, I. Ribeiro, R. Folgado, and E. Henriques, "A Life Cycle Engineering model for technology selection: A case study on plastic injection moulds for low production volumes," *Journal of Cleaner Production*, vol. 17, no. 9, pp. 846–856, Jun. 2009, ISSN: 09596526. DOI: `10.1016/j.jclepro.2009.01.001`.

[163] *ISO 14040:2006*. [Online]. Available: `https://www.iso.org/fr/standard/37456.html`.

[164] *ISO 14044:2006*. [Online]. Available: `https://www.iso.org/fr/standard/38498.html`.

[165] D. T. Nguyen, E. Yu, C. Barry, and W.-T. Chen, "Energy consumption variability in life cycle assessments of injection molding processes: A critical review and future outlooks," vol. 452, p. 142 229, May 2024, ISSN: 0959-6526. DOI: `10.1016/j.jclepro.2024.142229`.

[166] M. P. Tinoco, É. M. de Mendonça, L. I. C. Fernandez, L. R. Caldas, O. A. M. Reales, and R. D. Toledo Filho, "Life cycle assessment (LCA) and environmental sustainability of cementitious materials for 3D concrete printing: A systematic literature review," *Journal of Building Engineering*, vol. 52, Jul. 2022. DOI: `10.1016/j.jobe.2022.104456`.

[167] J. Faludi, C. Bayley, S. Bhogal, and M. Iribarne, "Comparing environmental impacts of additive manufacturing vs traditional machining via life-cycle assessment," *Rapid Prototyping Journal*, vol. 21, no. 1, pp. 14–33, Jan. 2015. DOI: `10.1108/RPJ-07-2013-0067`.

[168] M. Hosne Mobarak, M. Aminul Islam, N. Hossain, M. Zobair Al Mahmud, M. Thohid Rayhan, N. Jahan Nishi, and M. Asaduzzaman Chowdhury, "Recent advances of additive manufacturing in implant fabrication-A review," *Applied Surface Science Advances*, vol. 18, pp. 2666–5239, 2023. DOI: `10.1016/j.apsadv.2023.100462`.

[169] A. Ciroth, "Data Quality in Life Cycle Inventories," in *Life Cycle Inventory Analysis : Methods and Data*, A. Ciroth and R. Arvidsson, Eds., Cham: Springer International Publishing, 2021, pp. 97–122. DOI: `10.1007/978-3-030-62270-1_5`.

[170] M. A. J. Huijbregts, Z. J. N. Steinmann, P. M. F. Elshout, G. Stam, F. Verones, M. Vieira, M. Zijp, A. Hollander, and R. van Zelm, "ReCiPe2016: A harmonised life cycle impact assessment method at midpoint and endpoint level," *Int J Life Cycle Assess*, vol. 22, no. 2, pp. 138–147, Feb. 2017. DOI: `10.1007/s11367-016-1246-y`.

[171] O. US EPA, *Tool for Reduction and Assessment of Chemicals and Other Environmental Impacts (TRACI)*, Data and Tools, Dec. 2015. [Online]. Available: `https://www.epa.gov/chemical-research/tool-reduction-and-assessment-chemicals-and-other-environmental-impacts-traci` (visited on 05/25/2025).

[172] *CML-IA Characterisation Factors.* [Online]. Available: `https://www.universiteitleiden.nl/en/research/research-output/science/cml-ia-characterisation-factors` (visited on 05/25/2025).

[173] O. Jolliet, M. Saadé-Sbeih, S. Shaked, A. Jolliet, and P. Crettaz, *ENVIRONMENTAL LIFE CYCLE ASSESSMENT.* 2015. DOI: `10.1201/b19138`.

[174] *Comparative LCA of conventional manufacturing vs. additive manufacturing: The case of injection moulding for recycled polymers*, ISSN: 1939-7038. [Online]. Available: `https://www.tandfonline.com/doi/epdf/10.1080/19397038.2021.1990435?src=getftr&utm_source=mendeley&getft_integrator=mendeley` (visited on 05/18/2025).

[175] K. Kellens, R. Mertens, D. Paraskevas, W. Dewulf, and J. R. Duflou, "Environmental Impact of Additive Manufacturing Processes: Does AM Contribute to a More Sustainable Way of Part Manufacturing?" *Procedia CIRP*, vol. 61, pp. 582–587, 2017. DOI: `10.1016/j.procir.2016.11.153`.

[176] *Manufacturing Dental Implants using Powder Injection Molding*, Issue: 1 Publisher: iMedPub Volume: 2, Jan. 2016. [Online]. Available: `https://scispace.com/papers/manufacturing-dental-implants-using-powder-injection-molding-y18aezyxgh` (visited on 05/21/2025).

[177] *The Pros and Cons of Titanium Dental Implants | Chicago Dental Implants*, Section: Blog, Dec. 2023. [Online]. Available: `https://newteethchicagodentalimplants.com/the-pros-and-cons-of-titanium-dental-implants/` (visited on 01/17/2025).

[178] "Injection-molding versus extrusion as manufacturing technique for the preparation of biodegradable implants," *European Journal of Pharmaceutics and Biopharmaceutics*, vol. 48, no. 2, pp. 113–121, Sep. 1999, Publisher: Elsevier. DOI: `10.1016/S0939-6411(99)00034-X`.

[179] *Freedom of form and superior properties.* [Online]. Available: `https://mim.demcon.com/technology` (visited on 05/19/2025).

[180] *How to find your 3D printing application fit: 10 criteria to consider*, Jun. 2022. [Online]. Available: `https://anisoprint.com/blog/how-to-find-your-3d-printing-application-fit-10-criteria-to-consider/` (visited on 05/19/2025).

[181] *Desktop injection molding machine - products.* [Online]. Available: `https://www.microplast.com/products.html` (visited on 05/18/2025).

[182] F. Hesser, M. Mihalic, B. Paichl, and M. Wagner, "Injection moulding unit process for LCA: Energy intensity of manufacturing different materials at different scales," *Journal of Reinforced Plastics and Composites*, vol. 36, Oct. 2016. DOI: `10.1177/0731684416674565`.

[183] M. Khalid and Q. Peng, *Sustainability and Environmental Impact of Additive Manufacturing: A Literature Review.* May 2020, Pages: 332. DOI: `10.14733/cadconfP.2020.328-332`.

[184] *[PDF] The potential of 3D printing to reduce the environmental impacts of production - Free Download PDF.* [Online]. Available: `https://silo.tips/download/the-potential-of-3d-printing-to-reduce-the-environmental-impacts-of-production` (visited on 05/23/2025).

[185] L. Suárez and M. Domínguez, "Sustainability and environmental impact of fused deposition modelling (FDM) technologies," *The International Journal of Advanced Manufacturing Technology*, vol. 106, no. 3, pp. 1267–1279, Jan. 2020. DOI: `10.1007/s00170-019-04676-0`.

[186] JCGM, "Evaluation of measurement data-Guide to the expression of uncertainty in measurement Évaluation des données de mesure-Guide pour l'expression de l'incertitude de mesure," 2008.

[187] A. Ciroth and R. Arvidsson, Eds., *Life Cycle Inventory Analysis: Methods and Data* (LCA Compendium – The Complete World of Life Cycle Assessment). Cham: Springer International Publishing, 2021. DOI: `10.1007/978-3-030-62270-1`.

[188] T. Anh, *Environmental impacts of plastic injection molding | Micro Systems*, May 2023. [Online]. Available: `https://www.medicalmicromolding.com/environmental-impacts-of-plastic-injection-molding/` (visited on 05/26/2025).

[189] hqt, *The Environmental Impact of Injection Moulding in China*, Jan. 2023. [Online]. Available: `https://www.ace-mold.com/environmental-impact-of-injection-moulding/` (visited on 05/26/2025).

[190] Z.-C. Liu, F. Islam, I. Z. Era, and M. Grandhi, "LCA-based environmental sustainability assessment of hybrid additive manufacturing of a turbine blade," vol. 2, Jan. 2023. DOI: `10.20517/gmo.2022.08`.

[191] T. Peng, "Energy Modelling for FDM 3D Printing from a Life Cycle Perspective," *International Journal of Manufacturing Research*, vol. 11, p. 1, Jan. 2017. DOI: `10.1504/IJMR.2017.10003722`.

[192] T. a. T. Hazzard, *3D Print Power Consumption - How Much Power Does a 3D Printer Use?* May 2016. [Online]. Available: `https://3dstartpoint.com/3d-print-power-consumption-how-much-power-does-a-3d-printer-use/` (visited on 05/21/2025).

[193] M. Gao, L. Li, Q. Wang, C. Liu, X. Li, and Z. Liu, "Feature-based energy consumption quantitation strategy for complex additive manufacturing parts," *Energy*, vol. 297, p. 131 249, Jun. 2024. DOI: `10.1016/j.energy.2024.131249`.

[194] Z. Yan, J. Huang, J. Lv, J. Hui, Y. Liu, H. Zhang, E. Yin, and Q. Liu, "A New Method of Predicting the Energy Consumption of Additive Manufacturing considering the Component Working State," *Sustainability*, vol. 14, no. 7, p. 3757, Jan. 2022, Number: 7 Publisher: Multidisciplinary Digital Publishing Institute. DOI: `10.3390/su14073757`.

[195] K. Gee and A. J. Hart, "Parametric Analysis of Relationships Among Part Geometry, Build Time, and Energy Consumption for Laser Powder Bed Fusion," American Society of Mechanical Engineers Digital Collection, Nov. 2024. DOI: `10.1115/DETC2024-142824`.

[196] "Analysis of Process Parameters affecting Energy Consumption in Plastic Injection Moulding," *Procedia CIRP*, vol. 69, pp. 342–347, Jan. 2018, Publisher: Elsevier. DOI: `10.1016/J.PROCIR.2017.11.042`.

[197] A. Thiriez and T. Gutowski, "An Environmental Analysis of Injection Molding," in *Proceedings of the 2006 IEEE International Symposium on Electronics and the Environment, 2006.*, ISSN: 2378-7260, May 2006, pp. 195–200. DOI: `10.1109/ISEE.2006.1650060`. [Online]. Available: `https://ieeexplore.ieee.org/document/1650060` (visited on 05/17/2025).

[198] "Enhancing EDM Productivity for Plastic Injection Mold Manufacturing: An Experimental Optimization Study," *Polymers*, vol. 16, no. 21, pp. 3019–3019, Oct. 2024, Publisher: Multidisciplinary Digital Publishing Institute, ISSN: 2073-4360. DOI: `10.3390/polym16213019`.

[199] J. R. C. Dizon, A. D. Valino, L. R. Souza, A. H. Espera, Q. Chen, and R. C. Advincula, "Three-dimensional-printed molds and materials for injection molding and rapid tooling applications," *MRS Communications*, vol. 9, no. 4, pp. 1267–1283, Dec. 2019. DOI: `10.1557/mrc.2019.147`.

[200] D. V. Rosato, D. V. Rosato, and M. G. Rosato, Eds., *Injection Molding Handbook*. Boston, MA: Springer US, 2000. DOI: `10.1007/978-1-4615-4597-2`.

[201] *Injection Molding – What are the Advantages?* Apr. 2023. [Online]. Available: `https://www.3ds.com/make/solutions/blog/injection-molding-what-are-advantages` (visited on 05/20/2025).

[202] K. T. Gradin, *The common understanding of simplification approaches in published LCA studies—a review and mapping | The International Journal of Life Cycle Assessment.* DOI: `10.1007/s11367-020-01843-4`.

[203] Fairmat, *Part 1: Introduction to the "Simplified" LCA*, Sep. 2022. [Online]. Available: `https://www.fairmat.tech/blog/introduction-to-simplified-life-cycle-assessment/` (visited on 06/05/2025).

[204] M. Baumers, C. Tuck, R. Wildman, I. Ashcroft, and R. Hague, "Energy inputs to additive manufacturing: Does capacity utilization matter?" *22nd Annual International Solid Freeform Fabrication Symposium - An Additive Manufacturing Conference, SFF 2011*, Jan. 2011.

[205] A. H. Gutierrez-Osorio, L. Ruiz-Huerta, A. Caballero-Ruiz, H. R. Siller, and V. Borja, "Energy consumption analysis for additive manufacturing processes," *The International Journal of Advanced Manufacturing Technology*, vol. 105, no. 1, pp. 1735–1743, Nov. 2019. DOI: `10.1007/s00170-019-04409-3`.

[206] J. K. Watson and K. M. B. Taminger, "A decision-support model for selecting additive manufacturing versus subtractive manufacturing based on energy consumption,"

[207] M. R. Hasan, Z. Liu, and A. Rahman, *Energy Consumption Modeling for DED-based Hybrid Additive Manufacturing*, arXiv:2305.09104 [cond-mat], May 2023. DOI: `10.48550/arXiv.2305.09104`.

[208] "Specification for Additive Manufacturing Titanium-6 Aluminum-4 Vanadium ELI (Extra Low Interstitial) with Powder Bed Fusion," Feb. 2014. DOI: `10.1520/F3001-14`.

[209] *Brabender : Mélangeurs doseurs W30/W30 EHT et W50/W50 EHT*. [Online]. Available: `https://www.anton-paar.com/be-fr/produits/details/brabender-melangeurs-doseurs-w30w30-eht-et-w50w50-eht/` (visited on 01/17/2025).

[210] *Poly(ethylene glycol) 12,000 25322-68-3*. [Online]. Available: `https://www.sigmaaldrich.com/BE/en/product/aldrich/81285?msockid=183713cdeccb6b3c14ca0757ed9c6aa1` (visited on 05/26/2025).

[211] *MOWITAL® B 30 H | Product Finder.* [Online]. Available: `https://www.mowital.com/products/product-finder/b-30-h/` (visited on 05/26/2025).

[212] R. C. Hibbeler, *Engineering mechanics. Statics and dynamics.* New York : Macmillan ; London : Collier Macmillan, 1989, ISBN: 978-0-02-354461-3.

[213] F. Beer, *Mechanics of Materials*, ISBN: 978-1-260-11327-3.

[214] G. Author, *Polymer Blending, Mixing, Rheology, and R&D Extrusion*, Apr. 2010. [Online]. Available: `https://www.ulprospector.com/knowledge/1429/pe-polymer-blending-mixing-rheology/` (visited on 06/07/2025).

[215] *Compounder de laboratorio MC 15HT de Xplore.* [Online]. Available: `https://tecnosa.es/catalogo/plasticos/xplore/compounder-de-laboratorio-mc-15ht/` (visited on 03/21/2025).

[216] M. Das, "Effect of screw speed and plasticizer on the torque requirement in single screw extrusion of starch based plastics and their mechanical properties," *Indian Journal of Chemical Technology*, vol. 15, pp. 555–559, Nov. 2008.

[217] M. A. Gunning, L. M. Geever, J. A. Killion, J. G. Lyons, and C. L. Higginbotham, "Melt Processing of Bioplastic Composites via Twin Screw Extrusion and Injection Molding," *Polymer - Plastics Technology and Engineering*, vol. 53, no. 4, pp. 379–386, Mar. 2014. DOI: `10.1080/03602559.2013.844825`.

[218] *EN 843-1:2006 - Advanced technical ceramics - Mechanical properties of monolithic ceramics at room temperature - Part 1: Determination of flexural strength.* [Online]. Available: `https://standards.iteh.ai/catalog/standards/cen/9173f593-8000-4912-8bdd-cac344af379a/en-843-1-2006` (visited on 05/21/2025).

[219] rowanjenkins, *ASTM E8/E8M for Tension Testing of Metallic Materials in USA*, Mar. 2023. [Online]. Available: `https://matestlabs.com/test-standards/astm-e8/` (visited on 05/21/2025).

[220] C. Márquez Aragón, J. López, L. Cabrera, L. González, and J. Botana, "Study of the influence of laser energy density on the surface roughness of Scalmalloy ® samples manufactured by DMLS technology," *IOP Conference Series: Materials Science and Engineering*, vol. 1193, p. 012 036, Oct. 2021. DOI: `10.1088/1757-899X/1193/1/012036`.

[221] G. Wen, P. Cao, B. Gabbitas, D. Zhang, and N. Edmonds, "Development and Design of Binder Systems for Titanium Metal Injection Molding: An Overview," *Metallurgical and Materials Transactions A*, vol. 44, no. 3, pp. 1530–1547, Mar. 2013. DOI: `10.1007/s11661-012-1485-x`.

[222] A. Rodriguez, *8 Different Binders and Their Effects in Metal Injection Molding*, Dec. 2023. [Online]. Available: `https://redstonemanufacturing.com/8-different-binders-and-their-effects-in-metal-injection-molding/` (visited on 06/07/2025).

[223] TA Instruments, *RHEOLOGY APPLICATIONS NOTE.* [Online]. Available: `https://nopr.niscpr.res.in/bitstream/123456789/2869/1/IJCT%2015%286%29%20555-559.pdf` (visited on 06/06/2025).

[224] R. S. Lenk, "The Characterisation of Viscous Flow. Viscosity, Shear Rate and Shear Stress," in *Polymer Rheology*, R. S. Lenk, Ed., Dordrecht: Springer Netherlands, 1978, pp. 1–14. DOI: `10.1007/978-94-010-9666-9_1`.

[225] F. Briatico-vangosa, “Extrusion of metal powder-polymer mixtures: Melt rheology and process stability,” *Journal of Materials Processing Technology*, Jan. 2019. DOI: `10.1016/J.JMATPROTEC.2019.116250`.

[226] S. Leb, “Understanding Rheological Characterization in Polymer Extrusion for Additive Manufacturing,” vol. 13, p. 12, 2024. DOI: `10.4172/2319`.

[227] E. Hnatkova, B. Hausnerova, A. Hales, L. Jiranek, and J. M. A. Vera, “Rheological investigation of highly filled polymers: Effect of molecular weight,” p. 040 003, 2015. DOI: `10.1063/1.4918891`.

[228] S. Y. M. Amin, K. R. Jamaludin, and N. Muhamad, “RHEOLOGICAL PROPERTIES OF SS316L MIM FEEDSTOCK PREPARED WITH DIFFERENT PARTICLE SIZES AND POWDER LOADINGS,” vol. 71, 2009.

[229] R. M. German, *Powder injection molding.* Princeton, N.J: Metal Powder Industries Federation, 1990, Open Library ID: OL1853722M, ISBN: 978-0-918404-95-4.

[230] J. M. Dealy, “Melt Rheology and Its Role in Plastics Processing - Theory and Applications,” 1990.

[231] A. N. Muranov, V. R. Lysenko, and M. A. Kocharov, “Rheological Behavior Features of Feedstocks with a Two-Component Wax–Polyolefin Binder Compared to Analogs Based on Polyoxymethylene,” *Journal of Composites Science*, vol. 8, no. 6, p. 199, Jun. 2024, Number: 6 Publisher: Multidisciplinary Digital Publishing Institute. DOI: `10.3390/jcs8060199`.

[232] J.-s. Wang and R. S. Porter, “On the viscosity-temperature behavior of polymer melts,” *Rheologica Acta*, vol. 34, no. 5, pp. 496–503, Sep. 1995. DOI: `10.1007/BF00396562`.

[233] N. Padhye, “Polymer Physics and Dynamics of Polymer Melts,” in *Molecular Mobility in Deforming Polymer Glasses: Theories and Applications*, N. Padhye, Ed., Cham: Springer International Publishing, 2021, pp. 1–17. DOI: `10.1007/978-3-030-82559-1_1`.

[234] K. Rinawa, S. N. Maiti, R. Sonnier, and J.-M. Lopez Cuesta, “Dynamic rheological studies and applicability of time–temperature superposition principle for PA12/SEBS-g-MA blends,” *Polymer Bulletin*, vol. 72, no. 12, pp. 3305–3324, Dec. 2015. DOI: `10.1007/s00289-015-1467-4`.

[235] P. C. Dawson, “Flow Properties of Molten Polymers,” in *Mechanical Properties and Testing of Polymers: An A–Z Reference*, G. M. Swallowe, Ed., Dordrecht: Springer Netherlands, 1999, pp. 88–95. DOI: `10.1007/978-94-015-9231-4_21`.

[236] T. Instruments, “Introduction to polymer melt rheology and its application in polymer processing,” [Online]. Available: `https:%5C%5Cwww.chemeurope.com/en/whitepapers/1126916/introduction-to-polymer-melt-rheology-and-its-application-in-polymer-processing.html` (visited on 06/09/2025).

[237] J. Vlachopoulos and D. Strutt, “The Role of Rheology in Polymer Extrusion,”

[238] K. Hyun, J. G. Nam, M. Wilhellm, K. H. Ahn, and S. J. Lee, “Large amplitude oscillatory shear behavior of PEO-PPO-PEO triblock copolymer solutions,” *Rheologica Acta*, vol. 45, no. 3, pp. 239–249, Jan. 2006. DOI: `10.1007/s00397-005-0014-x`.

[239] E. M. Burgeson and S. A. Rogers, “The mathematics of oscillatory recovery rheology with applications to experiments, the Cox-Merz rules, and the nonlinear modeling of common amplitude sweep behaviors,” *Rheologica Acta*, vol. 63, no. 6, pp. 423–442, Jun. 2024. DOI: `10.1007/s00397-024-01448-w`.

[240] G. M. Swallowe, D. Brewis, and D. Briggs, Eds., *Mechanical Properties and Testing of Polymers* (Polymer Science and Technology Series). Dordrecht: Springer Netherlands, 1999, vol. 3. DOI: `10.1007/978-94-015-9231-4`.

[241] C. Rauwendaal, “Polymer Extrusion,” in *Polymer Extrusion (Fifth Edition)*, C. Rauwendaal, Ed., Hanser, Jan. 2014, pp. I–XVI. DOI: `10.3139/9781569905395.fm`.

[242] M. Kontopoulou, “Applied Polymer Rheology: Polymeric Fluids with Industrial Applications,” *Applied Polymer Rheology: Polymeric Fluids with Industrial Applications*, Nov. 2011. DOI: `10.1002/9781118140611`.

[243] *Basics of rheology | Anton Paar Wiki.* [Online]. Available: `https://wiki.anton-paar.com/en/basics-of-rheology/` (visited on 06/06/2025).

[244] S. Khandavalli and J. P. Rothstein, “Large amplitude oscillatory shear rheology of three different shear-thickening particle dispersions,” *Rheol Acta*, vol. 54, pp. 601–618, 2015. DOI: `10.1007/s00397-015-0855-x`.

[245] E. Miller and J. P. Rothstein, “Control of the sharkskin instability in the extrusion of polymer melts using induced temperature gradients,” *Rheologica Acta*, vol. 44, no. 2, pp. 160–173, Dec. 2004, ISSN: 00354511. DOI: `10.1007/S00397-004-0393-4/FIGURES/15`.

[246] G. Singh, J.-M. Missiaen, D. Bouvard, and J.-M. Chaix, “Additive manufacturing of 17–4 PH steel using metal injection molding feedstock: Analysis of 3D extrusion printing, debinding and sintering,” *Additive Manufacturing*, vol. 47, p. 102 287, Nov. 2021. DOI: `10.1016/j.addma.2021.102287`.

[247] T. Hanemann, R. Heldele, T. Müller, and J. Hausselt, “Influence of Stearic Acid Concentration on the Processing of ZrO2 Containing Feedstocks Suitable for Micropowder Injection Molding,” *International Journal of Applied Ceramic Technology*, vol. 8, pp. 865–872, Apr. 2010. DOI: `10.1111/j.1744-7402.2010.02519.x`.

[248] L. Viitanen, I. Y. Miranda-Valdez, J. Koivisto, A. Puisto, and M. Alava, “Thermal gelation of cellulose based suspensions,” *Cellulose*, vol. 30, no. 7, pp. 4215–4223, May 2023. DOI: `10.1007/s10570-023-05150-7`.

[249] A. G. Hasib, S. Niauzorau, W. Xu, S. Niverty, N. Kublik, J. Williams, N. Chawla, K. Song, and B. Azeredo, “Rheology scaling of spherical metal powders dispersed in thermoplastics and its correlation to the extrudability of filaments for 3D printing,” *Additive Manufacturing*, vol. 41, May 2021, ISSN: 22148604. DOI: `10.1016/J.ADDMA.2021.101967`.

[250] A. Das, E. Gilmer, S. Biria, and M. Bortner, “Importance of Polymer Rheology on Material Extrusion Additive Manufacturing: Correlating Process Physics to Print Properties,” *ACS Applied Polymer Materials*, vol. 3, Feb. 2021. DOI: `10.1021/acsapm.0c01228`.

[251] A. Y. Malkin and A. I. Isayev, “6 - APPLICATIONS OF RHEOLOGY,” in *Rheology Concepts, Methods, and Applications (Second Edition)*, A. Y. Malkin and A. I. Isayev, Eds., Oxford: Elsevier, Jan. 2012, pp. 365–420. DOI: `10.1016/B978-1-895198-49-2.50011-6`.

[252] T. G. Mezger, *The Rheology Handbook*. Dec. 2020, ISBN: 978-3-86630-864-0.

[253] K. Sakaue, "Viscoelastic and Viscoplastic Behavior of Polymer and Composite | SpringerLink," vol. 188, 2023.

[254] J. E. Mark, Ed., *Physical Properties of Polymers Handbook*. New York, NY: Springer, 2007. DOI: `10.1007/978-0-387-69002-5`.

[255] J. Li, Z. Hu, S. Zhang, H. Zhang, S. Guo, G. Zhong, Y. Qiao, Z. Peng, Y. Li, S. Chen, G. Chen, and A.-M. Cao, "Molecular engineering of renewable cellulose biopolymers for solid-state battery electrolytes," *Nature Sustainability*, vol. 7, no. 11, pp. 1481–1491, Nov. 2024, Publisher: Nature Publishing Group. DOI: `10.1038/s41893-024-01414-7`.

[256] P. Mohammadi, *Aligning cellulose nanofibril dispersions for tougher fibers | Scientific Reports*, 2017.

[257] T. Li, *Developing fibrillated cellulose as a sustainable technological material | Nature*, 2021. DOI: `10.1038/s41586-020-03167-7`.

[258] W. Lengauer, I. Duretek, M. Fürst, V. Schwarz, J. Gonzalez-Gutierrez, S. Schuschnigg, C. Kukla, M. Kitzmantel, E. Neubauer, C. Lieberwirth, and V. Morrison, "Fabrication and properties of extrusion-based 3D-printed hardmetal and cermet components," *International Journal of Refractory Metals and Hard Materials*, vol. 82, pp. 141–149, Aug. 2019. DOI: `10.1016/j.ijrmhm.2019.04.011`.

[259] G. Singh, J.-M. Missiaen, D. Bouvard, and J.-M. Chaix, "Copper additive manufacturing using MIM feedstock: Adjustment of printing, debinding, and sintering parameters for processing dense and defectless parts," *Int J Adv Manuf Technol*, vol. 115, no. 1, pp. 449–462, Jul. 2021. DOI: `10.1007/s00170-021-07188-y`.

[260] H. Giberti, M. Strano, and M. Annoni, "An innovative machine for Fused Deposition Modeling of metals and advanced ceramics," *MATEC Web of Conferences*, vol. 43, p. 03 003, 2016, Publisher: EDP Sciences. DOI: `10.1051/matecconf/20164303003`.

[261] W. Hassan, M. A. Farid, A. Tosi, K. Rane, and M. Strano, "The effect of printing parameters on sintered properties of extrusion-based additively manufactured stainless steel 316L parts," *Int J Adv Manuf Technol*, vol. 114, no. 9, pp. 3057–3067, Jun. 2021. DOI: `10.1007/s00170-021-07047-w`.

[262] L. Waalkes, J. Längerich, F. Holbe, and C. Emmelmann, "Feasibility study on piston-based feedstock fabrication with Ti-6Al-4V metal injection molding feedstock," vol. 35, p. 101 207, Oct. 2020. DOI: `10.1016/j.addma.2020.101207`.

[263] C. Suwanpreecha, P. Seensattayawong, V. Vadhanakovint, and A. Manonukul, "Influence of Specimen Layout on 17-4PH (AISI 630) Alloys Fabricated by Low-Cost Additive Manufacturing," *Metall Mater Trans A*, vol. 52, no. 5, pp. 1999–2009, May 2021. DOI: `10.1007/s11661-021-06211-x`.

[264] M. K. Agarwala, "Fused Deposition of Ceramics and Metals: An Overview," 1996.

[265] Y. Abe, T. Kurose, M. V. A. Santos, Y. Kanaya, A. Ishigami, S. Tanaka, and H. Ito, "Effect of Layer Directions on Internal Structures and Tensile Properties of 17-4PH Stainless Steel Parts Fabricated by Fused Deposition of Metals," *Materials*, vol. 14, no. 2, p. 243, Jan. 2021, Number: 2 Publisher: Multidisciplinary Digital Publishing Institute, ISSN: 1996-1944. DOI: `10.3390/ma14020243`.

[266] J. Gonzalez-Gutierrez, D. Godec, C. Kukla, T. Schlauf, C. Burkhardt, and C. Holzer, *SHAPING, DEBINDING AND SINTERING OF STEEL COMPONENTS VIA FUSED FILAMENT FABRICATION*. Jun. 2017.

[267] J. Gonzalez-Gutierrez, D. Godec, R. Guráň, M. Spoerk, C. Kukla, and C. Holzer, “3D printing conditions determination for feedstock used in fused filament fabrication (FFF) of 17-4PH stainless steel parts,” *Metalurgija -Sisak then Zagreb-*, vol. 57, pp. 117–120, Nov. 2017.

[268] X. Kan, D. Yang, Z. Zhao, and J. Sun, “316L FFF binder development and debinding optimization,” *Materials Research Express*, vol. 8, Nov. 2021. DOI: `10.1088/2053-1591/ac3b15`.

[269] C. Kukla, J. Gonzalez-Gutierrez, S. Cano Cano, S. Hampel, C. Burkhardt, T. Moritz, and C. Holzer, *FUSED FILAMENT FABRICATION (FFF) OF PIM FEEDSTOCKS*. Jun. 2017.

[270] T. Kurose, Y. Abe, M. V. A. Santos, Y. Kanaya, A. Ishigami, S. Tanaka, and H. Ito, “Influence of the Layer Directions on the Properties of 316L Stainless Steel Parts Fabricated through Fused Deposition of Metals,” *Materials*, vol. 13, no. 11, p. 2493, Jan. 2020, Number: 11 Publisher: Multidisciplinary Digital Publishing Institute. DOI: `10.3390/ma13112493`.

APPENDIX A

Feedstock formulations

Metal Injection Molding (MIM) Feedstocks

Alloy	**Powder Characteristics**	**Solid Loading**	**Binder**	**Feedstock Description**	**Debinding Process**	**Ref.**
17-4PH	SP 2-10 μm	93.5 wt.%	PEG + wax	PolyMIM	SD H_2O 60°C 12h, TD He-H_2 500°C	[54, 246]
316L	ND	55 vol.%	Thermoplastic	3 mm granules	TD 450°C + 600°C	[54]
WC-Co	ND	ND	TPE + PP	MIM 3 mm granules	SD H_2O + inhibitor, TD 600-800°C H_2/N_2	[258]
Cu	D50=5.9 μm	93.5 wt.%	PEG + wax	PolyMIM Cu999	SD H_2O 60°C 48-72h, TD He-H_2 500°C	[53, 259]
17-4PH	ND	79 vol.%	PEG	ND	SD H_2O 60°C 10h	[260]
316L	Sandvik Osprey	63 vol.%	Embemould K83	Granules	SD H_2O 40°C 48h, TD 145°C + 300°C	[261]
Ti6Al4V	D90=19 μm	66 vol.%	Element 22	<9 mm granules	None	[262]
AZ91	$<$ 45 μm	64 vol.%	ND	ND	SD hexane 40°C, TD 350–460°C (HR 0.5°C/min)	[262]

Table A.1: MIM feedstock compositions from literature

Material Extrusion (MEX/PAM) Feedstocks

Type	**Alloy**	**Powder Characteristics**	**Solid Loading**	**Binder**	**Feedstock Description**	**Debinding Process**	**Ref.**
Filament	17-4PH	D50=3.97 μm	63 vol.%	Polymeric blend	1.75 mm	SD > 12h, TD 450°C 1.7h	[153, 263]
Filament	17-4PH	325 mesh	60 vol.%	Wax/polymer/tackifier/elastomer	1.78 mm	ND	[264]
Filament	17-4PH	10 μm	60 vol.%	POM, PP, PW	1.73 mm	TD 600°C, N_2 2h	[265]
Filament	17-4PH	D10=4.2, D50=12.3, D90=28.2 μm	55 vol.%	Multicomponent	1.75 mm	SD 23–75°C, TD 650°C, N_2/H_2	[266, 267]
Filament	316L	D50=30.8 μm and 10 μm	50 vol.%	PP, SEBS, PW, SA	ND	SD cyclohexane 60–70°C, TD 350–440°C H_2/Ar	[268]
Filament	316L	D50=2.8 μm	50 vol.%	LDPE, TPE, SA	1.75 mm	SD cyclohexane 60°C, TD 370–470°C H_2	[98]
Filament	316L	SP D50=6.05 μm	55 vol.%	TPE, PO, compatibilizer	In-house	SD 60°C, 3–12h	[269]
Filament	316L	Epson-Atmix	55 vol.%	TPE + PO + compatibilizers	2 mm	ND	[269]
Filament	316L	ND	60 vol.%	POM, PW	1.73 mm	TD 600°C, N_2 2h	[270]

Table A.2: MEX/PAM feedstock compositions from literature

APPENDIX B

Rheological properties of Highly filled PEG/PVB binder

In this section, the rheological behavior of the F0SA0MC formulation, composed of a PEG/PVB (50/50) binder system filled with 55 vol.% Ti6Al4V powder, is evaluated to define a preliminary processing window prior to the incorporation of surfactants (SA) and methylcellulose (MC). Figure B.1 presents the evolution of shear stress (τ) as a function of shear rate ($\dot{\gamma}$) at four different temperatures: 100, 120, 140, and 160 °C. This plot is essential to characterize the flowability of the composite system under conditions representative of extrusion-based additive manufacturing processes.

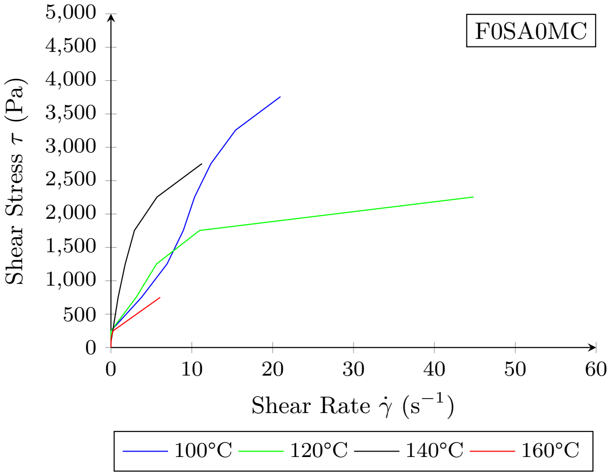

Figure B.1: Shear stress τ as a function of shear rate $\dot{\gamma}$ for F0SA0MC at 100, 120, 140 and 160°C.

At all temperatures, shear stress increases with shear rate, confirming the non-Newtonian behavior of the system. As temperature rises, the overall shear stress required to achieve a given shear rate decreases, indicating thermal softening of the binder and potential activation of polymer chain mobility. At 100°C, the feedstock exhibits high shear resistance, likely due to limited polymer chain mobility and increased solid-particle interaction. At 160°C, a smoother flow is observed, associated with reduced viscosity and improved wetting of the metal particles by the polymer matrix. This suggests that a processing window in the range of 140 to 160°C might be optimal, offering a compromise between sufficient fluidity and shape retention.

Figure B.2 illustrates the evolution of the complex viscosity (η^*) over time under a constant shear stress of 10 Pa and frequency of 1 Hz at 120°C. This time sweep test provides insights into the thermal and structural stability of the F0SA0MC feedstock over a duration of approximately 900 seconds.

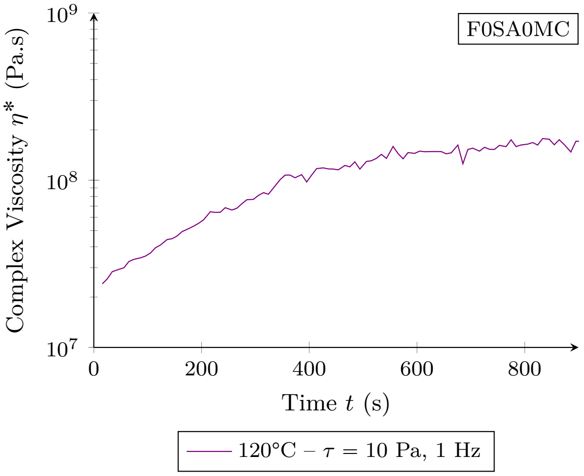

Figure B.2: Evolution of complex viscosity η^* as a function of time at τ = 10 Pa and f = 1 Hz at 120°C for F0SA0MC feedstock.

Initially, a rapid increase in viscosity is observed, likely corresponding to thermal equilibration and network structuring due to the interaction of polymer chains with the particulate surface. Following this phase, viscosity stabilizes around 10^8 Pa.s, suggesting no major degradation or phase separation occurs within this timeframe. This temporal stability is crucial for ensuring consistent flow and deposition quality during extrusion.

Figure B.3 examines the dependence of complex viscosity (η^*) on shear stress at different temperatures (100–160°C), recorded at a frequency of 1 Hz. This test allows us to assess the material's shear-thinning behavior, which is vital for printability and interlayer bonding.

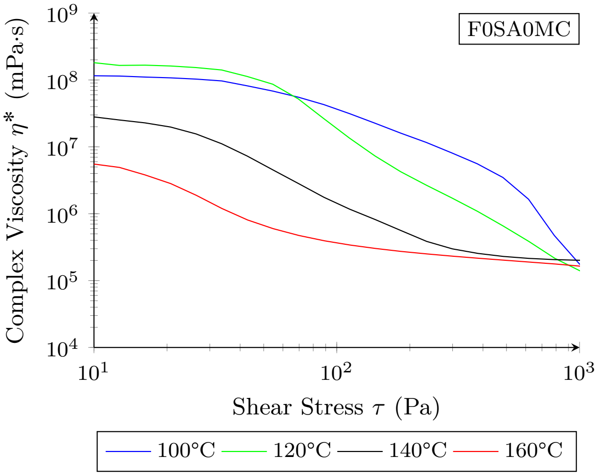

Figure B.3: Complex viscosity η^* as a function of shear stress τ at $f = 1$ Hz for F0SA0MC at 100, 120, 140, 160°C.

Across all temperatures, viscosity decreases with increasing shear stress, confirming a pseudoplastic or shear-thinning behavior. Notably, the viscosity drop is more pronounced at higher temperatures (140–160°C), implying that thermal energy facilitates polymer chain disentanglement and reorientation. The highest viscosity values are observed at 100°C, where the feedstock remains more solid-like. The clear separation between curves indicates a strong temperature dependency, reinforcing the need to operate above 120°C to maintain suitable processability.

Figure B.4 displays the complex viscosity (η^*) as a function of frequency (f) at a fixed shear stress of 10 Pa for temperatures ranging from 100 to 160°C. This frequency sweep is used to evaluate the viscoelastic behavior and time-dependent deformation capacity of the feedstock.

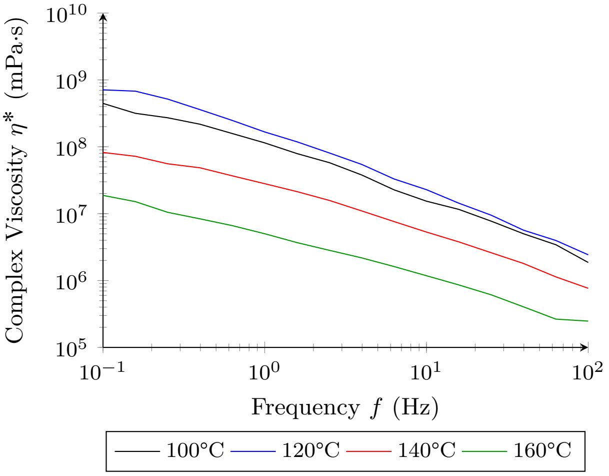

Figure B.4: Complex viscosity η^* as a function of frequency f at fixed shear stress $\tau = 10$ Pa for F0SA0MC feedstock ranging from 100 to 160°C.

The feedstock exhibits a typical decrease in viscosity with increasing frequency, characteristic of shear-thinning materials. At low frequencies, the high viscosity values reflect dominant elastic behavior due to entangled polymer chains and particle-particle interactions. As frequency increases, the system behaves more fluid-like, suggesting better flow dynamics under high deformation rates. This is beneficial for nozzle extrusion but requires balance to maintain part fidelity.

In Figure B.5, the apparent viscosity (η) is plotted against shear rate ($\dot{\gamma}$) in a log-log scale for the F0SA0MC feedstock. This measurement offers a macroscopic view of how the flow resistance of the composite evolves with processing intensity.

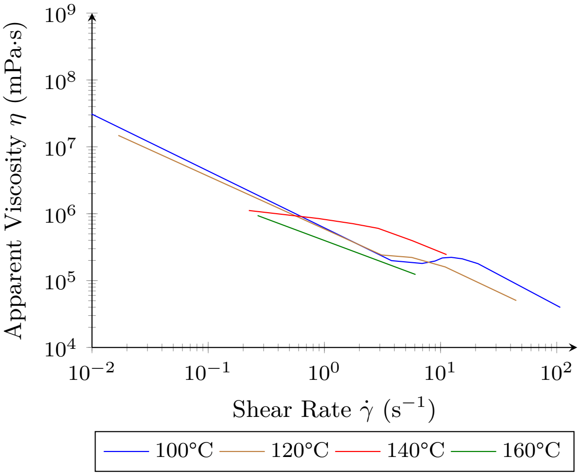

Figure B.5: Log-log plot of apparent viscosity η as a function of shear rate $\dot{\gamma}$ for F0SA0MC at different temperatures ranging from 100 to 160°C.

All curves exhibit a marked shear-thinning behavior with a slope close to -1 in the double-logarithmic domain, typical of filled polymer melts. This behavior is essential for PAM processes, where high shear in the nozzle is needed for deposition, followed by rapid solidification post-deposition. The temperature dependence is again evident, with the highest viscosities recorded at 100°C and progressively lower values at 160°C. This reinforces that the 140–160°C range offers an optimal processing zone.

Figure B.6 presents the storage modulus (G') and loss modulus (G") as a function of shear stress (τ) at 120°C. This dynamic stress sweep provides insight into the viscoelastic character and structural integrity of the feedstock under deformation.

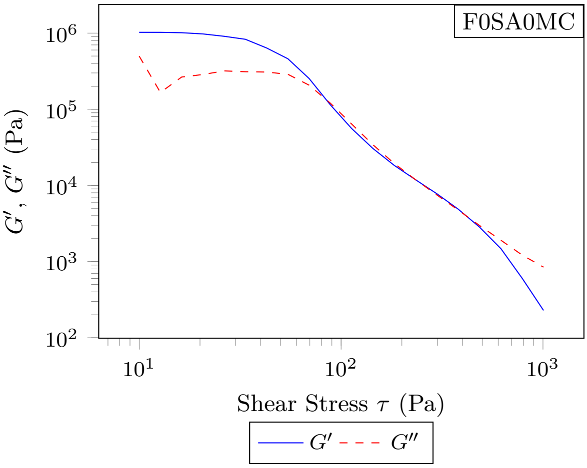

Figure B.6: Log-log plot of storage modulus (G') and loss modulus (G'') as a function of shear stress τ for F0SA0MC at 120°C.

At low shear stresses, G' > G" , indicating dominant elastic or solid-like behavior, likely due to strong interactions between the filler particles and the polymer matrix. As stress increases, both moduli decrease, and eventually G" > G', signaling a transition to a more viscous or liquid-like state. This crossover suggests the material yields under stress and begins to flow, a critical behavior to enable proper extrusion while retaining mechanical integrity in the deposited layer.

APPENDIX C

Thermogravimetric analysis

Thermogravimetric analysis was conducted on pure PEG to establish a thermal degradation baseline. The TGA curve (Figure C.1) shows a single, well-defined degradation step starting at approximately 290°C, with a peak decomposition rate observed at 356°C, as indicated by the DTG curve. The total mass loss reached 98%, leaving a minimal residue of about 2%, which confirms the complete volatilization of the organic compound under the test conditions. This sharp and symmetrical degradation profile is characteristic of PEG and aligns with literature values reported for PEG 4000–6000. These results provide a reference for evaluating the thermal behavior of more complex feedstock formulations, particularly those containing SA, PVB, and Ti6Al4V. Any shift in the onset temperature or change in the degradation profile in composite feedstocks would indicate interactions between PEG and other components.

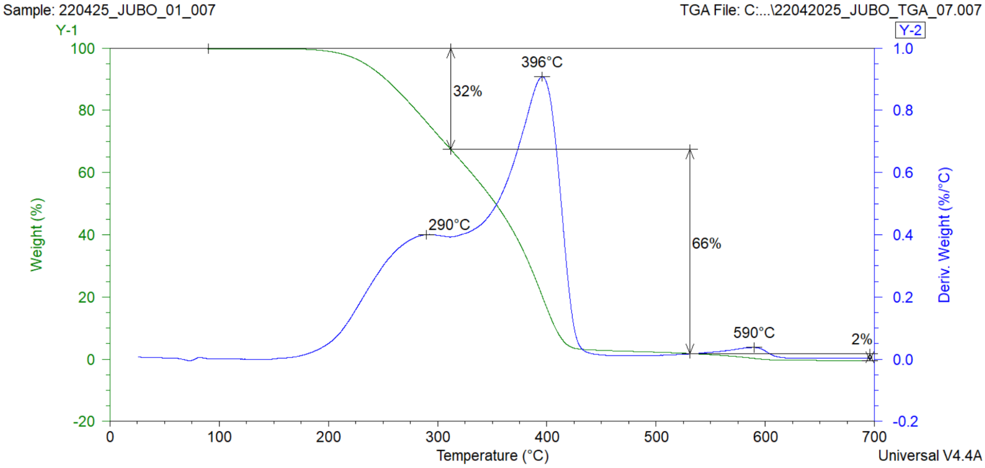

Figure C.1: TGA PEG

The thermogravimetric analysis of pure PVB is presented in Figure C.2. A single, sharp degradation event is observed, with the onset of weight loss beginning near 360°C and a peak degradation rate occurring at approximately 409°C. This indicates that PVB undergoes a rapid thermal decomposition in a narrow temperature range. The total mass loss reaches 98%, leaving only a small residue, which confirms the complete decomposition of the polymer under the experimental conditions. The absence of multiple steps suggests that the PVB used in this study is compositionally uniform, and its decomposition is not influenced by any other additives. This thermal behavior will serve as a reference for interpreting the stability of multi-component feedstocks containing PVB, such as those combined with PEG, SA, or titanium alloy powder.

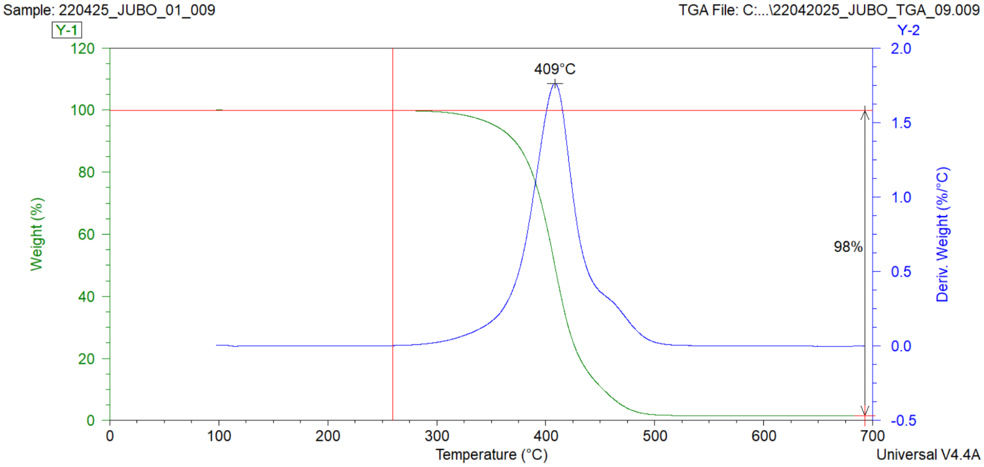

Figure C.2: TGA PVB

Figure C.3 presents the thermogravimetric profile of pure SA. The degradation starts sharply at around 250°C and reaches its maximum decomposition rate at approximately 274°C. The degradation occurs in a single, rapid step, with a complete mass loss (100%) observed, indicating full volatilization of the compound under the experimental conditions. No residual mass remains after thermal treatment, which is consistent with the low molecular weight and high volatility of SA. The narrow and symmetrical DTG peak confirms the purity and uniform decomposition behavior of the material. This thermal signature is particularly useful for evaluating the influence of SA in composite feedstocks, where early degradation could affect binder stability during the heating phase.

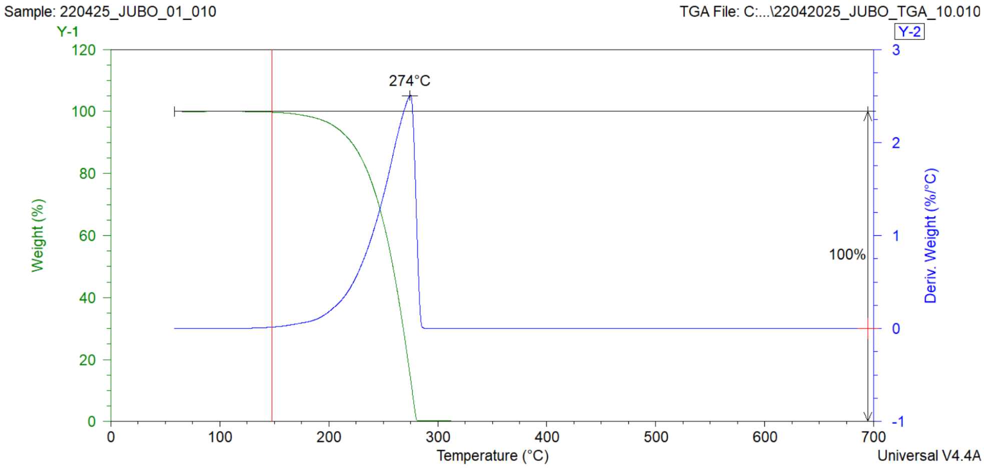

Figure C.3: TGA SA

The thermogravimetric analysis of MC is shown in Figure C.4. A single, pronounced degradation event is observed, beginning around 300°C and peaking at approximately 373°C. The mass loss reaches 91%, indicating that most of the polymer decomposes during this event. A small residue remains, likely due to inorganic components or char formation, which is common in cellulose-derived polymers. The narrow DTG peak suggests a relatively homogeneous decomposition mechanism. This thermal profile confirms that MC is thermally stable up to around 300°C, making it suitable for use as a binder component in feedstocks processed at moderate temperatures. However, its degradation temperature is higher than that of stearic acid and PEG, which may affect the order of degradation in multicomponent systems.

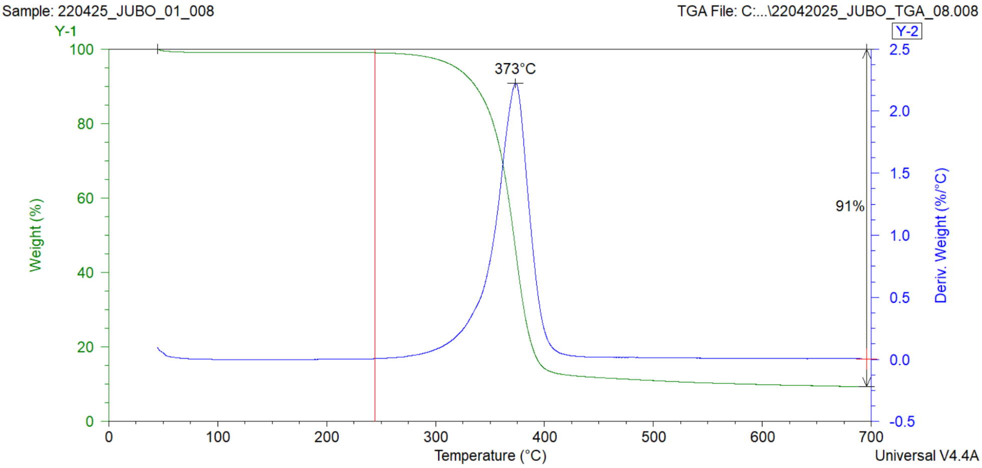

Figure C.4: TGA MC

APPENDIX D

Storage and Loss modulus of feedstock with SA or MC

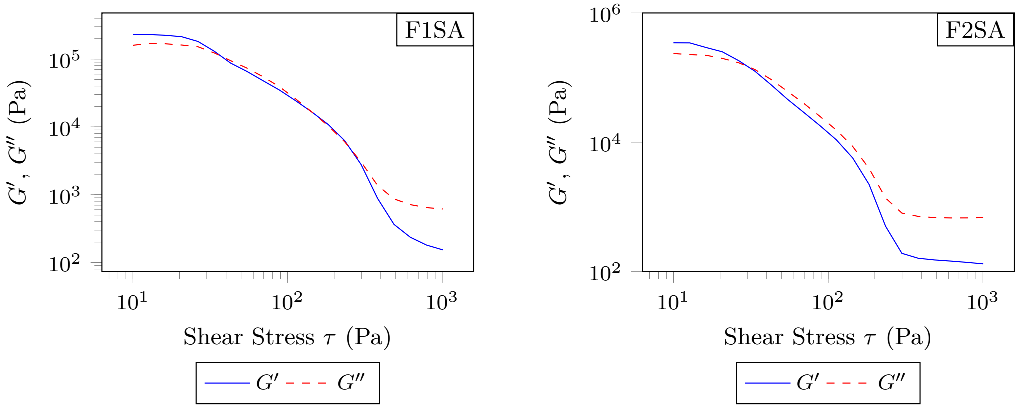

(a) F1SA

(b) F2SA

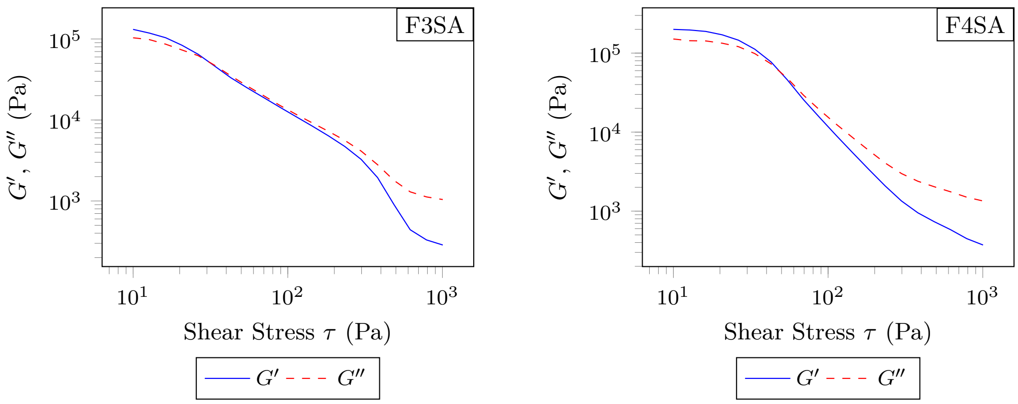

(c) F3SA

(d) F4SA

Figure D.1: Log-log plots of storage modulus (G') and loss modulus (G'') as a function of shear stress τ at 120°C for different feedstock formulations (F1SA to F4SA).

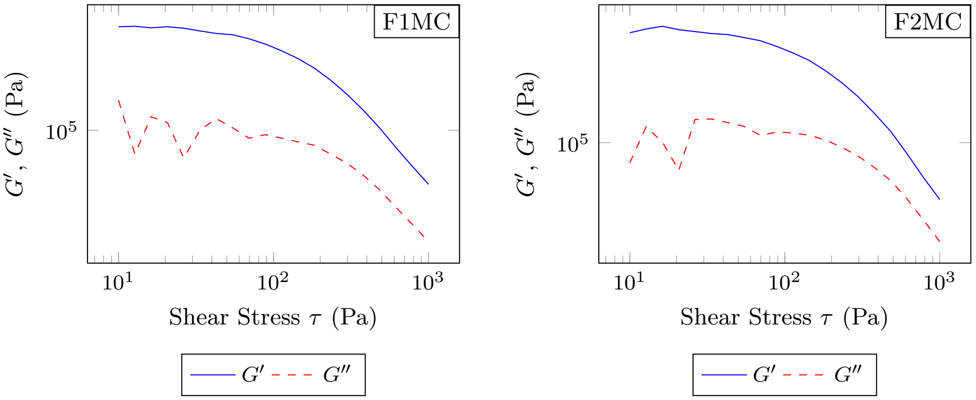

(a) F1MC (b) F2MC

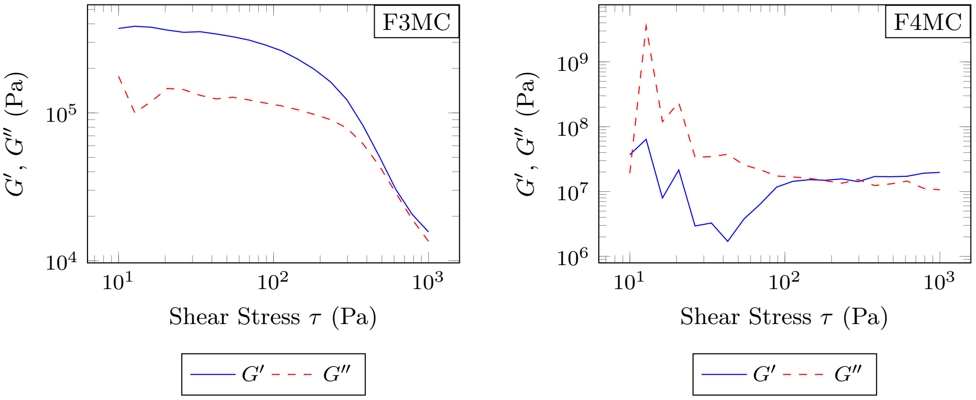

(c) F3MC (d) F4MC

Figure D.2: Log-log plots of storage modulus (G') and loss modulus (G'') as a function of shear stress τ for feedstocks F1MC to F4MC at 180°C.